Dynamically Enhancing Qubit-Photon Interactions with Anti-Squeezing

Marius Villiers

To cite this version:

Marius Villiers. Dynamically Enhancing Qubit-Photon Interactions with Anti-Squeezing. Quantum Physics [quant-ph]. Sorbonne Université, 2023. English. NNT : . tel-04209718

HAL Id: tel-04209718
https://hal.science/tel-04209718v1

Submitted on 18 Sep 2023

THÈSE DE DOCTORAT
SORBONNE UNIVERSITÉ

Spécialité : Physique
École doctorale nº564 : Physique en Île-de-France

réalisée
au Laboratoire de Physique de l'École Normale Supérieure
sous la direction de Zaki LEGHTAS

présentée par

Marius VILLIERS

pour obtenir le grade de :
DOCTEUR SORBONNE UNIVERSITÉ

Sujet de la thèse :

Accroissement dynamique du couplage entre un bit quantique et des photons comprimés

soutenue le 15 mai 2023

devant le jury composé de :

M.	Klaus MØLMER	Rapporteur
M.	Nicolas ROCH	Rapporteur
Mme	Audrey BIENFAIT	Examinatrice
M.	Nicolas TREPS	Examinateur
M.	Takis KONTOS	Membre invité
M.	Zaki LEGHTAS	Directeur de thèse

RÉSUMÉ

Les circuits supraconducteurs sont une plateforme de choix pour l'étude de l'interaction entre lumière et matière à l'échelle quantique. Lorsqu'un photon logé dans un oscillateur supraconducteur intéragit avec un système hybride tel qu'un mode mécanique, un ensemble de spins ou une boîte quantique, l'intensité de leur couplage dépend des fluctuations de point zéro de l'oscillateur. Le contrôle quantique du système hybride par les photons nécessite un couplage fort, c'est-à-dire un taux d'interaction supérieur aux taux de relaxations individuels. Ainsi, l'oscillateur doit être conçu de manière à maximiser les fluctuations du champ. Alors que certains systèmes prospèrent dans le régime de couplage fort, d'autres sont toujours en quête d'interactions croissantes.

À ce titre, il a récemment été proposé d'utiliser un oscillateur non-linéaire forcé par une excitation paramétrique hors-résonante. L'oscillateur de Bogoliubov (OB) qui en résulte apparait comme un oscillateur harmonique, dont les états propres sont des états de Fock comprimés. Lorsqu'il est couplé à un bit quantique, les fluctuations accrues des états propres de l'OB sont censées augmenter leur taux d'interaction. Cette thèse présente la première démonstration du couplage d'un OB électromagnétique à un bit quantique supraconducteur. L'OB est implémenté dans un résonateur supraconducteur intégrant des jonctions Josephson, et le bit quantique est de type transmon. Dans le régime dispersif, nous démontrons que la force d'interaction est multipliée par deux à 5,5 dB de compression. En outre, cette thèse présente une autre propriété intrigante des OB, à savoir leur capacité à amplifier des signaux sans être limités par le produit gain-bande passante, caractéristique très souhaitable pour les amplificateurs limités quantiquement. Enfin, le porte-échantillon JAWS est présenté, un élément clé d'ingénierie micro-ondes développé au LPENS.

En raison de l'omniprésence des forces électromagnétiques, cette thèse ouvre la voie au couplage des OB à une large gamme de systèmes hybrides. Elle met également en lumière les propriétés fascinantes de ces oscillateurs de photons comprimés, avec des applications allant de l'amplification limitée quantiquement à l'étude des transitions de phase quantiques.

REMERCIEMENTS

Il existe une blague donnant la partie ”Remerciements” d’une thèse comme étant la plus lue. Au fond, ce serait une bonne chose, car elle est celle qui fait la part belle à tous ceux sans qui un manuscrit comme celui-ci n’aurait jamais pu voir le jour.

Tout d’abord je souhaite remercier mon directeur de thèse, Zaki Leghtas, pour m’avoir enseigné l’art et la manière de résoudre des problèmes. Pendant ces longues années, j’ai toujours pu compter sur la finesse de ses analyses et son sang-froid très britannique pour aborder les situations les plus délicates, qu’elles soient d’ordre scientifique, expérimentales et théoriques, ou bien de nature humaine. C’est à ce soutien sans faille que je dois la réussite de ma thèse, et l’essentiel de ce que j’ai appris en chemin. Vient ensuite Takis Kontos, que je remercie pour m’avoir transmis son amour sans limites de la physique, et montré qu’aucun problème n’était trop compliqué pour oser s’y attaquer. Raphaël Lescanne et sa capacité de travail légendaire auront certainement eu un rôle déterminant dans mon parcours, comme l’exemple à suivre pour toujours continuer à avancer. Enfin je souhaite exprimer toute ma gratitude envers Clarke Smith pour les innombrables discussions de physique ou d’ailleurs que nous avons pu partager, et surtout pour avoir été un aussi bon ami.

Je tiens à remercier les membres de mon jury de thèse, mes rapporteurs Klaus Mølmer et Nicolas Roch pour leurs avis éclairés sur ce manuscrit, ainsi que mes examinateurs Audrey Bienfait et Nicolas Treps pour leur intérêt manifesté envers mes travaux. Viennent ensuite tous les membres de l’équipe Quantic, avec notamment Alexandru Petrescu et son apport théorique déterminant dans la dernière ligne droite de ma thèse, mais aussi Philippe Campagne-Ibarcq, Mazyar Mirrahimi, et Alain Sarlette pour leur soutien tout au long du projet. Cette équipe ne serait rien sans tous ses thésards et post-doctorants, avec notamment Alvise Borgognoni, Camille Berdou, Ulysse Réglade, Adrien Bocquet, Erwan Roverc’h, Aron Vanselow, Matthieu Praquin, Vincent Lienhard, Ronan Gautier, Christian Siegel, et Michiel Burgelman. La bonne humeur qui règne dans cette équipe me sera à jamais rappelée par la NintenJAW dont je remercie une fois de plus les créateurs Ulysse et Adrien. Au-delà de l'ENS et l'INRIA, cette thèse je la dois aussi à Emmanuel Flurin, Samuel Deléglise, Anil Murani, Sébastien Jezouin, et toute l'équipe d'Alice&Bob. Je souhaite également remercier toute l'équipe HQC, avec en premier lieu Matthieu Delbecq et Audrey Cottet pour la confiance qu'ils m'ont accordée en début de thèse, mais aussi Tino Cubaynes, Lauriane Contamin, William Legrand, Romaine Kerjouan, Vincent Vinel et François Mallet pour avoir partagé mes galères carbonées. Je souhaite bonne chance à la relève, menée par Benoît Neukelmance, Benjamin Hue, Lucas Jarjat, Jules Craquelin, Arnaud Thery et toute l'équipe de C12 pour leur quête de nanotubes et autres particules cachées de l'univers. Je voudrais aussi exprimer ma reconnaissance envers toutes les équipes du LPENS, la salle-blanche avec Michael Rosticher, José Palomo et Aurélie Pierret, les électroniciens Anne Denis et Philippe Pace, le bureau d'étude avec Pascal Morfin et Nabil Garroum, Matthieu Sardin de l'atelier mécanique, Olivier Andrieu de la cryo, et Olga Hodges des ressources humaines sans qui je n'aurais jamais pu signer de contrat de thèse.

Je souhaite remercier tous mes amis en dehors du laboratoire, Beurt, les Intellectuels, les Rtiz, les Divas et le Nunu, tous ceux qui m'ont accompagné pendant ces cinq années, qui m'ont soutenu dans les moments difficiles, mais qui ont aussi su se réjouir au gré de mes découvertes plus ou moins avérées. Merci à mes compagnons de couvre-feu, Marotte, Pilou, Marco et leurs sélections musicales, sans qui je n'aurais jamais pu me relever après tant d'agrafages ratés. Enfin je souhaite exprimer toute ma tendresse envers mes parents, Aliette et Henri, pour m'avoir toujours donné les moyens de réussir, ma soeur Fanny, pour son écoute et son réconfort, et mon beau-frère Andrés, nouveau compagnon de route à l'insatiable soif de savoir. Pour finir, c'est tout mon amour que je dirige vers Alice, soutien indéfectible de la dernière décennie, qui plus que tout autre m'aura porté au cours de cette longue aventure. Alice, cette thèse t'est dédiée.

ABSTRACT

Superconducting circuits are a prominent tool for the exploration of the interaction between light and matter in the quantum regime. Photons hosted in superconducting oscillators can be coupled to various hybrid systems such as mechanical vibrations, spin ensembles or quantum dots. Their interaction is mediated by electromagnetic forces, whose strength grows with the vacuum-field fluctuations of the oscillator. Quantum control of the hybrid system through the photons requires strong coupling, meaning an energy exchange rate greater than their individual relaxation rates. Thus, the oscillator ought to be designed as to maximize field fluctuations. While some hybrid systems are comfortably installed in the strong-coupling regime, some others are still seeking stronger interactions.

In that respect, it was recently proposed to use a nonlinear oscillator forced by a detuned parametric drive. The resulting Bogoliubov oscillator (BO) is effectively a harmonic oscillator, whose eigenstates are squeezed Fock states. When coupled to a qubit, the enhanced fluctuations of the BO eigenstates are expected to boost their interaction strength. This thesis presents the first demonstration of the squeezing-enhanced coupling of an electromagnetic BO to a superconducting qubit. The BO is emulated by a driven superconducting resonator enhanced by Josephson junctions, and the qubit is of the transmon design. In the dispersive regime, we demonstrate a two-fold increase of their interaction strength at 5.5 dB of squeezing. In addition, this thesis introduces another intriguing property of BOs, specifically, the ability to deliver amplification not constrained by the gain-bandwidth product. This is a highly desirable feature for quantum limited amplifiers, crucial for the operation of superconducting circuits. Finally, the JAWS sample-holder is presented, a key piece of engineering for microwave experiments designed at LPENS.

Owing to the ubiquity of electromagnetic forces, this thesis opens the way for the integration of BOs with a wide range of hybrid systems. It also sheds light on the fascinating properties of these oscillators of squeezed photons, applicable from quantum-limited amplification to the study of quantum phase-transitions.

CONTENTS

LIST OF FIGURES

LIST OF ACRONYMS

BO	Bogoliubov Oscillator
CPW	Coplanar WaveGuide
cQED	Circuit Quantum-ElectroDynamics
CNT	Carbon NanoTube
DPO	Degenerate Parametric Oscillator
JAWS	Joint Assembly for the Wiring of Superconducting circuits
JJ	Josephson Junction
QLE	Quantum Langevin Equation
RWA	Rotating-Wave Approximation
SNAIL	Superconducting Nonlinear Asymmetric Inductive eLement
SQUID	Superconducting QUantum Interference Device
SW	Schrieffer-Wolff
TLS	Two-Level System
TWPA	Traveling-Wave Parametric Amplifier

Even a stopped clock is right twice a day!
A physicist's nightmare envisioned by James Morgan ”Jimmy” McGill
a.k.a. Saul Goodman in *Better Call Saul*

1

INTRODUCTION

1.1 When the Rabi Hamiltonian meets the tank circuit

As elegantly demonstrated by Haroche and Raimond [Haroche and Raimond 2006], the quantum world can be very fruitfully described in terms *of spins and springs* (Fig. 1.1). On the one hand, a spin – understood to be a spin-1/2 – has only two possible configurations. It is the most nonlinear system imaginable, as the presence of a single excitation precludes the addition of another one. The Hilbert space of a spin-1/2 being limited to the span of two states, it is also refered to as a two-level system (TLS). While it is the rigorous description for the spin state of particles that actually posess a spin with value 1/2, any nonlinear system can be mapped onto an effective TLS, as soon as only two of its energy levels need consideration. For instance, the complex energy spectrum of an atom irradiated by a laser can be restricted to a pair of levels as soon the laser frequency is close from a single transition. Similarly, the vast stability diagram of a double quantum dot emulates a TLS under the appropriate biasing conditions [Petersson 2012]. On the other hand, a spring – meaning a quantum harmonic oscillator – is a linear system which can store an infinite number of excitations with the same quantum of energy. This powerful model maps to any quantum system slightly deviating from a stable equilibrium point, to lowest order in the deviation.

The modes of the electromagnetic field in free space can be quantized as harmonic oscillators. Yet, the harmonic approximation still holds in the presence of moving charges, in the limit where the mode wavelengths are large compared to the charge spatial extent [Cohen-Tannoudji 2001]. While the description of light involves linear degrees of freedom, the various forces holding matter together are the bedrock of nonlinearity. Thus, one of the most elementary modeling of the interaction between light and matter at the quantum level consists in a harmonic oscillator coupled to a TLS. The associated Hamiltonian was named after Rabi, and reads:

$$\boldsymbol{\mathcal{H}}/\hbar = \omega_{\mathrm{a}} \left(\mathbf{a}^\dagger \mathbf{a} + \frac{1}{2} \right) + \omega_q \frac{\boldsymbol{\sigma}_{\mathbf{z}}}{2} + g\big(\boldsymbol{\sigma}_{+} + \boldsymbol{\sigma}_{-}\big)\big(\mathbf{a} + \mathbf{a}^\dagger\big) \ . \tag{1.1}$$

The light part consists of a harmonic oscillator mode with frequency ω_{a},

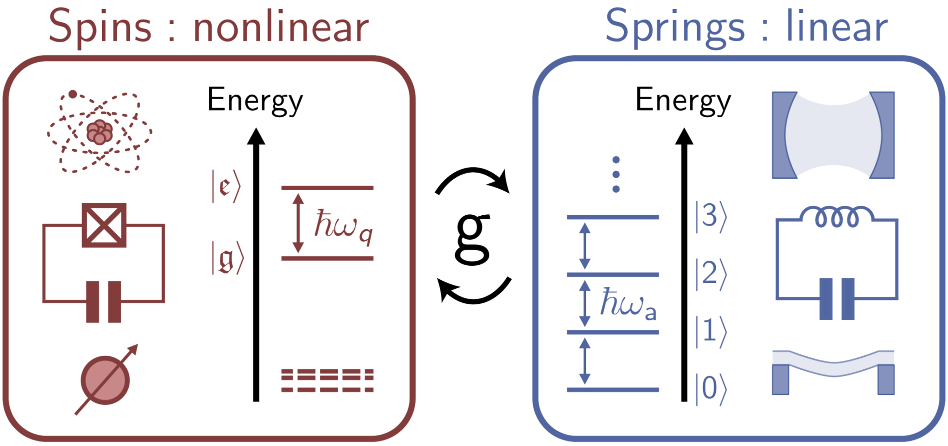

Figure 1.1 Coupling spins and springs. Spin-like degrees of freedom are systems nonlinear enough that only a couple of energy levels (labeled $|\mathfrak{g}\rangle$ and $|\mathfrak{e}\rangle$) are relevant to describe the physical process at stake. Among them we notably find atoms, Josephson circuits and spins. Spring-like degrees of freedom are linear systems that can be mapped to harmonic oscillators. Among them we notably find optical cavities, microwave oscillators and mechanical resonators. The Rabi Hamiltonian describes the coupled evolution of two such systems.

depicted by the bosonic annihilation operator $\mathbf{a}$, following the commutation relation $\left[\mathbf{a}, \mathbf{a}^\dagger\right] = \mathbb{1}$. The quantity $\hbar\omega_\mathrm{a}$, with $\hbar = h/2\pi$ the reduced Planck constant, gives the energy of the light quanta, namely, the photons. As for the matter part, it is reduced to a TLS with ground and excited levels $|\mathfrak{g}\rangle$ and $|\mathfrak{e}\rangle$, conveniently depicted in terms of Pauli raising and lowering operators $\boldsymbol{\sigma}_+ = |\mathfrak{e}\rangle\langle\mathfrak{g}|$ and $\boldsymbol{\sigma}_- = |\mathfrak{g}\rangle\langle\mathfrak{e}|$, with $\boldsymbol{\sigma}_\mathbf{z} = \left[\boldsymbol{\sigma}_+, \boldsymbol{\sigma}_-\right]$. The associated frequency ω_q yields the energy difference $\hbar\omega_q$ between the two states, akin to the Bohr frequency of an atomic transition. Finally, the interaction part consists in the simplest bilinear combination of creation and annihilation operators. The interaction rate g characterizes the susceptibility of the TLS transition to the light field. Owing to the duality of the electromagnetic field, the interaction process can be of electric or magnetic origin.

In addition to its exquisite simple formulation, the range of systems described by this Hamiltonian is unprecedented. While this description falls naturally at the heart of cavity-QED [Haroche and Raimond 2006], a wealth of inspired subfields has flourished over the past 20 years. Each of them deals with the interaction of light-like modes with matter-like modes. Among them we find solid-state cavity-QED in semiconducting heterostructures [İmamoğlu 1999], circuit-QED (cQED) where light and matter are emulated by collective excitations of superconductors at microwave frequencies [Blais 2021], cavity-optomechanics and cavity-electromechanics where radiation eitheir at optical or microwave frequency interacts with micromechanical resonators[1] [Aspelmeyer 2014], cavity-magnonics where microwave radiation interacts with spin-waves in ferromagnets [Lachance-Quirion 2019], hybrid-cQED with spins hosted either on quantum dots or in paramagnetic impurities [Clerk 2020], or even mesoscopic-cQED that focuses specifically on the coupling of superconducting circuits to fermionic degrees of freedom [Cottet 2017]. Finally, a TLS is the quantum equivalent of a classical bit – also called a quantum bit (qubit) – that is to say the simplest system able to store and process information. Thus, not only does Hamiltonian 1.1 give a very fundamental description of the interaction between light and matter, but it is also an elementary model for the treatment of quantum information.

The Rabi Hamiltonian can be derived from first principles in a variety of physical platforms. As it involves a single mode of light, most of its implementations rely on the confinement of a cavity. Like a particle trapped in a square potential [Basdevant and Dalibard 2002], light confined in a cavity unfolds in isolated modes. If the cavity finesse (or quality) is high enough, meaning if the modes are well separated, a single mode can be adressed consistently. Here we focus on a specific implementation of such a cavity, using superconducting circuits in a cQED architecture [Blais 2021]. Naturally endowed with small dissipation and high nonlinearity, superconducting circuits have benefited from a continuous improvement of nanofabrication techniques over the past 30 years to become a workhorse for experimental quantum physics. Using only three basic electrical components: the capacitor, the inductor, and the Josephson junction, cQED has succeeded in engineer-

---

[1] Mechanical systems are a special case. Apart from extreme structures such as carbon-nanotubes, their nonlinear response is usually accompanied by a breakdown of elasticity. Thus, they are mostly operated as linear systems, depicted by a bosonic operator $\mathbf{b}$. Then why do they appear in this listing? Their interaction with light is typically mediated by a radiation-pressure coupling, of nonlinear nature. Under driven evolution, this coupling yields a beam-splitter interaction [Regal 2008], whose Hamiltonian maps onto Eq. 1.1 by replacing $\boldsymbol{\sigma}_-$ by $\mathbf{b}$ [Clerk 2020]. Thus in the following of this introductory chapter, the fate of mechanical modes will be no different than the one of actual TLSs. In addition, one should notice a recent effort to use mechanics as a linear mode coupled to a superconducting qubit [Viennot 2018].

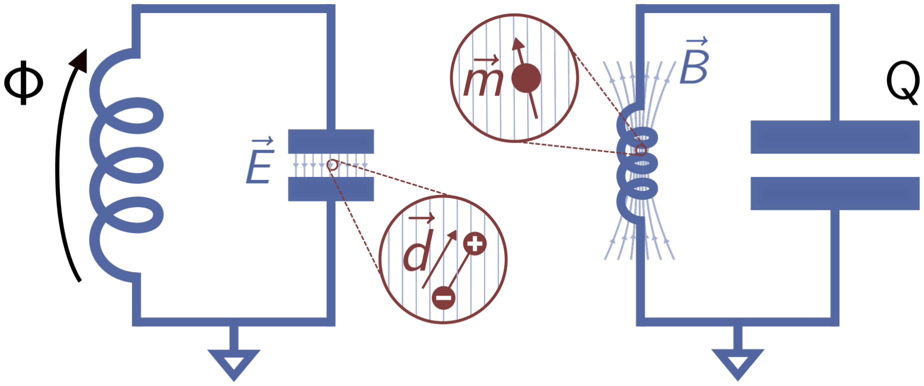

Figure 1.2 The Rabi Hamiltonian in cQED. A LC tank circuit (blue) is described in terms of the conjugate variables Φ and Q. The interaction with an electric dipole $\vec{d}$ is maximized when the electric field $\vec{E}$ is concentrated in a small capacitor (left). Conversely, the interaction with a magnetic dipole $\vec{m}$ is maximized when the magnetic field $\vec{B}$ is concentrated in a small inductor (right).

ing a wide class of Hamiltonians on chip, borrowed from quantum-optics to condensed-matter [Carusotto 2020]. In addition, owing to their great integrability, superconducting circuits are a prominent tool for the study of hybrid systems [Xiang 2013; Clerk 2020]. In this context, their simple operation and high sensitivity are leveraged to study faint signals emanating from complex media. While the naming found in the litterature is somewhat inconsistant, in this thesis we will refer to hybrid-cQED as the global effort to couple superconducting circuits to other types of systems.

The simplest linear superconducting circuit is the LC tank circuit, composed of an inductor L in parallel with a capacitor C (Fig. 1.2). It is a harmonic oscillator with frequency $\omega_\mathrm{a} = 1/\sqrt{LC}$, and when in contact with a bath of temperature T much less than $T_Q = \hbar\omega_\mathrm{a}/k_B$ with k_B the Boltzmann constant, it behaves quantum mechanically. There, it is conveniently described in terms of the flux $\boldsymbol{\Phi}$ threading the inductor, and the charge $\boldsymbol{Q}$ accumulated on the capacitor. These are the conjugate coordinates of the system, akin to the position and momentum of a mechanical oscillator, obeying the commutation relation $\left[\boldsymbol{\Phi}, \boldsymbol{Q}\right] = i\hbar$ [Vool and M. Devoret 2017]. One can resort to the quantum harmonic oscillator description by introducing:

$$\mathbf{a} = \frac{1}{2}\left(\frac{\boldsymbol{\Phi}}{\Phi_\mathrm{zpf}} + i\frac{\boldsymbol{Q}}{Q_\mathrm{zpf}}\right) \quad \Phi_\mathrm{zpf} = \sqrt{\frac{\hbar Z_0}{2}} \quad Q_\mathrm{zpf} = \sqrt{\frac{\hbar}{2Z_0}} \tag{1.2}$$

where $Z_0 = \sqrt{L/C}$ is the impedance of the circuit. Note that for a microwave oscillator with $\omega_\mathrm{a}/2\pi = 10$ GHz we find $T_Q = 480$ mK. Hence, at the lowest temperature stage of a dilution refrigerator ($T \approx 10$ mK), such circuits can be safely considered to be in there ground state. Note that this LC model is not limited to lumped-element circuits, but it is also a faithful representation of distributed-element oscillators [Pozar 2011]. The interaction of a LC circuit with a foreign TLS is mediated either by the electric field $\vec{E}$ stored in the capacitor, or by the magnetic field $\vec{B}$ stored in the inductor (Fig. 1.2). In the first case, introducing the transition electric dipole moment $d_{\mathfrak{eg}}$ between the two states of the TLS, the coupling strength to the tank circuit reads:

$$g = \frac{d_{\mathfrak{eg}} \times E_\mathrm{zpf}}{\hbar} \qquad E_\mathrm{zpf} \sim \frac{V_\mathrm{zpf}}{\sqrt[3]{v_E}} \qquad V_\mathrm{zpf} = \frac{Q_\mathrm{zpf}}{C} = \omega_\mathrm{a}\sqrt{\frac{\hbar Z_0}{2}} \tag{1.3}$$

where E_zpf are the zero-point fluctuations of the electric field, and v_E is the electric mode volume giving the typical scale over which the electric energy is stored. In the second case, introducing the transition magnetic dipole moment $m_{\mathfrak{eg}}$ between the two states of the TLS, the couping strength to the tank circuit reads:

$$g = \frac{m_{\mathfrak{eg}} \times B_\mathrm{zpf}}{\hbar} \qquad B_\mathrm{zpf} \sim \frac{I_\mathrm{zpf}}{\sqrt[3]{v_B}} \qquad I_\mathrm{zpf} = \frac{\Phi_\mathrm{zpf}}{L} = \omega_\mathrm{a}\sqrt{\frac{\hbar}{2Z_0}} \tag{1.4}$$

where B_zpf are the zero-point fluctuations of the magnetic fiel, and v_B is the magnetic mode volume giving the typical scale over which the magnetic energy is stored. Overall, the contribution of the bare oscillator to the coupling is set by the magnitude of its field fluctuations, ultimately set by the mode volume and its impedance.

So far, the nature of the TLS was left unspecified. Indeed, owing to the great integrability of superconducting circuits, the coupled system can be many things: as similar as another superconducting circuit [Blais 2021], or as different as a mechanical mode[2], an atom, a spin, or a fermionic reservoir [Xiang 2013; Clerk 2020]. Yet, as the difference between the coupled system and a superconducting circuit grows – meaning their sizes, energy scales, susceptibilities – their coupling is likely to diminish. Then, one may wonder how efficient a superconducting circuit can be in reading out the state of a system of a different kind, that we refer to as a *hybrid* system.

---

[2] Mechanical modes are usually very linear, see footnote 1 for details.

1.2 Strong coupling in hybrid circuit-QED

In an effort to explore the behaviour of hybrid systems using superconducting circuits, the LC oscillator presented earlier is typically used as a readout mode. It is coupled to a feedline at a rate κ, used by an observer to acquire information about the state of the coupled hybrid system. The latter can exchange energy with the oscillator at a rate g, but may also relax through internal channels at a rate γ. When the energy exchange rate between the oscillator and the hybrid part exceeds their individual relaxation rates ($g \gg \kappa,\ \gamma$), coupling can no longer be treated as a perturbation, and the system enters the strong-coupling regime. Only there can a full quantum control of the hybrid system be implemented through the oscillator.

Following the landmark experiment by the Yale group, that demonstrated strong coupling between a single photon in a microwave cavity and a superconducting qubit [A. Wallraff 2004], a quest started to reach a similar regime with hybrid systems. Notably, strong coupling was achieved with an acoustic mode [O'Connell 2010], with a paramagnetic spin ensemble [Kubo 2010; Schuster 2010], with the flexural mode of a mechanical resonator [Teufel 2011], with magnons [Huebl 2013], with Andreev bound states in an atomic contact [Janvier 2015], with the charge of a double quantum dot [Mi 2017; Stockklauser 2017], and with an electron spin trapped on a double quantum dot [Landig 2018; Mi 2018; Samkharadze 2018]. All these breakthrough were made possible by an optimization of the system parameters according to Eqs. (1.3, 1.4). Specifically, there are three strategies to increase g/ω_a.

The first one relies on tweaking the hybrid part to increase its transition dipole element ($d_\mathfrak{eg}$ or $m_\mathfrak{eg}$). Note that this strategy has been decisive in going from cavity-QED to cQED, where the dipole moment of artificial atoms emulated by superconducting circuits can be tuned at will, as opposed to real atoms [Blais 2004]. For instance in cavity-electromechanics, mechanical structures are routinely capacitively coupled to superconducting oscillators. While initial experiments used thin cantilevers embedded in capacitive elements, the shift to large mechanical membranes greatly increased the loaded charge of the mechanics, and in turn their electric dipole moment [Teufel 2011] (Fig. 1.3 a). For hybrid-cQED with actual spins, the size of an individual dipole cannot be tuned. Then, one can resort to a magnified dipole moment using collective excitations [Kubo 2010; Schuster 2010] (Fig. 1.3 c). Yet, this approach sacrificies the coherence properties of a single dipole. Thus, when collective effects are not an option, changing the nature of the dipole can be advantageous. This is the trick played by quasi-spin qubits, which rely on a combination of spin-orbit and large orbital-oscillator couplings to couple single spins to photons via charge degrees of freedom [Landig 2018; Mi 2018; Samkharadze 2018] (Fig. 1.3 d). In the same spirit, electromechanical flux coupling has recently been demonstrated, moving away from the paradigmatic charge coupling of a moving capacitor plate (Fig. 1.3 b).

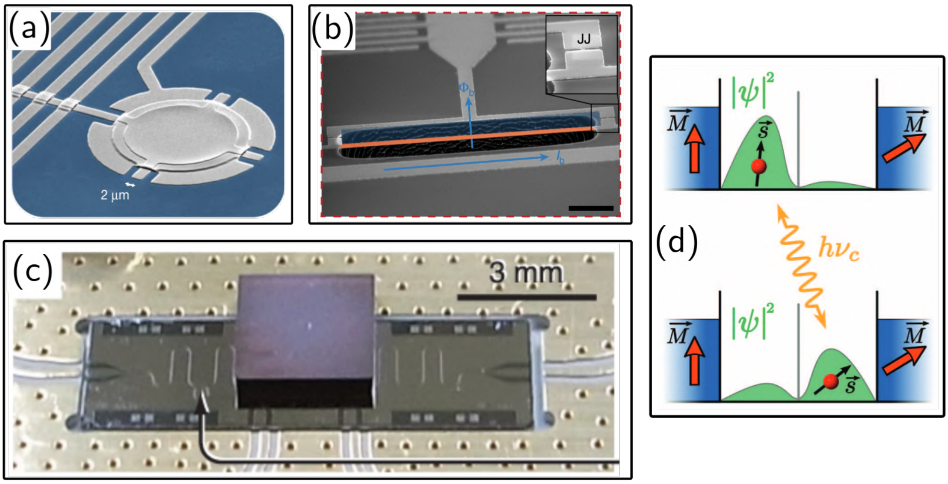

Figure 1.3 Quest for strong coupling: tweaking the dipole. (a) Vacuum gap capacitor of a LC resonator featuring a suspended micromechanical membrane [Teufel 2011]. (b) A nano-cantilever (orange) is flux coupled to an oscillator while embedded in a SQUID loop [Rodrigues 2019]. (c) Diamond crystal glued on top of a microwave oscillator [Kubo 2010]. (d) A quasi-spin qubit leverages the different magnetic environments (blue magnets) of the two localizations of an electron (green probabilities) to couple its spin to photons (orange arrow) [Viennot 2015].

The second one relies on minimizing the oscillator mode volume (v_E or v_B), concentrating the field lines around the hybrid system. Again this strategy was decisive for the advent of cQED, which benefited from a drastically reduced mode volume as compared to cavity-QED [Blais 2004]. Nowadays, field concentration remains a crucial parameter in the detection of paramagnetic spin impurities. Recently, a record detection volume of a few fL was reported in a LC oscillator featuring a nano-inductor, pushing the spin-photon coupling in the kHz range [Ranjan 2020] (Fig. 1.4 a). Yet, this strategy can only be implemented when the hybrid system is not dissipative, and concentrating field lines in its close neighboorhood does not degrade the oscillator quality.

Finally the third one relies on the oscillator impedance. It can be tuned geometrically by shaping the oscillator according to the coupling scheme. For instance, using large interdigitated capacitances lowers the oscillator impedance, and maximizes the coupling to magnetic dipoles (Fig. 1.4 a). Conversely, using very thin center conductors for distributed-element oscillators increases the mode impedance, and maximizes the coupling to eletric dipoles (Fig. 1.4 b). Next, the oscillator impedance can be increased beyond the vacuum impedance ($Z_{\mathrm{vac}} = \sqrt{\mu_0/\epsilon_0} \approx 377\ \Omega$) using high kinetic inductance materials [Landig 2018; Samkharadze 2018], or Josephson junction chains [Stockklauser 2017]. Yet, no such trick can be played to lower the impedance, since materials with large relative permittivity are usually very lossy, incompatible with superconducting circuits.

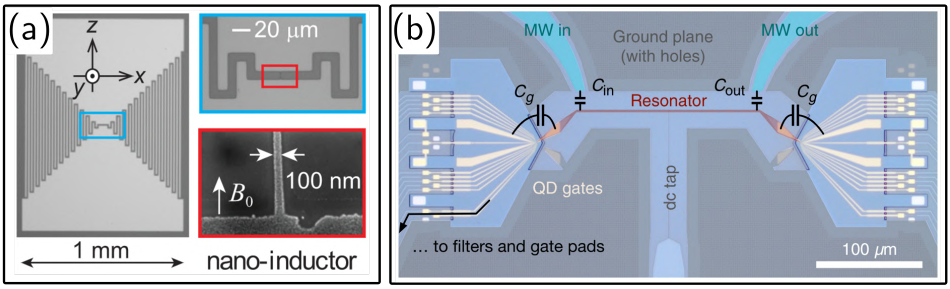

Figure 1.4 Quest for strong coupling: mode volume and impedance tuning. (a) An oscillator featuring a large interdigitated capacitance and a nano-inductor is patterned on top of a substrate implanted with spin impurities [Ranjan 2020]. It minimizes the magnetic mode volume, and the mode impedance ($Z_0 \approx 15\ \Omega$). (b) A high aspect-ratio CPW oscillator in NbTiN (red, $Z_0 \approx 3\ \mathrm{k}\Omega$) is charge-coupled to quantum dots on both ends [Harvey-Collard 2020]. Note the multiple control lines for the quantum dots (gold).

While these three strategies succeeded in bringing many hybrid systems into strong coupling with microwave photons, some others remain notoriously difficult to couple to. Leading this way are mesoscopic systems, as shown by the late demonstration of strong coupling in these platforms. Indeed, mesoscopic degrees of freedom behave quantum mechanically under strong confinement, so that their dipole cannot be easily enlarged. In addition, mesoscopic systems are usually dissipative and connected to multiple control lines (Fig. 1.4 b). Thus, reducing the mode volume comes at the risk of a degradation of the oscillator quality. Finally, impedance engineering appears like the last available trick, though it suffers from an unfavorable square-root power law (Eqs. 1.3, 1.4). Even though a charge qubit hosted on a double-dot was recently coupled to a Josephson junction-chain oscillator with $g/\omega_{\mathrm{a}} = 0.11$ [Scarlino 2022], high impedances remain very challenging to fabricate. Thus, another approach to consistently increase light-matter coupling is sought after.

1.3 Dynamical enhancement of light-matter interactions

In 2018, Leroux and co-authors presented a method where [Leroux 2018]:

> *... parametric (two-photon) driving of a cavity is used to exponentially enhance the light-matter coupling in a generic cavity-QED setup...*

While applicable to all the subfields of cavity-QED, this proposal was supplemented with a possible implementation in cQED. At the same time, Qin and co-authors presented a similar method that [Qin 2018]:

> *... exploits optical parametric amplification to exponentially enhance the atom-cavity interaction* [in a cavity-QED setup].

While mesoscopic systems were previously struggling with a square-root power-law for increased coupling through impendance engineering, the promise of an exponential enhancement is enticing.

Specifically, these proposals offer to replace the linear oscillator presented in section 1.1 by a nonlinear one, forced by a detuned parametric drive. Parametric driving is commonly known for producing squeezed states out of nonlinear oscillators [G. Milburn and D. F. Walls 1981]. These squeezed states display enhanced fluctuations, exponential in a parameter r refered to as the squeezing parameter [D. F. Walls 1983]. The trick of the proposed method lies in the *detuning* of the parametric drive [Carmichael 1984]. There, not only the output of the oscillator yields squeezed states, but the eigenstates of the oscillator themselves are squeezed (Fig. 1.5). Given that the coupling strength of an oscillator to a TLS is set by the magnitude of its field fluctuations (Eqs. 1.3, 1.4), squeezing of the eigenstates yields a coupling

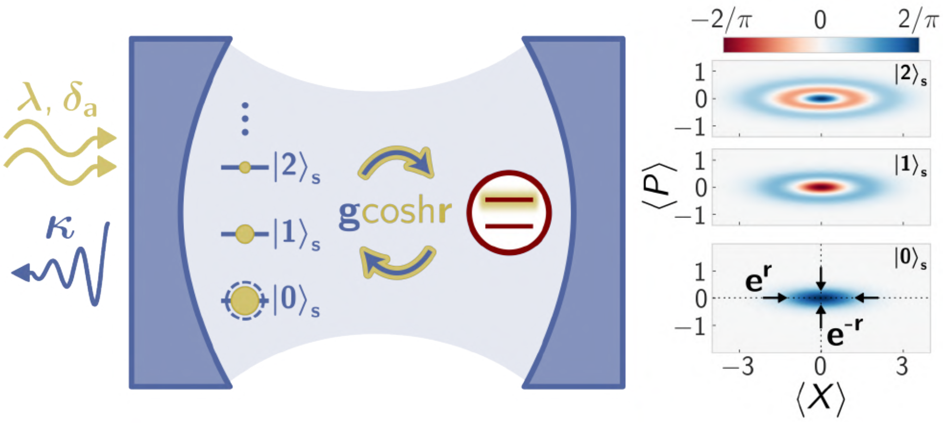

Figure 1.5 Squeezing-enhanced qubit-photon interactions. A cavity oscillator (blue mirrors) dissipating at a rate κ (blue arrow) is coupled to a TLS (red levels) at a rate g (blue exchange arrows). Driving the cavity with a two-photon pump with amplitude λ and detuning δ_a (gold double arrow) squeezes its eigenstates (blue levels), that consist of squeezed Fock states $|n_s\rangle$ (right insets: Wigners at $S = e^{2r} = 6$ dB). This results in an enhanced coupling $g\cosh r$ (gold exchange arrows). Simultaneously the drive brings an effective thermal population $\bar{n}_\mathrm{th} = \sinh^2 r$ in the oscillator (full circles) which induces TLS dephasing (gold fuzz).

boost exponential in r. Crucially, these enhanced fluctuations are not tied to either the electric or the magnetic component of the field, and cannot be recast into a modification of the mode impedance. As a consequence, the method proposed by these two references offers a fourth strategy for increased couplings. While the first three were associated with hardware design, this new one is the product of an external drive. Thus, it offers the possibility to dynamically control light-matter interactions.

In a typical hybrid-cQED setup, the oscillator is coupled to the hybrid system of interest on one hand, and decays into a feedline used for readout on the other hand. Thus, not only the squeezing is expected to boost the oscillator coupling to the TLS, but also to its feedline.

Increased coupling of the oscillator to a targeted TLS is a valuable ressource in all the subfields of cavity-QED [Zeytinoğlu 2017]. One can imagine using this scheme for improved read-out, fast gates [Burd 2021], quantum transduction [Zhong 2022], or even the study of quantum phase-

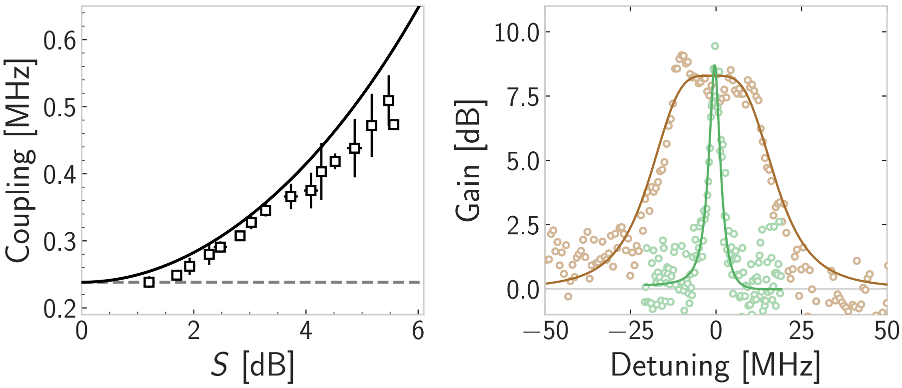

Figure 1.6 Main results of this thesis. Left: dispersive coupling strength (y-axis) of a qubit to an oscillator under detuned parametric driving, versus the oscillator squeezing (x-axis). The measured enhancement (squares) is well captured by the analytical model with no fit parameters (line). Right: gain response of a parametric amplifier in the presence of finite (brown) or vanishing (green) detuning. The amplification bandwidth in the detuned case is more than 3 times wider.

transitions [Zhu 2020; Chen 2021; Shen 2022] . There exists a wealth of theoretical proposals leveraging oscillator squeezing in cavity-QED [Qin 2018], cQED [Leroux 2018] and optomechanics [Lü 2015; Lemonde 2016]. Yet, to date, such schemes have only been demonstrated in two experiments. The first one is a trapped-ion experiment. There, multiple-qubit gates are routinely implemented using the motional states of the ions. In that context, detuned parametric driving of a phononic mode was demonstrated to speed up a Mølmer-Sørensen two-qubit gate [Burd 2021]. The second one is a NMR experiment. There, sequences of microwave pulses applied on molecules are used to simulate various dynamics. Indeed, making the most of the Holstein-Primakoff transformation, a collection of spins can be mapped onto bosons. In that context, an oscillator mode emulated by three nuclear spins showed increased interactions to a fourth spin upon squeezing [Chen 2021]. In turn, this thesis presents the first demonstration of the squeezing-enhanced coupling of an electromagnetic oscillator to a superconducting qubit (Fig. 1.6 left). This oscillator consists in a superconducting resonator enhanced by Josephson junctions, as routinely employed in cQED, and the coupled system is operated in the dispersive regime [Blais 2021]. This experiment could be easily generalized to all sorts of interacting modes, and bring squeezing as a useful ressource for hybrid systems seeking stronger interactions.

Increased coupling of the oscillator to its feedline may – in the context of hybrid-cQED – be understood as a detrimental effect. As we will later demonstrate, the enhanced coupling to the bath triggered by detuned parametric driving translates into a thermal population of the squeezed oscillator. The spread of the eigenstate population – following a Boltzmann distribution (Fig. 1.5) – dephases the coupeld TLS [Blais 2004]. While initially predicted by Shani and co-authors [Shani 2022], this thesis presents a complete experimental characterization of this induced dephasing mechanism in a cQED experiment.

Meanwhile, this enhanced dissipation can be leveraged away from a hybrid system, regarding the detuned DPO alone, as a quantum amplifier. Indeed, the primary effect of parametric driving is the production of gain at the output of the oscillator. This observation still holds for detuned parametric driving. However, the amplification bandwidth of the resulting amplifier strongly depends on the presence of the detuning. Specifically, conventional parametric amplifiers have an operational bandwidth limited by the output gain. Instead, the bandwidth of detuned parametric amplifiers is not limited by their gain (Fig. 1.6 right) [Metelmann 2022]. Finally, this thesis presents the impact of the detuning on a parametric amplifier both theoretically and experimentally.

1.4 Thesis outline

This thesis is organized as follows. In chapter 1, the nonlinear oscillator forced by a detuned parametric drive, a.k.a. the Bogoliubov oscillator, will be introduced. Following some general considerations, an implementation with superconducting circuits will be presented. In chapter 2, the coupling of such a Bogoliubov oscillator with a qubit will be envisioned. A short dataset in the resonant regime will be presented, as well as an extensive dataset in the dispersive regime. Both endeavors will be supported by original numerical simulations or analytical expressions. These first two chapters contain not only all the materials presented in [Villiers 2023], but also some exclusive contents, that one may find useful for the design of future Bogoliubov oscillators. Chapter 3 will be devoted to a short story on the operation of cQED experiments. There, the JAWS microwave package will be introduced. Finally, this typescript will end with some conclusive remarks on the future of Bogoliubov oscillators in cQED.

2

THE BOGOLIUBOV OSCILLATOR

2.1 The degenerate parametric oscillator

2.1.1 Model

The degenerate parametric oscillator (DPO) is a quantum optics model whose history is closely related to the quest for squeezed state generation [D. F. Walls 1983]. While the Heisenberg uncertainty principle sets a lower bound on the product of the measurement precisions on two conjugate variables, it does not limit the precision of an individual measurement. Specifically, building on the description of the harmonic oscillator presented in section 1.1, we introduce $\boldsymbol{X} = \boldsymbol{\Phi}/2\Phi_{\mathrm{zpf}}$ and $\boldsymbol{P} = \boldsymbol{Q}/2Q_{\mathrm{zpf}}$ the real and imaginary parts of the mode operator $\mathbf{a}$. They are the normalized quadratures of the field, obeying the commutation relation $\left[\boldsymbol{X}, \boldsymbol{P}\right] = i/2$. If $\langle \Delta \boldsymbol{X}^2 \rangle$ and $\langle \Delta \boldsymbol{P}^2 \rangle$ are the variances associated to the measurements of each quadrature, their conjugacy imposes $\langle \Delta \boldsymbol{X}^2 \rangle \langle \Delta \boldsymbol{P}^2 \rangle \geqslant \left|\left[\boldsymbol{X}, \boldsymbol{P}\right]\right|^2/4 = 1/16$. Among the states allowed by quantum mechanics we find symmetric states such that $\langle \Delta \boldsymbol{X}^2 \rangle = \langle \Delta \boldsymbol{P}^2 \rangle$, the simplest one being the vacuum which displays half a quantum of noise in each quadrature $\sqrt{\langle \Delta \boldsymbol{X}^2 \rangle_{\mathrm{vac}}} = \sqrt{\langle \Delta \boldsymbol{P}^2 \rangle_{\mathrm{vac}}} = 1/2$ (input state on Fig. 2.1). Squeezed states, on the other hand, display *squeezed* (reduced) flucations in one quadrature, at the expense of *anti-squeezed* (amplified) fluctuations in the conjugate quadrature (output state on Fig. 2.1). Crucialy these reduced fluctuations can be made smaller than the ones of vacuum, thus drawing a lot of attention to these states for precision measurement limited by quantum fluctuations [Caves 1981]. Squeezed states of light were first reported at the output of optical oscillators including a nonlinear element, such as an atomic cloud [Slusher 1985] or a nonlinear crystal [Wu 1986]. Shortly after, the nonlinearity of a Josephson junction was leveraged to prepare similar states at microwave frequencies [Yurke 1989]. In the optical domain, a continuous effort in developing squeezed-light sources reached its climax with their implementation in the detection

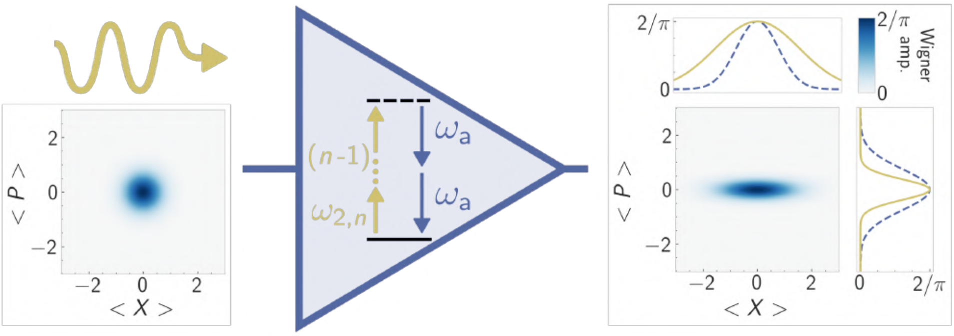

Figure 2.1 Squeezed state generation via parametric amplification. An oscillator with bare frequency ω_a is pumped at a frequency $\omega_{2,n}$ (gold arrow) through a (n+1)-wave mixing process (triangle). The input field originally in vacuum (left Wigner) yields an output field squeezed (anti-squeezed) along the $\boldsymbol{P}$ ($\boldsymbol{X}$) quadrature (right Wigner), as evidenced by the line cuts for the input (blue dashed line) and output field (gold solid line).

of gravitational waves [LIGO 2013], as initially proposed by Caves. As for the microwave domain, at first not much research spawned from the seminal experiment by Yurke. Yet more than 15 years later, squeezing microwave fields gained a renewed interest in the context of quantum-limited amplification in cQED [Castellanos-Beltran 2008]. Since then, parametric amplifiers based on Josephson junctions became a cornerstone of the characterization of quantum circuits [Murch 2013b], as well as a prominent tool for the search of dark matter axions [Malnou 2019].

At the heart of the DPO model lies a quantum harmonic oscillator augmented by a nonlinear element. By applying a strong drive on the oscillator nonlinearity – or in analogy with the stick-man going up and down on his swing, by *pumping* the nonlinearity – one of the defining parameters of the oscillator can be modulated, and in turn its resonant frequency. For instance, given a nonlinear crystal in an optical cavity, a strong electric field can modify the crystal refractive index, hence the cavity resonant frequency [Boyd 2008]. Alternatively, given a Josephson junction in a tank circuit, a strong current can modify the junction equivalent inductance, hence the resonant frequency of the circuit (section 2.2.1). When the frequency of this modulation approaches a parametric resonance $\omega_{2,n} = \frac{2\omega_\mathrm{a}}{n-1}$ with n and integer strictly greater to 1, parametric amplification occurs as a consequence of the pump injecting *pairs* of photons in the oscillator (Fig. 2.1). At this stage, it is worth pointing out that squeezed states are *even* coherent states. As detailed by Walls [D. F. Walls 1983], the prototype Hamiltonian for this interaction reads:

$$\boldsymbol{\mathcal{H}}_{(\boldsymbol{n})}/\hbar = \omega_{\mathrm{a}}\mathbf{a}^{\dagger}\mathbf{a} + \left(\chi^{(n)*}(\varepsilon)\mathbf{a}^{2} + \chi^{(n)}(\varepsilon)\mathbf{a}^{\dagger 2}\right) \ , \tag{2.1}$$

where $\chi^{(n)}(\varepsilon)$ is the n^{th} order nonlinear susceptibility of the dressed oscillator, and ε is the time-dependent pump amplitude. In this framework the pump field has been treated classicaly. Depending on the system, a specific order of the susceptibility will be responsible for parametric amplification:

$$\begin{aligned} \chi^{(2)}(\varepsilon) &= \varepsilon\chi^{(2)} && \left[\text{3-wave mixing}\right] , \\ \chi^{(3)}(\varepsilon) &= \varepsilon^{2}\chi^{(3)} && \left[\text{4-wave mixing}\right] , \\ &\dots \\ \chi^{(n)}(\varepsilon) &= \varepsilon^{n-1}\chi^{(n)} && \left[(n+1)\text{-wave mixing}\right] . \end{aligned} \tag{2.2}$$

What is the dominant nonlinear process? In a perturbative approach, the amplitudes $\chi^{(n)}(\varepsilon)$ decrease with the order of the nonlinearity, pointing towards 3-wave mixing as the dominant process. However, symmetries of the nonlinear medium can inhibit specific orders. As such, inversion symmetry prohibits even terms $\chi^{(2n)}$, and in particular 3-wave mixing [Boyd 2008]. For instance, nonlinear crystals belonging to a centrosymmetric point group possess inversion symmetry[1]. Similarly, the energy-phase relation of a SQUID being even, 3-wave mixing cannot be triggered through current pumping. Notably, it was only a few years ago that a superconducting dipole element natively lacking inversion symmetry was implemented [Frattini 2017] (section 2.2.1). Next, having identified the lowest-order non-vanishing process, its activation requires the interaction term to be nearly resonant. In the case of a monochromatic pumping scheme, where the time-dependent pump field can be written as $\varepsilon = \varepsilon_{\mathrm{p}}e^{i\omega_{\mathrm{p}}t}$, the n^{th} order parametric interaction is resonant when $(n-1)\times\omega_{\mathrm{p}} = 2\omega_{\mathrm{a}}$, that is to say $\omega_{\mathrm{p}} = \omega_{2,n}$. Thus it is instructive to look at Hamiltonian 2.1 in a frame rotating at $\frac{n-1}{2}\omega_{\mathrm{p}}$ (appendix B.1.3), such that its interaction part is steady:

$$\boldsymbol{\mathcal{H}}^{\omega}_{(n)}/\hbar = \delta_{(n)}\mathbf{a}^{\dagger}\mathbf{a} + \Lambda^{*}_{(n)}\mathbf{a}^{2} + \Lambda_{(n)}\mathbf{a}^{\dagger 2} \ , \tag{2.3}$$

---

[1] Which is indeed not the case of MgO:LiNbO$_3$ used in the first demonstration of squeezed state generation through 3-wave mixing [Wu 1986].

where $\delta_{(n)} = \omega_{\mathrm{a}} - \frac{n-1}{2}\omega_{\mathrm{p}}$ quantifies the pump frequency mismatch with the parametric resonance, and $\Lambda_{(n)} = \varepsilon_{\mathrm{p}}^{n-1}\chi^{(n)}$ quantifies the two-photon injection rate. This is the DPO Hamiltonian, emanating from a $(n+1)$-wave mixing process. Not only this prototype Hamiltonian captures nonlinear processes of arbitrary orders, but it can also faithfully represents driven dynamics of various complexity. Indeed, polychromatic pumping schemes can be implemented, and for $n > 2$ the various frequencies will get mixed through the nonlinearity. For instance, the 4-wave mixing process of a Josephson parametric amplifier can be triggered by a bichromatic pump [Boutin 2017]. Finally, this model can be generalized to higher-order parametric resonances $\omega_{k,n} = \frac{k\omega_{\mathrm{a}}}{n-1}$, that inject k-photons in the oscillator [Braunstein and McLachlan 1987]. While recently demonstrated in a supercondcuting circuit for $k = 3$ [Chang 2020], the states produced by such parametric processes are of great interest for quantum computation with continuous variables [Gottesman 2001; Hillmann 2020].

Since the parametric process requires a pump field to interact with the oscillator, a faithful description of the DPO has to account for external degrees of freedom, that consitute the *bath* of mode **a**. In the following, we focus on a single-sided oscillator (meaning with a single bath channel), augmented by a 3-wave mixing process ($n = 2$). The DPO model is a combination of a *photon* Hamiltonian and Lindblad loss operator:

$$\boldsymbol{\mathcal{H}}_{\mathbf{ph}}/\hbar = \delta_{\mathrm{a}}\mathbf{a}^{\dagger}\mathbf{a} - \frac{\lambda}{2}\left(\mathbf{a}^{2} + \mathbf{a}^{\dagger 2}\right) \;,\quad \boldsymbol{L}_{\mathbf{ph}} = \sqrt{\kappa}\mathbf{a}\,, \tag{2.4}$$

where δ_{a} is the detuning between the oscillator and half the pump frequency, λ is the amplitude of the two-photon pump, and κ is the coupling to the bath (assumed to be in vacuum). In this picture, the bath is a source of dissipation for the oscillator mode. Without loss of generality, λ is taken real and positive. So far the pump field has been treated classicaly, as motivated by its very high intensity in typical applications. Yet, following Walls and Milburn [Walls and Milburn 2008] a careful analysis of a fully quantum DPO would reveal a dynamical instability as $\lambda \geqslant \lambda_{\mathrm{crit}}$ where:

$$\lambda_{\mathrm{crit}} \equiv \sqrt{\frac{\kappa^{2}}{4} + \delta_{\mathrm{a}}^{2}}\,. \tag{2.5}$$

This critical value of the two-photon pump marks the onset of parametric oscillations, for which the oscillator field acquires a finite amplitude. The crossing of this threshold corresponds to a second-order quantum phase transition, with the steady-state oscillator field $\langle \mathbf{a} \rangle_\infty$ as an order parameter. It is not surprising that a full quantum treatment of the fields is required to account for this instability, as the transition is driven by the very quantum fluctuations of these fields. That being said, even with the classical treatment of the pump followed in this thesis, λ_{crit} will play an essential role in the characterization of the oscillator field moments (section 2.1.2). Note that in the remainder of this thesis, we will focus on the regime below threshold $\lambda < \lambda_{\text{crit}}$.

2.1.2 Squeezing and squeezing

The DPO has been introduced as a minimal model to account for the generation of squeezed radiations. Historically, a lot of attention was dedicated to the characterization of the squeezing of the oscillator output field, as it is the only accessible ressource in quantum optics experiment. Yet, not only the output field is in a squeezed state, but also the intra-oscillator field. With the advent of cavity-QED and later on cQED, the introduction of quantum detectors – namely spins (section 1.1) – at the heart of oscillators renewed the interest for intra-oscillator squeezing characterization. In the following, we will start by describing the squeezing of the steady-state field in the oscillator. Then, we will introduce another type of squeezing, relevant to the description of DPOs with $\delta_{\text{a}} \neq 0$.

Steady-state squeezing Introducing the density matrix of the system $\boldsymbol{\rho}$, the evolution of the state of the DPO in contact with its environment is governed by the Lindblad master equation:

$$\partial_t \boldsymbol{\rho}(\boldsymbol{t}) = -\frac{i}{\hbar} [\boldsymbol{\mathcal{H}}_{\mathbf{ph}}, \boldsymbol{\rho}(\boldsymbol{t})] + \mathcal{D}[\boldsymbol{L}_{\mathbf{ph}}]\boldsymbol{\rho}(\boldsymbol{t}) \ , \tag{2.6}$$

where the dissipation superoperator reads $\mathcal{D}[\bullet]\boldsymbol{\rho} = \bullet\boldsymbol{\rho}\bullet^\dagger - \frac{1}{2}\left\{\bullet^\dagger\bullet, \boldsymbol{\rho}\right\}$. The mean-value of an arbitrary operator in the Heisenberg picture $\boldsymbol{\mathcal{O}}(\boldsymbol{t})$ can be written in terms of the time-dependent density matrix $\langle \boldsymbol{\mathcal{O}} \rangle_t = \mathrm{Tr}(\boldsymbol{\mathcal{O}}\boldsymbol{\rho}(\boldsymbol{t}))$, where $\boldsymbol{\mathcal{O}}$ is the operator at a past reference time. It evolves in time following the equation:

$$\partial_t \langle \boldsymbol{\mathcal{O}} \rangle_t = \frac{i}{\hbar} \langle [\boldsymbol{\mathcal{H}}_{\mathbf{ph}}, \boldsymbol{\mathcal{O}}] \rangle_t + \langle \boldsymbol{L}_{\mathbf{ph}}^\dagger \boldsymbol{\mathcal{O}} \boldsymbol{L}_{\mathbf{ph}} \rangle_t - \frac{1}{2} \left\langle \left\{ \boldsymbol{L}_{\mathbf{ph}}^\dagger \boldsymbol{L}_{\mathbf{ph}}, \boldsymbol{\mathcal{O}} \right\} \right\rangle_t \ , \tag{2.7}$$

which is an extension of the Ehrenfest theorem to include dissipation. Since the squeezing is related to the field fluctuations, we seek second-order moments of the operator $\mathbf{a}$. Owing to the quadratic nature of the master equation, the differential system governing their evolution can be recast in a closed form. Introducing the vector $\boldsymbol{\Psi}$ such that $\boldsymbol{\Psi}^{\mathrm{T}} = (\mathbf{a}^\dagger\mathbf{a}, \mathbf{a}^2, \mathbf{a}^{\dagger 2}, \mathbf{a}, \mathbf{a}^\dagger, \mathbb{1})$, we find $\partial_t \langle \boldsymbol{\Psi} \rangle_t = M \langle \boldsymbol{\Psi} \rangle_t$ where:

$$M = \begin{bmatrix} -\kappa & -i\lambda & +i\lambda & 0 & 0 & 0 \\ 2i\lambda & -2i\delta_{\mathrm{a}} - \kappa & 0 & 0 & 0 & i\lambda \\ -2i\lambda & 0 & 2i\delta_{\mathrm{a}} - \kappa & 0 & 0 & -i\lambda \\ 0 & 0 & 0 & -i\delta_{\mathrm{a}} - \kappa/2 & i\lambda & 0 \\ 0 & 0 & 0 & -i\lambda & i\delta_{\mathrm{a}} - \kappa/2 & 0 \\ 0 & 0 & 0 & 0 & 0 & 0 \end{bmatrix} . \tag{2.8}$$

Solving this differential system in the steady-state yields:

$$\langle \mathbf{a}^\dagger \mathbf{a} \rangle_\infty = \frac{1}{2} \frac{\lambda^2}{\lambda_{\mathrm{crit}}^2 - \lambda^2} , \quad \langle \mathbf{a}^2 \rangle_\infty = \frac{\lambda}{2} \frac{\delta_{\mathrm{a}} + i\kappa/2}{\lambda_{\mathrm{crit}}^2 - \lambda^2} , \quad \langle \mathbf{a} \rangle_\infty = 0 , \tag{2.9}$$

from which we also deduce: $\langle \mathbf{a}\mathbf{a}^\dagger \rangle_\infty = 1 + \langle \mathbf{a}^\dagger \mathbf{a} \rangle_\infty$, and $\langle \mathbf{a}^{\dagger 2} \rangle_\infty = \langle \mathbf{a}^2 \rangle_\infty^*$. In the remainder of this manuscript, steady-state observables will be denoted as $\langle \boldsymbol{\mathcal{O}} \rangle_\infty = \mathrm{Tr}(\boldsymbol{\mathcal{O}} \boldsymbol{\rho}_\infty)$ where $\partial_t \boldsymbol{\rho}_\infty = 0$.

The amplification process is readily observable in the occupation of the oscillator $\langle \mathbf{a}^\dagger \mathbf{a} \rangle_\infty$. With the pump off ($\lambda = 0$), the oscillator is empty. As the pump is turned on, a finite occupation emerges, until it diverges as λ approaches the critical value. Further defining the tilted oscillator quadratures as:

$$\boldsymbol{X_\theta} = \frac{\mathbf{a}e^{-i\theta} + \mathbf{a}^\dagger e^{i\theta}}{2} \quad \text{and} \quad \boldsymbol{P_\theta} = \frac{\mathbf{a}e^{-i\theta} - \mathbf{a}^\dagger e^{i\theta}}{2i} , \tag{2.10}$$

we find:

$$\langle \boldsymbol{X}_{\boldsymbol{\theta}}^2 \rangle_\infty = \frac{1}{4} \frac{\lambda_{\mathrm{crit}}^2 + \lambda \left(\delta_{\mathrm{a}} \cos 2\theta + (\kappa/2) \sin 2\theta \right)}{\lambda_{\mathrm{crit}}^2 - \lambda^2} , \tag{2.11a}$$

$$\langle \boldsymbol{P}_{\boldsymbol{\theta}}^2 \rangle_\infty = \frac{1}{4} \frac{\lambda_{\mathrm{crit}}^2 - \lambda \left(\delta_{\mathrm{a}} \cos 2\theta + (\kappa/2) \sin 2\theta \right)}{\lambda_{\mathrm{crit}}^2 - \lambda^2} , \tag{2.11b}$$

On Fig. 2.2 we plot Wigner representations of the intra-oscillator field for various parameters. When $\lambda = 0$, the DPO is in vacuum and its steady-state field fluctuations are isotropic: $\forall \theta, \langle \boldsymbol{X}_{\boldsymbol{\theta}}^2 \rangle_\infty = \langle \boldsymbol{X}^2 \rangle_{\mathrm{vac}} = 1/4$. For $\lambda > 0$, the steady-state is squeezed along $\boldsymbol{P}_{\boldsymbol{\theta}_\infty}$ and anti-squeezed along $\boldsymbol{X}_{\boldsymbol{\theta}_\infty}$, where θ_∞ is such that:

$$\tan 2\theta_\infty = \frac{\kappa}{2\delta_{\mathrm{a}}} . \tag{2.12}$$

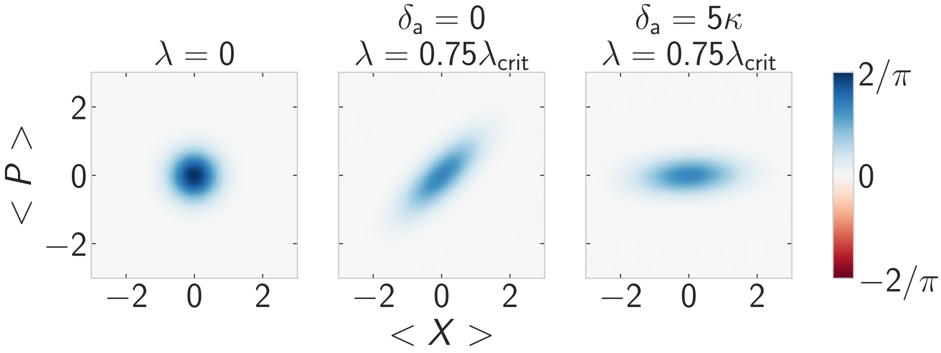

Figure 2.2 Wigner representations of the steady-state of a DPO with the pump off (left), 6 dB of resonant squeezing (center), and 6 dB of detuned squeezing (right). Even though it is not obvious at first sight, center and right pictures are equivalent through a mere rotation.

When $\delta_a = 0$, the squeezing is said to be *resonant*, and we recover $\theta_\infty = \pi/4$ (Fig. 2.2 center)[2]. When $\delta_a \neq 0$, the squeezing is said to be *detuned*, which tilts the previous picture. Maintaining the ratio λ/λ_{crit} preserves the anisotropy (Fig. 2.2 right). Notably for strongly-detuned squeezing, meaning $|\delta_a| \gg \kappa/2$, we find $\theta_\infty \approx 0$.

We define the steady-state squeezing and anti-squeezing amplitudes as[3]:

$$S_\infty \equiv \frac{\langle \boldsymbol{P}^2_{\boldsymbol{\theta}_\infty} \rangle_\infty}{\langle \boldsymbol{P}^2 \rangle_{vac}} = \frac{\lambda_{crit}}{\lambda_{crit} + \lambda}, \qquad \check{S}_\infty \equiv \frac{\langle \boldsymbol{X}^2_{\boldsymbol{\theta}_\infty} \rangle_\infty}{\langle \boldsymbol{X}^2 \rangle_{vac}} = \frac{\lambda_{crit}}{\lambda_{crit} - \lambda}. \tag{2.13}$$

As the two-photon pump amplitude approaches its critical value, the steady-state anti-squeezing grows indefinitely, while the squeezing saturates to 1/2. This is the well-known 3 dB-limit on intra-cavity squeezing, which applies to the DPO whether the squeezing is resonant or detuned [Carmichael 1984]. This limit is evidenced on Fig. 2.2 by a contrast reduction at the center of the blobs, necessary to ensure the normalization of the Wigner representation at squeezings above 3 dB. Yet the presence of a detuning deeply alters the physical process responsible for the dynamical convergence of the system. In

---

[2] An alternative definition of the squeezing term $-i\frac{\lambda}{2}(\mathbf{a}^2 - \mathbf{a}^{\dagger 2})$ would yield $\theta_\infty = 0$ in the resonant case [Eddins 2019].

[3] When numerical values of the (anti-)squeezing are quoted, we use the logarithmic scale $S\ [\mathrm{dB}] = 10\log_{10} S$. As a rule of thumb, for $\lambda/\lambda_{crit} = 0.75, 0.9, 0.99$, the steady-state anti-squeezing equals respectively $\check{S}_\infty = 6, 10, 20$ dB.

the resonant case we find $\lambda_{\mathrm{crit}} = \kappa/2$, as a signature of the DPO stabilization being mediated by dissipation only. Indeed, the dynamical system desribed by Eqs 2.4 with $\delta_{\mathrm{a}} = 0$ would be unstable if it were not for dissipation. On the contrary, in the strongly-detuned case we find $\lambda_{\mathrm{crit}} \approx |\delta_{\mathrm{a}}|$, showing that the pump frequency mismatch alone is sufficient to stabilize the system.

Eigenstate squeezing The presence of a non-vanishing detuning between the oscillator resonance and half the pump frequency calls for another layer of analysis. Indeed, in the detuned-squeezing regime, the Hamiltonian is diagonalizable by means of a Bogliubov transformation using the canonical basis:

$$\boldsymbol{\alpha} = \mathbf{a} \cosh r - \mathbf{a}^{\dagger} \sinh r \tag{2.14}$$

where the squeezing parameter r is defined as:

$$\tanh 2r = \frac{\lambda}{|\delta_{\mathrm{a}}|} \ . \tag{2.15}$$

This approach is equivalent to transforming the Hamiltonian through the squeezing unitary $\boldsymbol{\mathcal{U}}_s = e^{r/2(\mathbf{a}^2 - \mathbf{a}^{\dagger 2})}$ by noting that $\boldsymbol{\alpha} = \boldsymbol{\mathcal{U}}_s^{\dagger} \mathbf{a} \boldsymbol{\mathcal{U}}_s$. In the following we will say that given an arbitrary operator $\boldsymbol{\mathcal{O}}$, then $\boldsymbol{\mathcal{U}}_s \boldsymbol{\mathcal{O}} \boldsymbol{\mathcal{U}}_s^{\dagger}$ is the squeezed version of $\boldsymbol{\mathcal{O}}$, while $\boldsymbol{\mathcal{U}}_s^{\dagger} \boldsymbol{\mathcal{O}} \boldsymbol{\mathcal{U}}_s$ is its anti-squeezed version. In this new basis, Hamiltonian 2.4 reads:

$$\boldsymbol{\mathcal{H}}_{\mathbf{ph}}/\hbar = \Omega_{\mathrm{a}}[r] \boldsymbol{\alpha}^{\dagger} \boldsymbol{\alpha} \ , \tag{2.16}$$

where $\Omega_{\mathrm{a}}[r] = \delta_{\mathrm{a}} / \cosh 2r$. When $\lambda = 0$, the Hamiltonian $\boldsymbol{\mathcal{H}}_{\mathbf{ph}}$ is that of a simple harmonic oscillator, and its eigenstates are Fock states $\{|n\rangle\}$ with eigenenergies $n\delta_{\mathrm{a}}$, where n are integers. Instead, when a detuned two-photon pump is applied, the DPO enters the Bogoliubov oscillator (BO) regime where its eigenstates are squeezed Fock states $\{|n\rangle_s = \boldsymbol{\mathcal{U}}_s^{\dagger} |n\rangle\}$ with eigenenergies $n\Omega_{\mathrm{a}}[r]$ (Fig. 2.3). When it comes to eigenstate squeezing, the enhanced fluctuations in one quadrature are accompanied by conversely reduced fluctuations in the other quadrature, with no saturation. Hence there is no need to distinguish squeezing from anti-squeezing, and we relate the anisotropy of the eigenstates to a single parameter denoted the squeezing amplitude[4]:

$$S \equiv \frac{{}_s\langle n| \boldsymbol{X}_{\mathbf{0}}^2 |n\rangle_s}{\langle n| \boldsymbol{X}_{\mathbf{0}}^2 |n\rangle} = e^{2r} \ . \tag{2.17}$$

To avoid confusion, the eigenstate squeezing will be simply denoted *squeez-*

---

[4] Using the same notation as for steady-state squeezing, we would find $\breve{S} = S^{-1}$.

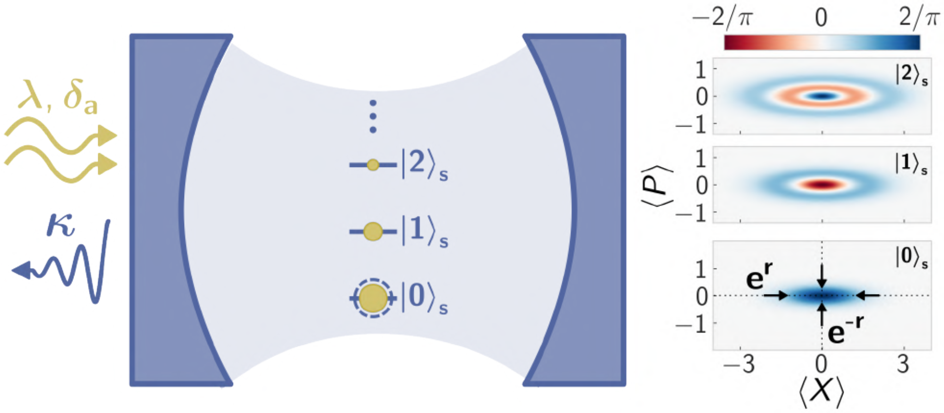

Figure 2.3 The Bogoliubov oscillator. A cavity oscillator (blue mirrors) is driven by a two-photon pump with amplitude λ and detuning δ_a (gold double arrow) while dissipating at rate κ (blue arrow). Its eigenstates (blue levels), that are effectively thermally occupied (full circles), consist of squeezed Fock states $|n_s\rangle$ (right insets: Wigners at $S = e^{2r} = 6$ dB).

ing, while the *steady-state squeezing* will always be recalled as such. Making the most of the hyperbolic-trygonometry table (appendix A), we point out the useful formulas[5]:

$$\Omega_a[r] = \sqrt{\delta_a^2 - \lambda^2} \quad \text{and} \quad S = \sqrt{\frac{\delta_a + \lambda}{\delta_a - \lambda}} \,. \tag{2.18}$$

The diagonalization of the Hamiltonian comes at the expense of a convoluted expression for the Lindblad loss operator in the Bogoliubov basis:

$$\boldsymbol{L}_{\mathbf{ph}} = \sqrt{\kappa}\big(\boldsymbol{\alpha}\cosh r + \boldsymbol{\alpha}^\dagger \sinh r\big) \,. \tag{2.19}$$

Indeed, the appropriate basis to account for the squeezing of the oscillator is the one of Bogoliubov excitations, which is an anti-squeezed version of the original one. Then, the single-photon loss channel of the bare mode translates into a squeezed-photon loss for the Bogoliubov mode. When entering the master equation 2.6, this squeezed bath operator will contribute to the evolution of the density matrix through:

$$\begin{aligned}\mathcal{D}[\boldsymbol{L}_{\mathbf{ph}}]\boldsymbol{\rho} = \kappa(1+\sinh^2 r)\mathcal{D}[\boldsymbol{\alpha}]\boldsymbol{\rho} + \kappa\sinh^2 r\mathcal{D}[\boldsymbol{\alpha}^\dagger]\boldsymbol{\rho} \\ + \kappa\frac{\sinh 2r}{2}\left(\mathcal{G}[\boldsymbol{\alpha}]\boldsymbol{\rho} + \mathcal{G}[\boldsymbol{\alpha}^\dagger]\boldsymbol{\rho}\right) \,,\end{aligned} \tag{2.20}$$

---

[5] Orders of magnitude: $\lambda/\delta_a = 0.9, 0.98, 0.9998$ leads to $S = 6.4, 10, 20$ dB.

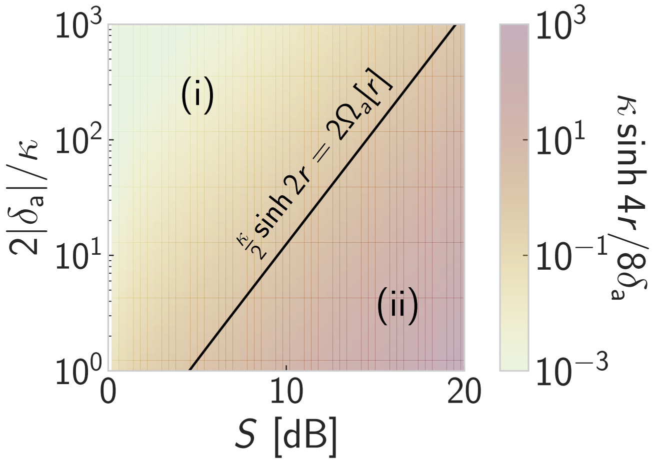

Figure 2.4 Condition for an effective thermal bath. The squeezed bath amounts to a thermal bath when $(\kappa/2)\sinh 2r < 2|\Omega_a[r]|$, that is to say $\kappa \sinh 4r/8\delta_a < 1$ [region (i)]. In the opposite case [region (ii)], the anomalous dissipator of Eq. 2.20 cannot be averaged out. The black line marks the separator between the two regions.

where the anomalous dissipator superoperator reads: $\mathcal{G}[\bullet]\boldsymbol{\rho} = \bullet\boldsymbol{\rho}\bullet - \frac{1}{2}\{\bullet^2, \boldsymbol{\rho}\}$. Owing to the harmonic evolution of the $\boldsymbol{\alpha}$ mode, it is instructive to look at the master equation in a frame rotating at $\Omega_a[r]$ (appendix B.1.3). There, the two terms of the first line of Eq. 2.20 will appear steady, while the ones of the second line will appear rotating at frequency $2|\Omega_a[r]|$. In the limit where their amplitude is smaller than their rotating frequency, averaging theorems apply, and we can neglect the contribution of the second line (section B.1.3). Thus, provided $\kappa\frac{\sinh 2r}{2} \ll 2|\Omega_a[r]|$, the Lindblad loss operator in the Bogoliubov basis resembles a thermal bath with mean-occupancy $\sinh^2 r$. This inequality translates into an lower bound on the ratio $2|\delta_a|/\kappa$ for the bath to be simply considered thermal: $2|\delta_a|/\kappa \gg \sinh 4r/4$ (knowing that $r > 0$). On Fig. 2.4 we plot the evolution of this bound for various squeezing amplitudes. For instance, when $\delta_a = 5\kappa$ (meaning $2|\delta_a|/\kappa = 10$), the inequality is saturated for 10 dB of squeezing. In this limit, and assuming an oscillator initially in vacuum, once in the BO regime the steady-state will appear as a thermal state with Boltzmann weights p_n, such that $p_n/p_{n-1} = \tanh^2 r$ (see golden circles on Fig. 2.3 showing the Boltzmann weights referenced to the unit circle in blue).

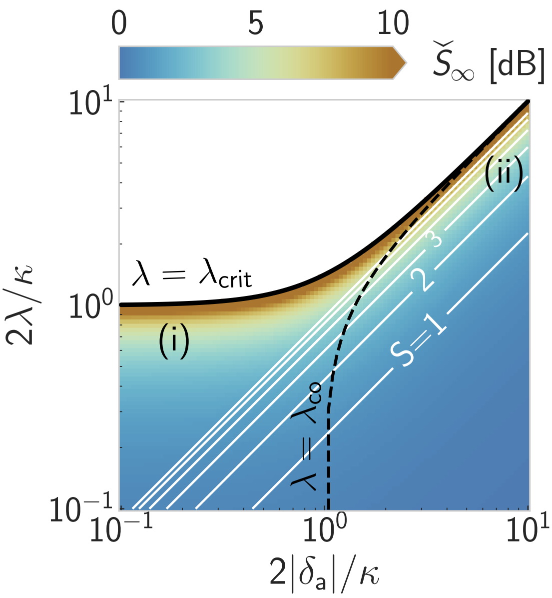

Figure 2.5 DPO Squeezing: steady-state anti-squeezing (color) versus two-photon pump amplitude (y-axis) and detuning (x-axis) both scaled by $\kappa/2$. When $\lambda > \lambda_\mathrm{crit}$ (white region, frontier as a black line), the system is dynamically unstable. The region (i) is typical for parametric amplification and squeezing generation, while the region (ii) marks the BO regime. The black dashed line marks the frontier of coalescence (Eq. 2.34). Eigenstate squeezing amplitude (in decibels) is overlaid as white-level lines (1 to 6 dB shown, this quantity diverges when $\lambda = |\delta_\mathrm{a}|$ on the first bisector)

DPO juice While the presence of a finite detuning in the DPO model preserves its steady-state squeezing properties, provided a mere redefinition of λ_crit, it also profoundly changes the nature of its eigenspectrum. Indeed, in the resonant case the DPO Hamiltonian can be recast in terms of the normalized quadratures as $\boldsymbol{\mathcal{H}}_\mathbf{ph} = \hbar\lambda(\boldsymbol{P}^2 - \boldsymbol{X}^2)$. It corresponds to an oscillator with an inverted potential, unbounded from the bottom. This potential being unconfining, the Hamiltonian spectrum is continuous, with non-normalizable eigenstates akin to the position operator in real space. Ultimately, its dynamics would be unstable in the absence of dissipation. In the detuned case, the DPO features a discrete set of energy levels, with eigenstates which are squeezed Fock states. While there is no simple connection between steady-state squeezing and eigenstate squeezing (Fig. 2.5), in the strongly detuned regime $|\delta_\mathrm{a}| \gg \kappa/2$, we find:

$$\check{S}_\infty \underset{\lambda\to|\delta_\mathrm{a}|}{\sim} \frac{S^2}{2} \, , \tag{2.21}$$

which reads in logarithmic scale: $\check{S}_\infty[\mathrm{dB}] \sim 2S[\mathrm{dB}] - 3$. The definition of the Bogoliubov basis appears to be the right analytical tool to describe a detuned DPO. Yet, does the eigenstate squeezing lead to measurable effects in the oscillator output field?

2.1.3 Gain response and coalescence

Having previously characterized the inner squeezing properties of a DPO, we now turn to the description of its output field. In an experiment driven approach, instead of computing the squeezing properties of the field, we will focus on the gain response of the DPO. Indeed, this quantity is straightforward to measure in a spectroscopy experiment, as opposed to squeezing. While the computation of the gain reponse of a DPO can be found in numerous references [Frattini 2018; Planat 2019], little attention has been devoted to commenting the impact of the detuning δ_a. After a standard derivation of the DPO response in the bare basis, we will shed light on this result by reproducing the calculation in the Bogoliubov basis. Finally, we will introduce the concept of *coalescence*, that reconciles detuned and resonant DPOs at high squeezing.

Bare basis computation First we perform the calculation using the basis of the bare oscillator mode. We use the input-output formalism to describe the evolution of the oscillator field in contact with its bath [Steck 2007] (appendix B.2). The oscillator Heisenberg operator obeys the Quantum Langevin equation (QLE):

$$\partial_t \mathbf{a}(\boldsymbol{t}) = \frac{i}{\hbar}\left[\boldsymbol{\mathcal{H}}_\mathbf{ph}, \mathbf{a}(\boldsymbol{t})\right] - \frac{\kappa}{2}\mathbf{a}(\boldsymbol{t}) + \sqrt{\kappa}\,\mathbf{a}_\mathbf{in}(\boldsymbol{t}) \, , \tag{2.22}$$

where $\mathbf{a}_\mathbf{in}(\boldsymbol{t})$ is the input field, a noisy quantum operator representing the fluctuations of the environment impinging on the DPO. This operator has 0-mean, obeys the commutation relations $\left[\mathbf{a}_\mathbf{in}(\boldsymbol{t}), \mathbf{a}_\mathbf{in}^\dagger(\boldsymbol{t'})\right] = \boldsymbol{\delta}(\boldsymbol{t}-\boldsymbol{t'})$ and $\left[\mathbf{a}_\mathbf{in}(\boldsymbol{t}), \mathbf{a}_\mathbf{in}(\boldsymbol{t'})\right] = 0$, and follows the statistics:

$$\langle \mathbf{a}_\mathbf{in}^\dagger(\boldsymbol{t}), \mathbf{a}_\mathbf{in}(\boldsymbol{t'})\rangle = \bar{n}_\mathrm{th}\delta(t-t') \, , \tag{2.23a}$$

$$\langle \mathbf{a}_\mathbf{in}(\boldsymbol{t}), \mathbf{a}_\mathbf{in}^\dagger(\boldsymbol{t'})\rangle = (1+\bar{n}_\mathrm{th})\delta(t-t') \, , \tag{2.23b}$$

$$\langle \mathbf{a}_\mathbf{in}(\boldsymbol{t}), \mathbf{a}_\mathbf{in}(\boldsymbol{t'})\rangle = 0 \, , \tag{2.23c}$$

where $\bar{n}_{\mathrm{th}}$ is the thermal occupancy of the bath. For an oscillator probed in reflection – a necessary evil for a single-sided DPO – the input-output relation reads[6]:

$$\mathbf{a}_{\mathbf{out}}(\boldsymbol{t}) + \mathbf{a}_{\mathbf{in}}(\boldsymbol{t}) = \sqrt{\kappa}\mathbf{a}(\boldsymbol{t}) \ , \tag{2.24}$$

where $\mathbf{a}_{\mathbf{out}}(\boldsymbol{t})$ is the output field, with similar properties as the input one. The QLE is most conveniently solved in Fourier space defined through the transformation:

$$\mathbf{a}[\boldsymbol{\omega}] = \int \mathrm{d}t e^{i\omega t}\mathbf{a}(\boldsymbol{t}) \ . \tag{2.25}$$

Details on the reverse transformation and the normalization convention can be found in appendix A. Most notably the Fourier transforms of the adjoint excitations are related to Fourier modes at negative frequencies:

$$\mathbf{a}[\text{-}\boldsymbol{\omega}]^{\dagger} = \int \mathrm{d}t e^{i\omega t}\mathbf{a}^{\dagger}(\boldsymbol{t}) \ . \tag{2.26}$$

Note that this computation is carried out in the rotating frame, hence ω is the deviation from half the pump frequency.

As a consequence of energy conservation during the parametric process, the two-photon pump induces correlations between excitations living at mirror frequencies with respect to $\omega_p/2$, that is to say $\pm\omega$. In addition, the Fourier transformation 2.26 relates the excitations at $-\omega$ to the adjoint operator $\mathbf{a}^{\dagger}(\boldsymbol{t})$. Thus, in order to solve for the DPO response, we write the Fourier transforms of both the QLE and the adjoint QLE:

$$\begin{cases} -i\omega\mathbf{a}[\boldsymbol{\omega}] = -\big(\kappa/2 + i\delta_{\mathrm{a}}\big)\mathbf{a}[\boldsymbol{\omega}] \quad + i\lambda\mathbf{a}[\text{-}\boldsymbol{\omega}]^{\dagger} + \sqrt{\kappa}\mathbf{a}_{\mathbf{in}}[\boldsymbol{\omega}] \\ -i\omega\mathbf{a}[\text{-}\boldsymbol{\omega}]^{\dagger} = -\big(\kappa/2 - i\delta_{\mathrm{a}}\big)\mathbf{a}[\text{-}\boldsymbol{\omega}]^{\dagger} - i\lambda\mathbf{a}[\boldsymbol{\omega}] \quad + \sqrt{\kappa}\mathbf{a}_{\mathbf{in}}[\text{-}\boldsymbol{\omega}]^{\dagger} \end{cases} . \tag{2.27}$$

Solving this system yields the Fourier modes of the intra-cavity field:

$$\begin{aligned} \mathbf{a}[\boldsymbol{\omega}] = &\frac{\sqrt{\kappa}(\kappa/2 - i(\omega + \delta_{\mathrm{a}}))}{\kappa^2/4 + \delta_{\mathrm{a}}^2 - \lambda^2 - \omega^2 - i\kappa\omega}\mathbf{a}_{\mathbf{in}}[\boldsymbol{\omega}] \\ &+ \frac{i\lambda\sqrt{\kappa}}{\kappa^2/4 + \delta_{\mathrm{a}}^2 - \lambda^2 - \omega^2 - i\kappa\omega}\mathbf{a}_{\mathbf{in}}[\text{-}\boldsymbol{\omega}]^{\dagger} \ . \end{aligned} \tag{2.28}$$

The second term proportional to λ clearly evidences the mixing of excitations at $\pm\omega$ mediated by the two-photon pump. Continuing with the closure relation 2.24, the output field of the DPO can be written as $\mathbf{a}_{\mathbf{out}}[\boldsymbol{\omega}] =$

---

[6] An alternative sign convention writes the QLE: $\partial_t\mathbf{a}(\boldsymbol{t}) = \frac{i}{\hbar}\left[\boldsymbol{\mathcal{H}}_{\mathbf{ph}}, \mathbf{a}(\boldsymbol{t})\right] - \frac{\kappa}{2}\mathbf{a}(\boldsymbol{t}) - \sqrt{\kappa}\mathbf{a}_{\mathbf{in}}(\boldsymbol{t})$, and the input-output relation: $\mathbf{a}_{\mathbf{out}}(\boldsymbol{t}) - \mathbf{a}_{\mathbf{in}}(\boldsymbol{t}) = \sqrt{\kappa}\mathbf{a}(\boldsymbol{t})$.

$\Gamma_{\mathrm{a}}[\omega]\mathbf{a_{in}}[\boldsymbol{\omega}] + \Gamma_i[\omega]\mathbf{a_{in}}[\boldsymbol{-\omega}]^\dagger$, where $\Gamma_{\mathrm{a}}[\omega]$ is the complex signal gain, and $\Gamma_i[\omega]$ is the complex idler gain. We find:

$$\Gamma_{\mathrm{a}}[\omega] = \frac{\kappa^2/4 - \delta_{\mathrm{a}}^2 + \lambda^2 + \omega^2 - i\kappa\delta_{\mathrm{a}}}{\kappa^2/4 + \delta_{\mathrm{a}}^2 - \lambda^2 - \omega^2 - i\kappa\omega}\,, \tag{2.29a}$$

$$\Gamma_i[\omega] = \frac{i\lambda\kappa}{\kappa^2/4 + \delta_{\mathrm{a}}^2 - \lambda^2 - \omega^2 - i\kappa\omega}\,. \tag{2.29b}$$

Given an input at a frequency $\omega_p/2 + \omega$ (in the laboratory frame), the signal gain is the quantity probed in a homodyne measurement, with an output detected at the same frequency. Conversely the idler gain, also known as intermodulation gain, is related to a heterodyne measurement, where the output is detected at the mirror frequency $\omega_p/2 - \omega$. For the record, in the presence of an extra internal-loss channel coupled to the DPO at a rate κ_i, the complex gains read:

$$\Gamma_{\mathrm{a}}[\omega] = \frac{(\kappa^2 - \kappa_i^2)/4 - \delta_{\mathrm{a}}^2 + \lambda^2 + \omega^2 - i\kappa\delta_{\mathrm{a}} + i\kappa_i\omega}{(\kappa + \kappa_i)^2/4 + \delta_{\mathrm{a}}^2 - \lambda^2 - \omega^2 - i(\kappa + \kappa_i)\omega}\,, \tag{2.30a}$$

$$\Gamma_i[\omega] = \frac{i\lambda\kappa}{(\kappa + \kappa_i)^2/4 + \delta_{\mathrm{a}}^2 - \lambda^2 - \omega^2 - i(\kappa + \kappa_i)\omega}\,. \tag{2.30b}$$

In the remainder of this section, we will neglect internal relaxation.

We plot on Fig. 2.6 (top) complex signal gains for increasing steady-state squeezing in the resonant regime $\delta_{\mathrm{a}} = 0$. With the pump off, the signal is a unit circle in the complex plane, as expected in the absence of internal dissipation. When the two-photon pump is added, the circle grows as a signature of signal amplification. One can also notice on the phase profile a sharpening of the lineshape, showing that amplification occurs at the expense of a reduced bandwidth.

Bogoliubov basis computation Second, we perform the same computation in the Bogoliubov basis. It is then restricted to the case $\delta_{\mathrm{a}} \neq 0$, and in the limit $\lambda < |\delta_{\mathrm{a}}|$. There, one can show that the QLE and the input-output relation read (appendix B.2):

$$\begin{gathered}\partial_t\boldsymbol{\alpha}(\boldsymbol{t}) = \frac{i}{\hbar}\left[\boldsymbol{\mathcal{H}}_{\mathbf{ph}}, \boldsymbol{\alpha}(\boldsymbol{t})\right] - \frac{\kappa}{2}\boldsymbol{\alpha}(\boldsymbol{t}) + \sqrt{\kappa}\big(\mathbf{a_{in}}(\boldsymbol{t})\cosh r - \mathbf{a_{in}^\dagger}(\boldsymbol{t})\sinh r\big)\\ \mathbf{a_{out}}(\boldsymbol{t}) + \mathbf{a_{in}}(\boldsymbol{t}) = \sqrt{\kappa}\big(\boldsymbol{\alpha}(\boldsymbol{t})\cosh r + \boldsymbol{\alpha}^\dagger(\boldsymbol{t})\sinh r\big)\end{gathered} \tag{2.31}$$

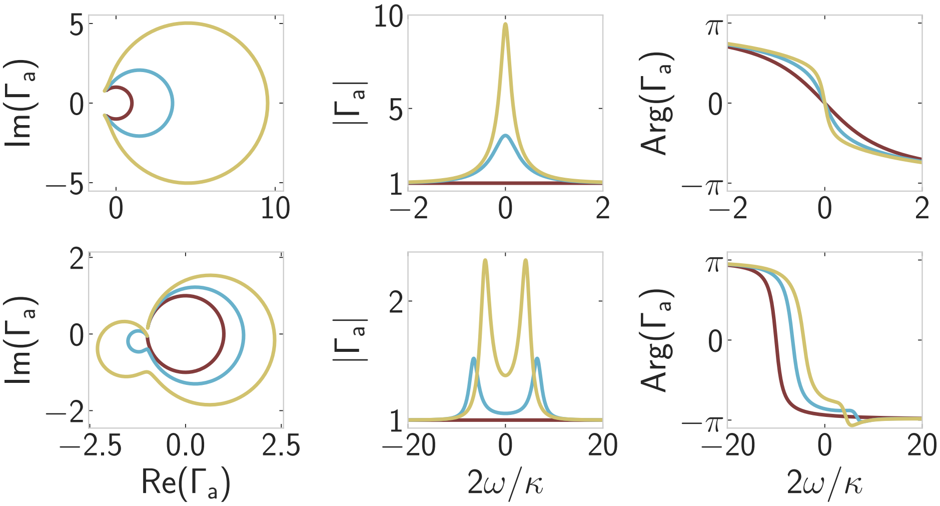

Figure 2.6 Signal gain of a DPO. (Top) Signal gain of a DPO for $\delta_\mathrm{a} = 0$ and $\breve{S}_\infty \in \{0, 6, 10\}$ dB (red, blue, gold) in the complex plane (left), in amplitude (center), and in phase (right). (Bottom) Same as top for $\delta_\mathrm{a} = 5\kappa$. Note the different frequency spans.

This result can be understood as follows[7]. As the Bogoliubov basis is an anti-squeezed version of the bare one, the QLE for the Bogoliubov mode features a coupling to an anti-squeezed version of the bath. Conversely, the closure relation for the input and output fields – written in terms of the bare mode – features scattering of squeezed Bogoliubov excitations. One must point out that the decay rate of the Bogoliubov excitations simply reads κ, which is not a trivial result. Following the same procedure as in the bare basis we find:

$$\Gamma_\mathrm{a}[\omega] = \Gamma_+[\omega] \cosh^2 r - \Gamma_-[\omega] \sinh^2 r \ , \tag{2.32a}$$

$$\Gamma_i[\omega] = \frac{\sinh 2r}{2} \left(\Gamma_-[\omega] - \Gamma_+[\omega] \right) \ , \tag{2.32b}$$

---

[7] As a reminder, the wording convention introduced in section 2.1.2 denotes:

$$\mathcal{U}_s \mathcal{O} \mathcal{U}_s^\dagger = \mathcal{O} \cosh r + \mathcal{O}^\dagger \sinh r \ : \quad \text{the squeezed version of } \mathcal{O} \ ,$$

$$\mathcal{U}_s^\dagger \mathcal{O} \mathcal{U}_s = \mathcal{O} \cosh r - \mathcal{O}^\dagger \sinh r \ : \quad \text{the anti-squeezed version of } \mathcal{O} \ .$$

where $\Gamma_\pm[\omega]$ is the complex gain response of a linear cavity measured in reflection, resonant at $\pm\Omega_\mathrm{a}[r]$ with linewidth κ:

$$\Gamma_\pm[\omega] = \frac{\kappa/2 + i(\omega \mp \Omega_\mathrm{a}[r])}{\kappa/2 - i(\omega \mp \Omega_\mathrm{a}[r])}\,. \tag{2.33}$$

One can check that in the domain of validity of the Bogoliubov transformation, Eqs. 2.32 map to Eqs. 2.29.

We plot on Fig. 2.6 (bottom) complex signal gains for increasing steady-state squeezing in the detuned regime $\delta_\mathrm{a} = 5\kappa$. When the two-photon pump is added, the circle not only grows in the same direction as before, but a protrusion emerges on the opposite side. The signal gain features two spectroscopic lines located near $\pm\Omega_\mathrm{a}[r]$, as one could have guessed by inspecting Eq. 2.32a. In the limit where $2|\Omega_\mathrm{a}[r]| > \kappa$, these two features are distinct, and the BO is said to be *resolved*. In the opposite case, the lines merge into a single peak, and the BO is said to be in the *coalescent* regime. The frontier of coalescence is defined through the parameter λ_co such that:

$$2|\Omega_\mathrm{a}[r]| < \kappa \quad\Longleftrightarrow\quad \lambda > \lambda_\mathrm{co} \equiv \sqrt{\delta_\mathrm{a}^2 - \frac{\kappa^2}{4}}\,. \tag{2.34}$$

It is only visible in the case where the pump is initally sufficiently detuned from the oscillator frequency $|\delta_\mathrm{a}| > \kappa/2$, for which λ_co can be defined as a real parameter (Fig. 2.5). Notably the coalescent regime extends beyond the domain of definition of the Bogliubov oscillator, up to the critical point of the DPO (Fig. 2.7).

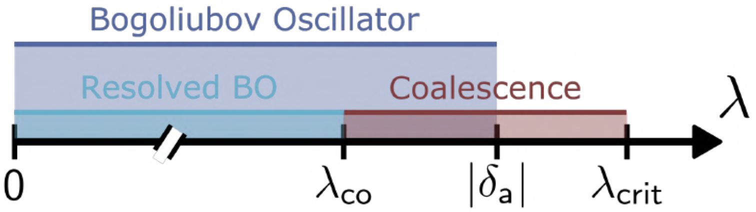

Figure 2.7 Resolving coalescence. A detuned DPO such that $|\delta_\mathrm{a}| > \kappa/2$ can be in the resolved BO regime, the coalescent BO regime, or simply the coalescent regime.

Amplifier mode As a matter of fact, a detuned DPO in the coalescent regime bears strong resemblance with a resonant DPO. We illustrate this thought using the signal power gain $|\Gamma_\mathrm{a}[\omega]|^2$, the quantity of interest when operating the DPO as a parametric amplifier. Starting from Eq. 2.29a, we find:

$$|\Gamma_\mathrm{a}[\omega]|^2 = 1 + \frac{\kappa^2\lambda^2}{\left(\omega^2 + \lambda^2 - \lambda_\mathrm{crit}^2\right)^2 + \kappa^2\omega^2} \tag{2.35}$$

Defining the maximum gain of the amplifier as $G = \max_\omega |\Gamma_\mathrm{a}[\omega]|^2$, we find two regimes depending on the variations of the signal power gain function. For nearly resonant squeezing ($|\delta_\mathrm{a}| < \kappa/2$) or in the coalescent regime ($|\delta_\mathrm{a}| > \kappa/2$ and $\lambda > \lambda_\mathrm{co}$), the signal power gain features one maximum when $\omega = \omega_0$ such that:

$$\omega_0 = 0 \quad \text{and} \quad G_0 = 1 + \frac{\kappa^2\lambda^2}{(\lambda_\mathrm{crit}^2 - \lambda^2)^2}\ . \tag{2.36}$$

It is quite remarkable that these two dissimilar regimes of operation share a common definition of the maximum gain, upon a mere redefinition of λ_crit. Yet, this strong resemblance is not surprising. Indeed, they both operate in close proximity to a dynamical instability, which appears to fuel the amplification process.

On the contrary, for detuned squeezing before coalescence ($|\delta_\mathrm{a}| > \kappa/2$ and $\lambda < \lambda_\mathrm{co}$), the signal power gain features two maxima when $\omega = \omega_\pm$ such that:

$$\begin{aligned} \omega_\pm = &\pm \sqrt{\Omega_\mathrm{a}^2[r] - \kappa^2/4} \\ &\pm \sqrt{\lambda_\mathrm{co}^2 - \lambda^2} \end{aligned} \quad \text{and} \quad G_\pm = \frac{\delta_\mathrm{a}^2}{\delta_\mathrm{a}^2 - \lambda^2} = \cosh^2 2r\ . \tag{2.37}$$

The absence of λ_crit in the previous formula reveals the peculiarity of the resolved Bogoliubov regime, which delivers substancial gain while operating far from any dynamical instability [Metelmann 2022]. It is also quite intriguing to see the maximum gain output by the amplifier solely defined by the fluctuations of the eigenstates. Finally, the absence of κ in the previous formula points towards another key property of the resolved BO: it is not constrained by the gain-bandwidth product.

2.1.4 Gain-bandwidth products

The gain-bandwidth product is a defining relation for many amplifier designs, that sets at a constant value the product of the signal gain to the amplification bandwidth. As a consequence, the bigger the gain, the smaller the bandwidth, which comes as a drastic limitation for wideband amplification purposes. In this part, we start by presenting the gain-bandwidth product for a DPO with resonant squeezing. Then we show that a DPO with detuned squeezing escapes this constraint, and even widen its bandwidth at the onset of coalescence. Finally we propose an extension of the definition of coalescence.

Resonant case For resonant squeezing ($\delta_\mathrm{a} = 0$), the signal power gain can be rewritten as:

$$|\Gamma_\mathrm{a}[\omega]|^2 = 1 + \frac{G_0 - 1}{1 + 2\omega^2 \dfrac{G_0}{\kappa^2/4 + \lambda^2}\left(1 + \dfrac{\omega^2}{2(\kappa^2/4 + \lambda^2)}\right)} . \tag{2.38}$$

Hence, around resonance $\omega = \omega_0 + \Delta\omega$ with $\omega_0 = 0$ and $\Delta\omega \ll \kappa/2$, the signal power gain follows a Lorentzian lineshape:

$$|\Gamma_\mathrm{a}[\Delta\omega]|^2 \underset{\Delta\omega \ll \kappa/2}{\approx} 1 + \frac{G_0 - 1}{1 + (2\Delta\omega/\Delta_\mathrm{3dB})^2} , \tag{2.39}$$

characterized by a 3 dB amplification bandwidth in the large gain limit:

$$\Delta_\mathrm{3dB} \underset{\lambda \to \kappa/2}{\sim} = \frac{\kappa}{\sqrt{G_0}} . \tag{2.40}$$

Hence the so-called gain-bandwidth product $\Delta_\mathrm{3dB}\sqrt{G_0}$ which is constrained by κ. In practice, it means that at 20 dB of output gain, the amplification bandwidth is one tenth of the initial one. Not only does this reduce the frequency multiplexing capabilities of the amplifier, but it also increases its sensitivity to spurious effects such as Kerr nonlinearity [Planat 2019].

Resolved BO regime In the resolved BO regime ($|\delta_\mathrm{a}| > 0$ and $\lambda < \lambda_\mathrm{co}$), it is instructive to rewrite Eq. 2.35 using the squeezing parameter:

$$|\Gamma_\mathrm{a}[\omega]|^2 \underset{\lambda < |\delta_\mathrm{a}|}{=} 1 + \frac{\kappa^2 \Omega_\mathrm{a}^2[r] \sinh^2 2r}{\left(\omega^2 + \kappa^2/4 - \Omega_\mathrm{a}^2[r]\right)^2 + \kappa^2 \Omega_\mathrm{a}^2[r]} \tag{2.41}$$

It is then straightforward to show that around resonance $\omega = \omega_\pm + \Delta\omega$ with $\Delta\omega \ll \kappa/2$, the signal power gain follows a Lorentzian linehsape:

$$|\Gamma_\mathrm{a}[\omega_\pm + \Delta\omega]|^2 \underset{\Delta\omega \ll \kappa/2}{\approx} 1 + \frac{G_\pm - 1}{1 + (2\Delta\omega/\kappa)^2} \,, \tag{2.42}$$

where the 3 dB linewdith in the large gain limit is simply given by κ.

Coalescent regime Next we turn to the description of the coalescent regime ($|\delta_\mathrm{a}| > \kappa/2$ and $\lambda_\mathrm{co} \leqslant \lambda < \lambda_\mathrm{crit}$). There, the signal power gain reads:

$$|\Gamma_\mathrm{a}[\omega]|^2 = 1 + \frac{G_0 - 1}{1 + 2\omega^2 \dfrac{\lambda^2 - \lambda_\mathrm{co}^2}{(\lambda_\mathrm{crit}^2 - \lambda^2)^2} + \dfrac{\omega^4}{(\lambda_\mathrm{crit}^2 - \lambda^2)^2}} \tag{2.43}$$

On the coalescent line $\lambda = \lambda_\mathrm{co}$, the gain profile takes the exact form of a fourth-order Bell shaped function:

$$|\Gamma_\mathrm{a}[\Delta\omega]|^2 = 1 + \frac{G_0 - 1}{1 + (2\omega/\Delta_\mathrm{3dB})^4} \,, \tag{2.44}$$

where $\Delta_\mathrm{3dB} = \sqrt{2}\kappa$. In addition to its enhanced bandwidth as compared to the bare oscillator, operating on the coalescent line offers a gain profile with a flat top which minimizes distorsion [Metelmann 2022].

Finally deep in the coalescent regime, it is instructive to introduce the small parameter $\delta\lambda$ such that:

$$\lambda^2 = \lambda_\mathrm{crit}^2 - \delta\lambda^2 \quad \Longleftrightarrow \quad \delta\lambda^2 = \frac{\kappa\lambda}{\sqrt{G_0 - 1}} \tag{2.45}$$

While the gain profile deep into coalescence does not assume a simple analytical form, we can still define a 3 dB bandwidth Δ_3dB as $|\Gamma_\mathrm{a}[\frac{1}{2}\Delta_\mathrm{3dB}]|^2 = G_0/2$. It obeys the quartic equation:

$$\frac{\Delta_\mathrm{3dB}^2}{4}\left(\kappa^2 - 2\delta\lambda^2 + \frac{\Delta_\mathrm{3dB}^2}{4}\right) = \frac{G_0}{G_0 - 2}\delta\lambda^4 \tag{2.46}$$

Near criticality, that is to say in the large gain limit, we find:

$$\Delta_\mathrm{3dB} \underset{\lambda \to \lambda_\mathrm{crit}}{\sim} \frac{2\lambda_\mathrm{crit}}{\sqrt{G_0}} \,, \tag{2.47}$$

As the detuned DPO falls deep into coalescence, we witness a resurgence of the gain-bandwidth constraint, as a signature of the proximity of the dynamical instability. The scaling of the amplification bandwidth with gain is identical to the resonant case for which $\lambda_\mathrm{crit} = \kappa/2$ (Eq. 2.40).

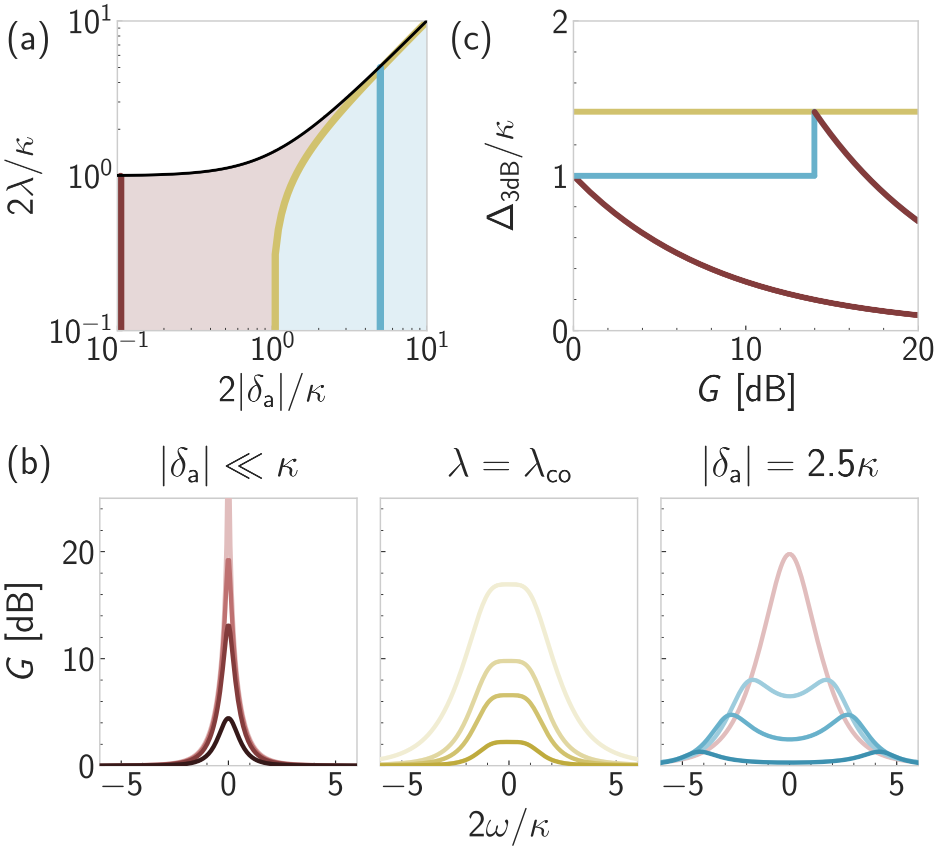

Figure 2.8 Gain-bandwidth products. (a) The DPO parameter space is split into 3 regions: the white region $\lambda \geqslant \lambda_{\text{crit}}$ is unstable, the red region $\text{Re}(\lambda_{\text{co}}) \leqslant \lambda < \lambda_{\text{crit}}$ is contrained by the gain-bandwidth product, and the blue region $\lambda < \text{Re}(\lambda_{\text{co}})$ is not. The gold coalescent line $\lambda = \lambda_{\text{co}}$ separates the two stable regions. (b) Signal power gain profiles for a resonant DPO (left), an ever-coalescent DPO (center), and a detuned DPO (right), for $\lambda/\lambda_{\text{crit}} \in \{0.5, 0.8, 0.9, 0.98\}$ (color of increasing lightness). (c) 3 dB amplification bandwidth scaled by the bare linewidth of the oscillator versus maximum gain, for the three regimes of operation depicted in (a,b). As a detuned DPO crosses the coalescent line, it goes from the blue to the red region.

DPO summary The frontier of coalescence is not visible in the small detuning limit $|\delta_{\rm a}| < \kappa/2$. Yet, we can give a unified description of the DPOs at all detunings by resorting to the real value of the parameter $\lambda_{\rm co}$ (Table 2.1). In the region where $\lambda \leqslant \mathrm{Re}(\lambda_{\rm co})$ (blue on Fig. 2.8), the DPO is sufficiently remote from the dynamical instability, and has the ability to deliver gain with a constant bandwidth. In this limit the gain is a direct manifestation of the eigenstate squeezing. In the region where $\mathrm{Re}(\lambda_{\rm co}) < \lambda < \lambda_{\rm crit}$ (red on Fig. 2.8), the DPO approaches the critical point, and an increasing gain is delivered at the expense of a reduced bandwidth. To some extent, a nearly-resonant DPO is always coalescent. As a conclusion, one can say that a BO unveils its true potential only in the resolved regime.

	Resolved BO	Coalescence	Unstable
Two-photon pump	$\lambda \leqslant \mathrm{Re}(\lambda_{\rm co})$	$\mathrm{Re}(\lambda_{\rm co}) < \lambda < \lambda_{\rm crit}$	$\lambda \geqslant \lambda_{\rm crit}$
Max. gain	$G_\pm = \dfrac{\delta_{\rm a}^2}{\delta_{\rm a}^2 - \lambda^2}$	$G_0 = 1 + \dfrac{\kappa\lambda}{(\lambda_{\rm crit}^2 - \lambda^2)}$	–
Max. gain frequency	$\omega_\pm = \pm\sqrt{\lambda_{\rm co}^2 - \lambda^2}$	$\omega_0 = 0$	–
Bandwidth	$\Delta_{\rm 3dB} = \kappa$	$\Delta_{\rm 3dB} = \dfrac{2\lambda_{\rm crit}}{\sqrt{G_0}}$	–

Table 2.1 DPO summary. A DPO with detuning $\delta_{\rm a}$ and bare linewdith κ such that: $\lambda_{\rm crit} = \sqrt{\delta_{\rm a}^2 + \kappa^2/4}$ and $\lambda_{\rm co} = \sqrt{\delta_{\rm a}^2 - \kappa^2/4}$.

2.2 A superconducting degenerate parametric oscillator

2.2.1 Josephson engineering

Circuit-QED relies on the flexibility of electrical circuits to study quantum phenomenas. While classical electronics uses dissipative elements to provide the nonlinearity necesseray to any non-trivial operation (like a diode or a transistor), quantum circuits can only feature lossless elements to preserve quantum coherence [Devoret and Martinis 2004]. In that respect, superconducting circuits consist in assembling three lossless elementary components to build arbitrarily complex systems: the linear capacitor, the linear inductor, and the Josephson junction (JJ). In this section we present the nonlinearity of the JJ, and how *Josephson circuits* are leveraged to engineer complex Hamiltonians. Finally we conlude with the presentation of two Josephson elements used for parametric amplification.

The Josephson effect When two pieces of superconductor are brought in close proximity, albeit separated by a non-superconducting barrier, the coherent tunneling of Cooper-pairs from one piece to the other leads to the Josephson effect. It is captured by two constituve relations. The first one relates the current flowing through the barrier (the JJ), to the superconducting phase difference φ between the two pieces of superconductor:

$$I = I_c \sin\varphi \ , \tag{2.48}$$

where I_c is the junction critical current. The second one relates the superconducting phase difference to the generalized flux coordinate:

$$\varphi(t) = \frac{2\pi}{\Phi_0}\Phi(t) \quad \text{where} \quad \Phi(t) = \int_{-\infty}^{t} \mathrm{d}\tau V(\tau) \ , \tag{2.49}$$

and $V(t)$ is the voltage drop accross the junction. The flux coordiante $\Phi(t)$ is generalized in a sense that it reproduces the constitutive relation of a linear inductor $V(t) = \dot{\Phi}(t)$, while not being limited to the magnetic flux stored in a winded piece of conductor. Indeed, a JJ is so small that it does not store much energy in the magnetic field induced by the moving charges: it has a negligible *geometric* inductance. Rather, its energy is mostly associated to the kinetic energy of the charges moving accross the barrier: its inductance is *kinetic*. The equivalent junction inducance is defined as $L_J(\varphi) = V(t)/\dot{I}(t) = L_{J0}/\cos\varphi$ where $L_{J0} = \Phi_0/2\pi I_c$.

As customary for inductive elements, the junction energy reads $U_J(\varphi) = \int_0^\Phi I(\Phi')\mathrm{d}\Phi' = E_J(1-\cos\varphi)$, with $E_J = (\Phi_0/2\pi)^2/L_{J0}$ the Josephson energy. When embedded in a superconducting circuit, a JJ will contribute to the inductive energy by $U_J(\varphi)$, just like a linear inductor L contributes by $U_L = \Phi^2/2L$. Considering flux as a position-like degree of freedom, inductive terms constitute the potential energy of the circuit.

Hamiltonian engineering Circuit quantization aims at giving a quantum mechanical description of the low-energy physics of a circuit, around a minimum of its potential energy. For a LC oscillator such as the one described in section 1.1, the confining potential is harmonic, and the mode linear: its Hamiltonian simply reads $\boldsymbol{\mathcal{H}}_{\mathbf{a,0}} = \hbar\omega_\mathrm{a}\mathbf{a}^\dagger\mathbf{a}$. The addition of a Josephson element to an otherwise linear circuit mode can be accounted for perturbatively, assuming its participation $\varphi_\mathrm{zpf}^{nl}$ in the total mode inductance is small [Nigg 2012; Minev 2021]. For such a weakly nonlinear system, corrections to the bare Hamiltonian stem from the expansion of the nonlinear potential around its minimum. They typically read $\boldsymbol{\mathcal{H}}_{\mathbf{a,nl}} = \sum_m c_m\big(\mathbf{a}+\mathbf{a}^\dagger\big)^m$, where the coefficients $c_m \sim (\varphi_\mathrm{zpf}^{nl})^m$ reflect the symmetries of the potential energy. The nonlinear part of the Hamiltonian presents two types of term. The resonant ones feature an equal number of $\mathbf{a}$'s and $\mathbf{a}^\dagger$'s, while the off-resonant ones do not. In the limit of weak nonlinearity, ω_a is the dominant energy scale and the off-resonant terms can be averaged out (section B.1.3). We are then left with resonant terms of Kerr type $\propto \mathbf{a}^{\dagger 2}\mathbf{a}^2$. These contributions renormalize the frequency of the bare oscillator every time an excitation is added, as if photons were interacting with each other.

If it were just for Kerr interactions, the applicability of Josephson circuits would be quite limited. However, activation of any other nonlinearity can be enforced using pumps. A pump is a microwave signal, typically off-resonant with the oscillator and of large amplitude. It is not meant to directly drive the system, but rather to trigger some nonlinearity. In the following, we focus on the two-photon injection process described in section 2.1.1. As we will justify in the next section, pumping the mode at a frequency ω_p can be accounted for at the level of $\boldsymbol{\mathcal{H}}_{nl}$ by replacing $\mathbf{a}$ by $\mathbf{a}+\xi e^{-i\omega_\mathrm{p}t}$, with $\xi \in \mathbb{C}$. Then, in a rotating frame at ω_a, one is left to check in the successive orders of the nonlinear Hamiltonian where resonant conditions are hidden:

$$m=3: \big(\mathbf{a}_t+\mathbf{a}_t^\dagger+\xi_t+\xi_t^*\big)^3 = 3\big(\mathbf{a}_t+\mathbf{a}_t^\dagger\big)^2\big(\xi_t+\xi_t^*\big)+\dots \tag{2.50a}$$

$$m=4: \big(\mathbf{a}_t+\mathbf{a}_t^\dagger+\xi_t+\xi_t^*\big)^4 = 6\big(\mathbf{a}_t+\mathbf{a}_t^\dagger\big)^2\big(\xi_t+\xi_t^*\big)^2+\dots \tag{2.50b}$$

$$\begin{aligned} m=5: \big(\mathbf{a}_t+\mathbf{a}_t^\dagger+\xi_t+\xi_t^*\big)^5 &= 30\big(\mathbf{a}_t+\mathbf{a}_t^\dagger\big)^2\big(\xi_t+\xi_t^*\big) \\ &\quad + 20\big(\mathbf{a}_t+\mathbf{a}_t^\dagger\big)^2\big(\xi_t+\xi_t^*\big)^3+\dots \end{aligned} \tag{2.50c}$$

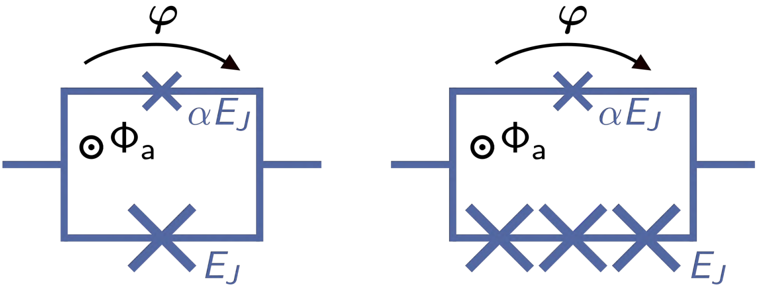

Figure 2.9 SQUID (left) vs SNAIL (right).

where we used the shortcut notation $\mathbf{a}_t = \mathbf{a}e^{-i\omega_\mathrm{a}t}$ and $\xi_t = \xi e^{-i\omega_\mathrm{p}t}$. We see that the injection of pairs of photons in mode **a** can be mediated by a 3-wave mixing term ($\omega_\mathrm{p} = 2\omega_\mathrm{a}$) at third and fifth order, by a 4-wave mixing term ($\omega_\mathrm{p} = \omega_\mathrm{a}$) at fourth order, by a 5-wave mixing term ($\omega_\mathrm{p} = 2\omega_\mathrm{a}/3$) at fifth order, and so on. Notably, parametric processes mixing an odd number of waves can only by mediated by odd order terms of the potential energy. Since the energy of a single junction $U_J(\varphi)$ is an even function, symmetric about its minimum, it cannot mediate 3-wave mixing. But then, who can?

A story of mollusks In the following, we will consider two special arrangements of JJs. The first one, the superconducting quantum interference device (SQUID), is a ubiquitous element of the physics of superconductivity [Tinkham 1996]. Here we focus on its implementation in the context of parametric amplification [Boutin 2017; Planat 2019]. It consists in a parallel assembly of a junction with Josephson energies E_J, and a smaller[8] one with energy αE_J ($0 < \alpha \leqslant 1$) (Fig. 2.9). Ensuring flux quantization within the loop lets us write its equivalent Josephson energy (discarding constant terms):

$$U_\mathrm{SQUID}(\varphi) = -E_J \cos(\varphi_\mathrm{a} - \varphi) - \alpha E_J \cos\varphi \ , \tag{2.51}$$

where $\Phi_\mathrm{a} = \varphi_\mathrm{a}\Phi_0/2\pi$ is the magnetic flux threaded through the loop. Since the SQUID potential energy is a sum of two cosine functions with same periodicity, it is symmetric about its minimum[9] (Fig. 2.10). When embedded in an oscillator, the lowest-order process for which a SQUID can mediate two-photon injection is then 4-wave mixing. Unfortunately, the same or-

---

[8] Smaller in energy ⇔ smaller in size ⇔ bigger in inductance.

[9] One can check that $U_\mathrm{SQUID}^{(2m+1)}(\varphi) = (-1)^m U'_\mathrm{SQUID}(\varphi)$, so that at the equilibrium point $U'_\mathrm{SQUID}(\varphi_\mathrm{eq}) = 0$, all odd derivatives vanish.

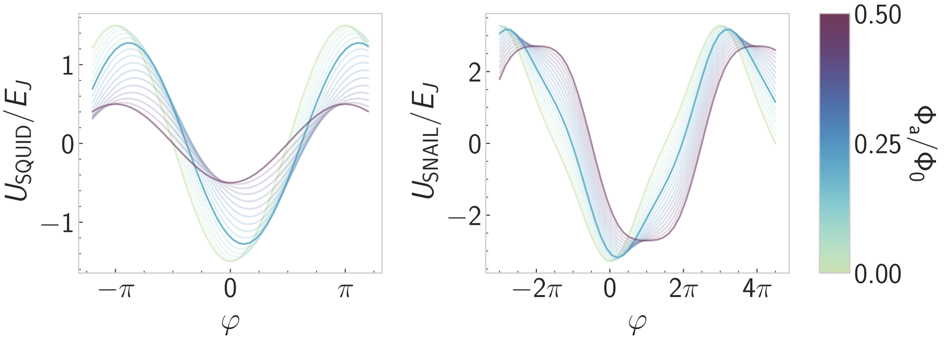

Figure 2.10 SQUID vs SNAIL potentials. Potential landscape of a SQUID with $\alpha = 0.5$ (left) and a SNAIL with $\alpha = 0.29$ (right) versus the superconducting phase accross the element (x-axis) and for varying external flux threaded through the loop (color). External fluxes of 0 (green), 0.375 (blue) and 0.5 (purple) times Φ_0 are highlighted. The SQUID potential is symmetric about its minimum for all external fluxes. The SNAIL potential is not symmetric about its minimum for intermediate fluxes, as depicted by the blue curve.

der induces Kerr effect in the oscillator, commonly known for degrading amplifier performances such as the 1 dB compression point [Frattini 2018].

The second one, the superconducting nonlinear asymmetric inductive element (SNAIL), consists in a parallel assembly of three junctions with energy E_J, and a smaller one αE_J (Fig. 2.9). The equivalent Josephson energy reads:

$$U_{\mathrm{SNAIL}}(\varphi) = -3E_J \cos\frac{\varphi_{\mathrm{a}} - \varphi}{3} - \alpha E_J \cos\varphi\ . \tag{2.52}$$

Notably, away from $\varphi_{\mathrm{a}} \equiv 0 \bmod \pi$ the potential is not symmetric about its minimum (Fig. 2.10), which justifies its denomination as a *3-wave mixing Josephson dipole element* [Frattini 2017]. Since it was first proposed, the SNAIL quickly established as a very useful tool for circuit-QED, from resonant [Sivak 2019] to travelling amplification [Ranadive 2022], or the stabilization of Kerr cats [Grimm 2020]. Indeed, the nonlinearity powering the amplification is of a lowest order than Kerr effect, limiting its spurious impact. In addition, the SNAIL possesses a flux point where the amplitude of the Kerr term vanishes, a key requirement to implement the DPO model (2.4) with minimal parasitic terms.

2.2.2 SNAIL-resonator

We emulate the DPO model in a quarter-wavelength resonator enhanced by a SNAIL (Fig. 2.11). In the following, we motivate this design choice.

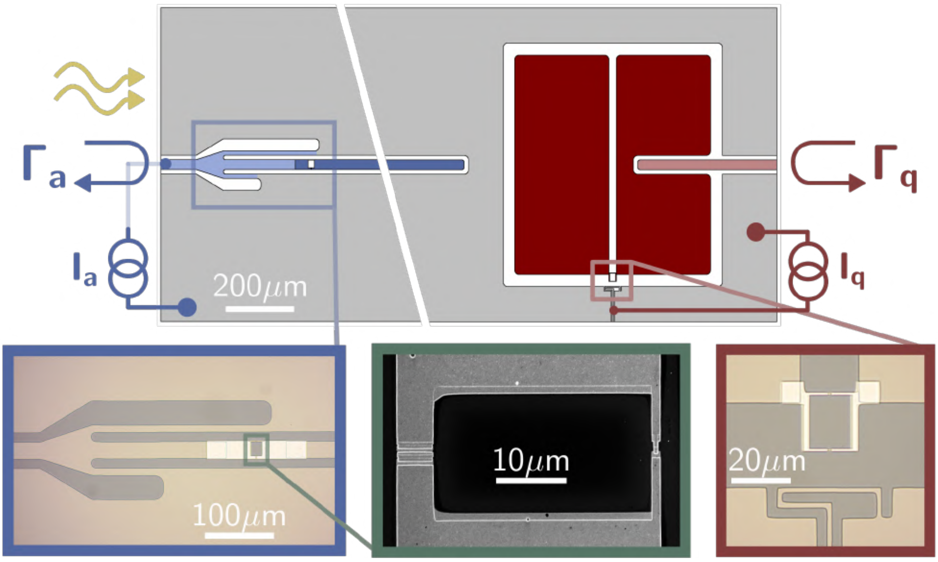

Figure 2.11 Superconducting circuit layout with a diagonal break for compactness. A quarter wavelength coplanar waveguide resonator (blue) implements the oscillator. The reflection spectrum Γ_a is measured through an inductive coupler (optical micrograph in blue inset), that also channels the pump signal and a DC current for flux biasing of the SNAIL loop (scanning electron microscope image in green inset rotated by 90°). The resonator is weakly capacitively coupled to a transmon qubit (bordeaux), which is overcoupled to a transmission line for direct reflection spectroscopy Γ_q. A DC line threads flux through its SQUID loop (optical micrograph in bordeaux inset).

Bare oscillator design The oscillator mode with frequency ω_a is the fundamental mode of a quarter-wavelength superconducting resonator, in a coplanar-waveguide architecture. This choice of geometry is essential to implement a strongly-detuned DPO. Indeed, given a distributed-element resonator with fundamental frequency ω_a, a half-wavelength implementaion would find its first harmonic in the vicinity of $2\omega_\mathrm{a}$. On the contrary, the first harmonic of a quarter-wavelength resonator lies near $3\omega_\mathrm{a}$. Thus, such a geometry could potentially emulate DPOs with detunings δ_a of the order of ω_a. The resonator is inductively coupled to a transmission line used to channel read-out and pump signals. The SNAIL is embedded at the tip of the inductive coupler [Bothner 2013; Besedin and Menushenkov 2018]. Owing to its asymmetric geometry, flowing a DC current from the inner conductor of the transmission line to ground will result in unequal intensities running on either side of the SNAIL. Thus, a finite offset flux can be threaded in its loop. This 3-in-1 coupler (signal, pump, DC) is another key element of this design, giving full control over the resonator and its nonlinearity with a single access port, thus limiting the introduction of extra radiative loss channels.

Nonlinear tuning Following [Frattini 2017], a SNAIL-resonator is most generally described by the Hamiltonian:

$$\boldsymbol{\mathcal{H}}_\mathbf{a}/\hbar = \omega_\mathrm{a}(\Phi_\mathrm{a})\mathbf{a}^\dagger\mathbf{a} + \sum_{m\geqslant 3} g_m(\Phi_\mathrm{a})\left(\mathbf{a}+\mathbf{a}^\dagger\right)^m \,, \tag{2.53}$$

where $g_m(\Phi_\mathrm{a})$ is the m^{th}-order nonlinearity inherited from the SNAIL potential energy (Eq. 2.52), depending on the flux Φ_a threading its loop. As detailed ealier, the fourth-order term of this expansion contributes to the Kerr nonlinearity of the oscillator. Owing to the specific choice of SNAIL parameters (Table 4.1), the Kerr amplitude vanishes at a given flux point [Frattini 2018]. We identify this specific flux point by performing a Kerr spectroscopy of the oscillator (Fig. 2.12). At each flux bias, we set a microwave drive 300 MHz above resonance populating the oscillator with increasing photon number $\bar{n}_\mathrm{d}$, and acquire its reflection spectrum. The resonance frequency shift $\Delta\omega_\mathrm{a} = \chi_\mathrm{aa}\bar{n}_\mathrm{d}$ is a direct measure of the Kerr amplitude χ_aa. As depicted in the insets of Fig. 2.12, its value can be positive, negative, and set close to zero. In the dataset of Fig. 2.12 we find a Kerr-free point at $\omega_\mathrm{a}^0/2\pi = 7.015$ GHz. Later in the cooldown, this operation point drifted to $\omega_\mathrm{a}^0/2\pi = 6.940$ GHz which is used in the rest of the thesis. The Kerr and resonance frequency versus flux pin down the non-linear resonator circuit parameters. From these parameters, we estimate a three-wave mixing amplitude at the Kerr-free point $g_3/2\pi = 18$ MHz.

DPO driven-emulator At the Kerr-free flux point, the SNAIL-resonator can be minimally described by an anharmonic oscillator with bare frequency ω_a, dressed by a third-order nonlinearity g_3. It is then an ideal platform for the emulation of the DPO model via 3-wave mixing. Activation of the

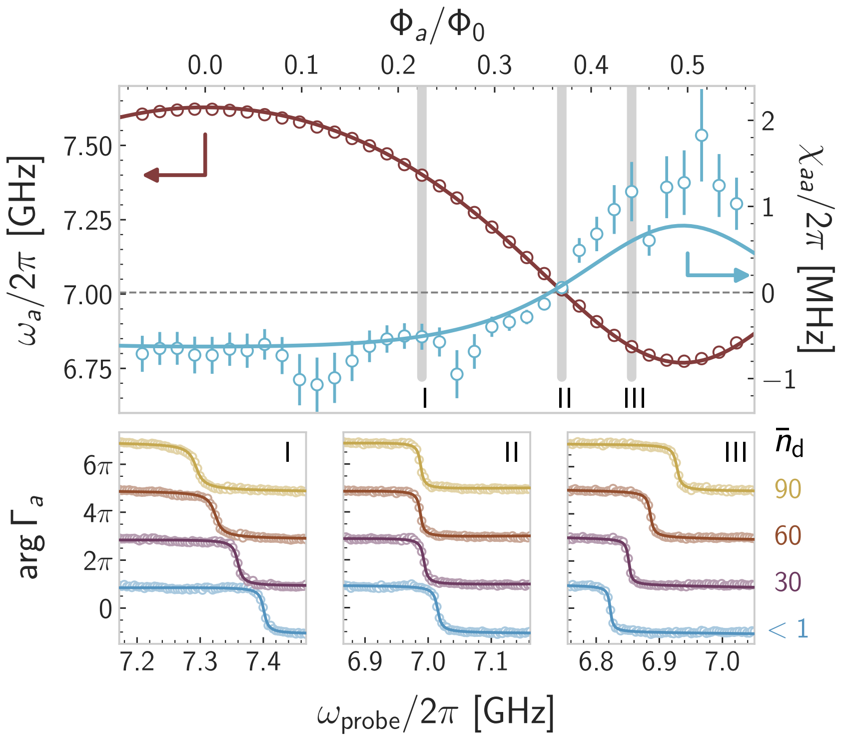

Figure 2.12 Kerr spectroscopy of the oscillator. Top: measured resonant frequency (left axis) and Kerr nonlinearity (right axis) of the oscillator versus flux threaded through the SNAIL loop (x-axis), in units of flux quantum $\Phi_0 = h/2e$. Fitting the data (open circles) to the theory extracted from Hamiltonian diagonalization (full lines) sets all oscillator circuit parameters. Bottom: phase response (y-axis) of the oscillator to a weak probe of variable frequency (x-axis) when populated by a +300 MHz detuned drive with increasing power (bottom to top, curves offset for clarity) in units of circulating photon number $\bar{n}_\mathrm{d}$ indicated on the right. Each panel corresponds to a flux point where the Kerr non-linearity is negative (I), close to zero (II) and positive (III). Fitted response (full lines) are overlaid to the data (open circles).

parametric process is accounted for at the Hamiltonian level by a pump with frequency ω_p and amplitude ε_p such that:

$$\mathcal{H}_\mathbf{a}/\hbar = \omega_\mathrm{a}\mathbf{a}^\dagger\mathbf{a} + g_3\left(\mathbf{a}+\mathbf{a}^\dagger\right)^3 + \varepsilon_\mathrm{p}\cos\omega_\mathrm{p}t\left(\mathbf{a}+\mathbf{a}^\dagger\right) . \tag{2.54}$$

Note that we use a different sign convention as opposed to [Villiers 2023]. As customary for driven systems, we displace operator **a** by its mean value $\mathbf{a} \to \mathbf{a} + \xi(t)$, where ξ is a complex time-dependent parameter verifying $\dot{\xi} = -i\omega_\mathrm{a}\xi - (\kappa/2)\xi + i\varepsilon_\mathrm{p}\cos(\omega_\mathrm{p}t)$ (Appendix B.1.2). At times $t \gg 1/\kappa$, and in the regime where $\kappa \ll |\omega_\mathrm{a} \pm \omega_\mathrm{p}|$:

$$\xi(t) \approx \frac{\varepsilon_\mathrm{p}/2}{\omega_\mathrm{p}-\omega_\mathrm{a}}e^{-i\omega_\mathrm{p}t} - \frac{\varepsilon_\mathrm{p}/2}{\omega_\mathrm{p}+\omega_\mathrm{a}}e^{i\omega_\mathrm{p}t} . \tag{2.55}$$

Further going to a frame rotating at half the pump frequency, resulting in $\mathbf{a} \to \mathbf{a}e^{-i\omega_\mathrm{p}t/2}$, the transformed Hamiltonian exactly writes:

$$\mathcal{H}_\mathbf{a}^{\xi,\omega}/\hbar = \delta_\mathrm{a}\mathbf{a}^\dagger\mathbf{a} + g_3\left(\mathbf{a}e^{-i\omega_\mathrm{p}t/2} + \mathbf{a}^\dagger e^{i\omega_\mathrm{p}t/2} + \Pi e^{-i\omega_\mathrm{p}t} + \Pi e^{i\omega_\mathrm{p}t}\right)^3 , \tag{2.56}$$

where $\delta_\mathrm{a} = \omega_\mathrm{a} - \omega_\mathrm{p}/2$. We place ourselves in the regime where $|\delta_\mathrm{a}| \ll \omega_\mathrm{a}$, hence $\Pi \approx \varepsilon_\mathrm{p}/3\omega_\mathrm{a}$. We next perform the rotating wave approximation (RWA), and define the time-averaged photon Hamiltonian as $\mathcal{H}_\mathbf{ph} \equiv \overline{\mathcal{H}_a^{\xi,\omega}}$ [Mirrahimi and Rouchon 2015]. We find:

$$\mathcal{H}_\mathbf{ph}/\hbar = \delta_\mathrm{a}\mathbf{a}^\dagger\mathbf{a} - \frac{\lambda}{2}\left(\mathbf{a}^2 + \mathbf{a}^{\dagger 2}\right) , \tag{2.57}$$

where $\lambda \approx -2g_3\varepsilon_\mathrm{p}/\omega_\mathrm{a}$ is the two-photon pump amplitude. Thus a SNAIL-resonator pumped near the parametric resonance $2\omega_\mathrm{a}$ emulates a degenerate parametric oscillator (DPO) [Carmichael 1984]. The validity of the RWA is granted by $g_3\Pi \ll \omega_\mathrm{p}$.

2.2.3 Resonant squeezing

First we look at the DPO gain response in the presence of resonant squeezing, setting the pump frequency to $\omega_\mathrm{p} = 2\omega_\mathrm{a}$. The pump power P_p applied on the system is calibrated at room temperature, so that the ratio between ε_p and $\sqrt{P_\mathrm{p}}$ – related to the attenuation of the microwave lines – is not precisely known (section 4.1.1). In the same spirit, our measurement setup does not access the signal gain directly, but rather the signal gain times an unknown transfer function. In order to reconstruct $\Gamma_\mathrm{a}[\omega]$, we acquire two spectra. The first one probes the resonator under the specified pumping conditions. The second one probes the same frequency window, with the pump off and after flux tuning the resonator out of the frequency window. It corresponds to a calibration of the transfer function. We divide the first trace by the second one to recover $\Gamma_\mathrm{a}[\omega]$. For varying pump powers, we fit every spectrum using Eq. 2.29a with the two-photon pump amplitude λ as the only free parameter, unveiling the mapping between $\sqrt{P_\mathrm{p}}$ and λ.

As the pump power increases, the DPO displays a growing signal power gain, centered at $\omega_\mathrm{a} = \omega_\mathrm{p}/2$ with a maximum reaching up to nearly 20 dB (Fig. 2.13a). For low to intermediate pump powers, the fitted response accurately represents the data (Fig. 2.13c,d), and the fitted parameter λ grows quadratically with the pump power (Fig. 2.13e). This low-power region is referred to as the *linear* regime. For larger pump powers, we witness a saturation of the gain accommpanied by a pinching of its frequency response, which the analytical model fails to reproduce (top region of Fig. 2.13a,b). This large-power region corresponds to the departure of the fitted parameter λ from its quadratic trend, and is referred to as the *saturation* regime. The onset of saturation is defined through the power $P_\mathrm{p,sat}$ for which the fitted parameter λ differs in more than 5% from the linear extrapolation inferred from the fitted values deep in the linear regime. We find $P_\mathrm{p,sat} \approx 9\ \mu\mathrm{W}$, and the associated critical gain and steady-state antisqueezing: $G_\mathrm{sat} = 14$ dB and $\breve{S}_{\infty,\mathrm{sat}} = 7.3$ dB.

The saturation of the DPO signal gain may be explained by two distinct mechanisms. The first one relies on a residual Kerr effect. As the gain increases, so does the mean occupation of the oscillator, and hence the magnitude of the Kerr-induced frequency shifts. When such shifts become comparable with the bandwidth of the amplifier $\Delta_\mathrm{3dB} = \kappa/\sqrt{G}$ (section 2.1.4), the pump frequency is no longer matching the parametric resonance, and the amplification process is weakened. The second one relies on the pump depletion mechanism. When the power output by the amplifier becomes comparable with the one input by the pump, the pump can no longer be considered *stiff*, meaning one needs to account for its finite power-delivery capacity. What is the dominant mechanism responsible for saturation in our setup?

We start with an estimation of the pump stiffness at the saturation point. While $P_\mathrm{p,sat} \approx 9\ \mu\mathrm{W}$, the power of the probe-tone used for spectroscopy is $P_\mathrm{probe} \approx 2$ nW. Both values are given at the input of the fridge at 300K. Both the pump and the probe tones travel down the sample through the same

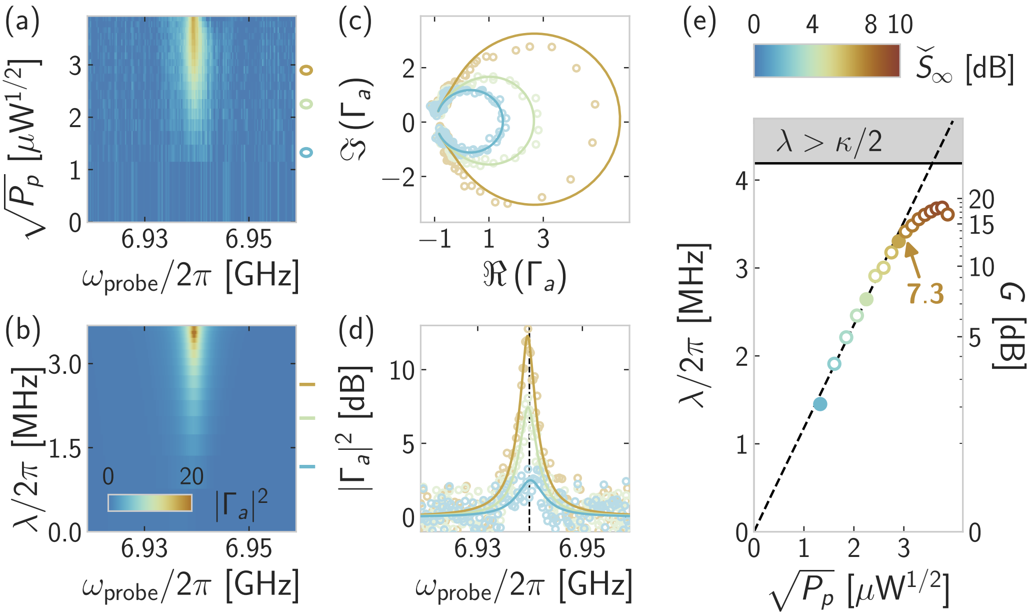

Figure 2.13 Microwave response of the DPO under resonant squeezing. (a) Reflection gain (color) versus probe frequency (x-axis) and the square root of the pump power at 300 K (y-axis). (b) Fitted reflection gain with λ as the only free parameter. Colorbar common with (a). (c) Line-cuts of the measured (open cicles) and fitted (solid lines) complex signal for increasing steady-state anti-squeezing (color). (d) Same as (c), in power units. The dashed line marks half the pump frequency. Colored dots and segments in (a,b) indicate the location of the line-cuts. (e) Two-photon pump amplitude resulting from fits of Eq. 2.29a (y-axis, left), and maximum power reflection gain (y-axis, right) versus the square root of the microwave pump power at 300 K (x-axis). The steady-state squeezing (color) is deduced from Eq. 2.13. Colorbar common with (a,b,c,d). The dashed line is a linear extrapolation of the fit before saturation. The full dots mark the powers used in (c,d). The colored arrow indicates the maximum steady-state anti-squeezing in decibels before saturation. The shaded area marks the instability region where $\lambda > \kappa/2$.

microwave lines. Calibration of the lines at cryogenic temperatures lets us estimate the insertion losses[10] at both the frequencies of the oscillator $\mathrm{IL_a}$, and the pump $\mathrm{IL_p}$. This quantity is defined such that the pump power reaching the sample at saturation is $P_{\mathrm{p,sat}}^{\mathrm{10mK}} = \mathrm{IL_p^{-1}} P_{\mathrm{p,sat}}$, and similarly for the probe $P_{\mathrm{probe}}^{\mathrm{10mK}} = \mathrm{IL_a^{-1}} P_{\mathrm{probe}}$. The power output by the amplifier at the onset of saturation reads $P_{\mathrm{out}}^{\mathrm{10mK}} = G_{\mathrm{sat}} P_{\mathrm{probe}}^{\mathrm{10mK}}$. In practice, we find $\mathrm{IL_p} = 4 \times \mathrm{IL_a}$ (6 dB more losses at the pump frequency), and $G_{\mathrm{sat}} = 25$ (in linear units), so that $P_{\mathrm{out}}^{\mathrm{10mK}} \approx P_{\mathrm{p,sat}}^{\mathrm{10mK}}/45$. This difference of 16 dB between the output signal power and the input pump power, already at the onset of saturation, is not sufficient to consider the pump stiff. A separation of 20 dB is typically required to ensure that the pump is not significantly depleted by the output signal.

We continue with an estimation of the residual Kerr at the saturation point. Further calibrations presented in section 3.2.3 reveal that the probe tone injects $\bar{n}_{\mathrm{d}} = 0.25$ photons in the DPO. These injected photons are amplified into $G_{\mathrm{sat}} \times \bar{n}_{\mathrm{d}} \approx 6$ circulating photons. At the same time, the amplification bandwidth at the saturation point is $\Delta_{\mathrm{3dB,sat}} \approx 1.7$ MHz. Thus, it would take a residual Kerr of at least ± 200 kHz to significantly shift the resonance. Yet the calibration of the Kerr-free flux points sets $|\chi_{\mathrm{aa}}| < 100$ kHz. As a conclusion, pump depletion is the most likely dominant source of saturation in our device.

2.2.4 Detuned squeezing

Second we enter the BO regime by detuning the pump away from the parametric resonance $\omega_{\mathrm{p}} = 2\omega_{\mathrm{a}} - 2\delta_{\mathrm{a}}$, where the detuning verifies $|\delta_{\mathrm{a}}| \gg \kappa/2$. In the following we present results for $|\delta_{\mathrm{a}}|/2\pi = 30$ MHz (Fig. 2.14), but the data for $|\delta_{\mathrm{a}}|/2\pi \in \{20, 40\}$ MHz display similar features. When $\delta_{\mathrm{a}} > 0$, as we increase the pump power the oscillator resonance shifts down from ω_{a} to $\omega_{\mathrm{p}}/2$, following the theoretical prediction $\omega_{\mathrm{p}}/2 + \Omega_{\mathrm{a}}[r]$ (section 2.1.2). Moreover, this resonator of squeezed photons responds to regular plane waves at a mirror frequency $\omega_{\mathrm{p}}/2 - \Omega_{\mathrm{a}}[r]$. This idler peak merges into the signal peak in the coalescent regime. Both signal and idler peaks display gain, in equal amount. Symmetrically, for $\delta_{\mathrm{a}} < 0$, the oscillator resonance shifts up from ω_{a} to $\omega_{\mathrm{p}}/2$. This symmetric behavior differs from the response of a Kerr oscillator to a detuned pump, where the sign of the Kerr sets the

---

[10] As defined by Pozar [Pozar 2011], the insertion loss IL is the transmission coefficient between two points of a circuit. As a rule of thumb, the insertion loss of the stainless-steel coaxial cables used as descent lines increases by 10 dB every 10 GHz.

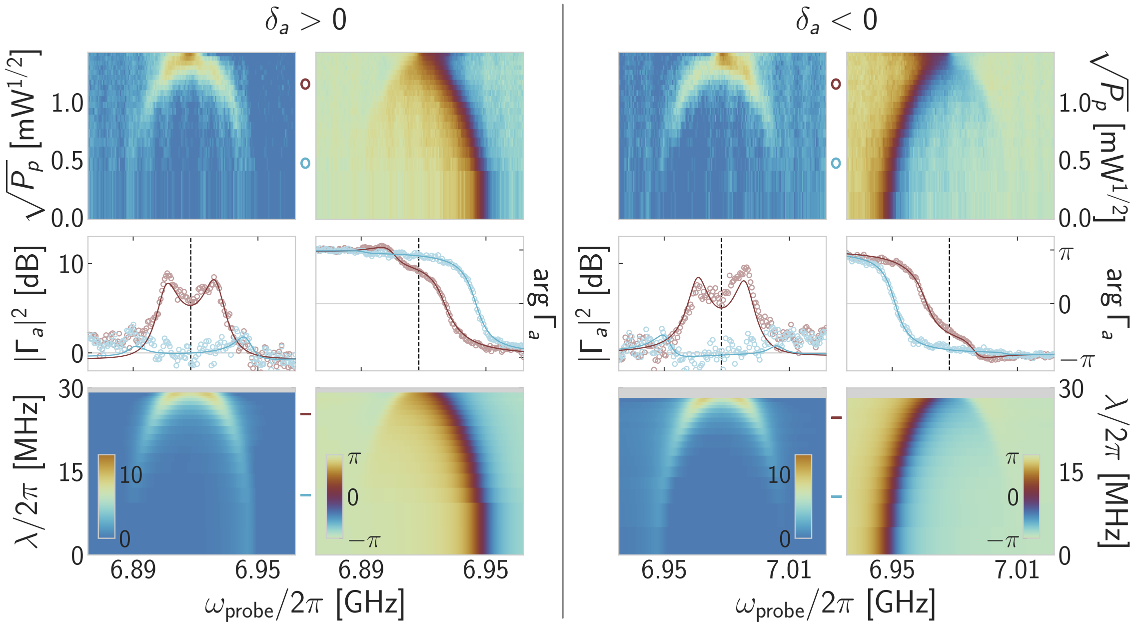

Figure 2.14 Microwave response of the Bogoliubov oscillator. ($\delta_\mathrm{a} > 0$) The pump detuning is set to $\delta_\mathrm{a}/2\pi = +30$ MHz. Top: Reflection gain [left] and phase [right] (color) versus probe frequency (x-axis) and the square root of the pump power at 300 K (y-axis). The colorbars (in decibels and radians) are indicated in the bottom panels. Bottom: fitted reflection gain [left] and phase [right] from input-output theory applied to Eq. 2.29a, with λ as the only free parameter. Middle: line-cuts of the measured (open circles) and fitted (solid lines) gain [left] and phase [right] (y-axis) versus probe frequency (x-axis). Colored dots and segments in the top and bottom panels indicate the location of the line-cuts. The vertical dashed line marks half the pump frequency. ($\delta_\mathrm{a} < 0$) Same with a pump detuning set to $\delta_\mathrm{a}/2\pi = -30$ MHz. The data for $\delta_\mathrm{a}/2\pi = \pm 20, \pm 40$ MHz (not represented) display the same features.

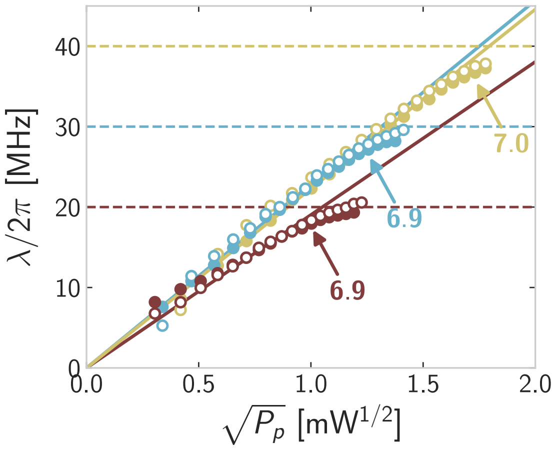

Figure 2.15 Calibration of the two-photon pump in the BO regime. Two-photon pump amplitude (y-axis) as fitted from the complex response (Eq. 2.29a) versus the square root of the microwave pump power at 300 K (x-axis) applied through the high-power port, for $|\delta_\mathrm{a}|/2\pi \in \{20, 30, 40\}$ MHz (color) and $\delta_\mathrm{a} > 0$ (empty circles) or $\delta_\mathrm{a} < 0$ (full circles). Colored solid lines are linear extrapolations of the fit trends before saturation. Colored arrows indicate the maximum squeezing in decibels before saturation. Colored dashed lines mark the onset of the unstable region $\lambda = |\delta_\mathrm{a}|$.

direction of the shift, independently of the pump frequency. The results of Fig. 2.14 demonstrate that λ – the only fit parameter relating data and theory – is reliably identified at every pump power, thereby fully characterizing the BO.

Similarly to the resonant squeezing case, we observe a saturation of the fitted two-photon pump amplitude (Fig. 2.15). The onset of saturation is again defined based on the deviation of the fitted parameter λ from a quadratic trend with respect to the pump power. Interestingly, saturation occurs regardless of the ratio δ_a/κ at a similar squeezing value of 7 dB. This invariance can be traced down to the fact that in the BO regime, the gain of the DPO is a function of the eigenstate squeezing only (section 2.1.3).

Finally, we devote some time to the calibration of the operating point of the DPO in the BO regime. There, the notion of residual Kerr effect unfolds differently. For strongly detuned squeezing, the two-photon pump not only triggers gain in the system, but also shifts its resonant frequency. Even though a precise flux point has been calibrated as free of Kerr in an experiment akin to Fig. 2.12, the Kerr effect is dressed when the detuned squeezing is activated. In Fig. 2.16 we detail the procedure of adjusting the flux in order to reduce this dynamical Kerr effect. We display the phase response of the oscillator in the presence of an increasing pump power at $\omega_\mathrm{p} = 2\omega_\mathrm{a}^0 - 2\delta_\mathrm{a}$ for $|\delta_\mathrm{a}|/2\pi = 30$ MHz. Whether δ_a is negative or positive, the critical value λ_crit is not reached for the same critical power $P_\mathrm{p,crit}$. Indeed, when $\delta_\mathrm{a} > 0$, a positive dynamical Kerr accelerates the collapse of the oscillator signal and idler peaks. Conversely when $\delta_\mathrm{a} < 0$, it slows down this process. The critical values λ_crit for each sign of the detuning only match when this spurious dynamical Kerr effect becomes negligible. When $|\delta_\mathrm{a}|/2\pi = 30$ MHz and the oscillator initially sits at the Kerr-free flux point, the dynamical Kerr $\chi_\mathrm{aa}^\mathrm{dyn}$ is found to be positive (Fig. 2.16 top panels). Tweaking the flux bias towards higher frequencies, the two pictures can be symmetrized (middle panels), or bent in the other direction (bottom panels). All the data presented in this paper always uses the dynamical Kerr-free point associated with each value of $|\delta_\mathrm{a}|$, as recorded on Table 2.2.

$\delta_\mathrm{a}/2\pi$ [MHz]	**0**	**±20**	**±30**	**±40**
$\omega_\mathrm{a}^*/2\pi$ [GHz]	6.940	6.951	6.948	6.938

Table 2.2 Dynamical Kerr-free points ω_a^* for all the pump detunings used in this report. As an order of magnitude, given the flux tunability of the device, a frequency shift of 10 MHz corresponds to 6 mΦ_0.

As a conclusion, we demonstrated that a SNAIL-resonator could be operated as a BO, with squeezings as high as 7 dB in the linear regime. In this implementation, the constituve ratio $2|\delta_\mathrm{a}|/\kappa$ was limited to 10. Indeed, for higher values of the detuning, no flux point could provide a fair calibration of the dynamical Kerr-free point. In that sense, residual Kerr is most likely the dominant source of saturation for the BO mode of operation.

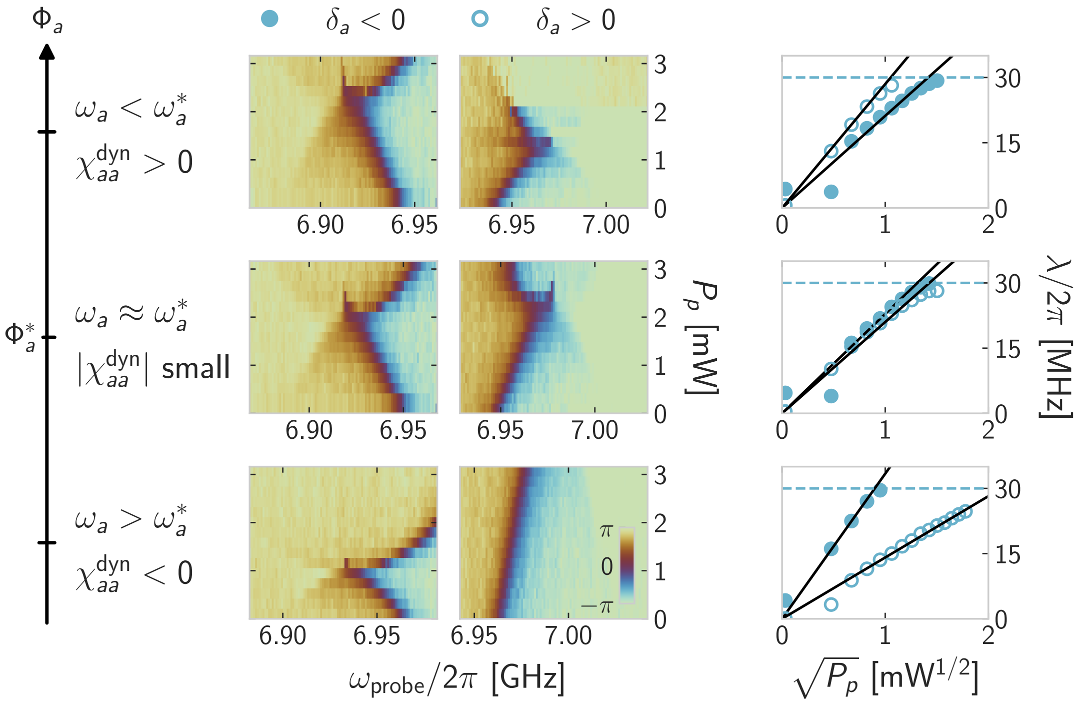

Figure 2.16 Calibration of the dynamical Kerr-free point $\Phi_{\rm a}^*$ when $|\delta_{\rm a}|/2\pi = 30$ MHz. From bottom to top the flux threading the SNAIL loop is increased, setting the bare oscillator frequency to 6.963 GHz (bottom), 6.949 GHz (middle) and 6.941 GHz (top). Left column: reflection phase response (color) versus input signal frequency (x-axis) and applied pump power at 300 K (y-axis) when the detuning between the bare cavity and half the pump frequency is $\delta_{\rm a}/2\pi = -30$ MHz. Center column: same as left for $\delta_{\rm a}/2\pi = +30$ MHz. The colorbar (in radians) is indicated in the bottom panel. Right column: Two-photon pump amplitude (y-axis) fitted at each pump power (x-axis) when the detuning is negative (full dots) or positive (open dots). The right and center plots of the middle panels are nearly symmetric, as demonstrated by the matching of the two types of fit on the right plot: this defines the dynamical Kerr-free point.

2.2.5 Beating the gain-bandwidth constraint

In the resonant regime $\delta_\mathrm{a} = 0$, the 3 dB amplification bandwidth Δ_3dB reduces with gain G according to the gain-bandwidth product constraint $\Delta_\mathrm{3dB}\sqrt{G} = \kappa$ (solid line on Fig. 2.17 right). In contrast, in the detuned regime, following either the signal or idler peak we observe a constant amplification bandwidth, independently of the gain (dashed line). This amplifier, praised for evading the fundamental gain-bandwidth constraint, has been coined the Bogoliubov amplifier [Metelmann 2022].

As the BO enters coalescence, the two peaks merge and the amplification bandwidth more than doubles. This increase is larger than the theoretical value $\sqrt{2}$ (section 2.1.4). This difference must not be interpreted as an inconsistency of the theory, but rather an experimental challenge of precisely identifying the onset of coalescence. Indeed in our implementation, coalescence belongs entirely to the saturation regime (Fig. 2.15), where the BO response is not canonical. Allowing for some ripples at the top of the gain profile lead us to call for coalescence prematurely, thus overestimating the amplification bandwidth. Future realizations of Bogoliubov amplifiers could benefit from the diluted nonlinearity of SNAIL chains to minimize spurious Kerr, and hopefully increase their dynamical range.

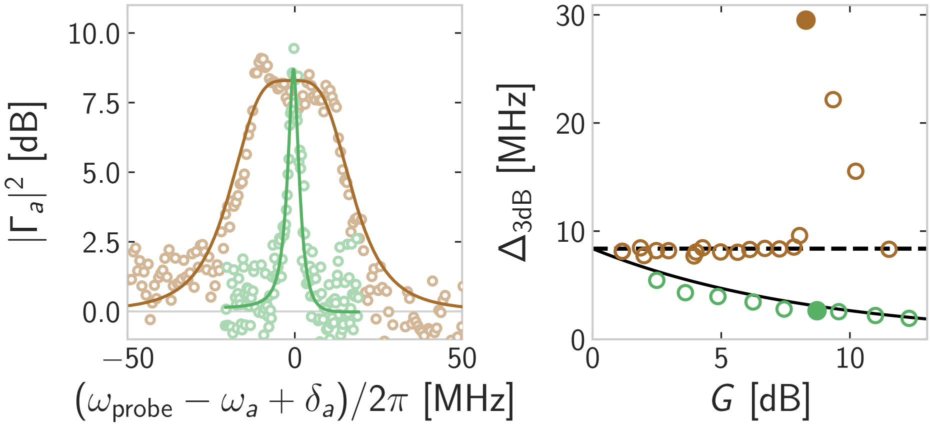

Figure 2.17 The Bogoliubov amplifier. Left: reflection gain (y-axis) versus input signal frequency (x-axis). For a similar maximum gain of about 9 dB, the amplification bandwidth for $\delta_\mathrm{a}/2\pi = +30$ MHz (brown) is much larger than for $\delta_\mathrm{a} = 0$ (green). Right: 3 dB amplification bandwidth (y-axis) versus maximum gain(x-axis).

3

INTERACTION OF A DEGENERATE PARAMETRIC OSCILLATOR WITH A QUBIT

In the previous chapter, the stability diagram of a DPO was described. It unveiled two stable regions, resulting from the interplay between pump detuning and dissipation. Whether the induced squeezing is resonant or detuned, the intra-oscillator field always converges to a squeezed steady-state. However, only in the BO regime are the oscillator eigenstates identified with squeezed Fock states. We now turn to the coupling of a DPO to a qubit. This chapter aims at demonstrating that the peculiar eigenstructure of the BO is the root cause for enhanced interactions. After a set of preliminary remarks, the dispersive interaction of a DPO to a qubit will be characterized, from the linear regime (pump off) to the nonlinear regimes of resonant and detuned squeezing.

3.1 Preliminary remarks

3.1.1 The proposals and beyond

The proposals [Leroux 2018; Qin 2018] consider the coupling of a qubit to a DPO, operated in the BO regime. As presented in section 2.1, the DPO models a certain class of nonlinear oscillators under driven evolution. In the original frame, the interaction between the qubit dipole moment and the oscillator field translates into a Rabi coupling (Eq. 1.1). Meanwhile, in the frame rotating a half the pump frequency necessary to capture the DPO model out of the driven oscillator, the interaction takes the form of a Jaynes-Cummings coupling $g\big(\mathbf{a}\boldsymbol{\sigma}_{+} + \mathbf{a}^{\dagger}\boldsymbol{\sigma}_{-}\big)$ (Appendix B.1.3) [Jaynes and Cummings 1963]. Overall, the DPO-qubit Hamiltonian reads:

$$\boldsymbol{\mathcal{H}}_{\delta_{\mathrm{a}},\lambda}/\hbar = \delta_{\mathrm{a}}\mathbf{a}^{\dagger}\mathbf{a} - \frac{\lambda}{2}\big(\mathbf{a}^{2} + \mathbf{a}^{\dagger 2}\big) + \delta_{q}\frac{\boldsymbol{\sigma}_{\mathbf{z}}}{2} + g\left(\mathbf{a}\boldsymbol{\sigma}_{+} + \mathbf{a}^{\dagger}\boldsymbol{\sigma}_{-}\right) \ , \qquad (3.1)$$

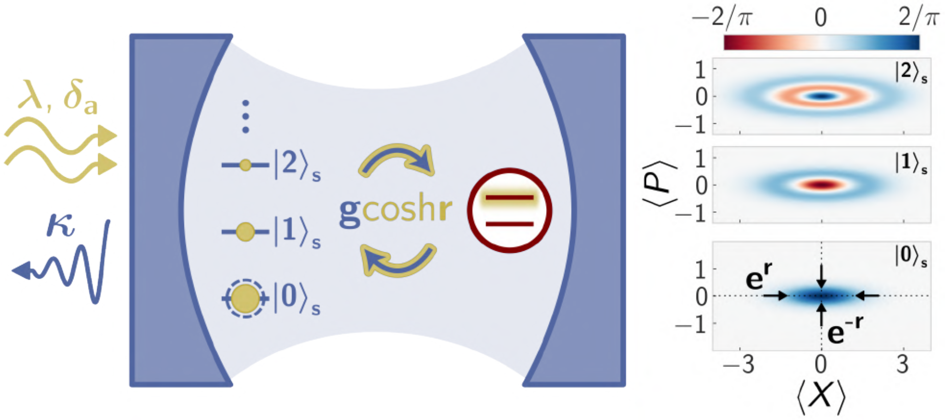

Figure 3.1 Coupling a Bogoliubov oscillator to a qubit. Building on Fig. 2.3, a qubit (red levels) is introduced, coupled at a rate g (blue arrows) to the bare oscillator. In the BO regime, not only the coupling is enhanced by $\cosh r$ (golden arrows), but the qubit is also dephased (gold fuzz) by the finite BO population.

where $\delta_q = \omega_q - \omega_\mathrm{p}/2$ is the qubit detuning. The Lindblad operators associated to the qubit relaxation and dephasing are $\boldsymbol{L}_- = \sqrt{\gamma_1}\boldsymbol{\sigma}_-$ and $\boldsymbol{L}_\phi = \sqrt{\gamma_\phi/2}\boldsymbol{\sigma}_\mathbf{z}$. The interaction of a TLS with a DPO has already been implemented experimentally in the resonant case $\delta_\mathrm{a} = 0$, either in the dispersive limit [Eddins 2019], or on resonance [**Vine2022**]. There, the steady-state squeezing of the DPO was leveraged to increase the SNR of the TLS readout implemented by the oscillator.

Instead, we focus on the strongly-detuned regime $|\delta_\mathrm{a}| \gg \kappa/2$. There, the system is suitably described in the Bogoliubov basis:

$$\begin{aligned}\boldsymbol{\mathcal{H}}_{\delta_\mathrm{a},\lambda}/\hbar = \Omega_\mathrm{a}[r]\boldsymbol{\alpha}^\dagger\boldsymbol{\alpha} + \delta_q\frac{\boldsymbol{\sigma}_\mathbf{z}}{2} &+ g\cosh r\left(\boldsymbol{\alpha}\boldsymbol{\sigma}_+ + \boldsymbol{\alpha}^\dagger\boldsymbol{\sigma}_-\right)\\ &+ g\sinh r\left(\boldsymbol{\alpha}\boldsymbol{\sigma}_- + \boldsymbol{\alpha}^\dagger\boldsymbol{\sigma}_+\right)\ .\end{aligned} \tag{3.2}$$

The enhanced interaction strength is immediately visible in Eq. 3.2 where g is multiplied by $\cosh r$ [resp: $\sinh r$] for the excitation-number conserving [resp: non-conserving] terms. This observation is at the heart of proposals [Leroux 2018; Qin 2018], which offer to use the enhanced fluctuations of the BO to boost its coupling to a qubit. In addition, provided $|\delta_q + \Omega_\mathrm{a}[r]| \gg g\sinh r$, averaging theorems apply and the interaction reduces to an enhanced Jaynes-Cummings coupling (Appendix B.1.3):

$$\boldsymbol{\mathcal{H}}_{\delta_\mathrm{a},\lambda}/\hbar \approx \Omega_\mathrm{a}[r]\boldsymbol{\alpha}^\dagger\boldsymbol{\alpha} + \delta_q\frac{\boldsymbol{\sigma}_\mathbf{z}}{2} + g\cosh r\left(\boldsymbol{\alpha}\boldsymbol{\sigma}_+ + \boldsymbol{\alpha}^\dagger\boldsymbol{\sigma}_-\right)\ . \tag{3.3}$$

This excitation-number conserving interaction has the advantage of unveiling strong resonant-coupling through a clear and simple signature, namely, vacuum-Rabi splitting [A. Wallraff 2004]. In this limit, the effect of squeezing could be unambiguously revealed through an increased splitting. Naturally, the curiosity of a physicist does not stop where excitation-number non-conserving terms start to matter [Frisk Kockum 2019]. However, coupled systems in the ultra-strong coupling regime being notoriously difficult to analyse, the Jaynes-Cummings regime is the perfect test bench for the demonstration of squeezing-enhanced couplings.

Still, this simple picture is blurred by the squeezed bath that populates higher BO energy levels, and precludes the observation of a simple *vacuum*-Rabi splitting. Indeed, owing to the nonlinearity of the Jaynes-Cummings ladder, the resonant interaction of a qubit with an oscillator held away from vacuum leads to exotic spectroscopic signatures [Fink 2008; Bishop 2009; Fink 2010; Bonsen 2022]. Moreover, as highlighted by Shani and co-authros [Shani 2022] this finite population is expected to broaden the qubit spectral line. For a weakly coupled system, the latter effect may hinder the observation of an increased splitting. The proposals [Leroux 2018; Qin 2018] circumvent this problem by injecting orthogonally squeezed vacuum, so that the bath viewed by the BO remains in vacuum. While possible in principle, injecting squeezed vacuum in cQED is easily contaminated by damping in transmission lines and cavity internal losses, thereby remaining a technical challenge [Murch 2013a; Bienfait 2017; Eddins 2018].

In addition, in an effort to witness a simple signature of these enhanced interactions, a fundamental complexity arises due to the presence of the excitation non-conserving terms in Eq. 3.2. In the resonant case $\delta_q = \Omega_{\mathrm{a}}[r]$, averaging of this term requires that the bare coupling g remains smaller than $g_{\cancel{\mathrm{RWA}}}$ such that:

$$2|\Omega_{\mathrm{a}}[r]| \gg g \sinh r \quad \Leftrightarrow \quad g \ll g_{\cancel{\mathrm{RWA}}} \equiv \frac{2\delta_{\mathrm{a}}}{\cosh 2r \sinh r} \, . \tag{3.4}$$

While [Leroux 2018] proposes to use a gigantic detuning to accomodate large squeezing amplitudes, specifically $\delta_{\mathrm{a}} = 2000\kappa$ in their superconducting circuit implementation, this solution does not come free of charge. Indeed, as compared to a resonant-DPO, approaching criticality in such a detuned-DPO would require a two-photon pump amplitude 4000 times more intense. In practice, this would mean a microwave pump carrying 72dB more power. Not only the cryostat may dangerously heat up before reaching the desired pumping amplitude, but spurious nonlinearites such as residual Kerr are very likely to become significant on the way. As a practical tool, we plot on Fig. 3.2 the maximum bare coupling before the averaging approximation breaks down $g_{\mathrm{RWA}} = g_{\cancel{\mathrm{RWA}}}/10$, as a function of DPO detuning and squeezing. The BO implementation detailed in the previous section demonstrated squeezings as high as 7 dB for $2\delta_{\mathrm{a}}/\kappa$ as high as 10 (Fig. 2.15). For such values, we find that the maximum bare g the system can support to remain in the Jaynes-Cummings limit is around $\kappa/2$. There, we may expect an increase in g by a factor 1.34. This analysis lets us design the right bare qubit-oscillator coupling, in order to get a chance to witness an increased Rabi-splitting with realistic exprimental parameters. Finally, it is also worth pointing out the overall modest increase factor that one can expect from this scheme (see top axis of Fig. 3.2).

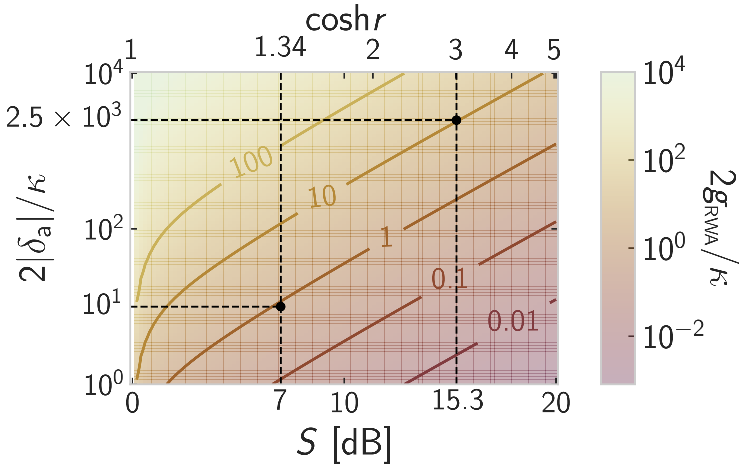

Figure 3.2 Critical bare coupling for enhanced vacuum-Rabi splittin (color) versus DPO detuning (y-axis) and squeezing (x-axis, bottom). Both frequencies are scaled in unit of $\kappa/2$. The squeezing is converted into a coupling enhancement factor (x-axis, top). One can read this figure as follows: given a system with $2g/\kappa = 10$, increasing g by a factor 3 requires 15.3 dB of squeezing, which falls under inequality 3.4 only if $2|\delta_{\mathrm{a}}|/\kappa > 2.5.10^3$. Alternatively, for a system with $2|\delta_{\mathrm{a}}|/\kappa = 10$ and $2g/\kappa = 1$, inequality 3.4 requires $S \leqslant 7$ dB.

3.1.2 Transmon characterization

The experimental implementation of the proposals presented in this thesis uses a transmon as a qubit. We begin this part with a short description of this superconducting design, which does not aim exhaustivity, but rather the introduction of three key properties. Then, we present spectroscopic characterization of the transmon from which we extract its defining parameters.

Transmon 101 The transmon is a superconducting qubit design introduced as a variation of the Cooper-pair box (CPB) [Nakamura 1999]. They both consist in a Josephson junction with energy E_J, shunted by a capacitor with energy $E_C = e^2/2C$, thus delimiting an isolated superconducting island with offset charge Q_g. In this description, the shunt capacitance includes the self-capacitance of the junction. Both designs are desribed by the same Hamiltonian:

$$\boldsymbol{\mathcal{H}}_{\mathbf{CPB}} = \frac{\left(\boldsymbol{Q} - Q_g\right)^2}{2C} - E_J \cos 2\pi \frac{\boldsymbol{\Phi}}{\Phi_0} \, . \tag{3.5}$$

The CPB operates in a regime where the charging energy is the dominant scale $E_J < E_C$, so that the two levels of the qubit are approximately charge states, coupled by the tunneling of a Cooper-pair through the junction. The frequency of this qubit is very sensitive to charge fluctuations on the island – charge noise – drastically limiting its coherence. The transmon operates in the opposite regime $E_J \gg E_C$, for which the eigenstates display large charge fluctuations. Thus, the first key property of this design consists in its *insensitivity to charge noise* [Koch 2007].

In the transmon regime, the wide charge fluctuations are accompanied by reduced fluctuations in the conjugate quadrature, the flux. This observation motivates a Taylor expansion of the cosine term of Eq. 3.5, so that the transmon Hamiltonian reads to lowest order:

$$\boldsymbol{\mathcal{H}}_{\mathbf{t}} = 4E_C\boldsymbol{N}^2 + \frac{1}{2}E_J\boldsymbol{\varphi}^2 - \frac{1}{4!}E_J\boldsymbol{\varphi}^4 \tag{3.6}$$

where we introduced the Cooper-pair number operator $\boldsymbol{N} = \boldsymbol{Q}/2e$, and the reduced flux $\boldsymbol{\varphi} = 2\pi\boldsymbol{\Phi}/\Phi_0$, obeying $\left[\boldsymbol{\varphi}, \boldsymbol{N}\right] = i$. We also discarded the offset charge, to which the transmon is insensitive. Next we introduce the annihilation operator $\mathbf{b}$ that diagonalizes the quadratic part of Eq. 3.6:

$$\mathbf{b} = \frac{1}{2}\left(\frac{\boldsymbol{\varphi}}{\varphi_{\text{zpf}}} + i\frac{\boldsymbol{N}}{N_{\text{zpf}}}\right) \quad \varphi_{\text{zpf}} = \sqrt[4]{\frac{2E_C}{E_J}} \quad N_{\text{zpf}} = \frac{1}{2}\sqrt[4]{\frac{E_J}{2E_C}} \, , \tag{3.7}$$

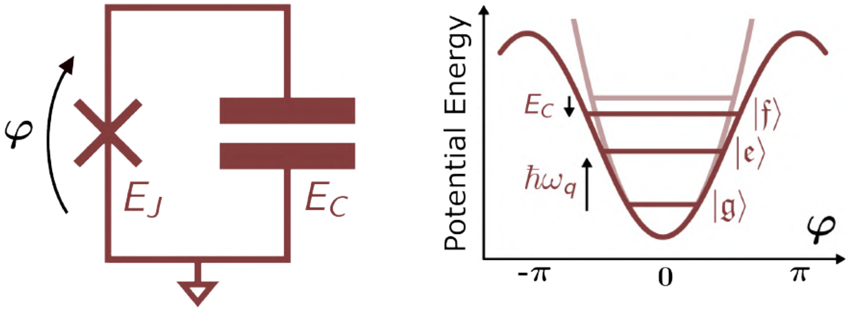

Figure 3.3 The transmon is a single-mode circuit featuring a Josephson junction shunted by a large capacitor, and described by the reduced flux variable φ. Its potential energy is cosinusoidal (dark red), yet weakly deviating from a parabola (light red) in the limit $E_J \gg E_C$. Figure freely inspired from [Blais 2021].

and obeys the commutation relation $\left[\mathbf{b}, \mathbf{b}^\dagger\right] = \mathbb{1}$. Using this bosonic representation, the transmon Hamiltonian reads:

$$\mathcal{H}_\mathbf{t} = \sqrt{8E_JE_C}\mathbf{b}^\dagger\mathbf{b} - \frac{E_C}{12}\left(\mathbf{b} + \mathbf{b}^\dagger\right)^4 \approx \hbar\omega_q + \frac{\hbar\chi_q}{2}\mathbf{b}^{\dagger 2}\mathbf{b}^2 \,, \qquad (3.8)$$

where $\omega_q = \frac{1}{\hbar}\left(\sqrt{8E_JE_C} - E_C\right)$ is the qubit transition frequency, and $\chi_q \approx -E_C/\hbar$ is the anharmonicity. Since $|\chi_q| \ll \omega_q$ in the transmon limit, we discarded excitation-number non-conserving terms in a final approximation akin to a RWA [Blais 2021]. The transmon appears to be a *weakly anharmonic oscillator*, which is the second key property of this design. In the limit where the linewdith of the first transition is much less than the anharmonicity, the two lowest-energy states can be adressed independently, and the transmon can effectively be considered as a qubit. The bosonic representation 3.8 will prove useful for input-output calculations. In this representation, Lindblad operators read: $\boldsymbol{L}_- = \sqrt{\gamma_1}\mathbf{b}$ and $\boldsymbol{L}_\phi = \sqrt{2\gamma_\phi}\mathbf{b}^\dagger\mathbf{b}$.

Finally, the large shunting capacitance gives a large electric dipole moment to the transmon, facilitating its coupling to the electric field stored in an oscillator. Yet, it appears that selection rules in the $E_J \gg E_C$ limit forbid charge transitions between non-neighboring eigenstates. Thus as a first approximation, a single transmon state outside the qubit manifold is necessary to capture its dynamics when charge-coupled to an oscillator. This third key property leads to the description of the transmon as *a three-level* *system* with Hamiltonian:

$$\boldsymbol{\mathcal{H}}_{\mathfrak{t}}/\hbar = \sum_{k \in \{\mathfrak{g},\mathfrak{e},\mathfrak{f}\}} \omega_k \, |k\rangle\langle k| \ , \tag{3.9}$$

where $|\mathfrak{g}\rangle$, $|\mathfrak{e}\rangle$, $|\mathfrak{f}\rangle$ denote its three lowest-energy states. The $|\mathfrak{g}\rangle$ and $|\mathfrak{e}\rangle$ states define the qubit states, with transition frequency $\omega_{\mathfrak{ge}} = \omega_{\mathfrak{e}} - \omega_{\mathfrak{g}} = \omega_q$. Single-photon excitations to the $|\mathfrak{f}\rangle$ state are detuned from the qubit transition by the anharmonicity such that: $\omega_{\mathfrak{ef}} = \omega_q + \chi_q$.

Single-tone spectroscopy In the present experiment, the transmon Josephson element is a SQUID (Fig. 2.11). Controlling the flux Φ_q threading the SQUID loop lets us tune its equivalent Josephson energy, hence the transmon resonant frequency [Koch 2007]. Moreover, the transmon is strongly coupled to a microwave feedline, such that photon leakage through this port dominates over every other relaxation channel. This feature was chosen to mimick the small coherence times of typical mesoscopic qubits [Cottet 2017], and also to let us record the reflection spectrum of the transmon directly, without relying on an extra readout mode. On the top panel of Fig. 3.4 is plotted the transmon spectroscopy versus flux, displaying a tunability range greater than 2.5 GHz. This uncommonly wide range is the result of fabrication constraints on the SQUID loop, whose junctions could not be made sufficiently asymmetric to limit flux dispersion (section 4.3).

Next we turn to the description of the direct readout scheme. We record the reflection spectrum of a weak signal on the transmon port. This microwave probe with frequency ω_{probe} and amplitude $\varepsilon_{\text{probe}}$ is accounted for at the Hamiltonian level through: $\boldsymbol{\mathcal{H}}_{\boldsymbol{d}}(\boldsymbol{t}) = -i\varepsilon_{\text{probe}} \cos \omega_{\text{probe}} t \big(\mathbf{b} - \mathbf{b}^\dagger\big)$ (section B.1.1). If the probe is such that the transmon population remains much less than 1 photon, we can leave aside the quartic term of Eq. 3.8. Then, the driven transmon Hamiltonian simply reads $\boldsymbol{\mathcal{H}}_{\mathbf{t+d}}(\boldsymbol{t}) = \hbar\omega_q \mathbf{b}^\dagger \mathbf{b} + \boldsymbol{\mathcal{H}}_{\boldsymbol{d}}(\boldsymbol{t})$. In a frame rotating at the probe frequency and under the RWA (section B.1.3), it is approximated by:

$$\overline{\boldsymbol{\mathcal{H}}^{\omega}_{\mathbf{t+d}}}/\hbar = \big(\omega_q - \omega_{\text{probe}}\big)\mathbf{b}^\dagger \mathbf{b} + i\frac{\varepsilon_{\text{probe}}}{2} - i\frac{\varepsilon^*_{\text{probe}}}{2} \ . \tag{3.10}$$

Using Eq. 2.7, we can write the mean-value of **b** in the steady state:

$$\langle \mathbf{b} \rangle_\infty = \frac{-\varepsilon^*_{\text{probe}}/2}{\gamma_1/2 + \gamma_\phi - i(\omega_{\text{probe}} - \omega_q)} \ . \tag{3.11}$$

Since the port used for readout dominates over every other relaxation channels, the input-output relation reads: $\mathbf{b}_{\mathbf{out}}[\boldsymbol{\omega}] + \mathbf{b}_{\mathbf{in}}[\boldsymbol{\omega}] = \sqrt{\gamma_1}\mathbf{b}[\boldsymbol{\omega}]$, where

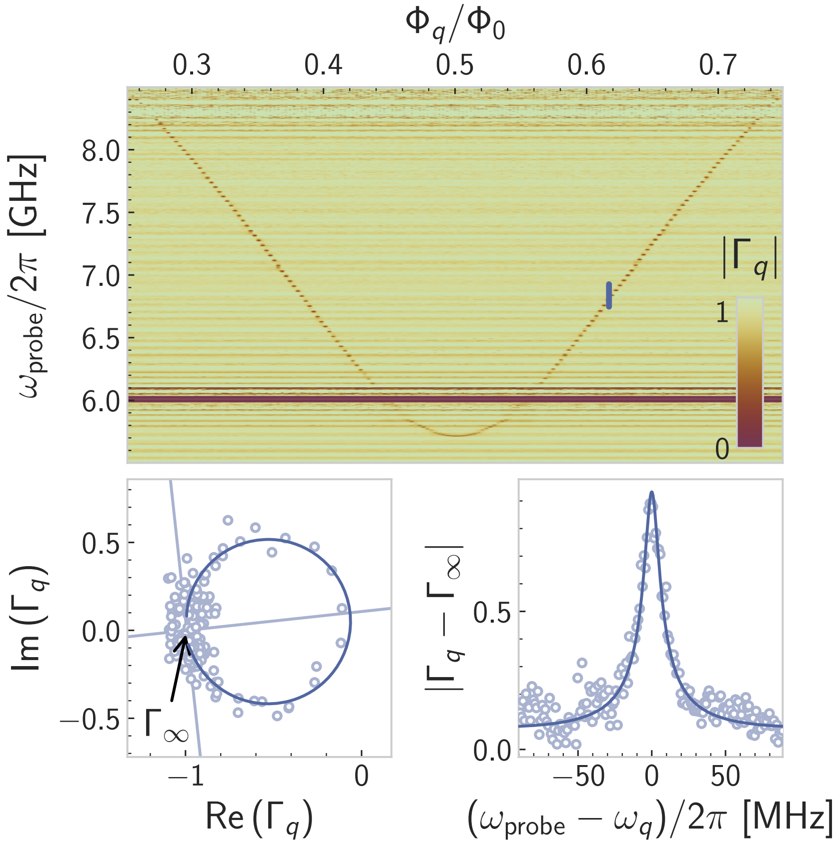

Figure 3.4 Transmon spectroscopy versus flux. Top: Amplitude $|\Gamma_q|$ of a weak reflected signal on the transmon port (color) versus the frequency of the probe tone (y-axis) and the flux threading the SQUID loop (x-axis) in unit of the flux quantum $\Phi_0 = h/2e$. The detection bandwidth is interrupted by the TWPA dispersive feature around 6 GHz, and cropped by the amplifier roll-off above 8.2 GHz. Bottom: Cut of the previous map along the blue line, where $\omega_q/2\pi = 6.837$ GHz. Left: Complex amplitude of the reflected signal. The data is normalized to a reference background so that the accumulation point Γ_∞ is located at coordinates (-1,0). Right: Amplitude of the reflected signal referenced to the accumulation point. Fitted response (line) is overlaid to the data (circles). Light blue lines on the left plot show the symmetric axis of the circular trajectory, and its perpendicular at the accumulation point, obviously tilted in the complex frame.

the input and output fields are defined similarly as Eqs. 2.23. The microwave probe acts as a displacement of the input field at the probe frequency: $\langle \mathbf{b_{in}} \rangle_\infty = -\varepsilon^*_{\text{probe}}/2\sqrt{\gamma_1}$. Thus, the output field at the probe frequency reads $\langle \mathbf{b_{out}} \rangle_\infty = \Gamma_q[\omega_{\text{probe}}] \langle \mathbf{b_{in}} \rangle_\infty$ where:

$$\Gamma_q[\omega_{\text{probe}}] = -1 + \frac{\gamma_1}{\gamma_t/2 - i(\omega_{\text{probe}} - \omega_q)} , \tag{3.12}$$

and $\gamma_t = \gamma_1 + 2\gamma_\phi$ is the total linewidth of the transmon spectral line. The latter equation describes a circular trajectory in the complex plane, symmetric about the real axis, with an accumulation point[1] $\Gamma_\infty = -1$. In principle, the reflection spectroscopy of such a system can distinguish the coupling rate to its feedline (here, γ_1) from the other contributions to the total linewidth (here, $2\gamma_\phi$). Using Eq. (3.12) to fit the data presented in Fig. 3.4 (bottom panels, fit not shown) would yield $\gamma_1/2\pi = 5.0$ MHz and $\gamma_\phi/2\pi = 2.2$ MHz, thus placing the system near critical coupling $\gamma_1 = \gamma_t/2$. However, in this very regime, fitting both rates is prone to errors due to imperfections of the experimental setup [Rieger 2022]. These imperfections can lead to deviations from the canonical spectroscopic response, such as tilted circles in the complex plane. It turns out that such tilts are present in the data. As a consequence, we renounce on fitting γ_1 and γ_ϕ separately. Rather, we employ a fit function representing circles with any orientation in the complex plane, thus sensitive to γ_t only (see Fig. 3.4 bottom panels, blue lines). This procedure lets us fit the total linewidth of the transmon line reliably and accurately.

Two-tone spectroscopy So far, the anharmonicity of the transmon has been disregarded. Unlike the previous discussion, driving the transmon with higher powers unravels its multi-level structure. We reveal transmon states beyond the qubit manifold by performing a two-tone spectroscopy, saturating the $\mathfrak{g}$-$\mathfrak{e}$ transition with a resonant microwave drive, and then probing the transmon with a weak tone (see Fig. 3.5). Due to the finite occupation of the $|\mathfrak{e}\rangle$ state provided by the saturation drive, the $\mathfrak{e}$-$\mathfrak{f}$ transition can be revealed by the weak tone. Note that the spectroscopic tone is about 5000 times less powerful than the saturation one. We repeat the experiment at multiple flux

---

[1] In practice we record the transmon reflection spectrum in a similar way as the oscillator (section 2.2.3): we reconstruct $\Gamma_q[\omega]$ by acquiring two spectra. The first one probes the transmon under the specified experimental conditions. The second one probes the same frequency window after flux tuning the transmon out of it. It corresponds to a calibration of the transfer function of the detection setup. We divide the first trace by the second one to recover $\Gamma_q[\omega]$.

points, thus varying the qubit frequency. The fitted anharmonicty fluctuates around -100 MHz, the value predicted by electromagnetic simulations of the transmon design.

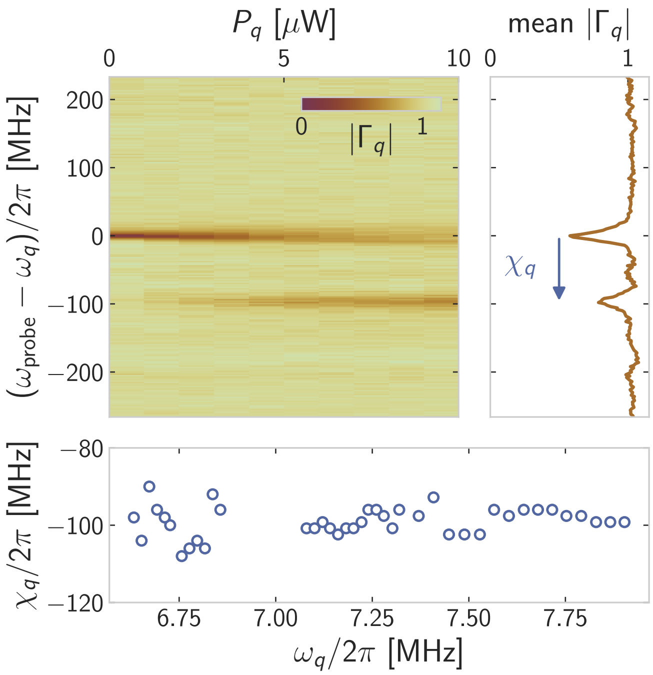

Figure 3.5 Transmon two-tone spectroscopy. Top: (Left) Amplitude Γ_q (color) of a weak reflected signal with frequency ω_{probe} on the transmon port , while the transmon is driven on resonance at ω_q with a microwave tone of power P_q at 300 K (x-axis). (Right) Average signal over all powers P_q. The distance between the $\mathfrak{g}$-$\mathfrak{e}$ transition peak at resonance and the emerging $\mathfrak{e}$-$\mathfrak{f}$ transition peak yields the anharmonicity χ_q. Bottom: Anharmonicity versus resonant frequency of the transmon, as extracted by repeating the experiment shown in the top panels at mutliple flux points Φ_q.

3.1.3 The resonant case

Making the most of the wide tunability range of the transmon, we characterize its interaction with the DPO in the resonant regime. First we will present the calibration of the coupling strength in the linear case, with no pump on the DPO. Second, we will look into the reponse of the coupled system in the BO regime with $\delta_\mathrm{a}/2\pi = -30$ MHz. There, the calibrated parameters are such that $2\delta_\mathrm{a}/\kappa = 7$ and $2g/\kappa = 1.4$. Then, for moderate squeezing amplitudes below 5 dB, the system is supposed to be in a safe regime regarding both the thermal bath approximation (Fig. 2.4) and the Jaynes-Cummings simplification (Fig. 3.2). Will it be sufficient to witness a clear signature of the expected coupling boost?

Linear regime Setting the oscillator to its Kerr-free flux point, we record its reflection spectrum as the transmon frequency is swept accross (Fig. 3.6). From input-output theory and following the same line of reasoning that lead to Eqs. 2.35 and 3.12, we expect the following response:

$$\Gamma_\mathrm{a}[\omega_\mathrm{probe}, \omega_q] = -1 + \frac{\kappa}{\dfrac{\kappa}{2} - i(\omega_\mathrm{probe} - \omega_\mathrm{a}) + \dfrac{g^2}{\frac{\gamma_t}{2} - i(\omega_\mathrm{probe} - \omega_q)}}\,. \quad (3.13)$$

Having previously calibrated the decay rates of the oscillator ($\kappa/2\pi = 8.7$ MHz) and the transmon ($\gamma_t/2\pi = 8.0$ MHz at the frequency of the oscillator Kerr-free point), the recorded map can be fitted using the coupling strength g as the only fitting parameter. When the transmon and the oscillator are on resonance, the oscillator spectrum displays a partially resolved splitting. Indeed, the coupling amplitude $g/2\pi = 6.1$ MHz is smaller than the decay rates of both modes, thus placing the system just below the resonant strong-coupling regime. Interestingly in this weak coupling regime, analysis of Eq. 3.13 reveals that two spectroscopic features translate the value of the coupling strength. First, the distance between the two peaks, which scales like $2g$. Second, the depth of the gap between the two peaks at resonance, which scales like $4g^2/\kappa\gamma_t$.

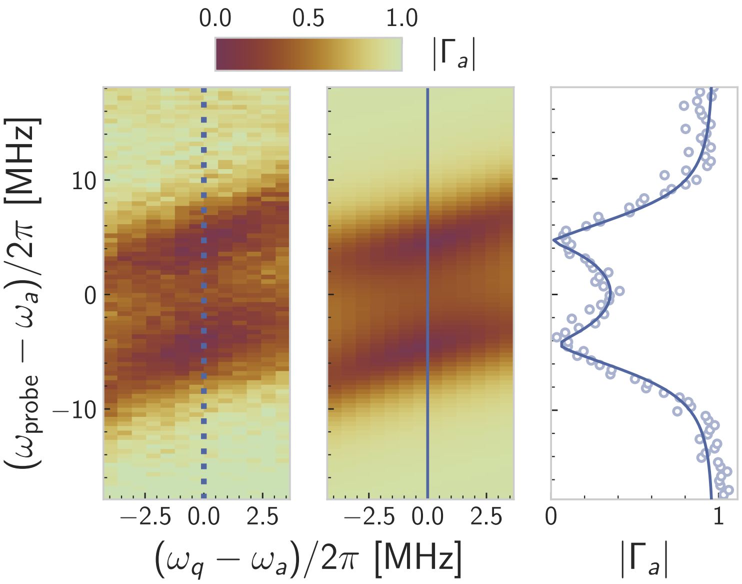

Figure 3.6 Transmon-oscillator resonant coupling in the linear regime. Left: Amplitude Γ_{a} (color) of a weak reflected signal with frequency ω_{probe} on the oscillator port (y-axis), versus the qubit frequency (x-axis), referenced to the oscillator frequency at the Kerr-free point. Center: amplitude of the fitted response with the coupling rate g as the only fitting parameter. Right: line-cut of the measured spectrum (open circles) and the fitted response (solid line) at resonance as indicated by the dotted (full) line in the left (middle) plot.

BO regime Next, we look into the resonant interaction of the transmon with a DPO in the BO regime. We set the pump detuning to $\delta_{\mathrm{a}}/2\pi = -30$ MHz, and adjust the DPO frequency so that it sits at its dynamical Kerr-free point (Fig. 2.16). For increasing two-photon pump amplitudes squeezing the BO up to $S = 3$ dB, we sweep the transmon frequency accross the BO signal line, and record the full 2d maps akin to Fig. 3.6. Then we fit all the maps with Eq. 3.13 using g as the only fitting parameter. The splitting curves at resonance and the extracted coupling are reported on Fig. 3.7. As the squeezing increases, the center of the anticrossing shifts up in frequency, following the BO signal line (section 2.2.4). In addition, the fitted value for g significantly drops, clearly contradicting the expected $\cosh r$ trend (dashed line).

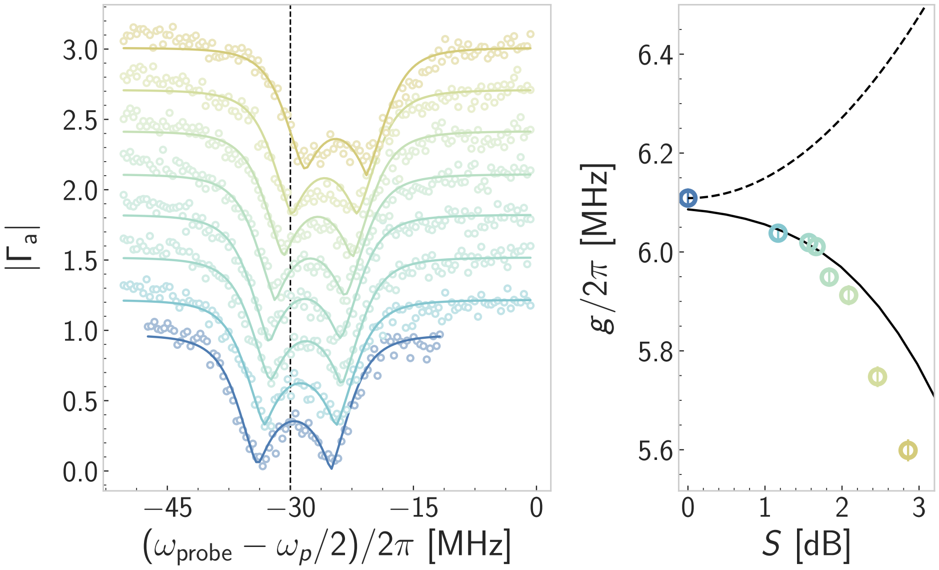

Figure 3.7 Transmon-BO resonant coupling, the experiment. The DPO detuning is set to $\delta_a/2\pi = -30$ MHz. Left: DPO amplitude reflection spectrum (y-axis) while at resonance with the transmon for increasing squeezing (color, scale on x-axis of right plot) (offset for clarity), versus detuning between the probe and half the pump frequency (x-axis). The data (open circles) is fitted (lines) using Eq. 3.13. The vertical dashed line marks the resonant frequency of the bare system (pump off). Right: resonant coupling strength (y-axis) vs DPO squeezing (x-axis) as fitted from experimental anticrossings (colored circles) or from simulated anticrossings (black circle-line, see details on Fig. 3.8). The expected boosted coupling $g \cosh r$ is also plotted (dashed line).

Simulations At the same time we can reproduce numerically the previous spectroscopic data. Using the Quantum Toolbox in Python `QuTiP` [Johansson 2012], we implement an experiment-driven algorithm in order to compute the emission spectrum of the oscillator. It follows the protocol of a time-resolved spectroscopy experiment. The oscillator, initially in vacuum, is first excited by a weak microwave drive, that will displace its state. Second, as the drive stops, the oscillator releases photons through its feedline. A spectroscopic experiment reveals the absorption properties of the oscillator by collecting these photons. Given a dynamical system with Lindbladian $\mathcal{L}$, we translate this protocol numerically into:

1. Solving for the steady-state density matrix $\boldsymbol{\rho}_\infty$ such that $\boldsymbol{\mathcal{L}}\boldsymbol{\rho}_\infty = 0$.
2. Solving for the time evolution of the system $\partial_t \boldsymbol{\rho}(t) = \boldsymbol{\mathcal{L}}\boldsymbol{\rho}(t)$, using as an initial condition $\boldsymbol{\rho_0} = \boldsymbol{\mathcal{U}_\epsilon}\boldsymbol{\rho}_\infty$ where $\boldsymbol{\mathcal{U}_\epsilon}$ is the displacement operator of the mode **a** by the complex quantity ϵ (section B.1.2). For a small displacement $|\epsilon| \ll 1$, this step simulates the ring-down of the system after a long microwave pulse of small amplitude on the oscillator.
3. Computing the absorption spectrum as: $S[\omega] = \int \mathrm{d}\tau e^{-i\omega\tau} \langle \mathbf{a} \rangle_\tau$. During the ring-down, we use $\langle \mathbf{a} \rangle_\tau$ as a proxy for the output field since in the absence of excitation the input-output relation reads on average: $\langle \mathbf{a_{out}} \rangle_\tau = \sqrt{\kappa}\langle \mathbf{a} \rangle_\tau$.

Since time-resolved and continuous wave spectroscopy yield similar results, this algorithm is well adapted to reproduce our experimental data acquired with a PNA (section 4.1.1). This algorithm reproduces the quantum regression theorem [Steck 2007] which was used in the proposal [Leroux 2018] for the computation of the qubit spectrum.

We begin with a simulation of the full {DPO+transmon} model, whose Lindbladian[2] is given by the following Hamiltonian and Lindblad oeprators:

Squeezed Jaynes-Cummings in a vacuum bath (SJCVB)

$$\boldsymbol{\mathcal{H}}/\hbar = \delta_\mathrm{a}\mathbf{a}^\dagger\mathbf{a} - \frac{\lambda}{2}\left(\mathbf{a}^2 + \mathbf{a}^{\dagger 2}\right) + \delta_q \mathbf{b}^\dagger\mathbf{b} + \frac{\chi_q}{2}\mathbf{b}^{\dagger 2}\mathbf{b}^2 + g(\mathbf{a}\mathbf{b}^\dagger + \mathbf{a}^\dagger\mathbf{b})$$
$$\boldsymbol{L} \in \left\{\sqrt{\kappa}\,\mathbf{a},\ \sqrt{\gamma_1}\,\mathbf{b},\ \sqrt{2\gamma_\phi}\,\mathbf{b}^\dagger\mathbf{b}\right\}$$

All the parameters used in the simulations are deduced from previous calibrations. The oscillator Fock space is truncated to 40 states, and the transmon one to 3. By repeating the simulation as δ_q is swept accross the BO signal frequency, we reconstruct full anticrossings akin to Fig. 3.6. We then identify the symmetrical points $\delta_q = \Omega_\mathrm{a}[r]$, and plot the resonant spectra on Fig. 3.8 (top). The obvious difference between experimental and simulated lineshapes is a mere visualization artefact, as the complex spectra measured experimentally and simulated numerically are not referenced to the same accumulation point. As the squeezing increases, we witness two effects. First, the gap in between the two peaks fills up. Second, the splitting becomes asymmetric, a signature typically associated with the onset of a full Rabi coupling where excitation-number non-conserving terms cannot be neglected. Using Eq. 3.13 we fit the spectra with g as only fitting parameter, and plot the results on Fig. 3.7 to compare with the data. Experiment and numerics agree on the decreasing trend with squeezing, and we find a quantitative

---

[2] In the presence of multiple Lindlbad operators we find: $\boldsymbol{\mathcal{L}} = -\frac{i}{\hbar}[\boldsymbol{\mathcal{H}}, \cdot] + \sum_{\boldsymbol{L}} \mathcal{D}[\boldsymbol{L}]\cdot$

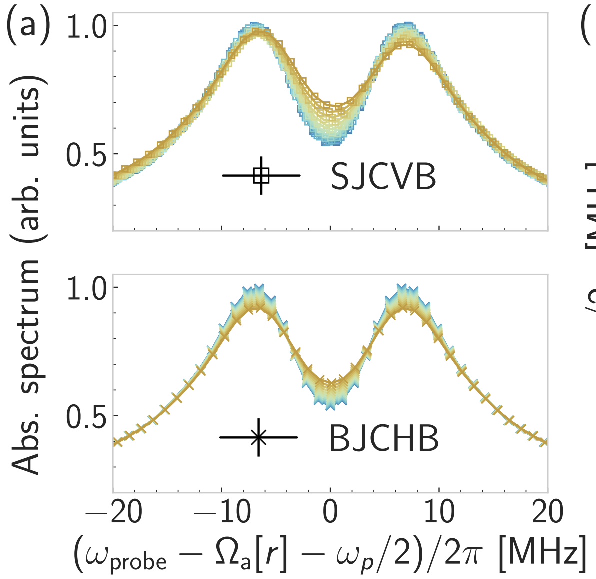

Figure 3.8 Transmon-BO resonant coupling, the simulation. (a) Top [Bottom]: simulated DPO emission spectrum (y-axis) while at resonance with the transmon for increasing squeezing (color, scale on x-axis right plot), versus detuning between the probe and the resonance frequency (x-axis, moving with squeezing amplitude) for the SJCVB [BJCHB] model. (b) Resonant coupling strength (y-axis) vs DPO squeezing (x-axis) as fitted from simulated anticrossings on the SJCVB model (line and circles) or the BJCHB model (line and crosses). Fitting error bars lie within the marker size.

agreement up to $S = 2$ dB. How can we explain this drastic difference with the expected $\cosh r$ trend?

In order to disentangle the coupling boost – potentially beyond the Jaynes-Cummings approximation – from the squeezed bath – potentially beyond the thermal approximation – we proceed with the simulation of another model. Specifically, we consider a simplified Lindbladian keeping only the well-controlled features of the complete one. Using a fictious squeezing parameter r, this model features a boosted excitation-number preserving coupling $g \cosh r$, and a thermal bath $\sinh^2 r$. The so-called *Boosted Jaynes-*

Cummings in a hot bath model reads:

Boosted Jaynes-Cummings in a hot bath (BJCHB)

$$\mathcal{H}/\hbar = \delta_{\mathrm{a}}\mathbf{a}^\dagger\mathbf{a} + \delta_q\mathbf{b}^\dagger\mathbf{b} + \frac{\chi_q}{2}\mathbf{b}^{\dagger 2}\mathbf{b}^2 + g\cosh r(\mathbf{a}\mathbf{b}^\dagger + \mathbf{a}^\dagger\mathbf{b})$$

$$\boldsymbol{L} \in \left\{\sqrt{\kappa}\cosh r\,\mathbf{a},\ \sqrt{\kappa}\sinh r\,\mathbf{a}^\dagger,\ \sqrt{\gamma_1}\,\mathbf{b},\ \sqrt{2\gamma_\phi}\,\mathbf{b}^\dagger\mathbf{b}\right\}$$

We compute the resonant spectra for increasing squeezing parameter r, and plot the results on Fig. 3.8 (bottom). Even though the gap between the two peaks also fills up, albeit in a slower fashion, the figure remains symmetric for all squeezing amplitudes. Finally we fit the coupling rate g, which displays a similar decreasing trend, yet less pronounced. We know for sure that the increased coupling of this second model must contribute to an enhanced splitting. It is then clear that the hot bath leads to a filling of the split lineshape, which spoils the fitting of the coupling rate. Indeed, Eq. 3.13 used to fit the data does not account for finite temperatures[3].

While the squeezed Jaynes-Cummings model fell short of demonstrating a clear enhanced Rabi splitting, it turns out that even a boosted Jaynes-Cummings Hamiltonian in contact with a hot bath cannot produce such a simple signature. This limitation is the product of the squeezed bath, effectively hot. At the onset of strong-coupling, this modified bath leads to the same spectral feature as a *decreasing* coupling strength. One could obviously adjust Eq. 3.13 to account for a finite bath occupation. Yet, it seems unwise to rely on the same spectral feature – that is the depth of the gap – to fit both the coupling and the bath occupation. We are thus looking for another regime to characterize the effect of squeezing on the qubit-oscillator coupling.

---

[3] The spectral response of a linear oscillator is ignorant of the bath temperature. One can check that Eq. 2.33 is left unchanged in the presence of a bath with occupation $\bar{n}_{\mathrm{th}}$. Indeed, the susceptibility of a linear mode is independent of its temperature, or in other words, a linear mode cannot be used as a thermometer. However, coupling a linear oscillator with a transmon brings the nonlinearity necessary to count bath excitations.

3.2 Linear weak-dispersive regime

The dispersive regime is well adapted to characterizing qubit-oscillator interactions even in the presence of non-vanishing bath occupation [Schuster 2007; Ong 2013; Viennot 2018; Dassonneville 2021]. It is thus the perfect test-bench for the study of the coupling between a qubit and a BO. We begin with the linear regime (pump off), before moving on with the addition of DPO squeezing, either resonant (section 3.3) or detuned (section 3.4). Each section will follow the same progression, starting with a definition of the appropriate dispersive transformation, continuing with measurement-induced dephasing theory and finishing with experimental results. The discussion will be limited to the weak-dispersive regime, where the renormalization of the mode dynamical properties can be treated perturbatively.

3.2.1 Dispersive transformation

When no pump is applied on the DPO, the system is most conveniently described in a frame rotating at the oscillator frequency for both the oscillator and the qubit (section B.1.3):

$$\mathcal{H}_{\mathbf{0},\mathbf{0}}/\hbar = \Delta\frac{\boldsymbol{\sigma}_{\mathbf{z}}}{2} + g\big(\mathbf{a}\boldsymbol{\sigma}_{+} + \mathbf{a}^{\dagger}\boldsymbol{\sigma}_{-}\big) \ , \tag{3.14}$$

where $\Delta = \omega_q - \omega_{\mathrm{a}}$ is the qubit-oscillator detuning. It turns out that this Hamiltonian, which is nothing but the Jaynes-Cummings Hamiltonian in a rotating frame, is diagonalizable exactly [Boissonneault 2009; Blais 2021][4]. Yet, anticipating on the added complexity of the two-photon pump, we present an approximation method based on second-order non-degenerate perturbation theory. As justified in the following section, the discussion will be limited to the regime:

Linear dispersive limit: $|\Delta| \gg g,\ \kappa,\ \gamma_1,\ \gamma_\phi$

First, we will present the approximation method for the Hamiltonian of the system. Second, we will detail its implications on the Lindblad operators. Finally, we will extend these results to a DPO coupled to a multi-level system, like a transmon.

---

[4] At this stage, it is worth pointing out that the Rabi model has also been solved exactly [Braak 2011].

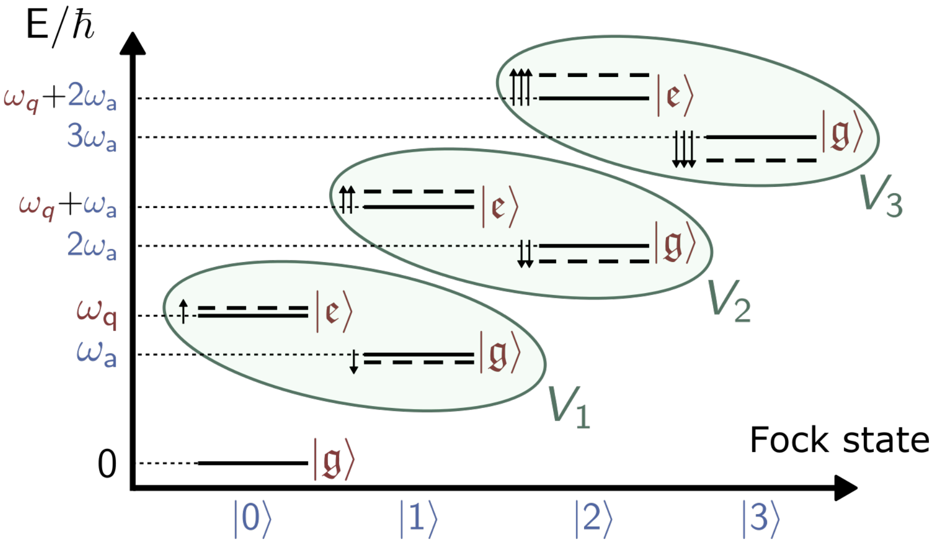

Figure 3.9 Jaynes-Cummings spectrum in the dispersive limit. For the sake of clarity we plot the frequency spectrum of the Hamiltonian in the laboratory frame: $\boldsymbol{\mathcal{H}}_{\mathbf{JC}} = \omega_a \mathbf{a}^\dagger \mathbf{a} + \frac{\omega_q}{2}\boldsymbol{\sigma}_\mathbf{z} + g\big(\mathbf{a}\boldsymbol{\sigma}_+ + \mathbf{a}^\dagger \boldsymbol{\sigma}_-\big)$. The full lines represent the energy levels of the unperturbed Hamiltonian ($g = 0$). The dashed lines show the energy levels in the dispersive limit. Vertical arrows mark frequency shifts in units of g^2/Δ.

Transformed Hamiltonian The eigenstates of the unperturbed ($g = 0$) Hamiltonian are the states $|n, \sigma\rangle = |n\rangle \otimes |\sigma\rangle$, where $|n\rangle$ is the n$^{\text{th}}$ Fock state of the oscillator, and $|\sigma\rangle$ represents the state of the qubit, either ground ($\sigma = \mathfrak{g}$) or excited ($\sigma = \mathfrak{e}$) (full lines on Fig. 3.9). The Jaynes-Cummings Hamiltonian commutes with the operator $\boldsymbol{\mathcal{N}} = \mathbf{a}^\dagger \mathbf{a} + (\boldsymbol{\sigma}_\mathbf{z} + 1)/2$ giving the total number of excitations in the system. The spectrum of $\boldsymbol{\mathcal{N}}$ is made of non-negative integers $n \in \mathbb{N}$. Thus, the Hilbert space decomposes into an infinite sum of invariant manifolds V_n, formed by the states sharing the same quantum number. They can be written in terms of the unperturbed states $V_n = \text{span}\big\{\, |n, \mathfrak{g}\rangle, |n-1, \mathfrak{e}\rangle \big\}$ for $n \geqslant 1$, leaving aside the 0-excitation singleton $V_0 = \{|0, \mathfrak{g}\rangle\}$. In the dispersive limit, specifying $\Delta > 0$ without loss of generality, the spectrum of the restriction of Hamiltonian 3.14 to V_n decomposes into a low-energy subspace $\{|n, \mathfrak{g}\rangle\}$, and a high-energy subspace $\{|n-1, \mathfrak{e}\rangle\}$. When $g = 0$ the spectrum is gapped by Δ. The perturbation couples this two subspaces at a rate $g\sqrt{n}$, shifting the bare eigenvalues by at most $g\sqrt{n}$. Hence, provided $2g\sqrt{n} < \Delta$, the spectrum remains gapped in the presence of the perturbation, and one can find a unitary transformation that decouples the two subspaces at a given order in $g\sqrt{n}/\Delta$: this unitary is called a Schrieffer-Wolff (SW) transformation $\mathcal{U}_{\mathbf{SW}}$ [Bravyi 2011].

Specifically, introducing $\eta = g/\Delta$, we expect the single-excitation manifold to be transformed at first order in η according to:

$$\widetilde{|1,\mathfrak{g}\rangle} = \mathcal{U}_{\mathbf{SW}}\,|1,\mathfrak{g}\rangle = |1,\mathfrak{g}\rangle + \eta\,|0,\mathfrak{e}\rangle + \mathcal{O}(\eta^2)\ , \tag{3.15a}$$

$$\widetilde{|0,\mathfrak{e}\rangle} = \mathcal{U}_{\mathbf{SW}}\,|0,\mathfrak{e}\rangle = |0,\mathfrak{e}\rangle - \eta\,|1,\mathfrak{g}\rangle + \mathcal{O}(\eta^2)\ , \tag{3.15b}$$

and $\widetilde{\langle 0,\mathfrak{e}|}\widetilde{|1,\mathfrak{g}\rangle} = 0$. This is the essence of the SW technique: redefine the bare eigenbasis to incorporate the effect of the perturbation at a given order. Extending this line of thought for the entire Fock basis, all n-excitation manifolds can be diagonalized simultaneously – here at first order in η – through the SW transformation $\mathcal{U}_{\mathbf{SW}} = e^{\boldsymbol{\mathcal{S}}_{\mathbf{0,0}}}$ where:

$$\boldsymbol{\mathcal{S}}_{\mathbf{0,0}} = \eta\mathbf{a}\boldsymbol{\sigma}_{+} - h.c. \tag{3.16}$$

A technique to find analytically this generator is presented in Appendix B.1.4. In the transformed frame, the single-excitation operators are dressed at first order in η according to:

$$e^{\boldsymbol{\mathcal{S}}_{\mathbf{0,0}}}\mathbf{a}e^{-\boldsymbol{\mathcal{S}}_{\mathbf{0,0}}} = \mathbf{a} + \eta\boldsymbol{\sigma}_{\text{-}} + \mathcal{O}(\eta^2)\ , \tag{3.17a}$$

$$e^{\boldsymbol{\mathcal{S}}_{\mathbf{0,0}}}\boldsymbol{\sigma}_{\text{-}}e^{-\boldsymbol{\mathcal{S}}_{\mathbf{0,0}}} = \boldsymbol{\sigma}_{\text{-}} + \eta\mathbf{a}\boldsymbol{\sigma}_{\mathbf{z}} + \mathcal{O}(\eta^2)\ . \tag{3.17b}$$

As usual in perturbation theory, in order to consistently account for a dressing of the states at first-order, one needs to account for a renormalization of the energies at second-order. Thus, up to irrelevant constant terms, the transformed Hamiltonian reads:

$$e^{\boldsymbol{\mathcal{S}}_{\mathbf{0,0}}}\boldsymbol{\mathcal{H}}_{\mathbf{0,0}}e^{-\boldsymbol{\mathcal{S}}_{\mathbf{0,0}}} = \Delta\left(1+\eta^2\right)\frac{\boldsymbol{\sigma}_{\mathbf{z}}}{2} + \eta^2\Delta\mathbf{a}^{\dagger}\mathbf{a}\boldsymbol{\sigma}_{\mathbf{z}} + \mathcal{O}(\eta^3)\ . \tag{3.18}$$

Note that the generator of the SW transformation was chosen to cancel the coupling within the n-excitation manifolds at first order only. Rewriting the SW generator in order to cancel the coupling at order k in η would yield corrections at order $k+1$ in the previous Hamiltonian. Moreover, as the coupling within the n-excitation manifold goes like $g\sqrt{n}$, one should adjust the approximation bound with the Fock state number. This moving bound is understood as a critical photon number for the oscillator, whose occupancy needs to remain below $n_{\text{crit}} = \Delta^2/4g^2$ for the approximation to be valid.

Finally, in the transformed basis $\mathbf{a} \rightarrow e^{-\mathcal{S}_{0,0}}\mathbf{a}e^{\mathcal{S}_{0,0}}$ and $\boldsymbol{\sigma}_\mathbf{z} \rightarrow e^{-\mathcal{S}_{0,0}}\boldsymbol{\sigma}_\mathbf{z}e^{\mathcal{S}_{0,0}}$, the qubit-photon Hamiltonian reads:

$$\boldsymbol{\mathcal{H}}_{\mathbf{0,0}} = \left[\Delta + \chi_0\left(\mathbf{a}^\dagger\mathbf{a} + \frac{1}{2}\right)\right]\frac{\boldsymbol{\sigma}_\mathbf{z}}{2}\,, \tag{3.19}$$

where $\chi_0 = 2g^2/\Delta$ is the dispersive coupling strength. In the dispersive limit, the first-order excitation-swapping coupling term of Hamiltonian 3.14 does not lead to actual transitions between the unperturbed eigenstates of the system. Instead, the coupled system experiences virtual transitions, whose effect is well captured by the second-order energy-renormalizing coupling term of Hamiltonian 3.19.

Transformed Lindblad operators In the new basis the qubit is said to be dressed by the oscillator field. In particular, the decoherence mechanisms imparting the bare oscillator will act on the dressed qubit, and vice-versa. A thorough description of these processes requires to perform the SW transformation at the level of the system-bath Hamiltonian (Appendix B), and leads to a redefinition of the decoherence rates [Boissonneault 2008; Boissonneault 2009; Blais 2021]. Yet, a mere transformation of the Lindblad operators is sufficient to introduce the concepct of dressed decoherence. In the transfomed basis, the Lindblad operators take the form of composite channels:

$$\boldsymbol{L}_{\mathbf{ph}} = \sqrt{\kappa}\left(\mathbf{a} + \frac{g}{\Delta}\boldsymbol{\sigma}_{\text{-}}\right)\,, \tag{3.20a}$$

$$\boldsymbol{L}_{-} = \sqrt{\gamma_1}\left(\boldsymbol{\sigma}_{\text{-}} + \frac{g}{\Delta}\mathbf{a}\boldsymbol{\sigma}_\mathbf{z}\right)\,, \tag{3.20b}$$

$$\boldsymbol{L}_{\phi} = \sqrt{\frac{\gamma_\phi}{2}}\left(\boldsymbol{\sigma}_\mathbf{z} - \frac{2g}{\Delta}\mathbf{a}\boldsymbol{\sigma}_+ - \frac{2g}{\Delta}\mathbf{a}^\dagger\boldsymbol{\sigma}_{\text{-}}\right)\,, \tag{3.20c}$$

which correlate decoherence in both modes. When entering the Lindblad master equation[5], the mixed contributions of these composite loss operators will lead to rotating terms at a frequency Δ. Introducing the dimensionless parameter η such that: $g, \kappa, \gamma_1, \gamma_\phi < \eta \times \Delta$, and in the limit $\eta \ll 1$, these fast rotating terms will have negligible amplitudes compared to their oscillating

---

[5] For instance the contribution of $\boldsymbol{L}_{\mathbf{ph}}$ to the master equation reads:
$\mathcal{D}[\boldsymbol{L}_{\mathbf{ph}}]\boldsymbol{\rho} = \kappa\mathcal{D}[\mathbf{a}]\boldsymbol{\rho} + \kappa\frac{g^2}{\Delta^2}\mathcal{D}[\boldsymbol{\sigma}_{\text{-}}]\boldsymbol{\rho} + \kappa\frac{g}{\Delta}\left(\mathbf{a}\boldsymbol{\rho}\boldsymbol{\sigma}_+ + \boldsymbol{\sigma}_{\text{-}}\boldsymbol{\rho}\mathbf{a}^\dagger - \frac{1}{2}\{\mathbf{a}^\dagger\boldsymbol{\sigma}_{\text{-}} + \boldsymbol{\sigma}_+\mathbf{a}, \boldsymbol{\rho}\}\right)$
so that in a frame rotating at each mode frequency, the first two terms are steady while the last part rotates at Δ, with amplitude $\kappa g/\Delta \sim \Delta \times \eta^2$.

frequencies. They can be averaged out up to second order in η, giving rise to the independent loss channels:

$$\boldsymbol{L}_{\mathbf{ph}} = \sqrt{\kappa}\mathbf{a} \qquad \boldsymbol{L}^{-}_{\mathbf{ph}} = \sqrt{\gamma_\kappa}\boldsymbol{\sigma}_{\text{-}} \ , \tag{3.21a}$$

$$\boldsymbol{L}_{-} = \sqrt{\gamma_1}\boldsymbol{\sigma}_{\text{-}} \qquad \boldsymbol{L}^{\mathbf{ph}}_{-} = \sqrt{\kappa_\gamma}\boldsymbol{\sigma}_{\mathbf{z}}\mathbf{a} \ , \tag{3.21b}$$

$$\boldsymbol{L}_{\phi} = \sqrt{\frac{\gamma_\phi}{2}}\boldsymbol{\sigma}_{\mathbf{z}} \qquad \boldsymbol{L}^{+}_{\phi} = \sqrt{\gamma_\Delta}\mathbf{a}\boldsymbol{\sigma}_{+} \qquad \boldsymbol{L}^{-}_{\phi} = \sqrt{\gamma_\Delta}\mathbf{a}\boldsymbol{\sigma}_{\text{-}} \ . \tag{3.21c}$$

Among them we find the Purcell loss rate induced by the oscillator on the qubit, $\gamma_\kappa = (g/\Delta)^2\kappa$, which depicts the fraction of the bare qubit energy stored in the oscillator that can leak through it. The converse effect arises with the Purcell loss rate induced by the qubit on the oscillator: $\kappa_\gamma = (g/\Delta)^2\gamma_1$. Also the dressed dephasing processes with rate $\gamma_\Delta = (2g/\Delta)^2\gamma_\phi$, which lead to spurious qubit transitions when the oscillator is populated, fuelled by the bare qubit dephasing. Finally, it is worth mentionning that all these dressed decoherence mechanisms are of order 3 in η, so that at the order of approximation that lead to Hamitlonian (3.19) they need not be considered.

Beyond the TLS approximation Finally we extend the previous treatment to account for the multi-level structure of the transmon (section 3.1.2). Following [Koch 2007], the transmon-oscillator Hamiltonian reads in a frame rotating at the oscillator frequency:

$$\boldsymbol{\mathcal{H}}_{\mathbf{t:0,0}}/\hbar = \sum_k \Delta_k \left|k\right\rangle\left\langle k\right| + \sum_k g_{k,k+1}\left(\mathbf{a}\left|k+1\right\rangle\left\langle k\right| + \text{h.c.}\right) \tag{3.22}$$

where $\Delta_k = \omega_k - k \times \omega_{\text{a}}$ and $g_{k,k+1} \approx g\sqrt{k+1}$. Thanks to the transmon selection rules, we omit multi-photon transitions (section 3.1.2). Moving on with the dispersive transformation, the generator of the SW unitary reads:

$$\boldsymbol{\mathcal{S}}_{\mathbf{t:0,0}} = \sum_k \frac{g_{k,k+1}}{\Delta_{k,k+1}}\left(\mathbf{a}\left|k+1\right\rangle\left\langle k\right| - \text{h.c.}\right) \tag{3.23}$$

where $\Delta_{k,k+1} = \Delta_{k+1} - \Delta_k$. We introduce a dimensionless parameter η such that: $\forall k,\ g_{k,k+1} < \eta \times \min(|\Delta_{k,k+1}|)$. This dispersive transformation requires that all the allowed transmon transitions are detuned from the bare oscillator frequency. In the transformed basis $\mathbf{a} \to e^{-\boldsymbol{\mathcal{S}}_{\mathbf{t:0,0}}}\mathbf{a}e^{\boldsymbol{\mathcal{S}}_{\mathbf{t:0,0}}}$, and $\forall k,\ \left|k\right\rangle \to e^{-\boldsymbol{\mathcal{S}}_{\mathbf{t:0,0}}}\left|k\right\rangle$, the restriction of Hamiltonian (3.22) to the two lowest energy transmon levels reads at second-order in η [Blais 2021]:

$$\boldsymbol{\mathcal{H}}_{\mathbf{t:0,0}}/\hbar = \frac{\chi_{t:0} - \chi_0}{2}\mathbf{a}^\dagger\mathbf{a} + \left[\Delta + \frac{\chi_0}{2} + \chi_{t:0}\,\mathbf{a}^\dagger\mathbf{a}\right]\frac{\boldsymbol{\sigma}_{\mathbf{z}}}{2} \ , \tag{3.24}$$

where we introduced the qubit-manifold spin operator $\boldsymbol{\sigma}_{\mathbf{z}} = |\mathfrak{e}\rangle\langle\mathfrak{e}| - |\mathfrak{g}\rangle\langle\mathfrak{g}|$, and:

$$\chi_{t:0} = \frac{2g^2}{\Delta}\frac{\chi_q}{\chi_q + \Delta} \ . \tag{3.25}$$

The dispersive interaction strength of the qubit transition ($\mathfrak{g}$-$\mathfrak{e}$) is dressed by the second excited level of the transmon. It is singular when $\chi_q + \Delta = 0$, that is to say when the oscillator is resonant with the transmon $\mathfrak{e}$-$\mathfrak{f}$ transition. Notably the qubit Lamb shift g^2/Δ is no longer equal to half the dispersive interaction strength, and the oscillator inherits a finite frequency shift. Yet, one can check that in the TLS limit $|\chi_q| \gg |\Delta|$, Hamiltonian 3.24 maps to Hamiltonian 3.19.

3.2.2 Measurement induced dephasing

In the dispersive limit, the interaction process is captured by a qubit-frequency shift conditioned on the occupation of the oscillator (Eq. 3.19). Conversely, the oscillator frequency is expected to move depending on the qubit state, a phenomenon at the heart of the dispersive readout protocol [Blais 2021]. In practice, probing the oscillator involves driving it with coherent signals. Together with thermal noise and quantum noise, these drives populate the oscillator with a mean-photon number $\bar{n}_\mathrm{a}$, fluctuating by $\delta n_\mathrm{a}(t)$. Computing the impact of this finite population on the qubit spectral properties is the topic of this part [Blais 2004; Gambetta 2006]. Specifically, we will limit the discussion to the weak-dispersive regime where $|\chi_0| \ll \kappa$.

Gaussian approximation A qubit initialized in a coherent superposition of its basis states at a time t_0 will pickup a relative phase according to its dispersive interaction with the oscillator (Eq. 3.19). After an interaction time t, we write this phase: $\varphi(t) \equiv \bar{\varphi} + \delta\varphi(t)$. The mean part reads:

$$\bar{\varphi} = \left(\Delta + \frac{\chi_0}{2} + \chi_0 \bar{n}_\mathrm{a}\right)(t - t_0) \ , \tag{3.26}$$

which displays the Lamb-shifted qubit detuning $\Delta + \chi_0/2$, and the AC-Stark contribution $\chi_0 \bar{n}_\mathrm{a}$, with $\bar{n}_\mathrm{a}$ the mean-occupation of the oscillator. The fluctuating part reads:

$$\delta\varphi(t) = \chi_0 \int_{t_0}^{t_0+t} \mathrm{d}\tau \delta n_\mathrm{a}(\tau) \ , \tag{3.27}$$

and its randomness is at the heart of the dephasing mechanism. As the oscillator excitations are short-lived compared to the typical qubit-oscillator interaction time ($\kappa \gg |\chi_0|$ in the weak-dispersive limit), $\delta\varphi$ can be thought of as a sum of independent random variables. Hence the central limit theorem applies, and $\delta\varphi$ follows a Gaussian distribution. Since δn_{a} has zero mean, so does $\delta\varphi$. The induced dephasing by the oscillator on the qubit $\Delta\gamma_\phi$ is commonly defined as $e^{-\Delta\gamma_\phi t} \equiv \langle\langle e^{i\delta\varphi}\rangle\rangle$, where $\langle\langle\cdot\rangle\rangle$ refers to the average over multiple noise realizations (statistical ensemble average). Owing to the previously detailed statistics of $\delta\varphi$, we find that $\langle\langle e^{i\delta\varphi}\rangle\rangle = e^{-\frac{1}{2}\langle\langle\delta\varphi^2\rangle\rangle}$, so that the induced dephasing reads:

$$\Delta\gamma_\phi = \frac{\chi_0^2}{2t} \iint_{t_0}^{t_0+t} \mathrm{d}t_1 \mathrm{d}t_2 \mathcal{C}(t_1,t_2) \ , \tag{3.28}$$

where the fluctuation-fluctuation correlation function reads:

$$\mathcal{C}(t_1,t_2) \equiv \langle \delta n_{\mathrm{a}}(t_2)\delta n_{\mathrm{a}}(t_1)\rangle = \langle(\boldsymbol{n}_{\mathbf{a}}(\boldsymbol{t_2}) - \bar{n}_{\mathrm{a}})(\boldsymbol{n}_{\mathbf{a}}(\boldsymbol{t_1}) - \bar{n}_{\mathrm{a}})\rangle \ , \tag{3.29}$$

and $\boldsymbol{n}_{\mathbf{a}}(\boldsymbol{t}) = \mathbf{a}^\dagger(\boldsymbol{t})\mathbf{a}(\boldsymbol{t})$. To lowest order in χ_0/κ, the average $\langle\cdot\rangle$ denotes the expectation value of the uncoupled system. Elucidating the dispersive and dissipative effects of the oscillator on the qubit amounts to computing the mean-photon number at long times $\bar{n}_{\mathrm{a}} = \langle\mathbf{a}^\dagger\mathbf{a}\rangle$, and the correlation function $\mathcal{C}(t_1,t_2) = \langle\boldsymbol{n}_{\mathbf{a}}(\boldsymbol{t_2})\boldsymbol{n}_{\mathbf{a}}(\boldsymbol{t_1})\rangle - \bar{n}_{\mathrm{a}}^2$.

Oscillator statistics A monochromatic drive of amplitude ε_d, resonant with the oscillator, can be accounted for at the level of Hamiltonian 3.14 through the contribution $\boldsymbol{\mathcal{H}_d}/\hbar = (\varepsilon_d/2)\mathbf{a} + (\varepsilon_d^*/2)\mathbf{a}^\dagger$ (Appendix B.1). Thus, the QLE for the $\mathbf{a}$ mode simply reads:

$$\partial_t\mathbf{a}(\boldsymbol{t}) = -i\frac{\varepsilon_d^*}{2} - \frac{\kappa}{2}\mathbf{a}(\boldsymbol{t}) + \sqrt{\kappa}\mathbf{a_{in}}(\boldsymbol{t}) \ . \tag{3.30}$$

It is most conveniently solved in a displaced frame. Specifically we write $\mathbf{a}(\boldsymbol{t}) = \underline{\mathrm{a}}(t) + \boldsymbol{d}(\boldsymbol{t})$, where $\underline{\mathrm{a}}(t)$ solves the classical part of Eq. 3.30, and $\boldsymbol{d}(\boldsymbol{t})$ its quantum part. The displaced oscillator operator $\boldsymbol{d}$ follows the same commutation relations as the original one. We find:

$$\underline{\mathrm{a}}(t) = \underline{\mathrm{a}}(t_0)e^{-(\kappa/2)(t-t_0)} - i\frac{\varepsilon_d^*}{\kappa}\left(1 - e^{-(\kappa/2)(t-t_0)}\right) \ , \tag{3.31a}$$

$$\boldsymbol{d}(\boldsymbol{t}) = \boldsymbol{d}(\boldsymbol{t_0})e^{-(\kappa/2)(t-t_0)} + \sqrt{\kappa}\int_{t_0}^{t} \mathrm{d}\tau\mathbf{a_{in}}(\tau)e^{-(\kappa/2)(t-\tau)} \ . \tag{3.31b}$$

The mean-photon number can be readily computed as $\bar{n}_{\mathrm{a}} = |\underline{\mathrm{a}}(t)|^2 + \langle\boldsymbol{d}^\dagger(\boldsymbol{t})\boldsymbol{d}(\boldsymbol{t})\rangle$. Moreover, owing to the quadratic nature of the system-bath

Hamiltonian, we can use Wick's theorem [Molinari 2017] to compute the correlation function:

$$\begin{aligned} \mathcal{C}(t_1,t_2) = &\langle \boldsymbol{d_2^\dagger d_1^\dagger}\rangle\langle \boldsymbol{d_2 d_1}\rangle + \langle \boldsymbol{d_2^\dagger d_1}\rangle\langle \boldsymbol{d_2 d_1^\dagger}\rangle \\ &+ \underline{\mathrm{a}}_2^*\underline{\mathrm{a}}_1^*\langle \boldsymbol{d_2 d_1}\rangle + \underline{\mathrm{a}}_2\underline{\mathrm{a}}_1\langle \boldsymbol{d_2^\dagger d_1^\dagger}\rangle \\ &+ \underline{\mathrm{a}}_2\underline{\mathrm{a}}_1^*\langle \boldsymbol{d_2^\dagger d_1}\rangle + \underline{\mathrm{a}}_2^*\underline{\mathrm{a}}_1\langle \boldsymbol{d_2 d_1^\dagger}\rangle \ , \end{aligned} \tag{3.32}$$

where $\boldsymbol{d_i} = \boldsymbol{d}(\boldsymbol{t_i})$ and $\underline{\mathrm{a}}_i = \underline{\mathrm{a}}(t_i)$. We then focus at the long time limit $t \geqslant t_0 \gg \kappa^{-1}$ for which the oscillator converges to a limit cycle with amplitude:

$$\underline{\mathrm{a}}(t) = -i\varepsilon_d^*/\kappa \ . \tag{3.33}$$

This finite amplitude contributes to a coherent population $\bar{n}_\mathrm{d} = |\varepsilon_d|^2/\kappa^2$. Next we turn to the statistical properties of the quantum part in the long time limit $t_1, t_2 \geqslant t_0 \gg \kappa^{-1}$. We find:

$$\langle \boldsymbol{d_2^\dagger d_1}\rangle = \bar{n}_\mathrm{th} e^{-\kappa|t_2-t_1|/2} \ , \tag{3.34a}$$

$$\langle \boldsymbol{d_2 d_1^\dagger}\rangle = (1+\bar{n}_\mathrm{th})\, e^{-\kappa|t_2-t_1|/2} \ , \tag{3.34b}$$

$$\langle \boldsymbol{d_2 d_1}\rangle = 0 \ . \tag{3.34c}$$

Overall, the mean-photon number reads $\bar{n}_\mathrm{a} = \bar{n}_\mathrm{d} + \bar{n}_\mathrm{th}$. We also deduce the correlation function at long times:

$$\mathcal{C}(t_1, t_2|\bar{n}_\mathrm{th}) = \bar{n}_\mathrm{th}\big(1+\bar{n}_\mathrm{th}\big)e^{-\kappa|t_2-t_1|} + \bar{n}_\mathrm{d}\big(1+2\bar{n}_\mathrm{th}\big)e^{-\kappa|t_2-t_1|/2} \ . \tag{3.35}$$

Qubit response Finally the qubit frequency shift and linewidth broadening induced by the oscillator read:

$$\Delta\omega_q = \chi_0\left(\frac{1}{2} + \bar{n}_\mathrm{th} + \bar{n}_\mathrm{d}\right) \ , \tag{3.36a}$$

$$\Delta\gamma_\phi = \frac{2\chi_0^2}{\kappa}\bar{n}_\mathrm{d}\big(1+2\bar{n}_\mathrm{th}\big) + \frac{\chi_0^2}{\kappa}\bar{n}_\mathrm{th}\big(1+\bar{n}_\mathrm{th}\big) \ . \tag{3.36b}$$

From left to right, the first contribution to Eq. 3.36a comes from vacuum fluctuations of the oscillator field, and is commonly known as the Lamb shift. The two following terms, related to the thermal and coherent occupation of the oscillator, contribute on an equal footing to the qubit frequency shift. The coherent one is known as the AC-Stark shift. As for Eq. 3.36b, the first term corresponds to the measurement-induced dephasing exerted by the coherent population of the cavity [Gambetta 2006], renormalized by the finite thermal population. The second one is related to the thermal population alone, and differs notably from the coherent contribution [Bertet 2005; Rigetti 2012]. It is worth pointing out that the contribution mixing coherent and thermal populations is not a standard result.

Beyond the TLS approximation We extend the previous result to the qubit transition of a transmon. While the Lamb shift is proportional to the pure TLS dispersive interaction χ_0, all the other processes involve the coefficient renormalized by the transmon $|\mathfrak{f}\rangle$ state:

$$\Delta\omega_q = \frac{\chi_0}{2} + \chi_{t:0}\big(\bar{n}_{\mathrm{th}} + \bar{n}_{\mathrm{d}}\big) \ , \tag{3.37a}$$

$$\Delta\gamma_\phi = \frac{2\chi_{t:0}^2}{\kappa}\bar{n}_{\mathrm{d}}\big(1 + 2\bar{n}_{\mathrm{th}}\big) + \frac{\chi_{t:0}^2}{\kappa}\bar{n}_{\mathrm{th}}\big(1 + \bar{n}_{\mathrm{th}}\big) \ . \tag{3.37b}$$

3.2.3 Experiment

The dispersive interaction strength can be revealed through a measurement of the transmon suscpetibility to a coherent drive on the oscillator. Specifically, for a resonant drive with power P_{drive}, and in the limit of negligible thermal population, the AC-Stark shift and induced dephasing of the transmon read:

$$\Delta\omega_q[\bar{n}_{\mathrm{d}}] = \chi_{t:0}\bar{n}_{\mathrm{d}} \ , \quad \Delta\gamma_\phi[\bar{n}_{\mathrm{d}}] = \frac{2\chi_{t:0}^2}{\kappa}\bar{n}_{\mathrm{d}} \ , \quad \bar{n}_{\mathrm{d}} = \frac{P_{\mathrm{drive}}}{P_0} \ , \tag{3.38}$$

where P_0 is the drive power maintaining one photon in the oscillator. Following [Schuster 2005], both the dispersive coupling $\chi_{t:0}$ and the photon-number calibration P_0 can be extracted from the joint fitting of the AC-Stark shift and induced dephasing with the applied drive power.

We implement this procedure for multiple transmon-oscillator detunings, by setting the oscillator to its Kerr-free point and sweeping the qubit frequency. Top panels of Fig. 3.10 (a) display the amplitude reflection spectrum of the transmon for detunings of -84 MHz (left, triangles), -26 MHz (center, circles) and 61 MHz (right, squares). For each microwave drive power (according to the color code referenced to the x-axis of the bottom panels), the AC-Stark shift $\Delta\omega_q[\bar{n}_{\mathrm{d}}]$ and induced dephasing $\Delta\gamma_\phi[\bar{n}_{\mathrm{d}}]$ are extracted by fitting the complex data (open symbols) to circles in the complex plane (solid lines) (section 3.1.2). Middle panels of Fig. 3.10 (a) display the transmon frequence shift versus the applied drive power on the oscillator at 300 K. Similarly, the bottom panels of Fig. 3.10 (a) display the linewdith broadening. While in principle the photon number calibration and the dispersive interaction strenght could be fitted independently at every detuning, the small amplitude of the measured signals leads to large fitting uncertainties. However, since the oscillator frequency is kept the same for the whole dataset, so does the photon number calibration. Thus we fit the entire dataset

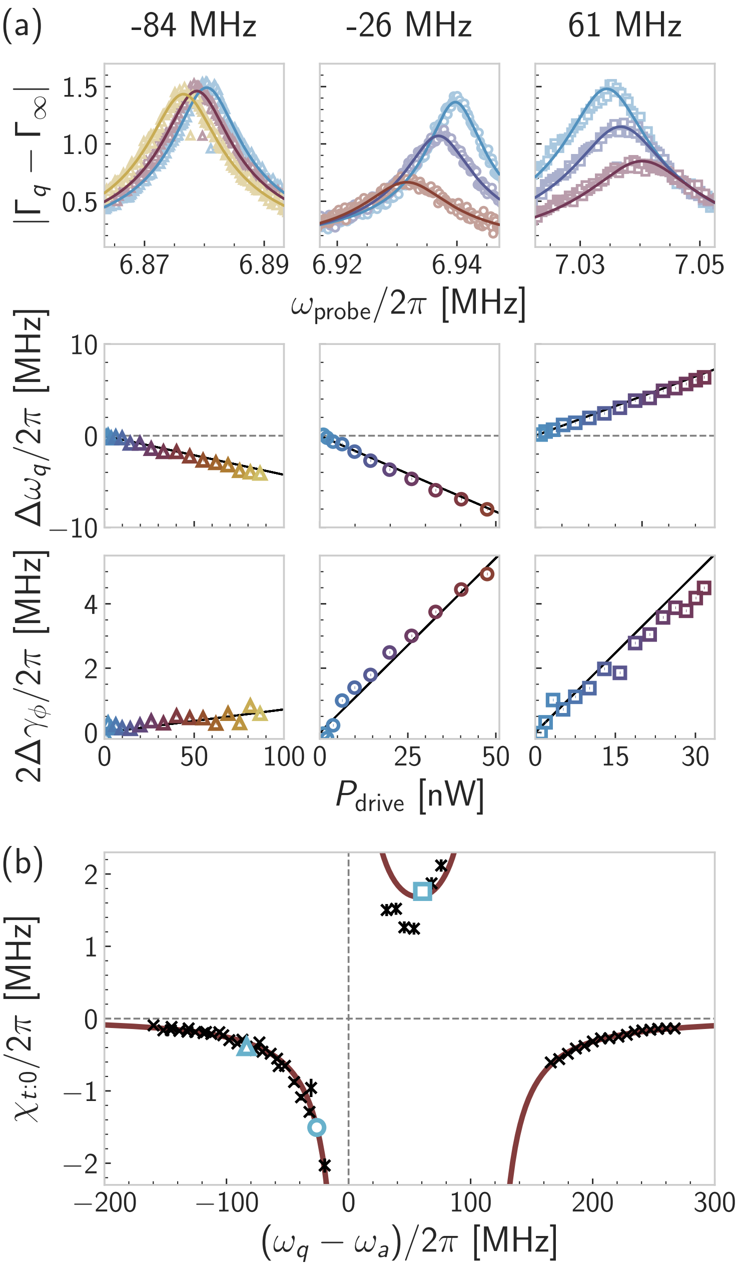

Figure 3.10 Linear dispersive interaction: straddling regime. See description main text.

to Eqs. 3.38 keeping as free parameters: $\chi_{t:0}$ at every detuning, and a single power calibration P_0. The linear interpolations of the AC-Stark shift and induced dephasing are plotted as black lines on Fig. 3.10 (a), and the fitted values of $\chi_{t:0}$ are presented on Fig. 3.10 (b). We find $P_0 = 8.1 \pm 0.3$ nW.

The evolution of $\chi_{t:0}$ with qubit-oscillator detuning clearly displays the straddling regime: when the oscillator frequency lies between the $\mathfrak{g}$-$\mathfrak{e}$ and $\mathfrak{e}$-$\mathfrak{f}$ transitions, virtual transitions to the $|\mathfrak{f}\rangle$ state strongly affects the dispersive interaction strength [Koch 2007]. We fit the extracted $\chi_{t:0}$ versus detunings to the analytical result accounting for the transmon $|\mathfrak{f}\rangle$ state (Eq. 3.25). Keeping as free parameters g and χ_q, we find $g/2\pi = 4.9$ MHz and $E_C/h = -\chi_q/2\pi = 114$ MHz, which are close to the values extracted from the anti-crossing and two-tone spectroscopy described in section 3.1.

3.3 Nonlinear weak-dispersive regime: resonant squeezing

Building on the characterization of the dispersive interaction in the linear regime of the oscillator, we continue with the nonlinear case of resonant squeezing (section 2.1.2). The dispersive coupling of a resonant DPO to a qubit has already been envisioned [Eddins 2019]. There, emphasis was made on the enhanced signal-to-noise ratio of the qubit-readout provided by the gain output by the DPO. Instead, in this part, we focus on the impact of steady-state squeezing on the dispersive interaction strength.

3.3.1 Dispersive transformation

When the DPO undergoes resonant squeezing, the system is most conveniently described in a frame rotating at half the pump frequency for both the oscillator and the qubit:

$$\boldsymbol{\mathcal{H}}_{\mathbf{0},\boldsymbol{\lambda}}/\hbar = -\frac{\lambda}{2}\left(\mathbf{a}^2 + \mathbf{a}^{\dagger 2}\right) + \delta_q \frac{\boldsymbol{\sigma}_{\mathbf{z}}}{2} + g\left(\mathbf{a}\boldsymbol{\sigma}_+ + \mathbf{a}^\dagger \boldsymbol{\sigma}_-\right)\,. \tag{3.39}$$

In that case, since $\omega_\mathrm{a} = \omega_\mathrm{p}/2$, the qubit detuning $\delta_q = \omega_q - \omega_\mathrm{p}/2$ is equal to the qubit-oscillator detuning (labeled Δ in section 3.2). The eigenspectrum of a resonant DPO is continuous (section 2.1.2). Thus, we cannot follow the line of reasoning of the previous section, based on the gapped nature of the eigenspectrum. However, we can still find a transformation that leaves invariant the uncoupled part of the Hamiltonian, and trades the first-order excitation-swapping coupling term, for a second-order energy-renormalizing one (Appendix B.1.4). Its generator reads[6]:

$$\boldsymbol{\mathcal{S}}_{\mathbf{0},\boldsymbol{\lambda}} = \frac{g\delta_q}{\delta_q^2 - \lambda^2}\mathbf{a}\boldsymbol{\sigma}_+ + \frac{g\lambda}{\delta_q^2 - \lambda^2}\mathbf{a}\boldsymbol{\sigma}_- - \text{h.c.}\ . \tag{3.41}$$

Since the dynamical stability of the resonant DPO requires $\lambda < \lambda_\mathrm{crit} = \kappa/2$, the parameter regime of interest remains unchanged:

$$\textbf{Nonlinear dispersive limit } \boldsymbol{\delta_\mathrm{a}}\textbf{=0 :} \quad |\Delta| \gg g,\ \kappa,\ \gamma_1,\ \gamma_\phi\ .$$

Introducing the dimensionless parameter η such that: $g,\ \kappa,\ \gamma_1,\ \gamma_\phi < \eta \times |\delta_q|$, and under the assumption that $\eta \ll 1$, Hamiltonian 3.39 reads in the transformed basis $\mathbf{a} \to e^{-\boldsymbol{\mathcal{S}}_{0,\lambda}}\mathbf{a}e^{\boldsymbol{\mathcal{S}}_{0,\lambda}}$, $\boldsymbol{\sigma}_\mathbf{z} \to e^{-\boldsymbol{\mathcal{S}}_{0,\lambda}}\boldsymbol{\sigma}_\mathbf{z}e^{\boldsymbol{\mathcal{S}}_{0,\lambda}}$ up to second order in η:

$$\boldsymbol{\mathcal{H}}_{\mathbf{0},\boldsymbol{\lambda}}/\hbar = -\frac{\lambda}{2}\left(\mathbf{a}^2 + \mathbf{a}^{\dagger 2}\right) + \left[\delta_q + \chi_0\left(\mathbf{a}^\dagger\mathbf{a} + \frac{1}{2}\right)\right]\frac{\boldsymbol{\sigma}_\mathbf{z}}{2}\ , \tag{3.42}$$

where $\chi_0 = 2g^2/\delta_q$ is the bare dispersive interaction parameter. Corrections to χ_0 occur at order four in η. In addition, Lindblad operators are not modified up to order 3 in η. While the analytical derivation leading to Hamiltonian 3.42 is flawless, its physical motivation remains quite obscure due to the peculiarity of the bare DPO eigenspectrum. Fortunately, the SW procedure presented in section 3.2.1 can be generalized to dissipative systems [Kessler 2012]. There, the eigenvalues of the Liouvillian operator are partitioned in the complex plane, in order to write an effective dynamics for a subset of the Hilbert space. As a conclusion, it appears that steady-state squeezing does not change the strength of the coupling between the oscillator and the qubit.

Beyond the TLS approximation The addition of a pump resonant with $2\omega_\mathrm{a}$ does not change the set of spurious resonances between the oscillator and the transmon higher transitions. In the following, we will merely adjust

---

[6] Note that in the presence of a finite detuning δ_a, the generator reads:

$$\boldsymbol{\mathcal{S}}_{\boldsymbol{\delta}_\mathbf{a},\boldsymbol{\lambda}} = \frac{g(\delta_q + \delta_\mathrm{a})}{\delta_q^2 - \delta_\mathrm{a}^2 - \lambda^2}\mathbf{a}\boldsymbol{\sigma}_+ + \frac{g\lambda}{\delta_q^2 - \delta_\mathrm{a}^2 - \lambda^2}\mathbf{a}\boldsymbol{\sigma}_- - \text{h.c.} \tag{3.40}$$

For nearly resonant squeezing $|\delta_\mathrm{a}| < \kappa/2$, and within the second order approximation, the Hamiltonian in the transformed basis amounts to Eq. 3.42 plus the oscillator contribution $\delta_\mathrm{a}\mathbf{a}^\dagger\mathbf{a}$. However, for detuned squeezing in the BO regime $\kappa/2 \ll \lambda < |\delta_\mathrm{a}|$, a non-negligible anomalous dispersive term arises, as presented by [Shani 2022].

Hamiltonian 3.42 in a similar fashion as in the linear case (section 3.2) in order to account for the transmon $|\mathrm{f}\rangle$ state:

$$\boldsymbol{\mathcal{H}}_{\mathbf{t:0,\lambda}}/\hbar = -\frac{\lambda}{2}\left(\mathbf{a}^2 + \mathbf{a}^{\dagger 2}\right) + \left[\delta_q + \frac{\chi_0}{2} + \chi_{t:0}\,\mathbf{a}^\dagger\mathbf{a}\right]\frac{\boldsymbol{\sigma}_\mathbf{z}}{2}\,. \tag{3.43}$$

3.3.2 Measurement-induced dephasing

Following the derivation of section 3.2.2, the dressing of the qubit spectral features are deduced from the statistical properties of the oscillator at long times. The QLE for the driven resonant-DPO reads:

$$\partial_t\mathbf{a}(\boldsymbol{t}) = i\lambda\mathbf{a}^\dagger(\boldsymbol{t}) - i\frac{\varepsilon_d^*}{2} - \frac{\kappa}{2}\mathbf{a}(\boldsymbol{t}) + \sqrt{\kappa}\mathbf{a}_\mathbf{in}(\boldsymbol{t})\,. \tag{3.44}$$

Since $\delta_\mathrm{a} = 0$, the drive frequency is commensurate with the pump frequency, and their relative phase is expected to modify the system response [Eddins 2019]. The drive complex amplitude is defined as $\varepsilon_d = |\varepsilon_d|e^{i(\theta-\pi/4)}$, so that when $\theta = 0$ the in-phase component of the drive lies along the squeezed quadrature of the oscillator (section 2.1.2). While the induced dephasing of a driven resonant-DPO coupled to a qubit has been covered in [Eddins 2019], here we focus on the AC-Stark shift contribution in the absence of thermal excitations $\bar{n}_\mathrm{th} = 0$. Thus, we are left with solving the classical part of Eq. 3.44, which yields at long times:

$$\underline{\mathrm{a}}(t) = -i\frac{\varepsilon_d^*}{\kappa}\frac{\kappa^2/4}{\kappa^2/4-\lambda^2} - \frac{\varepsilon_d}{\kappa}\frac{\lambda\kappa/2}{\kappa^2/4-\lambda^2} \tag{3.45}$$

The AC-Stark shift simply reads $\Delta\omega_q[\lambda,\bar{n}_\mathrm{d}] = \chi_0|\underline{\mathrm{a}}(t)|^2$, and we find:

$$\Delta\omega_q[\lambda,\bar{n}_\mathrm{d}] = \frac{\kappa^2}{4}\frac{\kappa^2/4+\lambda^2-\lambda\kappa\cos 2\theta}{(\kappa^2/4-\lambda^2)^2}\bar{n}_\mathrm{d}\chi_0\,, \tag{3.46}$$

where $\bar{n}_\mathrm{d} = |\varepsilon_d|^2/\kappa^2$ is the mean photon number injected by the coherent drive with the pump off. Together with the phase dependent induced dephasing (see Eq. (4) of [Eddins 2019]), we can infer the dispersive interaction strength from a joint fitting of the qubit spectral features versus the drive phase, at a fixed drive amplitude.

Beyond the TLS approximation The previous result can be trivially extended to a transmon by replacing χ_0 by $\chi_{t:0}$ in Eq. 3.46.

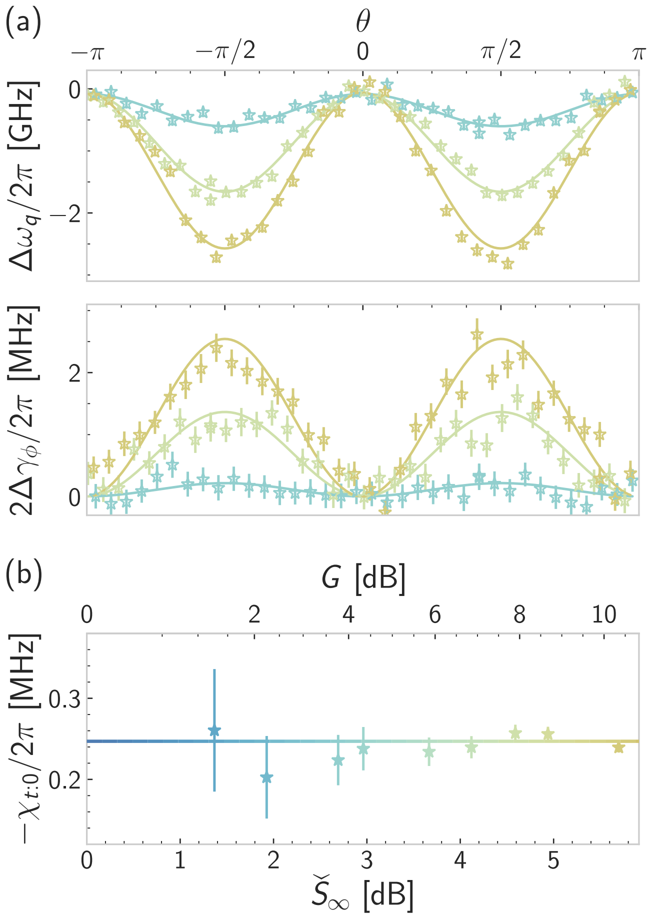

Figure 3.11 Nonlinear dispersive interaction: resonant squeezing. See description main text.

3.3.3 Experiment

This procedure is presented in Fig. 3.11 with a transmon-oscillator detuning of $(\delta_q - \delta_\mathrm{a})/2\pi = -100$ MHz, thus placing the system in the weak dispersive regime $\chi_{t:0}/2\pi = -250$ kHz. For various resonant two-photon pump amplitudes generating up to 10 dB of gain at the output of the DPO, we drive the oscillator with a resonant tone, and roll the phase between the two commensurate frequencies. The resonant drive is calibrated as to inject $\bar{n}_\mathrm{d} = 0.8$ photons, and every measured gain is converted into a steady-state anti-squeezing amplitude (section 2.1). For every relative phase, we record a transmon reflection spectrum (akin to Fig. 3.10), and fit the AC-Stark shift $\Delta\omega_q[\lambda, \bar{n}_{\rm d}]$ and induced dephasing $\Delta\gamma_\phi[\lambda, \bar{n}_{\rm d}]$. On Fig. 3.11(a), we plot both quantites referenced to the undriven case (but with the pump on). Solid lines are fit to Eq. 3.46 and Eq. (4) of [Eddins 2019], yielding $\chi_{t:0}$ – the only fitting parameter – for each steady-state anti-squeezing value. We find a dispersive interaction strength independent of the steady-state anti-squeezing over the whole measurement range.

3.4 Nonlinear weak-dispersive regime: detuned squeezing

Finally, we turn to the characterization of the dispersive interaction of a qubit to a detuned DPO, in the BO regime.

3.4.1 Dispersive transformation

When the DPO undergoes detuned squeezing – in the BO regime – the system is most conveniently described in a frame rotating at half the pump frequency for both the oscillator and the qubit, and in the Bogoliubov basis for the oscillator:

$$\begin{aligned}\boldsymbol{\mathcal{H}}_{\boldsymbol{\delta_{\rm a},\lambda}}/\hbar = \Omega_{\rm a}[r]\boldsymbol{\alpha}^\dagger\boldsymbol{\alpha} + \delta_q\frac{\boldsymbol{\sigma_{\rm z}}}{2} &+ g\cosh r\left(\boldsymbol{\alpha}\boldsymbol{\sigma}_+ + \boldsymbol{\alpha}^\dagger\boldsymbol{\sigma}_-\right)\\ &+ g\sinh r\left(\boldsymbol{\alpha}\boldsymbol{\sigma}_- + \boldsymbol{\alpha}^\dagger\boldsymbol{\sigma}_+\right)\ .\end{aligned} \tag{3.47}$$

The appearance of the excitation-number non-conserving term breaks the symmetry of the Jaynes-Cummings model. Again, we can write a SW transformation that leaves invariant the uncoupled part of the Hamiltonian, and absorbs both the excitation-number conserving and non-conserving terms. Its generator reads:

$$\boldsymbol{\mathcal{S}}_{\boldsymbol{\delta_{\rm a},\lambda}} = \frac{g\cosh r}{\Delta[r]}\boldsymbol{\alpha}\boldsymbol{\sigma}_+ - \frac{g\sinh r}{\Sigma[r]}\boldsymbol{\alpha}\boldsymbol{\sigma}_- - \text{h.c.}\,, \tag{3.48}$$

where:

$$\Delta[r] = \delta_q - \Omega[r]\ , \quad \text{and} \quad \Sigma[r] = \delta_q + \Omega[r]\ . \tag{3.49}$$

While $\Delta[r]$ is the detuning between the qubit and the renormalized frequency of the BO, $\Sigma[r]$ is the detuning between the qubit and the BO idler photons. Thus the dispersive interaction to a BO is restricted to the regime where:

$$\textbf{Nonlinear dispersive limit } \boldsymbol{\delta_{\rm a} \neq 0} : \begin{cases} |\Delta[r]| \gg ge^r,\ \kappa,\ \gamma_1,\ \gamma_\phi \\ |\Sigma[r]| \gg ge^r,\ \kappa,\ \gamma_1,\ \gamma_\phi \end{cases} .$$

It is quite remarkable that the idler peak, resulting from the convertion of signal photons by the pump, comes not only as a clear spectroscopic feature of the BO (section 2.2.4), but also as a key ingredient of its interaction with a qubit. Introducing the dimensionless parameter η such that: $ge^r,\ \kappa,\ \gamma_1,\ \gamma_\phi < \eta \times \min(|\Delta[r]|,\ |\Sigma[r]|)$, and under the assumption that $\eta \ll 1$, Hamiltonian 3.39 reads in the transformed basis $\mathbf{a} \to e^{-\boldsymbol{\mathcal{S}}_{\delta_\mathrm{a},\lambda}}\mathbf{a}e^{\boldsymbol{\mathcal{S}}_{\delta_\mathrm{a},\lambda}}$, $\boldsymbol{\sigma}_\mathbf{z} \to e^{-\boldsymbol{\mathcal{S}}_{\delta_\mathrm{a},\lambda}}\boldsymbol{\sigma}_\mathbf{z}e^{\boldsymbol{\mathcal{S}}_{\delta_\mathrm{a},\lambda}}$ up to second order in η:

$$\begin{aligned}\boldsymbol{\mathcal{H}}_{\delta_\mathrm{a},\lambda}/\hbar = \Omega_\mathrm{a}[r]\boldsymbol{\alpha}^\dagger\boldsymbol{\alpha} + \delta_q\frac{\boldsymbol{\sigma}_\mathbf{z}}{2} + \chi[r]\left(\boldsymbol{\alpha}^\dagger\boldsymbol{\alpha} + \frac{1}{2}\right)\frac{\boldsymbol{\sigma}_\mathbf{z}}{2}\\ + \chi_a[r]\left(\boldsymbol{\alpha}^2 + \boldsymbol{\alpha}^{\dagger 2}\right)\frac{\boldsymbol{\sigma}_\mathbf{z}}{2}\,,\end{aligned} \tag{3.50}$$

where the dispersive interaction strength and its anomalous counterpart write:

$$\chi[r] = \frac{2g^2\cosh^2 r}{\delta_q - \Omega_\mathrm{a}[r]} + \frac{2g^2\sinh^2 r}{\delta_q + \Omega_\mathrm{a}[r]}\,, \tag{3.51a}$$

$$\chi_a[r] = \frac{g^2\sinh 2r}{\delta_q}\frac{\delta_q^2}{\delta_q^2 - \Omega_\mathrm{a}^2[r]}\,. \tag{3.51b}$$

In addition, Lindblad operators are not modified up to order 3 in η.

It appears that eigenstate squeezing profoundly changes the nature of the coupling between the oscillator and the qubit. Not only the dispersive interaction strength increases with squeezing – one can check that $|\chi[r]|$ is a strictly increasing function or r – but an anomalous dispersive channel based on Bogoliubov excitation squeezing arises. Note that the magnitude of the anomalous dispersive interaction term is of the same order as the usual one. That being said, in the limit $|\chi_a[r]| \ll |2\Omega_\mathrm{a}[r]|$, Hamiltonian 3.50 can be approximated by its secular part[7]:

$$\boldsymbol{\mathcal{H}}_{\delta_\mathrm{a},\lambda}/\hbar \approx \Omega_\mathrm{a}[r]\boldsymbol{\alpha}^\dagger\boldsymbol{\alpha} + \left[\delta_q + \chi[r]\left(\boldsymbol{\alpha}^\dagger\boldsymbol{\alpha} + \frac{1}{2}\right)\right]\frac{\boldsymbol{\sigma}_\mathbf{z}}{2}\,. \tag{3.52}$$

Finally it is instructive to look at the dispersive interaction strength in the limit $|\delta_q| \gg |\delta_\mathrm{a}|$. In this regime, the renormalization of the oscillator frequency is negligible when compared to the qubit-oscillator detuning, such that $\Delta[r] \approx \Sigma[r] \approx \delta_q$. Thus, the enhanced dispersive interaction strength simply reads $\chi[r] \approx \chi_0 \cosh 2r$.

---

[7] This approximation amounts to going to the interaction picture, then performing a RWA, and resorting to the original frame.

Beyond the TLS approximation We extend the previous result to the higher energy levels of the transmon, beyond the qubit manifold. Following section 3.2.1, the transmon-BO Hamiltonian reads in the Bogoliubov basis and under the RWA:

$$\begin{aligned}\boldsymbol{\mathcal{H}}_{\mathbf{t}:\boldsymbol{\delta}_{\mathbf{a}},\boldsymbol{\lambda}}/\hbar = {} & \Omega_{\mathrm{a}}[r]\boldsymbol{\alpha}^{\dagger}\boldsymbol{\alpha} + \sum_k \delta_k \left|k\right\rangle\!\left\langle k\right| \\ & + \sum_k g_{k,k+1}\cosh r \left(\boldsymbol{\alpha}\left|k+1\right\rangle\!\left\langle k\right| + \text{h.c.}\right) \\ & + \sum_k g_{k,k+1}\sinh r \left(\boldsymbol{\alpha}\left|k\right\rangle\!\left\langle k+1\right| + \text{h.c.}\right)\end{aligned} \tag{3.53}$$

where $\delta_k = \omega_k - k \times \frac{\omega_p}{2}$. Moving on with the dispersive transformation, the generator of the SW unitary reads:

$$\begin{aligned}\boldsymbol{\mathcal{S}}_{\mathbf{t}:\boldsymbol{\delta}_{\mathbf{a}},\boldsymbol{\lambda}} = & \sum_k \frac{g_{k,k+1}\cosh r}{\delta_{k,k+1} - \Omega_{\mathrm{a}}[r]} \left(\boldsymbol{\alpha}\left|k+1\right\rangle\!\left\langle k\right| - \text{h.c.}\right) \\ & - \sum_k \frac{g_{k,k+1}\sinh r}{\delta_{k,k+1} + \Omega_{\mathrm{a}}[r]} \left(\boldsymbol{\alpha}\left|k\right\rangle\!\left\langle k+1\right| - \text{h.c.}\right)\end{aligned} \tag{3.54}$$

where $\delta_{k,k+1} = \delta_{k+1} - \delta_k$. We introduce a dimensionless parameter η such that: $\forall k,\ g_{k,k+1}e^{r} < \eta \times \min(|\delta_{k,k+1} \pm \Omega_{\mathrm{a}}[r]|)$. This dispersive transformation requires that all the allowed transmon transitions are detuned from the BO signal and idler frequencies. This regime is safely maintained in our experiment. In the transformed basis $\boldsymbol{\alpha} \to e^{-\boldsymbol{\mathcal{S}}_{\mathbf{t}:\boldsymbol{\delta}_{\mathbf{a}},\boldsymbol{\lambda}}}\boldsymbol{\alpha}e^{\boldsymbol{\mathcal{S}}_{\mathbf{t}:\boldsymbol{\delta}_{\mathbf{a}},\boldsymbol{\lambda}}}$, and $\forall k,\ \left|k\right\rangle \to e^{-\boldsymbol{\mathcal{S}}_{\mathbf{t}:\boldsymbol{\delta}_{\mathbf{a}},\boldsymbol{\lambda}}}\left|k\right\rangle$, the secular restriction of Hamiltonian (3.53) to the two lowest energy transmon levels reads at second-order in η:

$$\boldsymbol{\mathcal{H}}_{\mathbf{t}:\boldsymbol{\delta}_{\mathbf{a}},\boldsymbol{\lambda}}/\hbar = \left(\Omega_{\mathrm{a}}[r] + \Omega_{\mathrm{a}}^{(2)}[r]\right)\boldsymbol{\alpha}^{\dagger}\boldsymbol{\alpha}^{\dagger} + \left[\delta_q + \delta_q^{(2)}[r] + \chi_t[r]\boldsymbol{\alpha}^{\dagger}\boldsymbol{\alpha}\right]\frac{\boldsymbol{\sigma}_{\mathbf{z}}}{2}\,, \tag{3.55}$$

where $\boldsymbol{\sigma}_{\mathbf{z}}$ is the Pauli Z operator of the transmon qubit-manifold, and:

$$\Omega_{\mathrm{a}}^{(2)}[r] = -\frac{g^2\cosh^2 r}{\Delta[r]} - \frac{g^2\sinh^2 r}{\Sigma[r]}\,, \tag{3.56a}$$

$$\delta_q^{(2)}[r] = \frac{g^2\cosh^2 r}{\Delta[r]} + \frac{g^2\sinh^2 r}{\Sigma[r]}\frac{\chi_q - \Sigma[r]}{\chi_q + \Sigma[r]}\,, \tag{3.56b}$$

$$\chi_t[r] = \frac{2g^2}{\Delta[r]}\frac{\chi_q}{\chi_q + \Delta[r]}\cosh^2 r + \frac{2g^2}{\Sigma[r]}\frac{\chi_q}{\chi_q + \Sigma[r]}\sinh^2 r\,. \tag{3.56c}$$

These coefficients were computed using Mathematica code with the invaluable help of Alexandru Petrescu. Finally, one can check that in the limit $|\chi_q| \gg |\Delta[r]|,\ |\Sigma[r]|$ we recover $\delta_q^{(2)}[r] \approx \chi_t[r]/2$, as customary for a dispersively coupled qubit.

3.4.2 Measurement-induced dephasing

Following the derivation of section 3.2.2, the dressing of the qubit spectral features are deduced from the statistical properties of the oscillator at long times. We consider a BO continuously squeezed, and coherently driven at its renormalized frequency. At long times, the occupation of the BO converges towards a mean-occupation $\bar{n}_\alpha$, and fluctuates by $\delta n_\alpha(t)$. The statistical properties of the BO occupancy reflect both the effects of the squeezing and the coherent drive. Using Eq. 2.31 and Appendix B we write the QLE for the driven Bogoliubov mode:

$$\begin{aligned}\partial_t \boldsymbol{\alpha}(\boldsymbol{t}) = &-i\Omega_\mathrm{a}\boldsymbol{\alpha}(\boldsymbol{t}) - i\frac{\varepsilon_d^* \cosh r}{2}e^{-i\Omega_\mathrm{a}t} - i\frac{\varepsilon_d \sinh r}{2}e^{i\Omega_\mathrm{a}t} \\ &-\frac{\kappa}{2}\boldsymbol{\alpha}(\boldsymbol{t}) + \sqrt{\kappa}\big(\mathbf{a_{in}}(\boldsymbol{t})\cosh r - \mathbf{a}^\dagger_\mathbf{in}(\boldsymbol{t})\sinh r\big)\ . \qquad (3.57)\end{aligned}$$

It is most conveniently solved in a displaced frame. Specifically we write $\boldsymbol{\alpha}(\boldsymbol{t}) = \underline{\alpha}(t) + \boldsymbol{d}(\boldsymbol{t})$, where $\underline{\alpha}(t)$ solves the classical part of Eq. 3.57, and $\boldsymbol{d}(\boldsymbol{t})$ its quantum part. The displaced BO operator follows the same commutation relations as the original one. We find:

$$\begin{aligned}\underline{\alpha}(t) &= \underline{\alpha}(t_0)e^{-(i\Omega_\mathrm{a}+\kappa/2)(t-t_0)} && (3.58\mathrm{a})\\ &\quad - i\int_{t_0}^{t}\mathrm{d}\tau\left\{\frac{\varepsilon_d^*}{2}e^{-i\Omega_\mathrm{a}\tau}\cosh r + \frac{\varepsilon_d}{2}e^{i\Omega_\mathrm{a}\tau}\sinh r\right\}e^{-(i\Omega_\mathrm{a}+\kappa/2)(t-\tau)}\ ,\\ \boldsymbol{d}(\boldsymbol{t}) &= \boldsymbol{d}(\boldsymbol{t_0})e^{-(i\Omega_\mathrm{a}+\kappa/2)(t-t_0)} && (3.58\mathrm{b})\\ &\quad + \sqrt{\kappa}\int_{t_0}^{t}\mathrm{d}\tau\Big\{\boldsymbol{a}_\mathbf{in}(\boldsymbol{\tau})\cosh r - \boldsymbol{a}^\dagger_\mathbf{in}(\boldsymbol{\tau})\sinh r\Big\}e^{-(i\Omega_\mathrm{a}+\kappa/2)(t-\tau)}\ .\end{aligned}$$

The mean Bogoliubov-excitation number can be readily computed as $\bar{n}_\alpha = |\underline{\alpha}(t)|^2 + \langle \boldsymbol{d}^\dagger(\boldsymbol{t})\boldsymbol{d}(\boldsymbol{t})\rangle$. Then we focus at the long time limit $t \geqslant t_0 \gg \kappa^{-1}$ for which the BO converges to a limit cycle with amplitude:

$$\underline{\alpha}(t) = -i\frac{\varepsilon_d^*\cosh r}{\kappa}e^{-i\Omega_\mathrm{a}t} - i\frac{\varepsilon_d \sinh r}{\kappa + 4i\Omega_\mathrm{a}}e^{i\Omega_\mathrm{a}t}\ . \qquad (3.59)$$

Far from coalescence (meaning $|\Omega_\mathrm{a}[r]| \gg \kappa/2$, see section 2.1.3), the classical part of the Bogoliubov mode reduces to an amplified coherent signal $\underline{\alpha}(t) \approx -ie^{-i\Omega_\mathrm{a}t}(\varepsilon_d^*/\kappa)\cosh r$. Indeed, in that regime, the BO induces negligible mixing between the signal and idler components of the drive. This finite amplitude contributes to a coherent population of the mode $|\underline{\alpha}(t)|^2 = \bar{n}_\mathrm{d}\cosh^2 r$, where $\bar{n}_\mathrm{d} = |\varepsilon_d|^2/\kappa^2$ is the number of circulating photons that the coherent drive would maintain in the oscillator in the absence of squeezing. Next we turn to the statistical properties of the quantum part in the long time limit $t_1, t_2 \geqslant t_0 \gg \kappa^{-1}$. We find:

$$\begin{aligned}
\langle \boldsymbol{d}_{\mathbf{1}}^\dagger \boldsymbol{d}_{\mathbf{1}} \rangle &= \big(\sinh^2 r + \bar{n}_{\mathrm{th}} + 2\bar{n}_{\mathrm{th}} \sinh^2 r\big) \ , \\
\langle \boldsymbol{d}_{\mathbf{2}}^\dagger \boldsymbol{d}_{\mathbf{1}} \rangle &= \langle \boldsymbol{d}_{\mathbf{1}}^\dagger \boldsymbol{d}_{\mathbf{1}} \rangle \, e^{i\Omega_{\mathrm{a}}(t_2-t_1)} e^{-\kappa|t_2-t_1|/2} \, , &\text{(3.60a)} \\
\langle \boldsymbol{d}_{\mathbf{1}} \boldsymbol{d}_{\mathbf{1}}^\dagger \rangle &= \big(1 + \sinh^2 r + \bar{n}_{\mathrm{th}} + 2\bar{n}_{\mathrm{th}} \sinh^2 r\big) \ , \\
\langle \boldsymbol{d}_{\mathbf{2}} \boldsymbol{d}_{\mathbf{1}}^\dagger \rangle &= \langle \boldsymbol{d}_{\mathbf{1}} \boldsymbol{d}_{\mathbf{1}}^\dagger \rangle \, e^{-i\Omega_{\mathrm{a}}(t_2-t_1)} e^{-\kappa|t_2-t_1|/2} \, , &\text{(3.60b)} \\
\langle \boldsymbol{d}_{\mathbf{1}} \boldsymbol{d}_{\mathbf{1}} \rangle &= \frac{i}{2} \frac{\kappa}{2\Omega_{\mathrm{a}}} \frac{\sinh 2r}{1 - i\kappa/2\Omega_{\mathrm{a}}} \left(1 + 2\bar{n}_{\mathrm{th}}\right) \ , \\
\langle \boldsymbol{d}_{\mathbf{2}} \boldsymbol{d}_{\mathbf{1}} \rangle &= \langle \boldsymbol{d}_{\mathbf{1}} \boldsymbol{d}_{\mathbf{1}} \rangle \, e^{-(i\Omega_{\mathrm{a}}+\kappa/2)|t_2-t_1|} \, . &\text{(3.60c)}
\end{aligned}$$

Note that when $r = 0$, we recover Eqs. 3.34. Also as pointed out on Figure 2.4, at zeroth order in $\eta = \kappa \sinh 2r / 2|\Omega_{\mathrm{a}}[r]|$, the anomalous correlator (3.60c) vanishes, and the displaced Bogoliubov mode $\boldsymbol{d}$ resembles a thermal field [Lemonde 2016]. In the following, we focus on the situation where the environment is held in vacuum $\bar{n}_{\mathrm{th}} = 0$, so that the mean-occupancy of this pseudo-thermal field simply reads: $\langle \boldsymbol{d}_{\mathbf{1}}^\dagger \boldsymbol{d}_{\mathbf{1}} \rangle = \sinh^2 r$.

At first order in η we find $\bar{n}_\alpha \approx \bar{n}_{\mathrm{d}} \cosh^2 r + \sinh^2 r$. Far from coalescence, the mean occupation of the BO results from the sum of the amplified drive and the effective thermal population. In addition, at the same order the correlation function reads:

$$\begin{aligned}
\mathcal{C}(t_1, t_2|r) \approx\ & \sinh^2 r \big(1 + \sinh^2 r\big) e^{-\kappa|t_2-t_1|} \\
& + \bar{n}_{\mathrm{d}} \cosh^2 r \big(1 + 2\sinh^2 r\big) e^{-\kappa|t_2-t_1|/2} \, . \qquad \text{(3.61)}
\end{aligned}$$

Note that it also features oscillatory terms proportional to $\mathrm{Re}\big(\eta e^{2i\Omega_{\mathrm{a}} t_1 - \kappa|t_2-t_1|/2}\big)$ that we omitted here, anticipating on the averaging performed when computing the induced dephasing. Comparing Eqs. (3.61) and (3.35) lets us confirm the resemblance of a BO with a hot oscillator with thermal occupancy $\sinh^2 r$.

Qubit response Finally, we can write the frequency shift of a qubit dispersively coupled to a driven BO far from coalescence as $\Delta\omega_q = \Delta\omega_q[r] + \Delta\omega_q[r, \bar{n}_\mathrm{d}]$ where:

$$\Delta\omega_q[r] = \chi[r]\Big(\frac{1}{2} + \sinh^2 r\Big) - \frac{1}{2}\chi_0\ , \tag{3.62a}$$

$$\Delta\omega_q[r, \bar{n}_\mathrm{d}] = \chi[r]\bar{n}_\mathrm{d}\cosh^2 r\ . \tag{3.62b}$$

The first contribution amounts to a modified Lamb shift accounting for the equivalent thermal occupation of the BO. The term $\chi_0/2$ is subtracted since we reference the frequency shift to the absence of pump ($r = 0$). The second contribution is an AC-Stark shift accounting for the amplification of the input drive by the BO anti-squeezing. Similarly the induced dephasing reads $\Delta\gamma_\phi = \Delta\gamma_\phi[r] + \Delta\gamma_\phi[r, \bar{n}_\mathrm{d}]$ where:

$$\Delta\gamma_\phi[r] = \frac{\chi^2[r]}{\kappa}\sinh^2 r\left(1 + \sinh^2 r\right)\ , \tag{3.63a}$$

$$\Delta\gamma_\phi[r, \bar{n}_\mathrm{d}] = \frac{2\chi^2[r]}{\kappa}\left(1 + 2\sinh^2 r\right)\bar{n}_\mathrm{d}\cosh^2 r\ . \tag{3.63b}$$

We can map the first term to the characteristic dephasing of a qubit dispersively coupled to a hot oscillator [Bertet 2005; Rigetti 2012]. This reveals that the qubit experiences the squeezed bath populating higher Bogoliubov energy levels, as a thermal bath. In principle, this induced decoherence, flagged by [Shani 2022], could be cancelled by injecting conversely squeezed radiation while preserving the interaction enhancement [Leroux 2018; Qin 2018]. The second term features the induced dephasing of a qubit measured by an amplified coherent drive on the oscillator, plus a cross term related to the equivalent BO thermal population.

Beyond the TLS approximation We extend the previous result to the qubit transition of a transmon:

$$\Delta\omega_q[r] = \delta_q^{(2)}[r] + \chi_{t:0}[r]\sinh^2 r - \frac{1}{2}\chi_0\ , \tag{3.64a}$$

$$\Delta\omega_q[r, \bar{n}_\mathrm{d}] = \chi_{t:0}[r]\bar{n}_\mathrm{d}\cosh^2 r\ , \tag{3.64b}$$

and:

$$\Delta\gamma_\phi[r] = \frac{\chi_{t:0}^2[r]}{\kappa}\sinh^2 r\left(1 + \sinh^2 r\right)\ , \tag{3.65a}$$

$$\Delta\gamma_\phi[r, \bar{n}_\mathrm{d}] = \frac{2\chi_{t:0}^2[r]}{\kappa}\left(1 + 2\sinh^2 r\right)\bar{n}_\mathrm{d}\cosh^2 r\ . \tag{3.65b}$$

3.4.3 Qubit spectroscopy in the presence of squeezed photons

Even in the absence of a measurement drive on the BO, its squeezing is expected to affect the qubit spectral properties (Eqs. 3.62a and 3.63a). In the following, we show experimental evidence of this effect, by probing a transmon while continuously squeezing a BO. We use a qubit-oscillator detuning of $(\delta_q - \delta_{\mathrm{a}})/2\pi = -100$ MHz, thus placing the system in the weak dispersive regime $\chi_t[r=0]/2\pi = -250$ kHz.

The pump detuning is set to $\delta_{\mathrm{a}}/2\pi = 30$ MHz. For increasing two-photon pump amplitudes inducing up to 8 dB of squeezing, we acquire the qubit reflection spectrum through its dedicated port. On Fig. 3.12a we plot the transmon response in the complex plane (top) and its modulus (bottom). As the power increases (according to the color code referenced to the x-axis of panel b) we witness two effects. First, the amplitude response shifts (see inset of bottom panel), as a consequence of the transmon resonant frequency moving. Second, the complex response circle shrinks and the amplitude response broadens, as a consequence of the induced dephasing on the transmon. The data (open circles) is fitted to circles in the complex plane (solid lines) (section 3.1.2). We extract the magntiude of the qubit frequency shift and linewidth broadening at every pump power, and plot them on Fig. 3.12b, referenced to $S = 0$ dB (pump off). While the transmon frequency shift displays a clear trend, the induced dephasing signal only takes out from the noise at high squeezing amplitudes. Indeed, the bare linewdith of the transmopn being $\gamma_t/2\pi = 9.4$ MHz, broadenings of less than 0.5 MHz cannot be consistently resolved. Finally we plot the expected trend as solid lines using Eqs. 3.64a and 3.65a with no fit parameter. It shows a qualitative agreement with the data.

We reproduce the same experiment for various pump detunings $\delta_{\mathrm{a}}/2\pi \in \{0, \pm 20, \pm 30, \pm 40\}$ MHz. For $\delta_{\mathrm{a}} = 0$ (Fig. 3.13 left) we reproduce the data of Fig. 3.11. There, the balance of resonant two-photon pumping and dissipation stabilizes a squeezed steady-state. At maximal steady-state anti-squeezing, the oscillator mean occupancy is found to be of less than 2 photons[8]. Hence, the variations of $\Delta\omega_q$ and $\Delta\gamma_\phi$ are consistent with a constant dispersive interaction strength. This is in stark contrast with the case $|\delta_{\mathrm{a}}| \gg \kappa/2$, where the two-photon pump is balanced, not by dissipation, but by the detuning δ_{a}. Three notable features are visible in Fig. 3.13 right. First,

---

[8] Using formulas of section 2.1, one can show that when $\delta_{\mathrm{a}} = 0$ then $\langle \mathbf{a}^\dagger \mathbf{a} \rangle = (\sqrt{G} - 1)/4$. At maximal steady-state anti-squeezing, $G < 18$ dB so that $\langle \mathbf{a}^\dagger \mathbf{a} \rangle < 1.75$.

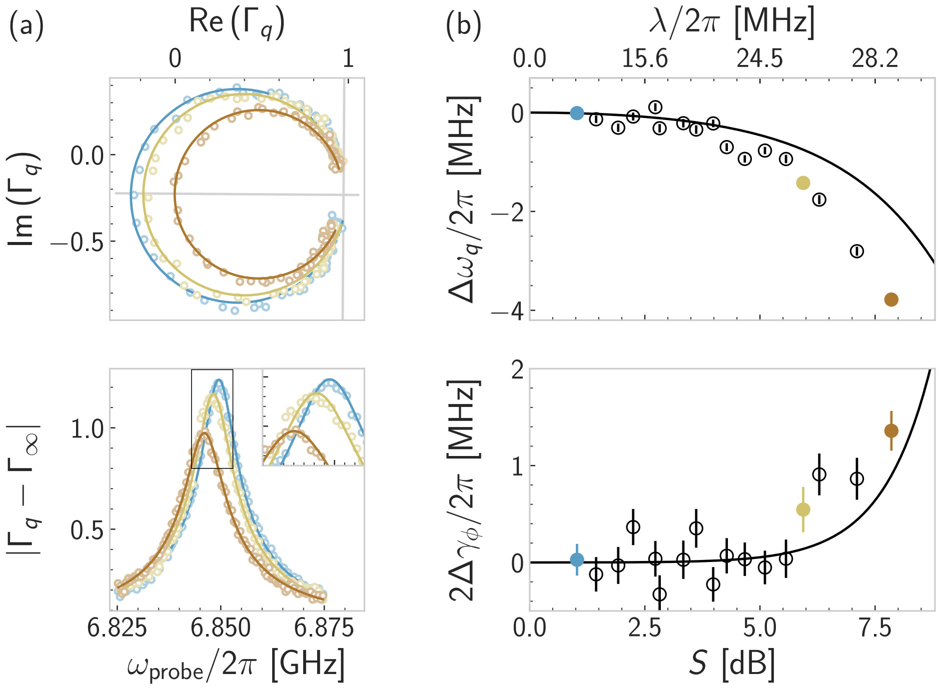

Figure 3.12 Spectral response of a qubit interaction with squeezed photons at $\delta_{\text{a}}/2\pi = 30$ MHz. See description main text.

for each detuning, as the pump amplitude approaches the instability point $\lambda = |\delta_{\text{a}}|$ where the squeezing parameter $r = \frac{1}{2}\tanh^{-1}\lambda/|\delta_{\text{a}}|$ diverges, we observe rapidly increasing frequency shifts and line broadenings, as detailed in Fig. 3.12. Second, the symmetry between positive and negative detunings is broken. Indeed, the BO frequency shifts towards the qubit for $\delta_{\text{a}} > 0$ and away from the qubit for $\delta_{\text{a}} < 0$. Interestingly, despite this asymmetry, the qubit frequency shifts down with increasing λ, regardless of the sign of δ_{a}, showing that the dominant effect at play is the BO enhanced fluctuations, and not a trivial modulation of the BO-qubit detuning. Finally, the magnitudes of the qubit spectral shift and broadening are large. At maximal squeezing, the qubit frequency shifts by at least 4 times the bare qubit-BO dispersive coupling. Such large shifts cannot be explained by an unchanged interaction strength and a simple increase in the BO population. Indeed, we estimate $\sinh^2 r \leqslant 1.2$ over this entire data-set, thus hinting towards a significant enhancement of the qubit-BO interaction strength.

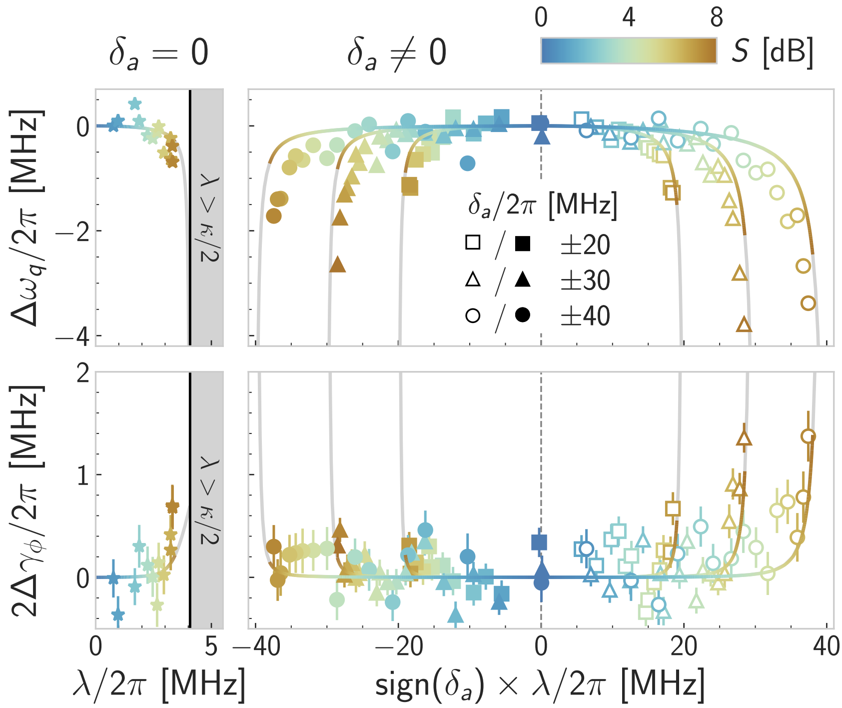

Figure 3.13 Spectral response of a qubit interacting with a DPO. Left: The pump frequency is set to $\omega_\mathrm{p} = 2\omega_\mathrm{a}$. Top (Bottom): qubit frequency shift (induced dephasing) versus pump amplitude (x-axis). The data (stars) are fitted with analytical expressions (solid lines) adapted from [Eddins 2019] (section 3.3). The shaded area marks the instability region. Right: same as left panels with the pump frequency set to $\omega_\mathrm{p} = 2\omega_\mathrm{a} - 2\delta_\mathrm{a}$, where $\delta_\mathrm{a}/2\pi \in \{\pm 20, \pm 30, \pm 40\}$ MHz. The solid lines correspond to Eqs. 3.64a and 3.65a with not fit parameter. A common colormap for the left and right panels maps the pump amplitude to an equivalent squeezing (steady-state anti-squeezing) for $\delta_\mathrm{a} \neq 0$ ($\delta_\mathrm{a} = 0$) in decibels.

3.4.4 Enhancing the dispersive interaction via anti-squeezing

Finally, using Eqs. 3.64b and 3.65b together with the photon-number calibration P_0, we extract the dispersive interaction strength from the suscpetibility of the transmon to a coherent drive resonant with the BO.

First we detail this procedure for $\delta_\mathrm{a}/2\pi = 20$ MHz on Fig. 3.14. For increasing two-photon pump power, triggering up to 5.8 dB of squeezing, we record the transmon relfection spectrum in the presence of an increasing resonant drive power on the BO. Top panels of Fig. 3.14a display the amplitude response for $S = 1.9, 2.9, 5.3$ dB (left, center, right). The color represents the number of injected photons by the resonant drive $\bar{n}_\mathrm{d} = \sqrt{P_\mathrm{drive}/P_0}$, as indicated on the x-axis of the bottom panels. The data (open circles) is fitted to circles in the complex plane (solid lines) (section 3.1.2), and the insets zoom-in on the peaks demonstrating the fit accuracy. The fitted values of the frequency shift and linewidth broadening referenced to the undriven case (but with the pump on), $\Delta\omega_q[r, \bar{n}_\mathrm{d}]$ and $\Delta\gamma_\phi[r, \bar{n}_\mathrm{d}]$, are plotted on the middle and bottom panels of Fig. 3.14 a. Using Eqs. 3.64b and 3.65b, we reconstruct the dispersive interaction strenght, and plot it on Fig. 3.14 b left. The full data record of 72 measurement runs (grey square) is coarse-grained (black squares), and compared with the analytical expression for the dispersive interaction with a transmon (Eq. 3.56c).

We reproduce the same experiment for various pump detunings $\delta_\mathrm{a}/2\pi \in \{0, \pm 20, \pm 30, \pm 40\}$ MHz. The left panel reproduces the data of Fig. 3.11 when $\delta_\mathrm{a} = 0$, that shows no enhancement in χ as expected by theory. The right panel displays χ versus λ in the BO regime $|\delta_\mathrm{a}| \gg \kappa/2$. As previously observed in Fig. 3.13, the symmetry between positive and negative detunings is broken. This is expected since two different effects contribute to the variation of χ_t with squeezing. First, the enhanced fluctuations of the BO result in an enhanced interaction strength, revealed by the $\cosh^2 r, \sinh^2 r$ factors in Eq 3.56c . This effect is independent of the sign of δ_a. Second, as the BO is squeezed, its frequency $\Omega_\mathrm{a}[r]$ varies thus modifying the qubit-BO detuning. It is this effect that depends on the sign of δ_a. For positive pump detunings (empty symbols), the BO shifts towards the qubit so the two contributions add, resulting in a significant increase in χ_t. We measure up to a two-fold increase in χ_t for $\delta_\mathrm{a}/2\pi = +20$ MHz, from $\chi_t/2\pi = -250$ kHz to $\chi_t/2\pi = -510$ kHz at $\lambda/2\pi = 17$ MHz corresponding to $S = 5.5$ dB of squeezing. Only 15% of this increase is attributed to the reduced qubit-BO detuning. The converse is true for negative pump detunings (full symbols): the BO moves away from the qubit. Remarkably, the effect of

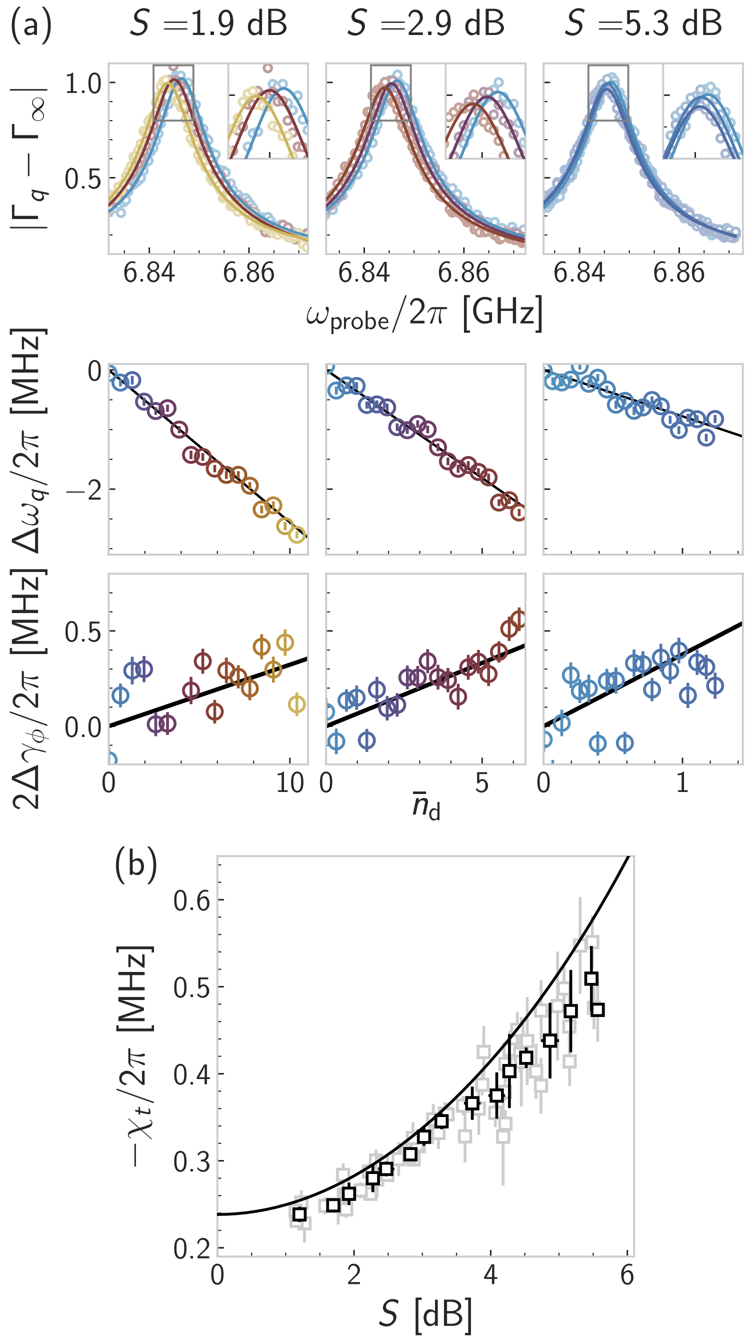

Figure 3.14 Dispersive interaction of a qubit with squeezed photons at $\delta_\text{a}/2\pi = 20$ MHz. See description main text.

enhanced fluctuations outweighs the effect of increased detuning, resulting in a measurable, yet modest, increase in χ_t even for negative detunings. The matching of theory to data noticeably degrades at large $+|\delta_\mathrm{a}|$, possibly due to the narrowing proximity of the idler peak to the qubit.

Out of the maximum two-fold increase of the dispersive interaction strength, 85% can be attributed to the squeezing. Neglecting the idler contribution proportional to $\sinh r$ in Eq. 3.51a would translate into a 1.3-time enhancement of the coupling strength g. This modest increase comes as a proof of concept of the potential of BOs in cQED.

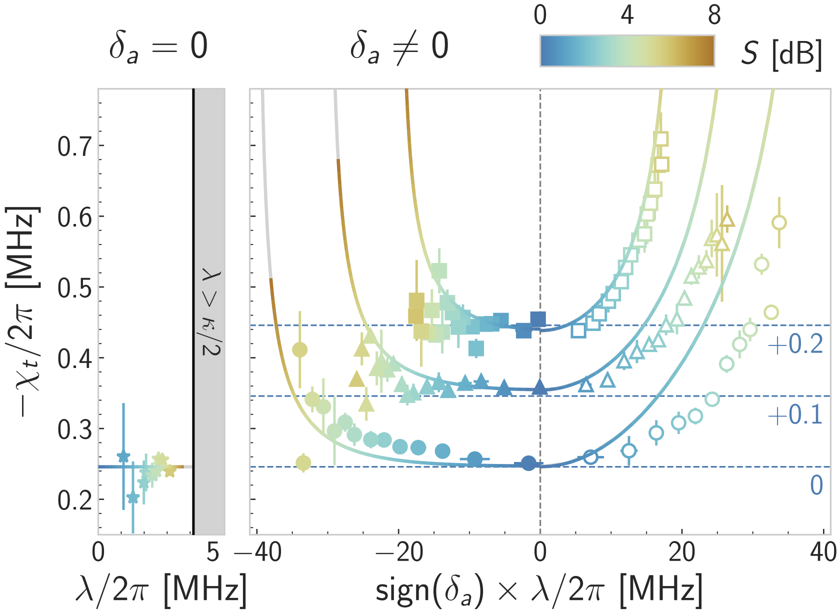

Figure 3.15 Dispersive interaction of a qubit with a DPO. Left: the pump frequency is set to $\omega_\mathrm{p} = 2\omega_a$. The dispersive interaction strength (y-axis) does not increase with the two-photon pump amplitude (x-axis). The solid line marks the bare dispersive coupling. Right: same as left panel for $\delta_\mathrm{a}/2\pi \in \{\pm 20, \pm 30, \pm 40\}$ MHz, where families of same $|\delta_\mathrm{a}|$ (squares, triangles, circles) are offset by $\{0.2, 0.1, 0\}$ MHz for clarity (empty symbols for $\delta_\mathrm{a} > 0$, full symbols for $\delta_\mathrm{a} < 0$). Solid lines correspond to Eq. 3.56c. A common colormap for the left and right panels maps the pump amplitude to an equivalent squeezing (steady-state anti-squeezing) for $\delta_\mathrm{a} \neq 0$ ($\delta_\mathrm{a} = 0$) in decibels.

4

OPERATING CIRCUIT-QED SYSTEMS

Quantum systems are fragile by nature. In the wake of the research surrounding quantum information technologies, there has been a growing interest in all topics related to their shielding from spurious noise sources. The target is a bit paradoxical. On the one hand, we wish to create highly coherent quantum systems to store and process information. But on the other hand, we seek a high level of control which requires the introduction of many connections to the outside world, and as many channels of decoherence [Devoret and Schoelkopf 2013]. Among all the competing platforms for quantum information processing, superconducting circuits offer a high level of controllability. The prime reason is their completely artifical nature, which enables tuning of each of their constituing parameters. They also benefit from the inherent versatility of electrical circuits, which are meant to combine core elements in bigger modules of higher complexity. This modular approach lead to the successful integration of arrays of hundred(s) of qubits on a single processor [Ball 2021]. There, the redundancy of large arrays is expected to protect information on timescales greater than the ones of individual qubits. Bringing so many quantum systems on a single processor, maintaining their indiviual coherence properties, is an outstanding achievement. Yet so far, the benefits of redundancy did not quite meet the price paid for complexity [Krinner 2022; Google Quantum AI 2023].

Alongside the quest for the integration of large qubit-arrays, the versatility and high sensitivity of superconducting circuits is also leveraged to study hybrid systems (section 1.2). Electromagnetic (EM) forces are ubiquitous from atomic to macroscopic scales, so that the range of systems coupling to superconducting EM oscillators is unprecedented. Since all these hybrid-cQED experiments share a common tool, they also require common hardware for their operation. This chapter presents some of the challenges faced by the integration of superconducting circuits in an experiment.

4.1 Preliminary remarks

4.1.1 Architecture overview

All the flavors of cQED share a few key elements required for the operation of superconducting circuits. In the following, we will focus on 2-dimensional architectures in coplanar-waveguide (CPW) geometry. There, the circuit modes are delimited by superconducting thin films deposited on top of a flat substrate, constituing the *sample*. The sample needs to be operated at cryogenic temperatures, typically in a dilution refrigerator ($T \leqslant 20$ mK). Mounting the sample in the cryostat requires a *microwave-package*. It features the following elements:

- The interposer hosts the sample. It typically consists of a printed circuit board (PCB), wirebonded to the sample on its inner side and connectorized on its outter side. It conveys electrical signals between microscopic circuit features and macroscopic lines. For a CPW sample, the PCB is usually also CPW, or CPW with ground [Pozar 2011].
- The sample-holder hosts the interposer. It takes the form of a metallic casing, well-anchored to the lowest temperature stage of the cryostat.

An extensive discussion on microwave-package design will be presented in section 4.2. As for the sample, a standard fabrication recipe will be detailed in section 4.3.

Next, the microwave-package is connected to signal lines, such that:

- On the descent path, filters are inserted to prevent noisy signals from reaching the circuit.
- On the ascent path, amplifiers are inserted to make the most of the tiny signals output by the circuit.

The design and typical performances of a quantum-limited parametric amplifier will be discussed in section 4.4.

As for the rest of the wiring diagram, it is detailed on Figure 4.1. We use the four channels of a Keysight PNA N5222A to measure the reflection spectra of the resonator and transmon ports, denoted Γ_a and Γ_q respectively. Two DC current sources Yokogawa GS200 are used to bias the flux loops of the SNAIL and the SQUID with fluxes Φ_a and Φ_q. The Traveling Wave Parametric Amplifier (TWPA) provided by the group of W. Oliver at Lincoln Labs is powered by a R&S SGS100A. It amplifies the transmon signal by about 20 dB away from its dispersive feature at 6.0 GHz. The tone that pumps the SNAIL is provided by an Agilent Technologies E8257D and travels to the sample either through the resonator PNA drive line, or through

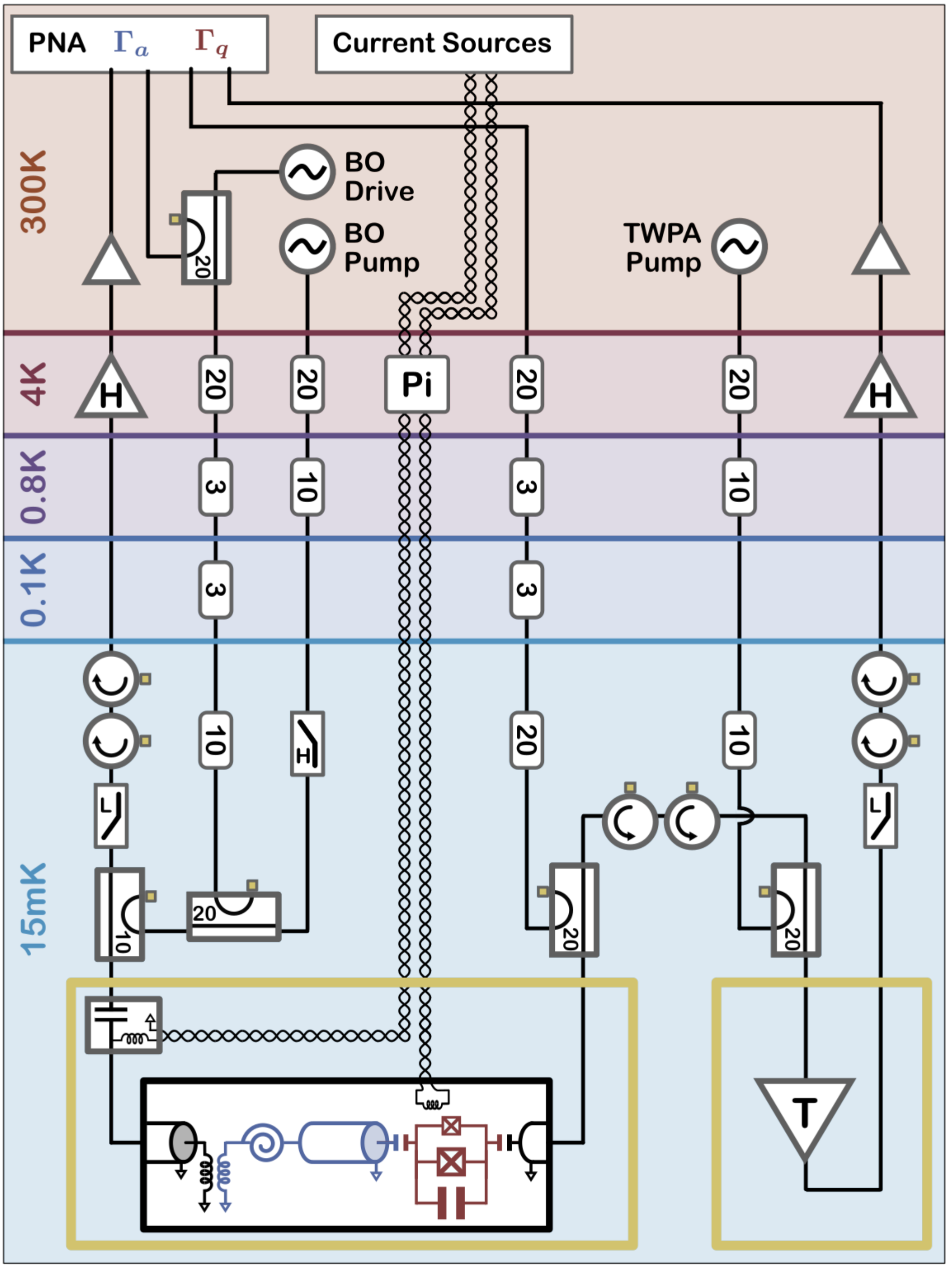

Figure 4.1 Experimental wiring

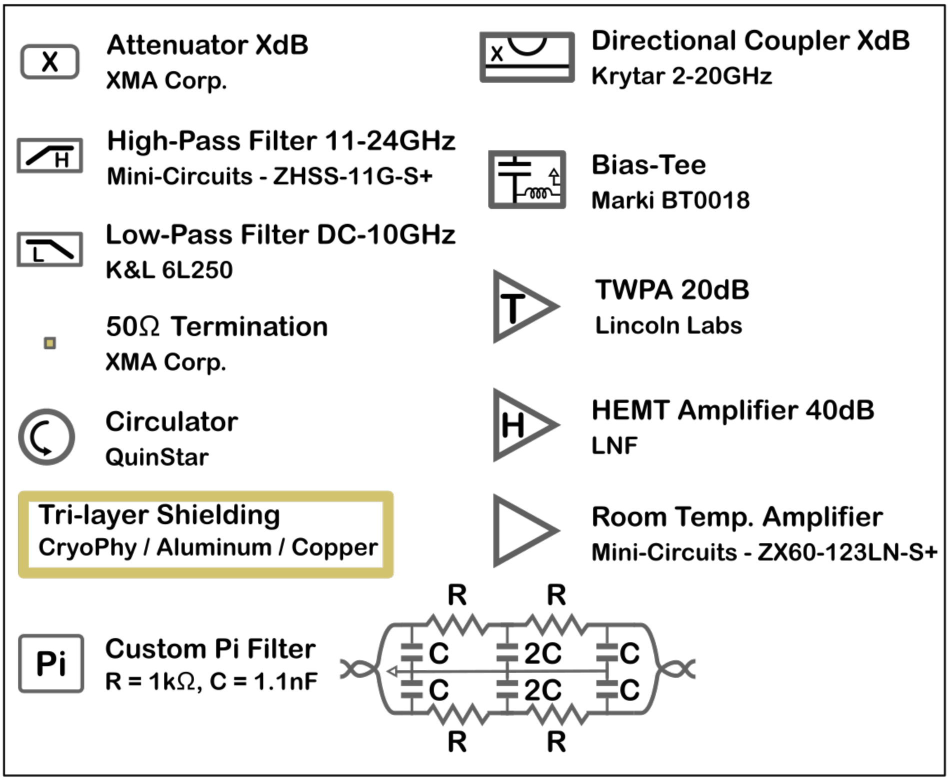

Figure 4.2 Experimental wiring - legend

a distinct one. In order to maximize the amount of pump power reaching the sample around the parametric resonance $\omega_{\mathrm{p}}/2\pi \approx 14$ GHz, without giving up on line attenuation at the resonance frequency $\omega_{\mathrm{a}}/2\pi \approx 7$ GHz, we designed a dedicated microwave line for the pump. It includes a smaller amount of flat attenuation than the drive line, but features a high-rejection high-pass filter, with a pass-band from 11 GHz to 24 GHz. This pump line displays around 26 dB less attenuation than the drive line above 11 GHz, while maintaining sufficient attenuation around the oscillator frequency. These two orders of magnitude were crucial to approach instability in the BO regime $\lambda \sim |\delta_{\mathrm{a}}| \gg \kappa/2$, without heating up the cryostat. Finally a R&S SMB100A provides the coherent drive on the resonator injecting photons to calibrate the dispersive interaction strength. All instruments are referenced to a Stanford Research Systems FS725 Rubidium clock.

4.1.2 Noise sources

What is so scary in the environment that we need to shield our dear superconducting circuit from? This part aims at giving a brief overview of the noise sources detrimental to the operation of superconducting circuits. We will define these sources, give their origins and introduce possible mitigation strategies.

Resonant noise EM fields oscillating near the characteristic frequencies of the circuit can induce spurious transitions. The potentially resonant frequencies range from 10MHz (transition frequency of a low-frequency qubit) to 20GHz (typical plasma frequency of an Aluminium Josephson junction), defining the operating bandwidth of the circuit. Since telecommunication frequencies belong to this bandwidth, it is maximally polluted. Resonant noise can access the sample either through the control lines, or as direct radiations impinging on the substrate.
→ Introducing attenuation in the control lines reduces the noise amplitude reaching the sample. As for direct radiations, they can be absorbed by a good conductor. In a metallic layer, EM radiations decay exponentially on a scale given by the skin depth $\delta_s = \sqrt{2/\omega\mu\sigma}$, where ω is the angular frequency of the noisy signal, and μ, σ are the permeability and conductivity of the medium [Pozar 2011]. For high purity copper[1], typically used as a mechanical support, we find $\delta_s[10\text{ MHz}] = 2.3\ \mu\text{m}$ and $\delta_s[20\text{ GHz}] = 50$ nm.

High-frequency noise The superconducting material delimiting the circuit modes has an intrisic energy scale $\boldsymbol{\Delta}$, giving the pairing energy of a Cooper pair[2]. Any EM radiation above this frequency is likely to break Cooper pairs in the metallic film, hence creating quasiparticles that could be detrimental to the coherence of the circuit modes [Wang 2014; Wilen 2021]. While the quasiparticle density in superconducting circuits is known to exceed the theoretically expected value by orders of magnitude [Visser 2011], their dominant generation mechanism is still under debate.
→ Dedicated infrared filters based on dielectric absorbents can be used to damp high-frequency noise propagating along the control lines [Serniak 2019; Danilin 2022]. As for direct radiations, a thin layer of a good conductor can again absorb these noisy fields. But one needs to be very careful with the

---

[1] With a residual-resistance ratio (RRR) of about a hundred: $\sigma_{\text{Cu}}^{100}[0\text{K}] = 5.10^9\text{S.m}^{-1}$

[2] $\boldsymbol{\Delta}$ is the pairing energy, or half the superconducting gap width: $\boldsymbol{\Delta}_{\text{Al}}/h \approx 40\text{GHz}$, $\boldsymbol{\Delta}_{\text{Ta}}/h \approx 170\text{GHz}$, $\boldsymbol{\Delta}_{\text{Nb}}/h \approx 370\text{GHz}$

overall light-thightness of the conductive enclosure: any seam or opening will let radiations with a shorter wavelength go through [Connolly 2023]. Coating metallic shields with absorbing materials has also been tested to limit exposure to infrared radiations [Kitzman 2022].

Stray electric fields Any isolated metallic island can acquire a DC offset charge, fluctuating over time. For multiple disjoint islands, the independent offset charges translate into noisy differential potentials. If the circuit mode of interest participates into several islands, these noisy potentials may affect its dynamical properties. This mechanism is called *charge noise*.
→ Regardless of the structure of the circuit mode – which can be engineered to eradicate the influence of charge noise [Koch 2007; Yan 2016] – it is essential to provide a stable charge reference for the circuit. Through the interposer, the circuit-ground is typically connected to the fridge skeleton which has a gigantic capacitance.

Stray magnetic fields Similarly to the charge noise argument, if the circuit mode of interest participates into a metallic loop, it will be imparted by noisy stray magnetic fields. This mechanism is called *flux noise*. The presence of macroscopic stray magnetic fields – such as the ones emanating from a nearby ferrite circulator, or the subway going under the laboratory building – obviously contributes to flux noise. In addition it is also the product of microscopic mechanisms, whose understanding is a longstanding goal of the field [Wellstood 1987].
→ In order to limit the amplitude of macroscopic stray fields, magnetic shields can be placed around or within the sample holder. They typically include a layer of a high-μ material surrounded by a thick type-I superconductor[3]. Also, the use of magnetic materials in the vicinity of the sample must be avoided. Thus, hybrid systems whose operation requires magnetic fields such as spin qubits hardly lives with flux-tunable devices.

Material sources The dominant source of decoherence for superconducting circuits lies in in their constituing materials, and consists in any degree of freedom with a finite suscpetibility to EM fields. Dielectric residues such as organic contaminant or oxyde layers accelerate energy relaxation [Woods 2019]. Similarly, gaseous adsorbents in the vicinity of superconducting loops may be responsible for flux noise [Kumar 2016; Aquino 2023].

---

[3] Note that the high-μ material needs to be inside the superconductor, and not the opposite [Krieger 2015].

→ Mitigation of material sources of decoherence can primarily be addressed through the optimization of the fabrication process [Woods 2019]. It includes various cleaning steps, before and after metallic deposition. It also consists in finding the materials which naturally grow with fewer deffects, such as recently introduced Tantalum whose oxyde is of higher quality than Niobium [Place 2021]. Finally, vacuum-tight packages have also been tested to limit gaseous contamination [Mergenthaler 2021].

Many tricks can be played to isolate the circuit from spurious noise sources. From the previous listing it is clear that a good Faraday cage – good meaning thick enough, seamless and well grounded – will prevent most of the EM spectrum to interact with the system. If no global magnetic field is required to adress the experiment, magnetic protection can also be advantageous. While the sample-holder and extra shields can readily address these issues, how must we design these parts to avoid adding extra decoherence channels?

4.2 Packaging free of package modes

The sample-holder is the mechanical support of the microwave-package assembly, tightly anchored to the cryostat base plate. It is metallic, typically made ouf ot high-purity copper, acting both as a Faraday cage, and a cold source for the interposer. It is also the closest mechanical structure from the sample, thus the one that needs to be designed with the greatest care.

As we are building a tight conductive enclosure around the sample, we are also shaping the density of states of its environment, singling out a few modes. These so-called *package* modes can interact with the sample circuit modes, and limit their coherence. This part is dedicated to the description of these package modes, and the demonstration of their detrimental effect on the system. Finally, we will present the Joint Assembly for the Wiring of Superconducting circuits (JAWS), a microwave-package design developped over the course of this thesis.

4.2.1 Package modes: where are they?

The CPW architecture features a top ground plane, delimiting the circuit modes of interest. There exists two types of package modes: the ones living in the substrate below the ground plane, dubbed *chip modes*, and the ones living in vacuum above the ground plane, dubbed *box modes*. Depending on the structure of the interposer, the chip modes can also extend away from the substrate.

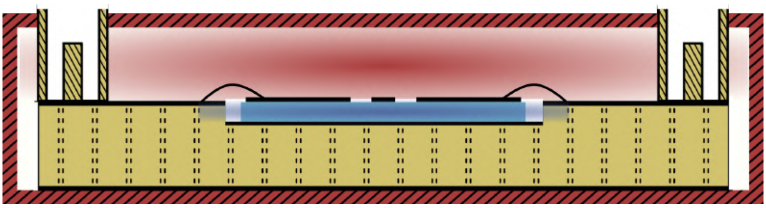

Figure 4.3 Sample-holder first guess and package modes. The sample (blue) sits in a pocket dug in the interposer (yellow), held by the sample holder (red). The interposer is connectorized with coaxial launchers on its outter rim (yellow), and wirebonded to the sample on its inner side (black). All the conductive parts are marked in black (either full lines, or dashes or stripes). The chip (box) modes live in the blue (red) shaded region.

As a concrete example, we consider the package design sketched on Fig. 4.3. If features a hollow sample-holder, holding an interposer in a CPW with ground geometry. It is also pierced with conductive vias. The sample is glued in a metallized pocket dug in the interposer dielectric. As a consequence, the chip modes are confined to the substrate only, and the box modes extend to the entire empty part of the package. This design first-guess is not irrational. Placing the interposer in a hollow sample-holder is mechanically reliable and easy to implement. Piercing the interposer with conductive vias is very standard for isolation of the signal lines. Finally, metallizing the back of the sample pocket is a fair choice: it ensures a wide surface contact between the sample and the interposer, which ought to be beneficial for thermalization purposes[4]. Yet so far, the location of the package modes – both in space and frequency – has not been taken into account.

---

[4] While the question of the sample thermalization will not be addressed in this thesis, we report the interested reader to [Swartz and Pohl 1989] for a historical review on thermal boundary resistance.

4.2.2 Package modes: who are they?

In this configuration, the chip and box modes resemble the ones of a rectangular dielectric cavity, coated in metal. In the following we present analytical results for such a cavity, that will let us estimate the package mode properties.

Following [Pozar 2011], the modes of a rectangular cavity with dimensions L_x, L_y, L_z are defined by three integers (m, n, l). Their resonant frequencies read:

$$\omega_{m,n,l} = \frac{c}{\sqrt{\mu_r \varepsilon_r}} \sqrt{\left(\frac{\pi m}{L_x}\right)^2 + \left(\frac{\pi n}{L_y}\right)^2 + \left(\frac{\pi l}{L_z}\right)^2}, \tag{4.1}$$

where c is the speed of light in vacuum and ε_r (μ_r) is the relative permittivity (permeability) of the cavity. In the absence of magnetic materials, dissipation of the EM field is mediated either by dielectric or conductive effects. The total quality factor reads:

$$\frac{1}{Q_{\text{tot}}^{m,n,l}} = \frac{1}{Q_{\text{diel}}^{m,n,l}} + \frac{1}{Q_{\text{cond}}^{m,n,l}}, \tag{4.2}$$

where $Q_{\text{diel}}^{m,n,l}$ and $Q_{\text{cond}}^{m,n,l}$ are the dielectric and conductive quality factors. The dielectric quality factor reads:

$$Q_{\text{diel}}^{m,n,l} = Q_{\text{diel}} = \frac{1}{\tan\delta}. \tag{4.3}$$

Notably for a rectangular cavity, this contribution does not depend on the mode geometry. It defines the inverse of the $\tan\delta$ parameter. As for conductive losses, they read:

$$Q_{\text{cond}}^{m,n,l} = 2\pi \frac{V_{m,n,l}}{\lambda_{m,n,l}^3} \frac{Z_0}{R_s} \sqrt{\frac{\mu_r}{\varepsilon_r}}, \tag{4.4}$$

where $Z_0 = \sqrt{\mu_0/\varepsilon_0}$ is the impedance of vacuum, $R_s = (\sigma\delta_s)^{-1}$ is the surface resistivity of the metallic coating, $\lambda_{m,n,l} = 2\pi c/\omega_{m,n,l}$ is the mode wavelength, and $V_{m,n,l}$ the effective mode volume. For a flat substrate ($L_x, L_y \gg L_z$), the lowest frequency modes are of the form $(1, n, 0)$ and $(m, 1, 0)$. The wavelengths and mode volumes for $(1, n, 0)$ read:

$$\lambda_{1,n,0} = \frac{2L_x L_y}{\sqrt{nL_x^2 + L_y^2}}, \qquad V_{1,n,0} \approx \frac{2L_x L_y L_z}{n^2 L_x/L_y + L_y/L_x}.$$

Formulas for $(m, 1, 0)$ are the same upon exchange of n by m and L_x by L_y. Specifically when $L_x = L_y$, we find $\lambda_{1,1,0} = \sqrt{2}L_x$ and $V_{1,1,0} \approx L_x^2 L_z$.

The substrate is covered in superconducting material on its top part, and rests on the metallized interposer pocket. Then, the chip modes are confined to the substrate (neglecting their extension in the volume of interposer before the first line of vias). For a silicon slab ($\varepsilon_r = 11.9$ and $\mu_r = 1$) of size $L_x \times L_y \times L_z = 11 \times 10 \times 0.3$ mm ^{3}, the fundamental mode resonates at $\omega_{110}/2\pi = 5.9$GHz. It falls exactly within the operating bandwidth of superconducting circuits. Conductive losses for the chip modes occur mostly in the metallic coating of the interposer pocket. For an interposer covered in electrodeposited gold[5], we find at the fundamental frequency $R_s \approx 8$ mΩ, so that $Q^{110}_{\mathrm{cond}} \approx 3.10^3$. In addition, high-resistivity silicon typically has $\tan\delta \approx 3.10^{-7}$, so that $Q_{diel} \approx 3.10^6$. Thus the overall quality factor of the fundamental mode is dominated by the conductive losses at the PCB interface, and its linewidth is $\kappa_{110}/2\pi \approx 2$ MHz.

As for the box modes, their properties strongly depend on the inner shape of the sample-holder cover. Yet, we can expect to find them in the same frequency range, and with similar coherences as the chip modes.

4.2.3 The risk of uncontrolled package modes

Let us imagine that we succeeded in fabricating a state-of-the-art qubit on the sample, with a coherence time exceeding 100 μs. What is the influence of a parasitic mode, for instance one of the package modes, on its coherence properties?

We use the Jaynes-Cummings model to estimate the impact of the parasitic mode – playing the role of the oscillator **a** – on the qubit (section 3.2.1). We denote Δ the detuning between both modes, and g their resonant coupling strength. As the fundamental chip mode frequency lies in the middle of the operating bandwidth of the circuit, it is credible – yet unlucky – that both modes are on resonance. If not, the detuning can be as high as a few GHz. Experiments have shown that the coupling strength can be as high as 10 MHz [Huang 2021]. In addition, as cQED experiments typically feature a collection of coherent tones applied on the system, the probability of driving a package mode is non-negligible. In that case, it would be populated with a finite number of coherent photons $\bar{n}_{\mathrm{d}}$. Finally, we denote $\bar{n}_{\mathrm{th}}$ the parasitic mode thermal population.

First, the qubit will be affected by dressed decoherence mechanisms. As introduced in section 3.2.1, in the dispersive limit $g \ll \Delta$, the qubit

---

[5] Electrodeposited gold typically has RRR=10, so that $\sigma^{10}_{Au}[0\mathrm{K}] = 4.10^8$ S.m^{-1} [Bernat 2007]

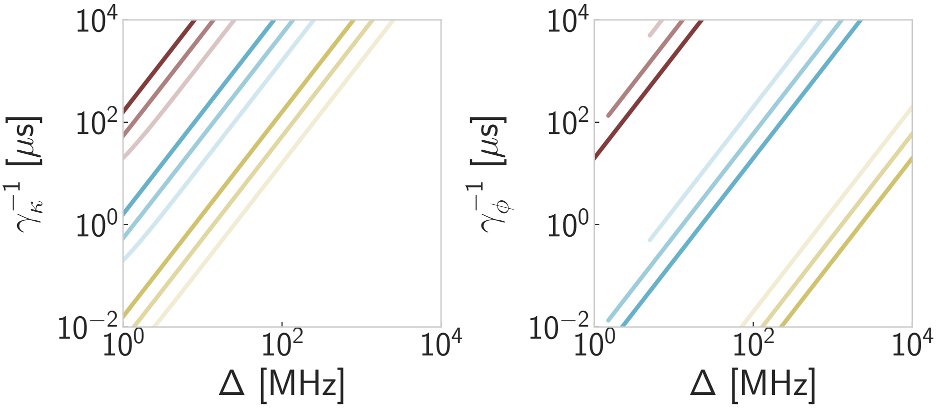

Figure 4.4 Coherence limitation inherited from parasitic modes. Purcell relaxation time (left) and induced dephasing time (right) versus the detuning between the qubit and the parasitic mode, for $g/2\pi \in \{0.1, 1, 10\}$ MHz (red, blue, yellow), and $\kappa/2\pi \in \{0.1, 0.3, 1\}$ MHz (dark to light colors) for $\bar{n}_\mathrm{d} = 1$ and $\bar{n}_\mathrm{th} = 0$. Notably the Purcell relaxation time decreases with κ, while the induced dephasing time increases with κ.

relaxation rate is enhanced by the so-called Purcell contribution. This result can actually be extended to the weak-resonant limit $\Delta \ll g \ll \kappa$. There, the Purcell decay rate induced by the parasitic mode on the qubit reads [Bienfait 2016]:

$$\gamma_\kappa = \frac{g^2\kappa}{\Delta^2 + \kappa^2/4} \ . \tag{4.5}$$

Note that for stronger couplings, hybridization of the modes at resonance leads to a non-perturbative redefinition of their spectral properties (section 3.1.3). Second, a finite population in the parastic mode will dephase the qubit. Given the moderate reported couplings to package modes, we limit the discussion to the weak-dispersive limit $\chi_0 = g^2/\Delta \ll \kappa$. There, the measurement-induced dephasing rate reads:

$$\gamma_\phi = \frac{2\chi_0^2}{\kappa}\bar{n}_\mathrm{d} + \frac{\chi_0^2}{\kappa}\bar{n}_\mathrm{th}(\bar{n}_\mathrm{th} + 1) \ . \tag{4.6}$$

On Fig. 4.4 we plot the Purcell-limited relaxation times γ_κ^{-1}, and induced-dephasing times γ_ϕ^{-1} of the qubit coupled to a parasitic mode. As expected, these spurious effects are less a limitation for the qubit as g decreases, or Δ increases. That being said, for typical spurious coupling values, while the induced relaxation is only stringent in a narrow frequency span around resonance, the induced dephasing is significant up to large detunings. In addition, the two effects follow inverse trends with κ. Indeed, while dressed decoherence is hindered by a parasitic mode with high coherence, measurement-induced dephasing is enhanced when the parasitic excitations are long-lived.

As a conclusion, the sample-holder design must be driven by a careful shaping of the package-mode distribution, both in space – to reduce their coupling to the circuit modes – and in frequency – to push them as far as possible from the operating bandwidth.

4.2.4 Package mode engineering and lightening effect

Earlier we made a first-guess for the sample-holder design, that lead to the proliferation of parasitic modes in the operating bandwidth of the circuit. How can we engineer these package modes so that they do not limit the performance of the circuit modes?

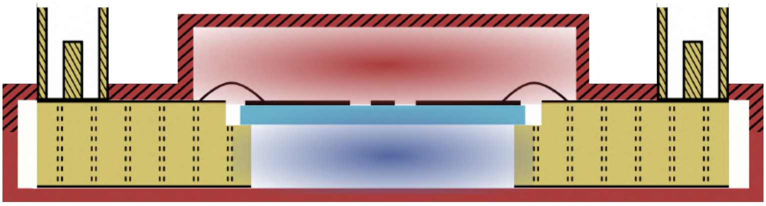

Figure 4.5 Sample-holder educated guess and lightening effect (same coloring as Fig. 4.3). Opening a vacuum gap below the chip draws the chip modes (shaded blue) away from the circuit, while lightening them. Constraining the volume above the chip to its bare minimum increases the box mode (shaded red) frequencies.

The answer is two-fold: the substrate needs to be suspended above vacuum [Lienhard 2019], and the sample-holder cover adjusted to fit the chip footprint (Fig. 4.5). As the conductive layer at the back of the substrate is removed, the chip modes are free to extend in the volume below. If on top of that this volume is free of PCB dielectric – in other words, the substrate is suspended – then the effective permittivity seen by the modes is significantly lessened. As a consequence, we expect the chip mode frequencies to increase as the volume of vacuum below the substrate gets bigger. This effect, that we refer to as *lightening* effect, is rather conterintuitive in the first place: increasing one's mode volume to increase one's frequency? Indeed, given that the substrate is flat ($L_x, L_y \gg L_z$), the lowest frequency modes have

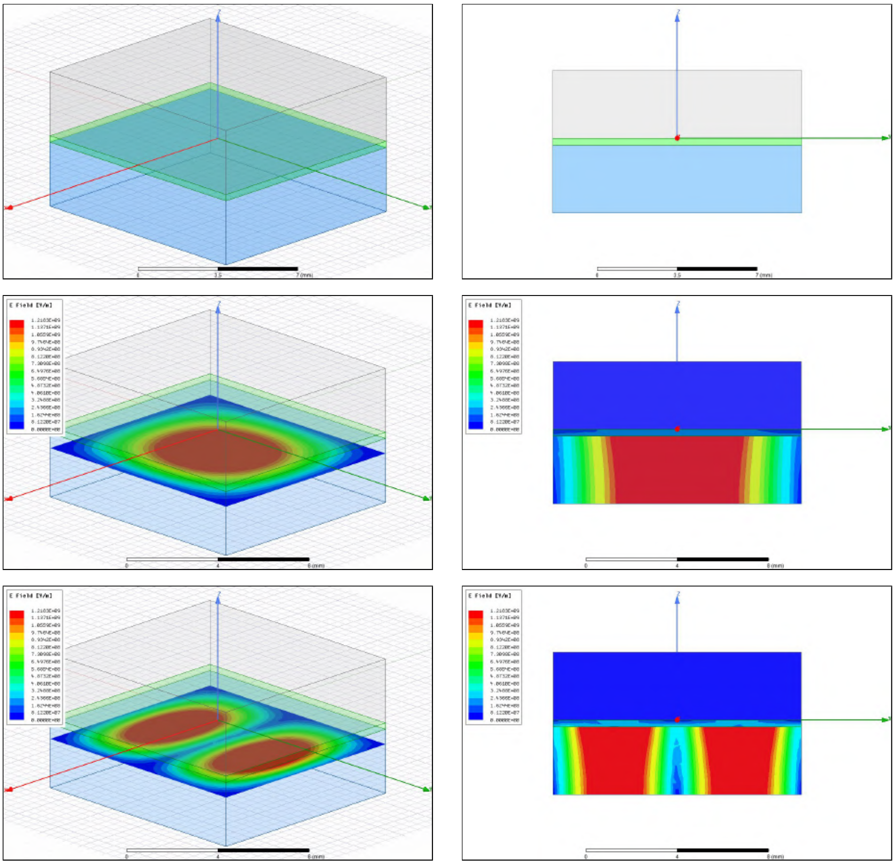

Figure 4.6 The suspended chip, geometry and field distribution. Top: geometry used for simulations. The substrate (green) is a flat silicon slab. A perfect conductor boundary condition is imposed on its top face to mimick CPW geometry. It is surrounded by vacuum from the top (grey) and the bottom (blue). Middle: (110) mode electric field profile, in a dimetric projection with a cut 1 mm below the substrate (left), and in a side-view in the yz-plane (right). Bottom: same for (120) mode. The colorscale displays the electric field from blue (low intensity) to red (high intensity) and is common to all plots.

no deformation in the z-direction. Thus changing the L_z dimension has no geometric impact on their frequencies (see Eq. 4.1), and the dominant effect is the mode lightening.

We check this assertion through EM finite-element simulations of an ideal geometry, namely, the suspended chip (Fig. 4.6 top). It features a flat slab of silicon ($\varepsilon_r = 11.9$) with dimensions $L_x \times L_y \times L_z = 11 \times 10 \times 0.3\ \mathrm{mm}^3$, surrounded by vacuum from above and below, both with the same depth L_{vac}. In order to mimick the CPW geometry, a perfect-conductor boundary condition is imposed on the top surface of the dielectric. First, computing the eigenmodes of this structure reveals the full spatial extent of the chip modes (Fig. 4.6 middle and bottom). In the presence of a vacuum pocket below the substrate, the electric field of the chip modes appears to be much more intense in the pocket than in the substrate (right panels). Second, as L_{vac} is increased from 0.1 mm to 3 mm, the frequencies of the first three chip modes increase significantly, freeing the operating range (Fig. 4.7). The fundamental box mode frequency is not imparted by the depth of the vacuum pocket. Indeed, as it lives completely in vacuum, it is not prone to the lightening effect. Finally, increasing L_{vac} beyond 3 mm does not significantly change the spectrum, up to $L_{\mathrm{vac}} = 10$ mm where the chip and box modes (011) and (101) come into play (not shown).

The coupling strength g between circuit and parasitic modes strongly depends on the geometry of the former. Yet, in a CPW architecture, the circuit modes extend primarily in a close neighboorhood of the substrate surface. Putting aside the symmetries of the modes, their coupling strength grows when their field distributions overlap. Thus, the greater the parasitic modes participate into the substrate, the more likely they are to couple to circuit modes. In order to gauge this overlap, we introduce the energy participation ratio of a mode (m, n, l) into a volume V_k of the system:

$$p^k_{m,n,l} = \frac{\int_{V_k} \varepsilon^k_r |\mathbf{E}_{m,n,l}(\mathbf{r})|^2 \mathrm{d}^3\mathbf{r}}{\sum_i \int_{V_i} \varepsilon^i_r |\mathbf{E}_{m,n,l}(\mathbf{r})|^2 \mathrm{d}^3\mathbf{r}}\,, \tag{4.7}$$

where $k \in \{\text{substrate, bottom pocket, top pocket}\}$, ε^k_r is the realtive permittivity of the volume V_k (assumed to be homogeneous), and $\mathbf{E}_{m,n,l}(\mathbf{r})$ is the electric field distribution of the mode (m, n, l). We plot this quantity for the fundamental chip mode in Fig. 4.7 right. As the depth of the vacuum pocket is increased, the energy stored in the fundamental chip mode is displaced from the substrate to the bottom pocket, which confirms the observation of Fig. 4.6 (middle and bottom right).

As a conclusion, opening a vacuum pocket underneath the substrate not only increases the chip mode frequencies, but also displaces their field lines away from the circuit. Even though the circuit modes are also imparted by this suspended architecture, the CPW geometry being self-sustaining, their geometry is marginally modified. In the end, suspending the chip appears to

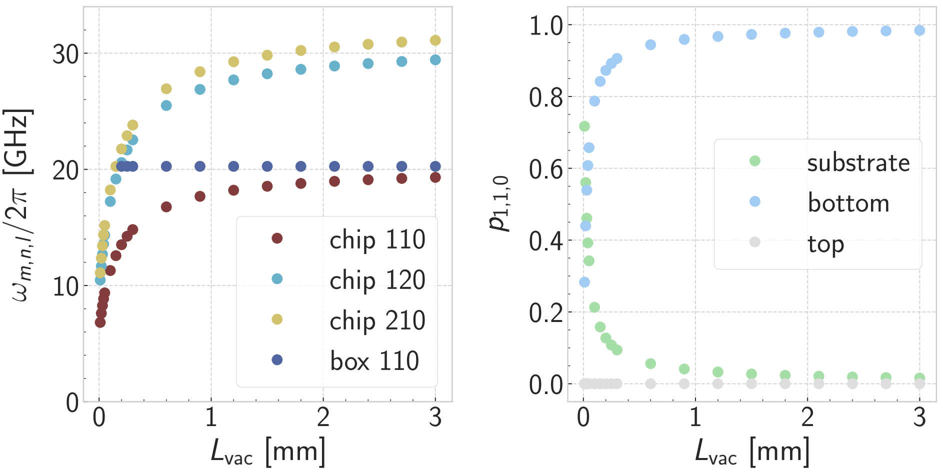

Figure 4.7 The suspended chip, frequency and participation. Left: parasitic mode frequencies (y-axis) versus vacuum depth below and above the substrate (x-axis). Right: participation ratio of the fundamental chip mode (y-axis) in every element of the system (color) versus vacuum depth.

be a winning strategy to free the operating region from spurious modes, and limit their coupling to the circuit modes.

4.2.5 Joint assembly for the wiring of superconducting circuits

The joint assembly for the wiring of superconducting circuits (JAWS)[6] is a microwave-package that was designed with two constraints:

(i) Eradicate spurious modes in the operating bandwidth of the circuit.
(ii) Make a robust package that could be reused from sample to sample, with minimal cycling maintenance.

Following the spurious-mode analysis of the previous sections, fullfilling (i) requires the substrate to be suspended in a tight enclosure. As for (ii), it requires the outter connectors to be mechanically attached to the sample-holder. Indeed, many package designs rely on connectors solely soldered to the interposer. There, after a few cycles, the solder joints are likely to break. At this stage, it is worth mentioning that ignoring (ii) leads quite naturally to the design developped by Will Oliver's group at MIT [Huang 2021].

---

[6] Full credit for Clarke Smith on this one.

What about the shark thing? Before turning to a detailed description of the package geometry, let us take a glance at the design. It features a gold plated copper box, with 6 SMA connectors for microwave signals, and a microD 9-pin connector (aka D-Sub) for DC signals (Fig. 4.8 left). The SMAs are threaded in the outter part of the metallic casing, and the D-Sub is attached by screws. DC signals are routed through wires coming out of the D-Sub, and soldered to the PCB. Microwave signals are routed through glass bead connectors, soldered in stepped-drilled pockets in the box walls. Each glass bead pin sticks out of the inner walls (Fig. 4.8 inset), where they are soldered to the PCB signal lines (soldered not shown on the close up). For each line, two solder joints are also used to ensure ground continuation at the interface. Since it is very hard to solder directly on a bulky piece of metal, two *shark fins* are extruded out of the inner package walls. Their small volume (~ 0.5 mm^3) eases the soldering process to the PCB ground plane. They also gave its name to the microwave-package: JAWS.

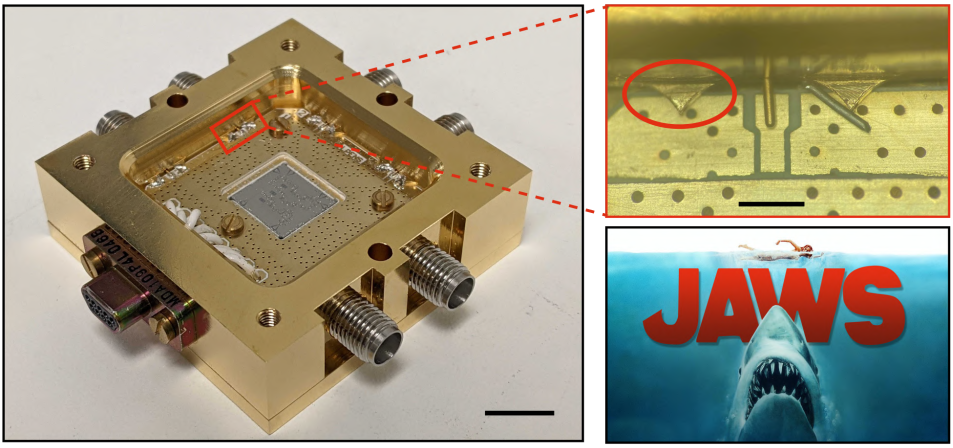

Figure 4.8 JAWS. Left: picture of the JAWS package, without its cover (picture courtesy of Samuel Deleglise). The black bar scales 10 mm. Red inset: close up on the box-to-PCB interface before soldering. The glass bead pin is aligned with the PCB signal line. The left shark fin is highlighted. A metallic rod is placed near the right one, ready for soldering. The black bar scales 2 mm. Bottom right: Roger Kastel's design of JAWS cover, the novel by Peter Benchley (1974) adapted on screen by Steven Spielberg (1975).

Assembly The sample-holder is a 3-story box featuring a top and a bottom part sandwiching a ring (Fig. 4.10). The ring is pierced with holes for DC and microwave connectors. The top and bottom parts are carved as to accomodate 5 mm deep rectangular cavities implementing the lightening effect (section 4.2.4). The PCB is attached to the bottom part with screws, and soldered to the ring through the glass bead pins and the shark fins. This over-constrained design[7] is a necessary evil for the integration of shark fins, which improve impedance matching at the box-to-PCB interface. The PCB is 1.52 mm thick, and is made out of 5 layers of ROGERS 4350B covered in 17 μm of electrodeposited copper with EPIG finish (nickel free). This multi-layer stack is used to distribute DC and microwave signals all around the sample (Fig. 4.9). The PCB is pierced with conductive vias ensuring isolations of the signal lines. The sample sits in a 0.4 mm deep and 11×10 mm^2 wide pocket, milled away everywhere but on 4 rectangular posts.

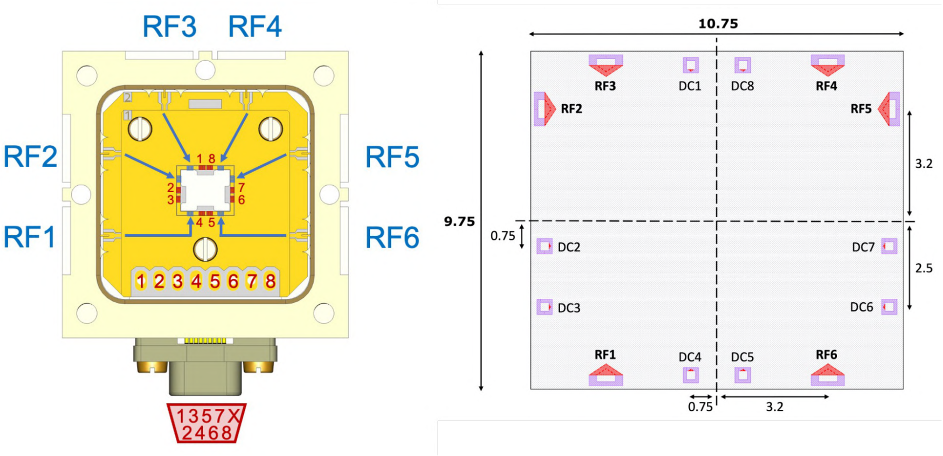

Figure 4.9 JAWS electrical layout. Left: PCB layout of the mapping between outter connectors and inner signal pads, for the microwave (RF) signals in blue, and DC signals in red (picture courtesy of Alex May). Note that the blue arrows do not represent the actual signal paths. Right: chip layout (distances in millimeters).

---

[7] The bottom part is screwed to the ring, the ring is soldered to the PCB, the PCB is screwed to the bottom part. Yet, there is no such thing as all-to-all connectivity in tight mechanical assemblies! One link has to be loose.

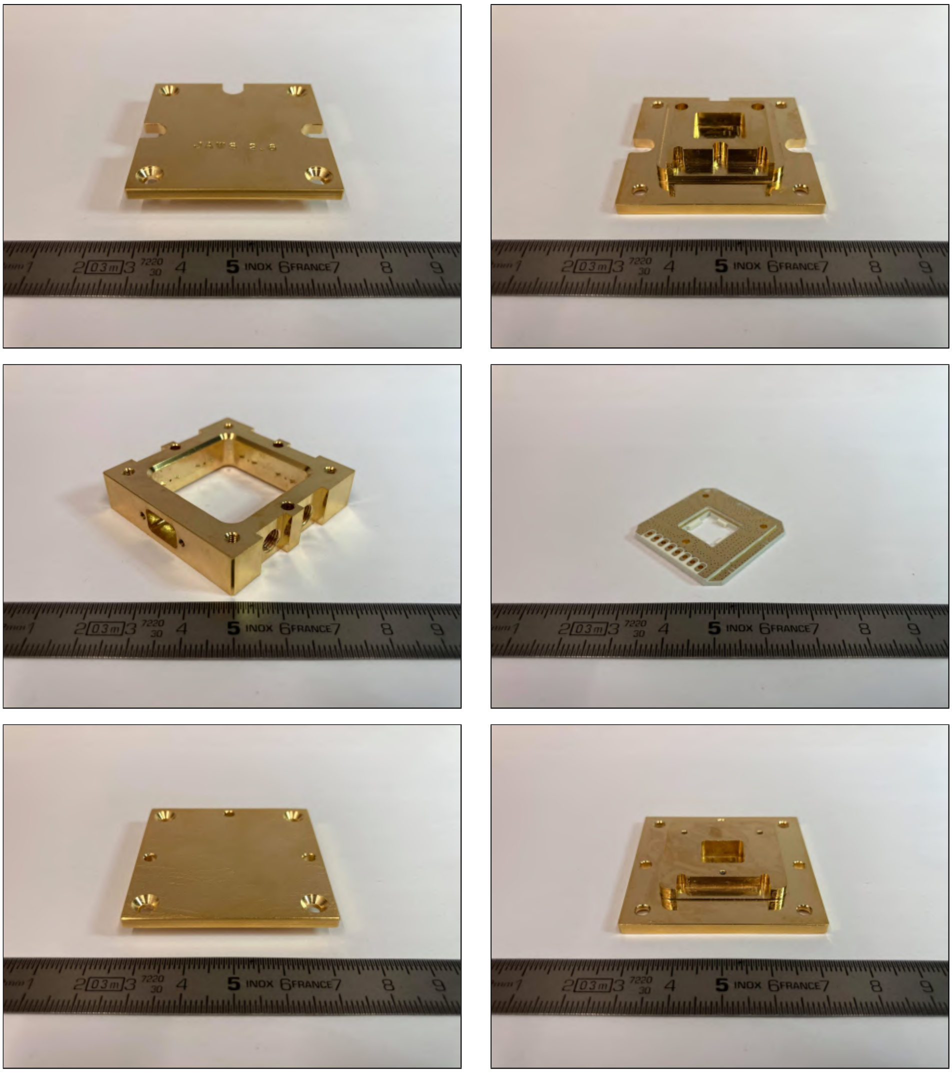

Figure 4.10 JAWS mechanical parts. Top: top part of the box. Middle: ring of the box and PCB. Bottom: bottom part of the box.

Lightening in JAWS The substrate is supsended on 4 dielectric posts, and it is surrounded by a 5 mm deep hollow cavity from the top, and similarly from the bottom. For the environment density of state to be effectively shaped, these two hollow cavities need to be merged into a unique one, through galvanical connection in the chip plane. This connection is ensured by the conductive vias regularly spaced around the sample, shorting the top and bottom planes of the PCB. Thus, one only needs to enforce contact between the PCB and the top part (since the PCB is already attached with screws to the bottom part). To this end, the box dimensions are adjusted so that when it is closed, the top part rests on the PCB surface, as demonstrated by the gap between the top part and the ring (Fig. 4.11).

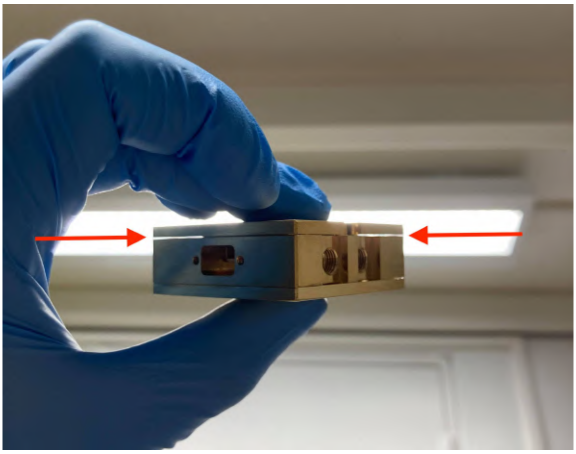

Figure 4.11 JAWS gap. Box closed with PCB inside: the gap between the top part and the ring is a signature of the contact between the top part and the PCB.

We reproduce the simulations of section 4.2.4 with a JAWS-like geometry. Specifically, we add a 1.52 mm thick volume of PCB dielectric (ROGERS 4350B, $\varepsilon_r = 3.66$) around the substrate. We use a square ring geometry in order to mimick the presence of conductive vias 1 mm away from the pocket edges (Fig. 4.12 top). We impose a perfect conuductor boundary condition on the top face of the PCB, and we consider a tight fit between the PCB and the substrate. Thus, the chip and box modes are still decoupled. Even though the eigenmodes of the suspended geometry (Fig.4.6) are dressed by the presence of the PCB, we recover the lightening effect freeing the operation bandwidth up to 16 GHz (Fig. 4.13).

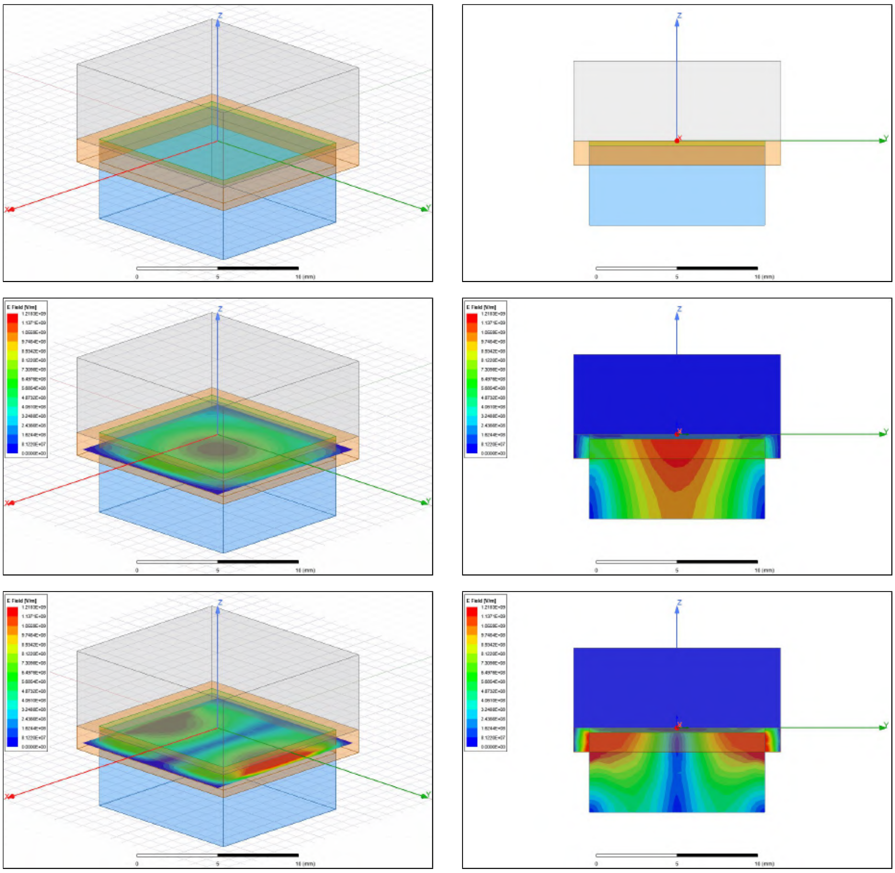

Figure 4.12 JAWS lightening effect, geometry and field distribution. Top: geometry used for simulations. The substrate (green, same as in Fig. 4.6), is surrounded by the PCB (orange). A perfect conductor boundary condition is also imposed on the PCB top face to mimick CPW geometry. Middle: (110) mode electric field profile, in a dimetric projection with a cut 1 mm below the substrate (left), and in a side-view in the yz-plane (right). Bottom: same for (120) mode. The colorbar displays the electric field from blue (low intensity) to red (high intensity) and is common to all plots.

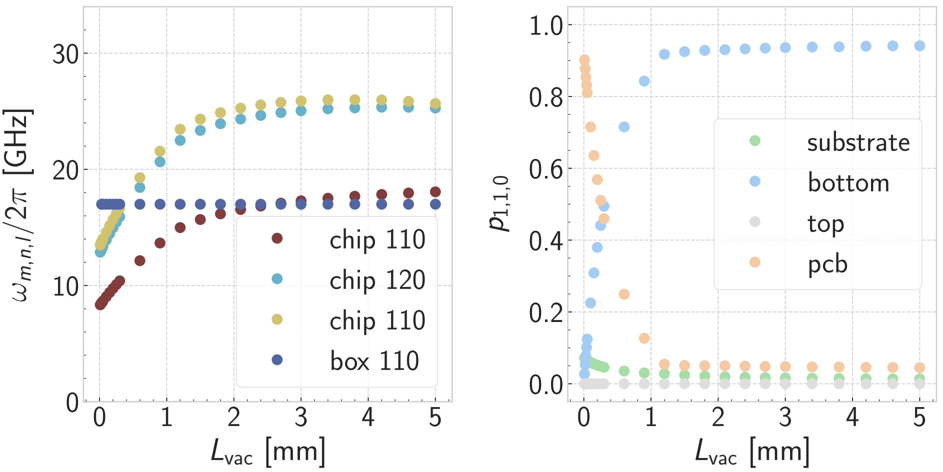

Figure 4.13 JAWS lightening effect, frequency and participation. Left: parasitic mode frequencies (y-axis) versus vacuum depth below and above the substrate (x-axis). Right: participation ratio of the fundamental chip mode (y-axis) in every element of the system (color) versus vacuum depth.

Performances The performances of the JAWS package were tested indirectly, through the measurement of actual samples. The argument is the following: if a sample is measured with a certain level of coherence, it means that the package does not limit it up to that level.

In the following, we present the results of the tests carried out by Emmanuel Flurin with a transmon[8] fabricated at CEA (Saclay). This device, measured in a JAWS package, displays an average relaxation time $T_1 = 170\ \mu$s (Fig. 4.14a). This state-of-art lifetime is the result of a careful optimization of the fabrication recipe. On top of that, it shows that JAWS can sustain long-lived mode on the order of 200 μs. Next, we perfom a Ramsey spectroscopy of the parasitic modes [Huang 2021]. It consists in repeating a Ramsey experiment on the qubit, while sweeping the frequency of another microwave tone applied on the same port. This extra drive probes the environment. When it hits a mode coupled to the device, the induced parasitic population dephases the qubit (Eq. 4.6), which limits the Ramsey coherence time T_{2R} (Fig. 4.14b). This protocol identifies three parasitic modes coupled to the transmon, at 15.4, 18.7, and 19.3 GHz. The lowest detected mode

---

[8] The substrate is in Sapphire, and the transmon pads are made out of sputtered Tantalum. The qubit frequency is $\omega_q/2\pi = 6.13$ GHz.

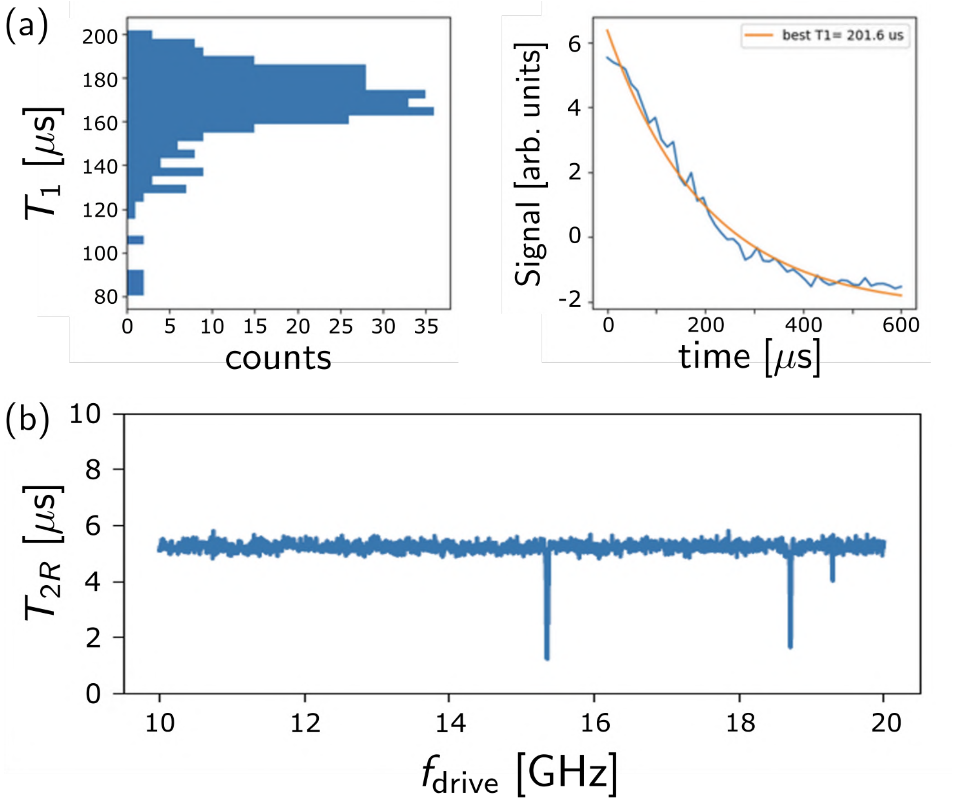

Figure 4.14 JAWS performances. (a) Left: histogram of relaxation times (y-axis) of a highly coherent transmon in a JAWS package, measured over 12 hours. Right: best T_1 experiment, demonstrating a relaxation time in excess of 200 μs. (b) Ramsey fringe decay time (y-axis) versus frequency of a drive probing the environment (x-axis).

could be either the chip (110) mode, or the box (110) mode, as predicted by simulations (Fig. 4.13). Yet it is impossible to precisely identify modes with a single experiment. Also, the circuit patterned on the chip and the presence of wirebonds at the surface are likely to dress the parasitic modes, and shift their frequencies. While this experiment would need to be repeated with qubits located all around the chip to rule out the presence of other parasitic modes, this first result is very promising. It demonstrates the potential of the JAWS package in freeing experiments of spurious modes up to 15 GHz.

Credits The JAWS package is the product of a joint effort at Laboratoire de Physique de l'École Normale Supérieure, orchestrated by the author of this thesis since late 2018. Zaki Leghtas and Clarke Smith took part in the inital design discussions. Then, Pascal Morfin and Anne Denis designed the mechanical parts and the PCB respectively. Not only did they translate those ideas on CAD files, but they also polished them, bridging the gap between physics and engineering. Finally, even though these shark fins are not deadly as the original JAWS ones, they proved difficult to machine. Matthieu Sardin has all the credit for crafting the first boxes in the laboratory machine shop. Since then, the JAWS package has switched to medium-scale production. Around 50 boxes have been delivered to mulitple research groups, including:

- Laboratoire de Physique ENS Paris - Quantic Team,
- CEA Saclay - Quantronics,
- LKB - Optomechanics and Quantum Measurements Group,
- Alice & Bob,
- Laboratoire de Physique ENS Lyon - Quantum Circuit Group,
- Laboratoire de Physique de l'École Polytechnique,
- Thales - unité mixte CNRS,
- ESPCI - Laboratoire de Physique et d'Étude des Matériaux.

The experiments carried out cover many flavours of cQED, demonstrating the great versatility of this package. Finally, we conclude with a list of publications that use the JAWS package:

- E. Albertinale, *et al.* "Detecting spins by their fluorescence with a microwave photon counter" - Nature **600** 434–438 (2021),
- W. C. Smith, *et al.* "Magnifying Quantum Phase Fluctuations with Cooper-Pair Pairing" - Phys. Rev. X **12**, 021002 (2022),
- C. Berdou, *et al.* "One hundred second bit-flip time in a two-photon dissipative oscillator" - Phys. Rev. X Quantum **4** 020350 (2023),
- E. Billaud, *et al.* "Microwave fluorescence detection of spin echoes" - arXiv:2208.13586 (2022),
- M. Villiers, *et al.* "Dynamically enhancing qubit-photon interactions with anti-squeezing" - arXiv:2212.04991 (2022),
- Z. Wang, L. Balembois *et al.* "Single electron-spin-resonance detection by microwave photon counting" - Nature **619** 276-281 (2023),
- Léo Balembois, *et al.* "Practical Single Microwave Photon Counter with 10^{22} W/$\sqrt{\mathrm{Hz}}$ sensitivity" - arXiv:2307.03614 (2023),
- B.-L. Najera-Santos, *et al.* "High-sensitivity AC-charge detection with a MHz-frequency fluxonium qubit" - arXiv:2307.14329 (2023).

4.3 Sample fabrication

In this section we give the recipe of the sample measured in chapter 2 & 3. It is made out of a 280 μm thick intrinsic silicon chip, sputtered with 100 nm of niobium. A first laser lithography step patterns the large features of the circuit on S1805 resist. It is revealed in MF319, and subsequently etched with SF_6. The Al/AlOx/Al Josephson junctions are fabricated during a second step of electronic lithography, using a Dolan bridge technique on a bilayer of MMA/MAA and PMMA. After reveal in a 1:3 H_2O/IPA solution at 6°C for 90 s followed by 10 s in IPA, the chip is loaded in a Plassys evaporator. A 2 min argon milling cleaning is implemented to ensure good electrical contact between the two metallic layers. Then the chip is evaporated with a 35 nm thick layer of Aluminium with an angle of -30°, followed by 5 min of oxydation in 5 mbar of pure oxygen, and the evaporation of 100 nm of Aluminium with a +30° angle. After lift-off, the chip is baked at 200°C for 1 h.

The resulting junctions are of three types as summarized in table 4.1. The SQUID embedded in the transmon features a big junction in parallel with a tiny one, while the SNAIL embedded in the resonator features three big junctions in parallel with a small one (see Fig. 2.11). Notably the big junction is 26 times bigger than the tiny one. Without relying on advance exposure optimization during electronic lithography, this is the maximum unbalance the fabrication process could support.

Junction type	Big	Small	Tiny
Surface [μm^2]	2.10	0.14	0.08
Inductance [nH]	0.19	2.57	4.48

Table 4.1 Characteristics of the three junction types, as measured on test structures fabricated on the same chip.

4.4 Amplification

Finally, we conclude this chapter with another aspect of the operation of cQED experiments: the amplification of microwave signals. While the measurement setup described in Fig. 4.1 features a TWPA as a first stage of amplification [Macklin 2015], this part can also be assumed by a resonant parametric amplifier. In this section, we present a design for such an amplifier, that was used in a cat-qubit experiment realized in the team [Lescanne 2020].

The device consists in a superconducting CPW half-wavelength resonator, augmented in its center by a chain of 20 SNAILs (Fig. 4.15). Dubbed the SNAIL parametric amplifier (SPA) [Frattini 2018; Sivak 2019], it is designed to emulate the DPO model 2.4, for the sake of gain production only. Thus, it is operated in the resonant regime, where the conversion efficieny from input pump power to output signal gain is the highest (Eq. 2.5). The concatenation of multiple Josephson elements is a typical trick in amplifier design. Indeed, in replacing a single Josephson element by a chain of M elements with the same total linear inductance, the amplitude of the fourth harmonic of the resulting potential is reduced, hence the Kerr (section 2.2.1). The reduction scales like M^2 [Eichler and Andreas Wallraff 2014], or M

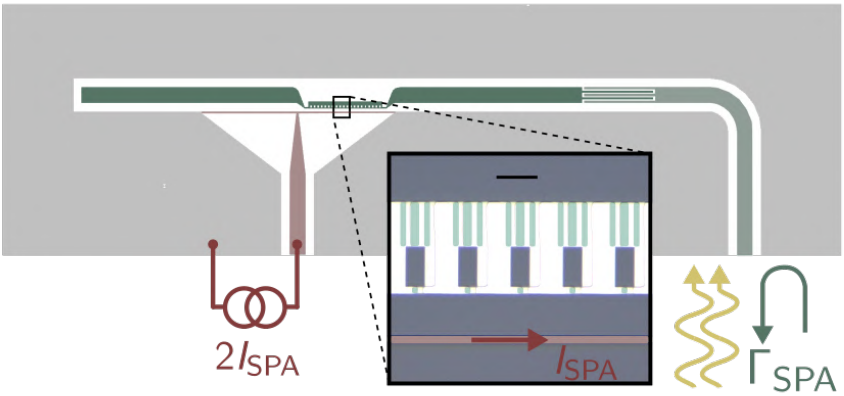

Figure 4.15 SNAIL parametric amplifier: layout. Superconducting circuit layout of the amplifier: antennas and SNAIL chain of the SPA (green), input line (light green) and flux bias line (red). The inset shows an optical micrograph of 5 SNAILs with junctions highlighted in green (mind the inverted colors, scale bar is 20 μm). Pumping the SPA (gold double arrow) induces gain for reflected signals (green arrow).

[Planat 2019], depending if the fabrication process of the chain is modified, or not, as opposed to a single element[9]. Either way, mitigation of the Kerr nonlinearity is crucial for amplifiers based on Josesphson junctions. Indeed, this spurious interaction comes as an important limitation of their dynamical range (section 2.2.3).

Even though they consist in different designs, the operation mode of the SPA is excatly similar to the system presented in chapter 2. Using a DC current I_{SPA} to control the flux threading the SNAIL loops Φ_{SPA}, the resonant frequency of the SPA mode can be tuned over nearly 3 GHz (Fig. 4.16a). It is overcoupled to its feedline at a rate $\kappa_{\mathrm{SPA}}/2\pi = 100$ MHz. Driving the amplifier with a strong pump, at twice the natural frequency of the SPA mode, amplifies signals reflected on its input port (Fig. 4.16b). In order to overcome the noise added by the following amplifier in the chain – a HEMT located at 4 K – the SPA is typically operated at 20 dB of gain[10]. There, the dynamical range of the SPA is characterized by the 1 dB compression point of the amplifier. It is defined as the input signal gain for which the output gain decreases by 1 dB. In our device we find $P_{\mathrm{1dB}} = -111$ dBm, in line with parametric amplifiers of the same complexity [Frattini 2018]. Finally, the added noise of this amplifier was estimated with a Noise Visibility Ratio experiment [Frattini 2017]. This last test (not shown) revealed that our design has the potential to operate as a quantum limited amplifier.

---

[9] The junctions at the heart of the SPA are the product of a different fabrication recipe as the one presented in section 4.3. Notably, the oxydation pressure was set to 200 mbar for 10 min, yielding junctions with a higher critical current. The equivalent inductance of the chain of 20 SNAILs is 2.5 nH.

[10] These 20 dB match the two orders of magnitude in temperature – hence noise – separating the SPA ($T = 20$ mK) from the HEMT ($T = 4$ mK).

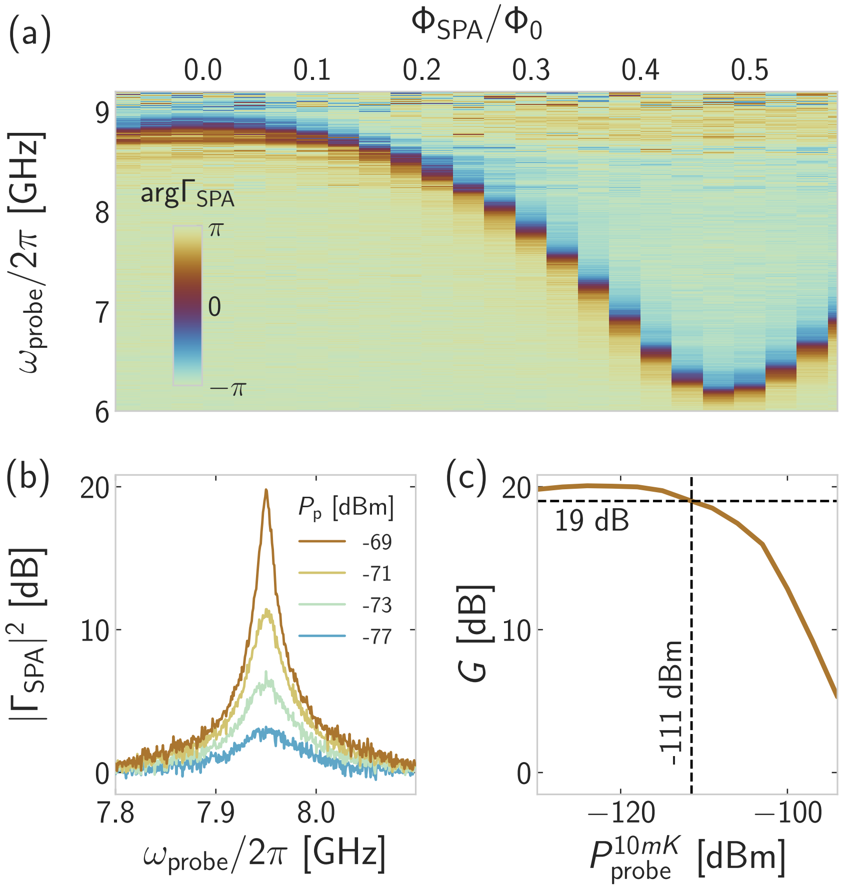

Figure 4.16 SNAIL parametric amplifier: performances. (a) Phase response (color) of a weak reflected signal ω_{probe} on the SPA port (y-axis) versus the flux threaded through the SNAIL loops (x-axis). (b) Gain profile (y-axis) versus probe frequency (x-axis) for increasing pump power (color) applied at twice the bare oscillator frequency (here, $\omega_{\mathrm{a}}/2\pi \approx 7.95$ GHz). (c) Maximum gain (y-axis) output by the amplifier under pumping conditions akin to brown curve on (b), with increasing input power (x-axis). We find $P_{1\mathrm{dB}} = -111$ dBm.

5

CONCLUSION

5.1 Summary

5.1.1 Spinning the springs

The spin and the spring are two limit cases of the quantum world (section 1.1). In between, there exists a continuous spectrum of linear systems dressed by some amount of nonlinearity. The beauty of Josephson circuits, at the heart of cQED, lies in the high level of control they offer in tailoring nonlinearities (section 2.2). On one end of the spectrum we find spin-like circuits, where the nonlinearity is sufficiently large for these systems to be operated as qubits [Clarke and Wilhelm 2008; Gyenis 2021]. While coupling a pure spring to a qubit is a staple process of cQED (section 3.2), there have been numerous demonstrations of the coupling of anharmonic springs to qubits – putting aside the case of flux-tunable oscillators, where nonlinearity is reduced to its static contribution. For instance, many experiments leveraged the bistability of Kerr oscillators for improved qubit readout [Siddiqi 2006; Lupaşcu 2007; Mallet 2009; Ong 2011]. Yet, the advent of the transmon design and the progress of quantum limited amplifiers quickly overcame the benefits of these nonlinear readout schemes [Murch 2013b]. Alternatively, a degenerate parametric oscillator (DPO) was coupled to a superconducting qubit [Eddins 2019], or an ensemble of spins [**Vine2022**]. There, resonant squeezing of the oscillator was leveraged for improving the TLS readout, once again.

This thesis presented another realization of the coupling of an anharmonic oscillator to a qubit, this time using a DPO undergoing detuned squeezing (section 2.1). This new regime of operation goes well beyond readout optimization. Indeed, Leroux, Quin an co-authors predicted that detuned squeezing of an oscillator could dynamically enhance its coupling to a qubit [Leroux 2018; Qin 2018]. This thesis gave the first demonstration of these enhanced interactions using an electromagnetic oscillator.

5.1.2 An electromagnetic Bogoliubov oscillator

While a DPO operated in the resonant regime features a continuous spectrum with non-normalizable eigenstates, a detuned DPO has distinct energy levels associated to squeezed Fock states (section 2.1). This results from the mismatch between the pump frequency and the oscillator parametric resonance, which brings the system away from a parametric instability. There, it is refered to as a Bogoliubov oscillator (BO). Even though this denomination is strictly valid as soon as $\delta_{\mathrm{a}} \neq 0$, the presence of the detuning significantly alters the DPO response only in the limit $|\delta_{\mathrm{a}}| \gg \kappa/2$ (Table 2.1). The amplified fluctuations of the BO eigenstates are the root cause for its enhanced interactions with any coupled system (section 3.1.1).

This assertion was tested in a cQED architecture, by coupling a SNAIL-resonator implementing a BO (section 2.2.2), to a transmon (section 3.1.2). Squeezing the BO eigenstates by 5.5 dB resulted in a two-fold increase of the dispersive interaction strength (section 3.4.4). This experiment was conducted in the weak-dispersive regime, where a perturbative analysis let us write analytical expressions accounting for this evolution (section 3.4.1). A test of squeezing-enhanced interactions was also performed in the resonant case, at the onset of strong-coupling (section 3.1.3). But there, the potential coupling boost was hindered by another consequence of squeezing, namely, the appearance of an effective thermal population in the BO.

Indeed, the Bogoliubov excitations being the anti-squeezed version of the original ones, the single-photon loss of the detuned DPO appears squeezed for the BO. In the limit $|\delta_{\mathrm{a}}| \gg \kappa/2$, this squeezed-photon loss channel turns into an effective thermal bath (section 2.1.2). This hot bath increases the fluctuations of the BO population, which in turn accelerates the qubit dephasing (section 3.4.2). In theory, nothing prevents the coupling enhancement to be revealed in the resonant regime. Yet, at the onset of strong coupling, the spectral response of the coupled system appeared to be more sensitive to the thermal bath than to a renormalization of the coupling strength. This motivated the exploration of the joint signatures of squeezed bath and enhanced coupling in the dispersive limit (section 3.4.3).

Last but not least, the peculiar eigenstructure of the BO was revealed through gain spectroscopy of the oscillator alone (section 2.2.4). Ruling out the interplay between dissipation and detuning, the coalescence frontier was introduced (section 2.1.4). Finally, the possibility of amplification evading the gain-bandwidth product constraint was demonstrated (section 2.2.5).

5.2 Outlook

5.2.1 Ready for use

Our experiment opens the door to a realm of applications for BOs, including fast two-qubit gates [Burd 2021], enhanced interactions to weakly coupled systems [Lü 2015; Xie 2020; Lü 2022], quantum transduction [Zhong 2022], and squeezing induced quantum phase transitions [Zhu 2020; Chen 2021; Shen 2022]. Yet, there is some room for optimization of the current design.

As suggested in section 2.1.4, the BO thrives in the resolved regime, where it can bear high squeezings while staying at a good distance from the DPO instability (Fig. 2.5). The potential to operate the system in this specific regime is ultimately set by the ratio $2|\delta_{\mathrm{a}}|/\kappa$. The electromagnetic BO presented in this thesis was implemented using a superconducting resonator augmented by a single SNAIL. There, this constitutive ratio was limited to 10, due to spurious Kerr effect (section 2.2.4). As customary in amplifier design, the Kerr nonlinearity might be mitigated by resorting to a chain of SNAILs of smaller inductance (section 4.4). Therefore, the BO would support pumps of higher intensity, opening the way for the exploration of higher values of $2|\delta_{\mathrm{a}}|/\kappa$. Recently, a high-kinetic inductance resonator – commonly known for bearing small residual Kerr – implemented a BO with $2|\delta_{\mathrm{a}}|/\kappa = 16$ [Vine 2023].

The regime of qubit-BO interactions presented in this thesis was limited to weak-couplings, either resonant or dispersive. One could naturally envision to increase the bare coupling strength, so that the system is initially strongly coupled. In the resonant case, excitation-number non-preserving interaction terms will quickly become non-negligible (Fig. 3.2). There, the qubit-BO system would be an interesting simulator for ultra-strong coupling physics [Marković 2018; Frisk Kockum 2019]. In the dispersive case, one could imagine using the qubit as a precise thermometer of the BO squeezed bath [Ong 2013; Dassonneville 2021]. There, a joint analytical effort would be necessary to account for the renormalization of the qubit lineshape beyond the Gaussian approximation [Gambetta 2008].

Continuing with theoretical endeavors, another question arises in the context of qubit readout: can a detuned DPO outperform a resonant DPO? Indeed, Eddins and co-authors described a qubit readout enhanced by the gain of a resonant DPO [Eddins 2019]. Then, it seems like a detuned DPO would not only benefit from wideband gain, but also from enhanced interactions.

5.2.2 Squeezed vacuum injection

The initial proposals had foreseen the non-trivial impact of the bath on the BO. They acutally offered to cancel the effects of the squeezed bath, by injecting conversely squeezed vacuum on the system. As a first step, we can look at the BO dynamics with an anti-squeezed Lindblad loss operator:

$$\boldsymbol{L}'_{\mathbf{ph}} = \boldsymbol{\mathcal{U}}_s^\dagger \boldsymbol{L}_{\mathbf{ph}} \boldsymbol{\mathcal{U}}_s = \sqrt{\kappa}\left(\mathbf{a}\cosh r - \mathbf{a}^\dagger \sinh r\right) , \tag{5.1}$$

so that the dissipator for the BO reads:

$$\mathcal{D}[\boldsymbol{L}'_{\mathbf{ph}}]\boldsymbol{\rho} = \kappa\mathcal{D}[\boldsymbol{\alpha}]\boldsymbol{\rho} . \tag{5.2}$$

With such a cancellation bath, the BO is expected to behave as a linear oscillator in contact with vacuum (no more gain, no more idler, no more finite population), except for enhanced interactions to the qubit. We test this assertion by simulating the full $\{\text{DPO-transmon}\}$ model in the presence of anti-squeezed vacuum on the oscillator:

Squeezed Jaynes-Cummings in anti-squeezed bath (SJCaSB)

$$\boldsymbol{\mathcal{H}}/\hbar = \delta_{\mathrm{a}}\mathbf{a}^\dagger\mathbf{a} - \frac{\lambda}{2}\left(\mathbf{a}^2 + \mathbf{a}^{\dagger 2}\right) + \delta_q \mathbf{b}^\dagger\mathbf{b} + \frac{\chi_q}{2}\mathbf{b}^{\dagger 2}\mathbf{b}^2 + g(\mathbf{a}\mathbf{b}^\dagger + \mathbf{a}^\dagger\mathbf{b})$$
$$\boldsymbol{L} \in \left\{\sqrt{\kappa}\left(\mathbf{a}\cosh r - \mathbf{a}^\dagger \sinh r\right),\ \sqrt{\gamma_1}\,\mathbf{b},\ \sqrt{2\gamma_\phi}\,\mathbf{b}^\dagger\mathbf{b}\right\}$$

We use the same parameters as in section 3.1.3. The oscillator Hilbert space is now truncated to 100 states, enabling the exploration of higher squeezing amplitudes. We plot the simulated oscillator absorption spectra (Fig. 5.1), as well as the fitted values for g (using Eq. 3.13). In the presence of the cancellation bath, the gap in the splitting figure does not fill up, as a sign of the coupled system staying in contact with a cold bath. At first, the fitted value for g increases significantly, closely following the expected $\cosh r$ trend. Then, a saturation occurs, together with the emergence of some asymmetry in the absorption spectra, which is a signature of the renewed significance of the full Rabi coupling.

Injecting squeezed radiation in cQED is notoriously hard, as every bit of loss between the injector and the main system degrades the purity of the squeezed state [Murch 2013a; Bienfait 2017]. Yet, the implementation of bath cancellation for a BO faces another set of challenges, related to the peculiar nature of the BO squeezing. How must the injected squeezed state be generated? Does it need to be provided by a replica of the main BO? Would a resonant DPO matching the frequency of the BO be sufficient? So many questions that require a thorough analysis of the casacade of two DPOs.

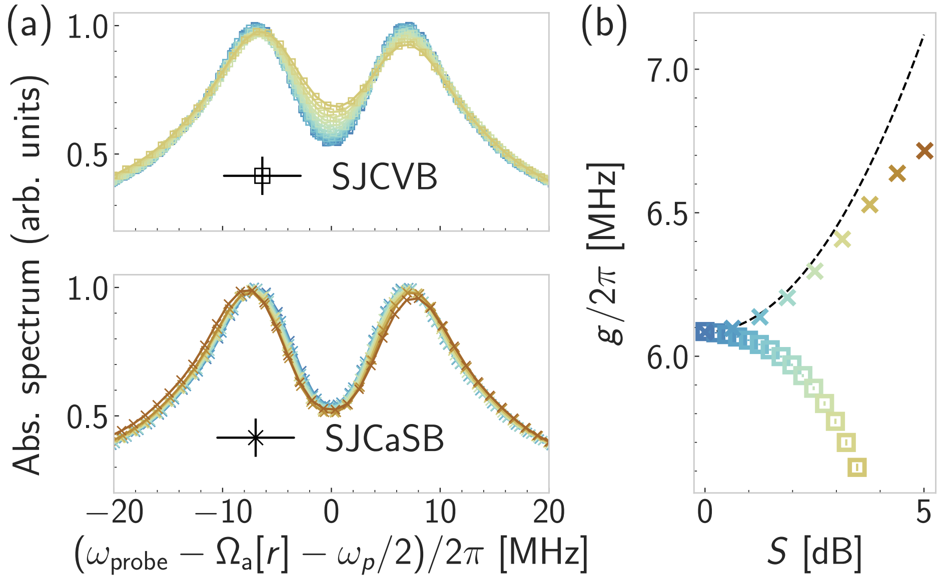

Figure 5.1 Transmon-BO coupling with anti-squeezed vacuum injection. (a) Same as Fig. 3.8, except for the bottom plot which corresponds to the SJCaSB model. (b) Results of the fitted value for the coupling strength g. The black dashed line shows the $\cosh r$ trend.

5.2.3 Coupling to hybrid systems

Finally, we envision the coupling of a BO to a hybrid system. In order to limit the complexity of the resulting experiment, we do not consider the injection of conversely squeezed vacuum. As a consequence, the coupled TLS will be suffering from BO-induced dephasing. Yet, the coherence of hybrid systems is typically not limited by radiation through the oscillator. For instance, spin ensembles are subjected to inhomogenous broadening, and quantum dots are very sensitive to charge noise [Cottet 2017]. In those cases, one could benefit from the enhanced coupling provided by the BO, while not being limited by the impact of its squeezed bath [Vine 2023]. Alternatively, one could leverage the eigenstate squeezing of the BO beyond enhanced couplings, for the study of the interaction between non-classical states of light and quantum matter [Souquet 2014].

In that respect, carbon-nanotubes (CNTs) hold great promises[1]. Single-walled CNTs are made out of a rolled-up graphene sheet with aspect ratios[2] in excess of $10,000:1$. Depending on the folding of the graphene lattice, they can be insulating, metallic, or semi-conducting, with solely 4 conduction channels. Through electrostatic gating, they can host quantum dots which were successfully coupled to microwave photons [Delbecq 2011]. In addition, they can be proximitized by either superconducting [Herrmann 2010; Bruhat 2018] or ferromagnetic materials [Cottet and Kontos 2010; Viennot 2015]. As a consequence, CNTs are a versatile platform for the observation of exotic phases of matter [Desjardins 2017; Desjardins 2019; Contamin 2022; Contamin 2023]. The following paragraphs will be dedicated to the presentation of a paradigmatic realization of hybrid-cQED pursued during my PhD, with a device integrating a Josephson circuit coupled to a CNT.

Coupling a CNT to a superconducting circuit is a difficult task. First, both systems operate on drastically different scales. Microwave resonators in cQED are typically millimeter long and a few tens of micrometer wide, while CNTs are tens of micrometer long and 2 nm wide. Second, CNT control requires a handful of electrical lines. They are either galvanically connected to the CNT, thus coined *contacts*, or capacitively coupled *gates*. When brought in close proximity with the superconducting resonator, these lines can degrade its quality. Finally, CNTs are commonly fabricated using chemical vapor deposition, a process incompatible with most metallic thin films used for superconducting circuits. Those challenges can be reconcilied using a flip chip process called *stapling* [Cubaynes 2020]. It involves patterning the microwave resonator and the CNT control lines on a main chip, and growing CNTs in between the teeth of on a auxilliary chip shaped like a comb. In a final stapling process, a single CNT can be transfered on the main chip (Figure 5.2a,e).

On Figure 5.2 we show a possible design for the main chip (b). It is patterned with a coplanar waveguide resonator (red), coupled to a transmission line (orange) through an inductive coupler (c). On one end, the resonator is shunted to ground through a SQUID (inset of c). On the other end it narrows down towards the control-*piano* (e, f), where it capacitively couples to the CNT. Besides the resonator microwave gate (red), the control-piano features DC gates (light blue) and galvanic contacts (navy blue) (see the cross-section sketched in a, not to scale) (CNT as a black wiggly line in

---

[1] The list of references presented in this paragraph is intentionally biased towards works realized at LPENS.

[2] Think about a pencil the size of the Eiffel tower.

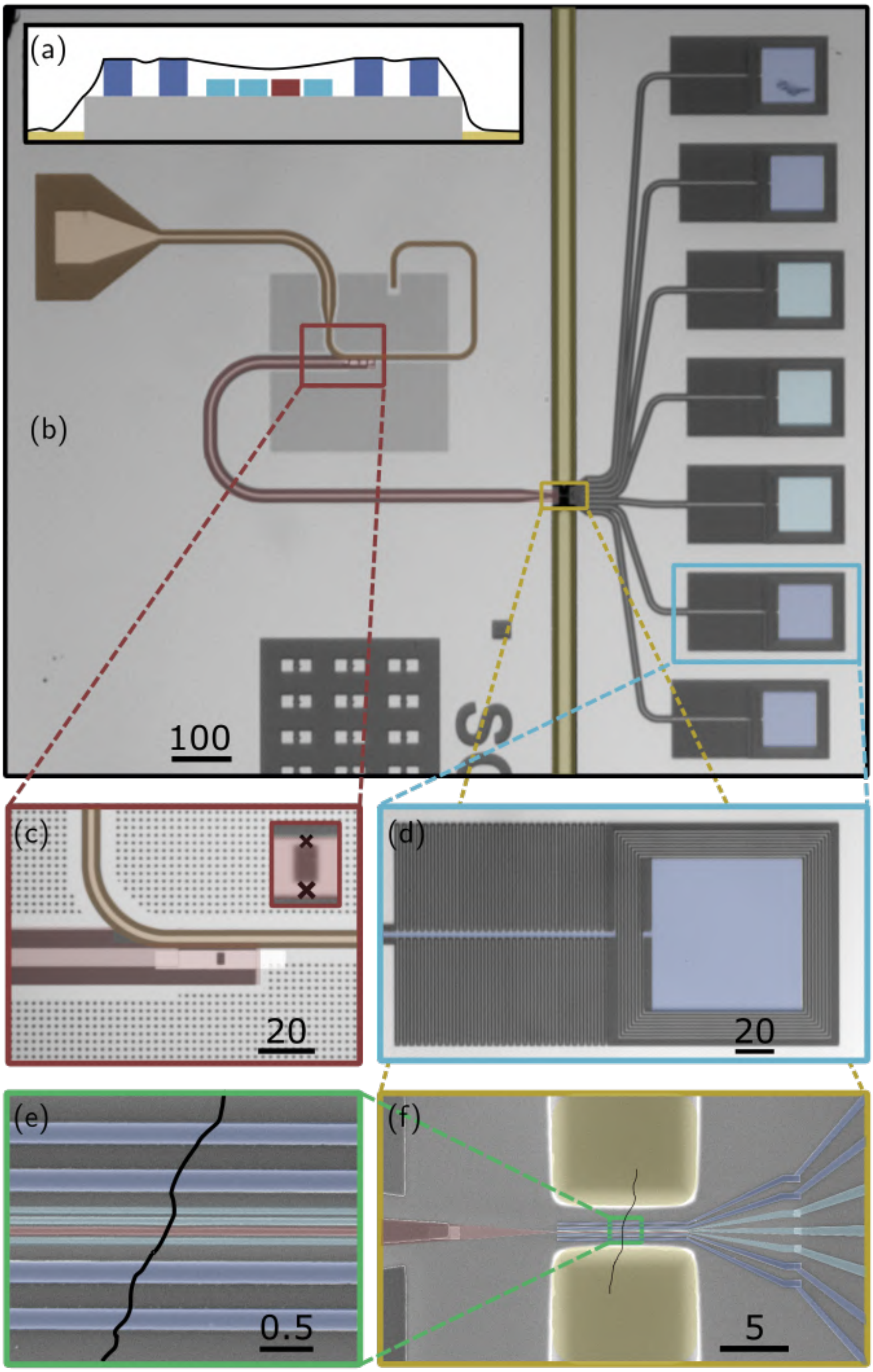

Figure 5.2 Hybrid-cQED with carbon-nanotubes. See description main text. Scale bars in micrometers. A fake CNT is drawn for concreteness on pictures (e) and (f).

b,e). These DC controls are routed out of the chip through LC filters (d), designed to preserve the resonator quality. Note that the main chip is dug with trenches around the control-piano (yellow in a, b, f), as required by the stapling process.

Over the course of my PhD, I fabricated dozens of samples like the one presented in Fig. 5.2, and conducted nearly as many stapling processes. Yet, only one CNT could be measured down to cryogenic temperatures (Fig. 5.2), and in transport only, as it showed no coupling to the superconducting resonator. All the other attempts fell short of demonstrating electrical contact at low temperatures, as required for tuning up of the device. High contact resistances is a common challenge with CNTs, that can be traced down to the presence of contaminants at the device surface, or material disorder.

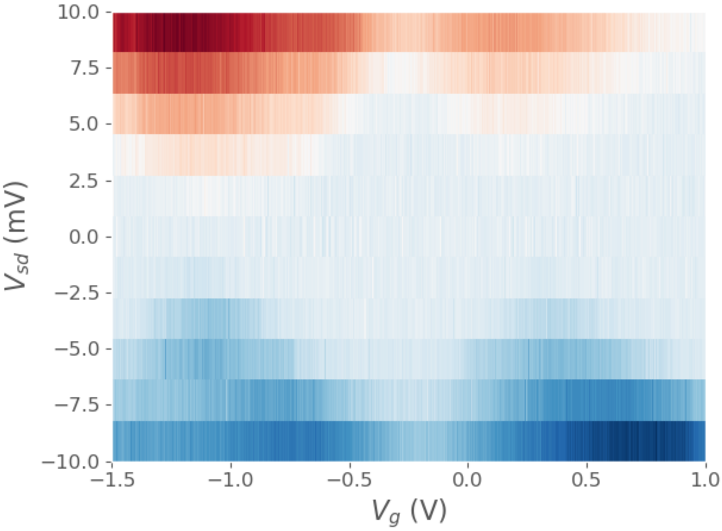

Figure 5.3 Coulomb diamonds in a CNT quantum dot. The color maps the current flowing through the dot, from positive (red) to negative (blue) values, as a fonction of the potential maintained between the two contacts (y-axis) and the dot gate voltage (x-axis).

In the end, the failure of the carbon-nanotube aspect of the experiment lead to the extensive characterization of the Bogoliubov oscillator presented in this thesis. Which in itself is, a short story of experimental physics.

A

MATHEMATICAL CONVENTIONS

Fourier transformation The temporal Fourier transform used in this thesis follows the convention:

$$f[\omega] = \mathcal{F}[f][\omega] = \int \mathrm{d}t e^{i\omega t} f(t) \ , \tag{A.1a}$$

$$f(t) = \mathcal{F}^{-1}[f](t) = \int \frac{\mathrm{d}\omega}{2\pi} e^{-i\omega t} f[\omega] \ . \tag{A.1b}$$

It is associtaed with the following Dirac distribution identities[1]:

$$\int \mathrm{d}\omega e^{-i\omega t} = 2\pi\delta(t) \tag{A.2a}$$

$$\int \mathrm{d}t e^{i\omega t} = 2\pi\delta[\omega] \tag{A.2b}$$

---

[1] We recall the technique to find the Fourier transform of the Dirac distribution δ, whatever the normalization convention is. As a reminder, δ is the singular distribution such that $\langle\delta(x_0), f(x)\rangle = f(x - x_0)$. The Fourier transform of a distribution is defined implicitely through the Fourier transform of the function that the distribution takes as an input: $\langle\mathcal{F}[\delta], f\rangle = \langle\delta, \mathcal{F}[f]\rangle$. Thus in the forward case:

$$\langle\mathcal{F}[\delta], f\rangle = \langle\delta, \int \mathrm{d}t e^{i\omega t} f(t)\rangle = \int \mathrm{d}t f(t) \ .$$

Where the last integral can be thought of as the regular distribution associated to the unit function: $\langle 1, f\rangle = \int \mathrm{d}t f(t)$. Thus we find $\mathcal{F}[\delta] = 1$. Application of the backward Fourier transformation yields the first Dirac identity. Conversely for the backward case:

$$\langle\mathcal{F}^{-1}[\delta], f\rangle = \langle\delta, \int \frac{\mathrm{d}\omega}{2\pi} e^{-i\omega t} f[\omega]\rangle = \int \frac{\mathrm{d}\omega}{2\pi} f[\omega] \ .$$

So that we find $\mathcal{F}^{-1}[\delta] = 1/2\pi$. Application of the forward Fourier transformation yields the second Dirac identity.

Hyperbolic tigonometry The hyperbolic functions $\cosh$, $\sinh$ and $\tanh$ are defined as:

$$\forall x \in \mathbb{R}\ , \quad \cosh x = \frac{e^x + e^{-x}}{2} \tag{A.3a}$$

$$\sinh x = \frac{e^x - e^{-x}}{2} \tag{A.3b}$$

$$\tanh x = \frac{e^x - e^{-x}}{e^x + e^{-x}} \tag{A.3c}$$

We deduce the following identities:

$$\cosh^2 x - \sinh^2 x = 1 \tag{A.4}$$

$$\cosh 2x = \cosh^2 x + \sinh^2 x \tag{A.5a}$$

$$\sinh 2x = 2 \cosh x \sinh x \tag{A.5b}$$

$$\cosh^2 x = \frac{1}{2}\big(\cosh 2x + 1\big) \tag{A.6a}$$

$$\sinh^2 x = \frac{1}{2}\big(\cosh 2x - 1\big) \tag{A.6b}$$

Finally we introduce the logarithmic form of the inverse $\tanh$ function:

$$\forall x \in (-1, 1)\ , \quad \tanh^{-1} x = \frac{1}{2} \ln \frac{1+x}{1-x}\ . \tag{A.7}$$

B

SURVEY OF ANALYTICAL TECHNIQUES

The parametric process responsible for the injection of pairs of photons in the SNAIL-resonator is triggered by driving the resonator with an external pump field. Similarly, the spectroscopy of both the qubit and the resonator are realized using drives. Thus, a complete description of the system $\{$SNAIL-resonator + transmon$\}$ has to account for external degrees of freedom – consituing the bath – supporting these drives. Crucially, the system can also relax energy through these bath modes. This appendix aims at presenting the various analytical techniques used to analyze the system in contact with its bath.

The Hamiltonian of the system $\{$SNAIL-resonator + transmon$\}$ reads:

$$\boldsymbol{\mathcal{H}}_{\mathbf{tot}} = \boldsymbol{\mathcal{H}}_{\mathbf{syst}} + \boldsymbol{\mathcal{H}}_{\mathbf{bath}} + \boldsymbol{\mathcal{H}}_{\mathbf{int}} \ . \tag{B.1}$$

First we will present the system Hamiltonian $\boldsymbol{\mathcal{H}}_{\mathbf{syst}}$ in the laboratory frame, and detail the transformations implemented to reach Eq. 3.1. The bath and interaction Hamiltonians $\boldsymbol{\mathcal{H}}_{\mathbf{bath}}$ and $\boldsymbol{\mathcal{H}}_{\mathbf{int}}$ will be subsequently introduced. As customary for open quantum systems, we will eliminate the bath modes in writing equations of motion for the system modes accounting for their finite relaxation. This final part will closely follow the derivation of input-output theory given by Steck [Steck 2007].

B.1 Transformations of the system Hamiltonian

B.1.1 The system Hamiltonian

The system is composed of a SNAIL-resonator coupled to a transmon, driven at three distinct frequencies. The total Hamiltonian reads:

$$\boldsymbol{\mathcal{H}}_{\mathbf{syst}}(\boldsymbol{t}) = \boldsymbol{\mathcal{H}}_{\mathbf{a}} + \boldsymbol{\mathcal{H}}_{\boldsymbol{q}} + \boldsymbol{\mathcal{V}} + \boldsymbol{\mathcal{H}}_{\mathrm{p}}(\boldsymbol{t}) + \boldsymbol{\mathcal{H}}_{\mathbf{d},\,\mathbf{a}}(\boldsymbol{t}) + \boldsymbol{\mathcal{H}}_{\mathbf{d},\boldsymbol{q}}(\boldsymbol{t}) \ . \tag{B.2}$$

Since the resonator is operated at its Kerr-free flux point, it is minimally described by a harmonic oscillator with frequency ω_{a} dressed by a third order nonlinearity g_3. Its Hamiltonian reads $\boldsymbol{\mathcal{H}}_{\mathbf{a}} = \boldsymbol{\mathcal{H}}_{\mathbf{a,0}} + \boldsymbol{\mathcal{H}}_{\mathbf{a,nl}}$ where:

$$\boldsymbol{\mathcal{H}}_{\mathbf{a,0}}/\hbar = \omega_{\mathrm{a}}\mathbf{a}^{\dagger}\mathbf{a} \;, \tag{B.3a}$$

$$\boldsymbol{\mathcal{H}}_{\mathbf{a,nl}}/\hbar = g_3\big(\mathbf{a} + \mathbf{a}^{\dagger}\big)^3 \;. \tag{B.3b}$$

The transmon is an anharmonic oscillator with frequency ω_q and Kerr-nonlinearity χ_q so that:

$$\boldsymbol{\mathcal{H}}_{\boldsymbol{q}}/\hbar = \omega_q\mathbf{b}^{\dagger}\mathbf{b} + \frac{\chi_q}{2}\mathbf{b}^{\dagger 2}\mathbf{b}^2 \tag{B.4}$$

The coupling between the resonator and the transmon is capacitive, mediated by the charge degree of freedom of both modes. Thus the coupling term reads:

$$\boldsymbol{\mathcal{V}}/\hbar = -g\big(\mathbf{a} - \mathbf{a}^{\dagger}\big)\big(\mathbf{b} - \mathbf{b}^{\dagger}\big) \tag{B.5}$$

Finally the system features three time-dependent excitation terms. The resonator is driven inductively with two tones. The first is weak with amplitude $\varepsilon_{\mathrm{d,a}}$, and near resonance with frequency $\omega_{\mathrm{a,d}}$. The second one is strong with amplitude ε_{p}, and near the parametric resonance with frequency ω_{p}. Since the parametric resonance is very far from the bare resonance, the second drive is called a *pump*. As for the transmon, it is driven capacitively and weakly near resonance, with amplitude $\varepsilon_{\mathrm{d},q}$ and frequency $\omega_{\mathrm{d},q}$. The Hamiltonian drive terms read:

$$\boldsymbol{\mathcal{H}}_{\mathbf{d,a}}(\boldsymbol{t})/\hbar = \varepsilon_{\mathrm{d,a}}\cos(\omega_{\mathrm{d,a}}t)\big(\mathbf{a} + \mathbf{a}^{\dagger}\big) \tag{B.6a}$$

$$\boldsymbol{\mathcal{H}}_{\mathbf{p}}(\boldsymbol{t})/\hbar = \varepsilon_{\mathrm{p}}\cos(\omega_{\mathrm{p}}t)\big(\mathbf{a} + \mathbf{a}^{\dagger}\big) \tag{B.6b}$$

$$\boldsymbol{\mathcal{H}}_{\mathbf{d},\boldsymbol{q}}(\boldsymbol{t})/\hbar = -i\varepsilon_{\mathrm{d},q}\cos(\omega_{\mathrm{d},q}t)\big(\mathbf{b} - \mathbf{b}^{\dagger}\big) \tag{B.6c}$$

The presence of external drives on a system relies intrisically on a non-vanishing system-bath coupling. While a complete treatment of this coupling will be presented in the Heisenberg picture in section B.2, here we introduce an alternate formulation in the Schrödinger picture. It relies on the Lindblad master equation for the system density matrix:

$$\partial_t\boldsymbol{\rho}(\boldsymbol{t}) = -\frac{i}{\hbar}\left[\boldsymbol{\mathcal{H}}_{\mathbf{syst}}(\boldsymbol{t}), \boldsymbol{\rho}(\boldsymbol{t})\right] + \sum_{\boldsymbol{L}}\mathcal{D}[\boldsymbol{L}]\boldsymbol{\rho}(\boldsymbol{t}) \;, \tag{B.7}$$

where $\boldsymbol{L} \in \{\sqrt{\kappa}\mathbf{a}, \sqrt{\gamma_1}\mathbf{b}, \sqrt{2\gamma_\phi}\mathbf{b}^{\dagger}\mathbf{b}\}$ are the Lindblad operators associated to single-photon loss in the resonator, single-photon loss in the transmon, and transmon dephasing respectively.

B.1.2 Displacement transformation

In the presence of the intense pump tone, the resonator field acquires a finite mean-value. Its dynamics is conveniently described in a displaced frame, looking only at deviations around its mean amplitude. We seek the right displacement transformation, so that the dynamics of the unpumped oscillator in the displaced frame maps the one of the pumped oscillator in the original frame. We will first look for this transformation on the linear part of the oscillator only. In a second step, we will transform the total Hamiltonian according to the displacement transformation.

Specifically, we are looking for the complex function $\xi(t)$ such that the displaced density matrix $\boldsymbol{\rho}^{\xi} = \boldsymbol{\mathcal{U}}_{\xi}\boldsymbol{\rho}\boldsymbol{\mathcal{U}}_{\xi}^{\dagger}$ where $\boldsymbol{\mathcal{U}}_{\xi} = \exp\left\{\xi^*(t)\mathbf{a} - \xi(t)\mathbf{a}^{\dagger}\right\}$ follows the master equation:

$$\partial_t \boldsymbol{\rho}^{\xi}(\boldsymbol{t}) = -i\left[\omega_{\mathrm{a}}\mathbf{a}^{\dagger}\mathbf{a}, \boldsymbol{\rho}^{\xi}(\boldsymbol{t})\right] + \kappa\mathcal{D}[\mathbf{a}]\boldsymbol{\rho}^{\xi}(\boldsymbol{t}) \ . \tag{B.8}$$

First, we expand the time derivative of the displaced density matrix, and find:

$$\begin{aligned}\partial_t \boldsymbol{\rho}^{\xi}(\boldsymbol{t}) = -\frac{i}{\hbar}\Big[&\boldsymbol{\mathcal{U}}_{\xi}\left(\boldsymbol{\mathcal{H}}_{\mathbf{a,0}} + \boldsymbol{\mathcal{H}}_{\mathrm{p}}(\boldsymbol{t})\right)\boldsymbol{\mathcal{U}}_{\xi}^{\dagger} - i\hbar\boldsymbol{\mathcal{U}}_{\xi}\dot{\boldsymbol{\mathcal{U}}}_{\xi}^{\dagger}, \boldsymbol{\rho}^{\xi}(t)\Big] \\ &+\kappa\mathcal{D}[\mathbf{a} + \xi(t)]\boldsymbol{\rho}^{\xi}(\boldsymbol{t}) \ .\end{aligned} \tag{B.9}$$

Second, making use of the following relations[1]:

$$\boldsymbol{\mathcal{U}}_{\xi}\mathbf{a}^{\dagger}\mathbf{a}\boldsymbol{\mathcal{U}}_{\xi}^{\dagger} = \mathbf{a}^{\dagger}\mathbf{a} + \xi(t)\mathbf{a}^{\dagger} + \xi^*(t)\mathbf{a} + |\xi(t)|^2 \tag{B.10a}$$

$$\mathcal{D}[\mathbf{a} + \xi]\boldsymbol{\rho}^{\xi}(\boldsymbol{t}) = \mathcal{D}[\mathbf{a}]\boldsymbol{\rho}^{\xi}(\boldsymbol{t}) + \frac{1}{2}\left[\xi^*(t)\mathbf{a} - \xi(t)\mathbf{a}^{\dagger}, \boldsymbol{\rho}^{\xi}(\boldsymbol{t})\right] \tag{B.10b}$$

$$\boldsymbol{\mathcal{U}}_{\xi}\dot{\boldsymbol{\mathcal{U}}}_{\xi}^{\dagger} = \dot{\xi}(t)\mathbf{a}^{\dagger} - \dot{\xi}^*(t)\mathbf{a} \tag{B.10c}$$

we find that for Eq. B.9 to map on Eq. B.8, the complex function $\xi(t)$ needs to satisfy:

$$\begin{aligned}\varepsilon_{\mathrm{p}}\cos(\omega_{\mathrm{p}}t)\big(\mathbf{a} + \mathbf{a}^{\dagger} + \xi(t) + \xi^*(t)\big) = \ & i\big(\dot{\xi}(t)\mathbf{a}^{\dagger} - \dot{\xi}^*(t)\mathbf{a}\big) \\ & - \omega_{\mathrm{a}}\big(\xi(t)\mathbf{a}^{\dagger} + \xi^*(t)\mathbf{a} + |\xi(t)|^2\big) \\ & - i\frac{\kappa}{2}\big(\xi^*(t)\mathbf{a} - \xi(t)\mathbf{a}^{\dagger}\big) \ .\end{aligned} \tag{B.11}$$

---

[1] While the first two relations are trivially deduced from the definition of the displacement operator $\boldsymbol{\mathcal{U}}_{\xi}$, the third one requires a bit more work.

Projecting this equation on $\langle 1| \cdot |0\rangle$ we find:

$$\dot{\xi}(t) = -i\omega_{\mathrm{a}}\xi(t) - \frac{\kappa}{2}\xi(t) - i\varepsilon_{\mathrm{p}}\cos(\omega_{\mathrm{p}}t) \ , \tag{B.12}$$

whose solution reads at times $t \gg 1/\kappa$:

$$\xi(t) = \frac{-i\varepsilon_{\mathrm{p}}/2}{\kappa/2 + i(\omega_{\mathrm{a}} - \omega_{\mathrm{p}})}e^{-i\omega_{\mathrm{p}}t} - \frac{i\varepsilon_{\mathrm{p}}/2}{\kappa/2 + i(\omega_{\mathrm{a}} + \omega_{\mathrm{p}})}e^{i\omega_{\mathrm{p}}t} \tag{B.13}$$

Since the pump tone is very off-resonant, the second term (counter-propagating) is not negligible with respect to the first one. Moreover, in the regime where $\kappa \ll |\omega_{\mathrm{a}} \pm \omega_{\mathrm{p}}|$ we find:

$$\xi(t) \approx \frac{\varepsilon_{\mathrm{p}}/2}{\omega_{\mathrm{p}} - \omega_{\mathrm{a}}}e^{-i\omega_{\mathrm{p}}t} - \frac{\varepsilon_{\mathrm{p}}/2}{\omega_{\mathrm{p}} + \omega_{\mathrm{a}}}e^{i\omega_{\mathrm{p}}t} \ . \tag{B.14}$$

We define the real quantity Π such that $\xi(t)+\xi^*(t) = \Pi(e^{-i\omega_{\mathrm{p}}t}+e^{i\omega_{\mathrm{p}}t})$. In the limit $|\delta_{\mathrm{a}}| \ll \omega_{\mathrm{a}}$ we find $\Pi \approx \varepsilon_{\mathrm{p}}/3\omega_{\mathrm{a}}$, and $\xi(t) - \xi^*(t) = 2\Pi(e^{-i\omega_{\mathrm{p}}t} - e^{i\omega_{\mathrm{p}}t})$.

Next, restoring the other contributions to the system Hamiltonian, we find in the displaced frame:

$$\partial_t\boldsymbol{\rho}^{\xi}(\boldsymbol{t}) = -\frac{i}{\hbar}\left[\boldsymbol{\mathcal{H}}^{\xi}_{\mathbf{syst}}(\boldsymbol{t}), \boldsymbol{\rho}^{\xi}(\boldsymbol{t})\right] + \sum_{\boldsymbol{L}}\mathcal{D}[\boldsymbol{L}]\boldsymbol{\rho}^{\xi}(\boldsymbol{t}) \tag{B.15}$$

where:

$$\boldsymbol{\mathcal{H}}^{\xi}_{\mathbf{syst}}(\boldsymbol{t}) = \boldsymbol{\mathcal{H}}_{\mathbf{a,0}} + \boldsymbol{\mathcal{H}}^{\xi}_{\mathbf{a,nl}}(\boldsymbol{t}) + \boldsymbol{\mathcal{H}}_{\boldsymbol{q}} + \boldsymbol{\mathcal{V}}^{\xi}(\boldsymbol{t}) + \boldsymbol{\mathcal{H}}^{\xi}_{\mathbf{d,a}}(\boldsymbol{t}) + \boldsymbol{\mathcal{H}}_{\mathbf{d},\boldsymbol{q}}(\boldsymbol{t}) \tag{B.16}$$

and:

$$\boldsymbol{\mathcal{H}}^{\xi}_{\mathbf{a,nl}}(\boldsymbol{t})/\hbar = g_3\big(\mathbf{a} + \mathbf{a}^{\dagger} + \Pi e^{-i\omega_{\mathrm{p}}t} + \Pi e^{i\omega_{\mathrm{p}}t}\big)^3 \tag{B.17a}$$

$$\boldsymbol{\mathcal{V}}^{\xi}(\boldsymbol{t})/\hbar = -g\big(\mathbf{a} - \mathbf{a}^{\dagger} + 2\Pi e^{-i\omega_{\mathrm{p}}t} - 2\Pi e^{i\omega_{\mathrm{p}}t}\big)\big(\mathbf{b} - \mathbf{b}^{\dagger}\big) \tag{B.17b}$$

$$\boldsymbol{\mathcal{H}}^{\xi}_{\mathbf{d,a}}(\boldsymbol{t})/\hbar = \varepsilon_{\mathrm{d,a}}\cos(\omega_{\mathrm{d,a}}t)\big(\mathbf{a} + \mathbf{a}^{\dagger} + \Pi e^{-i\omega_{\mathrm{p}}t} + \Pi e^{i\omega_{\mathrm{p}}t}\big) \tag{B.17c}$$

B.1.3 Rotating-wave approximation

In the displaced frame, time dependence has spread though the entire Hamiltonian. Yet, given the natural frequencies of the system ($\omega_{\mathrm{a}},\ \omega_q,\ \omega_{\mathrm{p}}$), there exist rotating frames in which some of the interaction processes are resonant. Then a natural question arises: to what extent can we neglect the other non-resonant processes?

In an attempt to make the parametric processes induced by the pump stand out, we move to a frame rotating at half the pump frequency for both modes. In this new frame, the system density matrix reads $\boldsymbol{\rho}^{\xi,\omega} = \boldsymbol{\mathcal{U}}_\omega \boldsymbol{\rho}^{\xi} \boldsymbol{\mathcal{U}}_\omega^\dagger$ where $\boldsymbol{\mathcal{U}}_\omega = \exp\left\{\frac{i\omega_\mathrm{p}t}{2}\left(\mathbf{a}^\dagger\mathbf{a} + \mathbf{b}^\dagger\mathbf{b}\right)\right\}$, and it follows the master equation:

$$\partial_t \boldsymbol{\rho}^{\xi,\omega}(t) = -\frac{i}{\hbar}\left[\boldsymbol{\mathcal{H}}_\mathbf{syst}^{\xi,\omega}(t), \boldsymbol{\rho}^{\xi,\omega}(t)\right] + \sum_{\boldsymbol{L}} \mathcal{D}[\boldsymbol{L}]\boldsymbol{\rho}^{\xi,\omega}(t)\ , \tag{B.18}$$

where $\boldsymbol{\mathcal{H}}_\mathbf{syst}^{\xi,\omega}(t) = \boldsymbol{\mathcal{U}}_\omega \boldsymbol{\mathcal{H}}_\mathbf{syst}^{\xi}(t)\boldsymbol{\mathcal{U}}_\omega^\dagger - i\hbar\boldsymbol{\mathcal{U}}_\omega \dot{\boldsymbol{\mathcal{U}}}_\omega^\dagger$ is the transformed Hamiltonian. Specifically we find:

$$\boldsymbol{\mathcal{H}}_\mathbf{syst}^{\xi,\omega}(t) = \boldsymbol{\mathcal{H}}_\mathbf{a,0}^{\omega} + \boldsymbol{\mathcal{H}}_\mathbf{a,nl}^{\xi,\omega}(t) + \boldsymbol{\mathcal{H}}_{\boldsymbol{q}}^{\omega} + \boldsymbol{\mathcal{V}}^{\xi,\omega}(t) + \boldsymbol{\mathcal{H}}_\mathbf{d,a}^{\xi,\omega}(t) + \boldsymbol{\mathcal{H}}_{\mathbf{d},\boldsymbol{q}}^{\omega}(t) \tag{B.19}$$

where:

$$\boldsymbol{\mathcal{H}}_\mathbf{a,0}^{\omega}/\hbar = (\omega_\mathrm{a} - \omega_\mathrm{p}/2)\mathbf{a}^\dagger\mathbf{a} \tag{B.20a}$$

$$\boldsymbol{\mathcal{H}}_\mathbf{a,nl}^{\xi,\omega}(t)/\hbar = g_3\left(\mathbf{a}e^{-i\omega_\mathrm{p}t/2} + \mathbf{a}^\dagger e^{i\omega_\mathrm{p}t/2} + \Pi e^{-i\omega_\mathrm{p}t} + \Pi e^{i\omega_\mathrm{p}t}\right)^3 \tag{B.20b}$$

$$\boldsymbol{\mathcal{H}}_{\boldsymbol{q}}^{\omega}/\hbar = (\omega_q - \omega_\mathrm{p}/2)\mathbf{b}^\dagger\mathbf{b} + \frac{\chi_q}{2}\mathbf{b}^{\dagger 2}\mathbf{b}^2 \tag{B.20c}$$

$$\begin{aligned}\boldsymbol{\mathcal{V}}^{\xi,\omega}(t)/\hbar = &-g\left(\mathbf{a}e^{-i\omega_\mathrm{p}t/2} - \mathbf{a}^\dagger e^{i\omega_\mathrm{p}t/2}\right)\left(\mathbf{b}e^{-i\omega_\mathrm{p}t/2} - \mathbf{b}^\dagger e^{i\omega_\mathrm{p}t/2}\right)\\ &- g\left(2\Pi e^{-i\omega_\mathrm{p}t} - 2\Pi e^{i\omega_\mathrm{p}t}\right)\left(\mathbf{b}e^{-i\omega_\mathrm{p}t/2} + \mathbf{b}^\dagger e^{i\omega_\mathrm{p}t/2}\right)\end{aligned} \tag{B.20d}$$

$$\boldsymbol{\mathcal{H}}_\mathbf{d,a}^{\xi,\omega}(t)/\hbar = \frac{\varepsilon_\mathrm{d,a}}{2}\left(e^{-i\omega_\mathrm{d,a}t} + e^{i\omega_\mathrm{d,a}t}\right)\left(\mathbf{a}e^{-i\omega_\mathrm{p}t/2} + \mathbf{a}^\dagger e^{i\omega_\mathrm{p}t/2}\right) \tag{B.20e}$$

$$\boldsymbol{\mathcal{H}}_{\mathbf{d},\boldsymbol{q}}^{\omega}(t)/\hbar = -i\frac{\varepsilon_{\mathrm{d},q}}{2}\left(e^{-i\omega_{\mathrm{d},q}t} + e^{i\omega_{\mathrm{d},q}t}\right)\left(\mathbf{b}e^{-i\omega_\mathrm{p}t/2} - \mathbf{b}^\dagger e^{i\omega_\mathrm{p}t/2}\right) \tag{B.20f}$$

In this rotating frame, the system Hamiltonian features two types of terms: some are steady, and some are rotating at frequencies $\omega_\mathrm{d,a} \pm \omega_\mathrm{p}/2,\ \omega_{\mathrm{d},q} \pm \omega_\mathrm{p}/2,\ \omega_\mathrm{p},\ \frac{3}{2}\omega_\mathrm{p},\ 3\omega_\mathrm{p}$. The oscillating terms have amplitudes of the order of $\varepsilon_\mathrm{d,a},\ \varepsilon_{\mathrm{d},q},\ g_3\Pi^2,\ g_3\Pi^3,\ g,\ g\Pi$, which appear to be all much smaller than the associated oscillating frequencies. The rotating-wave approximation (RWA) states that the solutions of Eq. B.18 are well approximated at long times by the solutions of a similar equation, where the Hamiltonian is replaced by its steady part [Mirrahimi and Rouchon 2015]:

$$\begin{aligned}\overline{\boldsymbol{\mathcal{H}}_\mathbf{syst}^{\xi,\omega}} = &\ \delta_\mathrm{a}\mathbf{a}^\dagger\mathbf{a} + 3g_3\Pi\mathbf{a}^2 + 3g_3\Pi\mathbf{a}^{\dagger 2}\\ &+\delta_q\mathbf{b}^\dagger\mathbf{b} + \frac{\chi_q}{2}\mathbf{b}^{\dagger 2}\mathbf{b}^2 + g\left(\mathbf{a}\mathbf{b}^\dagger + \mathbf{a}^\dagger\mathbf{b}\right)\ .\end{aligned} \tag{B.21}$$

where $\delta_\mathrm{a} = \omega_\mathrm{a} - \omega_\mathrm{p}/2$ and $\delta_q = \omega_q - \omega_\mathrm{p}/2$. Yet, given the scale separation between all the oscillatory terms:

$$\underbrace{\begin{matrix}\omega_\mathrm{d,a} - \omega_\mathrm{p}/2 \\ \omega_{\mathrm{d},q} - \omega_\mathrm{p}/2\end{matrix}}_{\text{Slow oscillating}} \ll \underbrace{\begin{matrix}\omega_\mathrm{d,a} + \omega_\mathrm{p}/2 \\ \omega_{\mathrm{d},q} + \omega_\mathrm{p}/2 \\ \omega_\mathrm{p}\end{matrix} \ll 3\omega_\mathrm{p}/2 \ll 3\omega_\mathrm{p}}_{\text{Fast oscillating}} \tag{B.22}$$

one can include the slow contributions from the drive terms in the approximate dynamics[2]. Overall, the system Hamiltonian reads:

$$\begin{aligned}\tilde{\boldsymbol{\mathcal{H}}}_\textbf{syst}(\boldsymbol{t}) &= \delta_\mathrm{a}\mathbf{a}^\dagger\mathbf{a} - \frac{\lambda}{2}\left(\mathbf{a}^2 + \mathbf{a}^{\dagger 2}\right) + \delta_q\mathbf{b}^\dagger\mathbf{b} + \frac{\chi_q}{2}\mathbf{b}^{\dagger 2}\mathbf{b}^2 + g\left(\mathbf{a}\mathbf{b}^\dagger + \mathbf{a}^\dagger\mathbf{b}\right) \\ &+ \frac{\varepsilon_\mathrm{d,a}}{2}\left(\mathbf{a}e^{i\delta_\mathrm{d,a}t} + \mathbf{a}^\dagger e^{-i\delta_\mathrm{d,a}t}\right) - i\frac{\varepsilon_{\mathrm{d},q}}{2}\left(\mathbf{b}e^{i\delta_{\mathrm{d},q}t} - \mathbf{b}^\dagger e^{-i\delta_{\mathrm{d},q}t}\right) ,\end{aligned} \tag{B.23}$$

where $\lambda = -2g_3\varepsilon_\mathrm{p}\omega_\mathrm{a}$ is the two-photon pump amplitude, and the drive detunings are $\delta_\mathrm{d,a} = \omega_\mathrm{d,a} - \omega_\mathrm{p}/2$ and $\delta_{\mathrm{d},q} = \omega_{\mathrm{d},q} - \omega_\mathrm{p}/2$. Finally in the Bogoliubov basis we find:

$$\begin{aligned}\tilde{\boldsymbol{\mathcal{H}}}_\textbf{syst}(\boldsymbol{t}) = \Omega_\mathrm{a}&\boldsymbol{\alpha}^\dagger\boldsymbol{\alpha} + \delta_q\mathbf{b}^\dagger\mathbf{b} + \frac{\chi_q}{2}\mathbf{b}^{\dagger 2}\mathbf{b}^2 \\ &+ g\cosh r\left(\boldsymbol{\alpha}\mathbf{b}^\dagger + \boldsymbol{\alpha}^\dagger\mathbf{b}\right) + g\sinh r\left(\boldsymbol{\alpha}\mathbf{b} + \boldsymbol{\alpha}^\dagger\mathbf{b}^\dagger\right) \\ &+ \frac{\varepsilon_\mathrm{d,a}}{2}\cosh r\left(\boldsymbol{\alpha}e^{i\delta_\mathrm{d,a}t} + \boldsymbol{\alpha}^\dagger e^{-i\delta_\mathrm{d,a}t}\right) \\ &+ \frac{\varepsilon_\mathrm{d,a}}{2}\sinh r\left(\boldsymbol{\alpha}^\dagger e^{i\delta_\mathrm{d,a}t} + \boldsymbol{\alpha}e^{-i\delta_\mathrm{d,a}t}\right) \\ &- i\frac{\varepsilon_{\mathrm{d},q}}{2}\left(\mathbf{b}e^{i\delta_{\mathrm{d},q}t} - \mathbf{b}^\dagger e^{-i\delta_{\mathrm{d},q}t}\right) .\end{aligned} \tag{B.24}$$

Having applied the RWA to the Hamiltonian part of the master equation, we turn to another situation, where it is used for the dissipative contributions. As mentioned in section 2.1.2, the single-photon loss for the oscillator reads in the Bogoliubov basis:

$$\begin{aligned}\mathcal{D}[\boldsymbol{L}_\textbf{ph}]\boldsymbol{\rho} &= \kappa(1 + \sinh^2 r)\mathcal{D}[\boldsymbol{\alpha}]\boldsymbol{\rho} + \kappa\sinh^2 r\mathcal{D}[\boldsymbol{\alpha}^\dagger]\boldsymbol{\rho} \\ &+ \kappa\frac{\sinh 2r}{2}\left(\mathcal{G}[\boldsymbol{\alpha}]\boldsymbol{\rho} + \mathcal{G}[\boldsymbol{\alpha}^\dagger]\boldsymbol{\rho}\right) ,\end{aligned} \tag{B.25}$$

where the anomalous dissipator superoperator reads: $\mathcal{G}[\boldsymbol{\cdot}]\boldsymbol{\rho} = \boldsymbol{\cdot}\boldsymbol{\rho}\boldsymbol{\cdot} - \frac{1}{2}\{\boldsymbol{\cdot}^2, \boldsymbol{\rho}\}$. Looking at the master equation B.18 in a frame rotating at $\Omega_\mathrm{a}[r]$ for the

---

[2] See exercice 1 part 2.1.3 in [Mirrahimi and Rouchon 2015].

Bogoliubov mode, the anomalous dissipator $\mathcal{G}[\boldsymbol{\alpha}]$ will lead to contributions rotating at $2\Omega_{\mathrm{a}}[r]$ with amplitude $\kappa\frac{\sinh 2r}{2}$. The RWA states that if the amplitude of the rotating terms is small compared to their oscillating frequency, the solutions of the master equation without these terms are a good approximation of the complete one.

B.1.4 Schrieffer-Wolff transformation

Finally we skecth the Schrieffer-Wolff transformation at the heart of the perturbative analysis followed in chapter 3. Looking at the undriven part of Eq. B.23, we find:

$$\tilde{\mathcal{H}}_{\mathbf{syst}} = \underbrace{\delta_{\mathrm{a}}\mathbf{a}^\dagger\mathbf{a} - \frac{\lambda}{2}\left(\mathbf{a}^2 + \mathbf{a}^{\dagger 2}\right) + \delta_q\frac{\boldsymbol{\sigma}_{\mathbf{z}}}{2}}_{\tilde{\mathcal{H}}_{\mathbf{0}}} + \underbrace{g\left(\mathbf{a}\boldsymbol{\sigma}_{\text{-}} + \mathbf{a}^\dagger\boldsymbol{\sigma}_+\right)}_{\tilde{\mathcal{V}}} , \tag{B.26}$$

and we define the parameter η such that $||\tilde{\mathcal{V}}|| = \eta||\tilde{\mathcal{H}}_{\mathbf{0}}||$, where $||\cdot||$ is any norm for operators. Depending on the regime of parameters, the dispersive limits presented in chapter 3 ensure that $\tilde{\mathcal{V}}$ can be treated as a perturbation to $\tilde{\mathcal{H}}_{\mathbf{0}}$. Using the Baker-Campbell-Hausdorff formula, we write a perturbative expansion of the system Hamiltonian:

$$e^{\mathcal{S}}\tilde{\mathcal{H}}_{\mathbf{syst}}e^{\text{-}\mathcal{S}} = \tilde{\mathcal{H}}_{\mathbf{0}} + \tilde{\mathcal{V}} + \sum_{n>0}\frac{1}{n!}\Big[\underbrace{\mathcal{S},\ldots[\mathcal{S}}_{n \text{ times}},\tilde{\mathcal{H}}_{\mathbf{0}} + \tilde{\mathcal{V}}]\Big] , \tag{B.27}$$

where $\mathcal{S}$ is the generator of the Schrieffer-Wolff (SW) transformation $\mathcal{U}_{\mathbf{SW}} = e^{\mathcal{S}}$. Assuming for the moment that $||\mathcal{S}|| = \mathcal{O}(\eta)$, we can reorganize this expansion into groups of successive orders of η:

$$\begin{aligned} e^{\mathcal{S}}\tilde{\mathcal{H}}_{\mathbf{syst}}e^{\text{-}\mathcal{S}} = {} & \tilde{\mathcal{H}}_{\mathbf{0}} && \mathcal{O}(1) \\ & + \tilde{\mathcal{V}} + \left[\mathcal{S},\tilde{\mathcal{H}}_{\mathbf{0}}\right] && \mathcal{O}(\eta) \\ & + \left[\mathcal{S},\tilde{\mathcal{V}}\right] + \frac{1}{2!}\Big[\mathcal{S},\left[\mathcal{S},\tilde{\mathcal{H}}_{\mathbf{0}}\right]\Big] && \mathcal{O}(\eta^2) \\ & + \ldots \end{aligned} \tag{B.28}$$

Then, we can find the SW generator that will cancel the perturbation to $\tilde{\mathcal{H}}_{\mathbf{0}}$ up to any order. Specifically, cancellation of the 1st order terms requires $\left[\mathcal{S},\tilde{\mathcal{H}}_{\mathbf{0}}\right] = -\tilde{\mathcal{V}}$, so that the approximate Hamiltonian reads:

$$e^{\mathcal{S}}\tilde{\mathcal{H}}_{\mathbf{syst}}e^{\text{-}\mathcal{S}} = \tilde{\mathcal{H}}_{\mathbf{0}} + \frac{1}{2}\left[\mathcal{S},\tilde{\mathcal{V}}\right] + \mathcal{O}(\eta^3) . \tag{B.29}$$

If the equation $\left[\boldsymbol{\mathcal{S}}, \tilde{\boldsymbol{\mathcal{H}}}_{\mathbf{0}}\right] = -\tilde{\boldsymbol{\mathcal{V}}}$ does not find a solution for $||\boldsymbol{\mathcal{S}}|| = \mathcal{O}(\eta)$, one can rewrite the perturbative expansion for $||\boldsymbol{\mathcal{S}}|| = \mathcal{O}(\eta^2)$ and look iteratively for solutions.

B.2 Input-output theory for squeezed photons

The resonator drives (pump and probe) are applied through an inductively coupled feedline hosting a continuum of modes $\{\boldsymbol{c}(\boldsymbol{\omega})\}_{\omega}$, which will ultimately interact with mode **a**. Similarly, the transmon drive is applied through a capacitevely coupled feedline hosting a continuum of modes $\{\boldsymbol{d}(\boldsymbol{\omega})\}_{\omega}$, which will ultimately interact with mode **b**. They can be thought of as set of harmonic oscillators at all possible frequencies $\omega \in [0, +\infty)$ described by the Hamiltonian:

$$\boldsymbol{\mathcal{H}}_{\mathbf{bath}}/\hbar = \int_0^\infty \mathrm{d}\omega' \omega' \boldsymbol{c}(\boldsymbol{\omega'})^\dagger \boldsymbol{c}(\boldsymbol{\omega'}) + \int_0^\infty \mathrm{d}\omega' \omega' \boldsymbol{d}(\boldsymbol{\omega'})^\dagger \boldsymbol{d}(\boldsymbol{\omega}) \ . \tag{B.30}$$

This bath Hamiltonian can be derived from first principles by analyzing the structure of the transmission lines [Blais 2021]. The bath operators follow the commutation relations:

$$\left[\boldsymbol{c}(\boldsymbol{\omega}), \boldsymbol{c}(\boldsymbol{\omega'})^\dagger\right] = \boldsymbol{\delta}(\boldsymbol{\omega}-\boldsymbol{\omega'}) \ , \qquad \left[\boldsymbol{d}(\boldsymbol{\omega}), \boldsymbol{d}(\boldsymbol{\omega'})^\dagger\right] = \boldsymbol{\delta}(\boldsymbol{\omega}-\boldsymbol{\omega'}) \ , \tag{B.31}$$

such that they are homogeneous to $[\omega^{-1/2}]$. The resonator (transmon) is inductively (capacitevely) coupled to its feedline at a rate κ (γ_1), so that the interaction Hamiltonian reads:

$$\begin{aligned} \boldsymbol{\mathcal{H}}_{\mathbf{int}}/\hbar = & \sqrt{\frac{\kappa}{2\pi}} \int_0^\infty \mathrm{d}\omega' \left(\mathbf{a} + \mathbf{a}^\dagger\right) \left[\boldsymbol{c}(\boldsymbol{\omega'}) + \boldsymbol{c}(\boldsymbol{\omega'})^\dagger\right] \\ & - \sqrt{\frac{\gamma_1}{2\pi}} \int_0^\infty \mathrm{d}\omega' \left(\mathbf{b} - \mathbf{b}^\dagger\right) \left[\boldsymbol{d}(\boldsymbol{\omega'}) - \boldsymbol{d}(\boldsymbol{\omega'})^\dagger\right] \end{aligned} \tag{B.32}$$

The latter expression assumes the Markov approximation which neglects the frequency dependence of the coupling constants: $\kappa(\omega) \approx \kappa$ and $\gamma_1(\omega) \approx \gamma_1$. This approximation is well verified in our experiment since the impedance of the transmission line is almost flat over the frequency windows sampled by the resonator and the transmon. As of now we extend the lower integration limit from 0 to $-\infty$. While mathematically convenient, this will not change the result as only a small frequency window around the bare mode frequencies will significantly couple to the system.

We follow the same treatment for the total Hamiltonian as in the previous subsection. While the bath part is trivially modified, the transformed interaction part writes in the Bogoliubov basis:

$$\begin{aligned}\overline{\boldsymbol{\mathcal{H}}_{\textbf{int}}^{\xi,\omega}}/\hbar =&\sqrt{\frac{\kappa}{2\pi}}\int_{-\infty}^{\infty}\mathrm{d}\omega'\Big\{\cosh r\Big[\boldsymbol{\alpha}\boldsymbol{c}(\boldsymbol{\omega}')^{\dagger}+\boldsymbol{\alpha}^{\dagger}\boldsymbol{c}(\boldsymbol{\omega}')\Big]\\ &\qquad\qquad\qquad\qquad+\sinh r\Big[\boldsymbol{\alpha}\boldsymbol{c}(\boldsymbol{\omega}')+\boldsymbol{\alpha}^{\dagger}\boldsymbol{c}(\boldsymbol{\omega}')^{\dagger}\Big]\Big\}\\ &+\sqrt{\frac{\gamma_1}{2\pi}}\int_{-\infty}^{\infty}\mathrm{d}\omega'\Big\{\mathbf{b}\boldsymbol{d}(\boldsymbol{\omega}')^{\dagger}+\mathbf{b}^{\dagger}\boldsymbol{d}(\boldsymbol{\omega}')\Big\}\ .\end{aligned}\tag{B.33}$$

At this stage the RWA is valid as long as $\kappa e^{r}/2 \ll \omega_p$ and $\gamma_1 \ll \omega_p$, a regime safely maintained for all squeezing values. In the following we set $g = 0$ to keep the notations short, as it will trivially modify the results. We write the equations of motion for the Heisenberg operators $\partial_t\boldsymbol{\mathcal{O}}(\boldsymbol{t}) = \frac{i}{\hbar}\big[\boldsymbol{\mathcal{H}}_{\textbf{tot}}, \boldsymbol{\mathcal{O}}(\boldsymbol{t})\big]$ such that:

$$\begin{aligned}\partial_t\boldsymbol{\alpha}(\boldsymbol{t}) =&-i\Omega_a[r]\boldsymbol{\alpha}(\boldsymbol{t})-i\frac{\varepsilon_{\mathrm{d,a}}\cosh r}{2}e^{-i\delta_{\mathrm{d,a}}t}-i\frac{\varepsilon_{\mathrm{d,a}}\sinh r}{2}e^{i\delta_{\mathrm{d,a}}t}\\ &-i\sqrt{\frac{\kappa}{2\pi}}\int_{-\infty}^{\infty}\mathrm{d}\omega'\ \Big\{\boldsymbol{c}(\boldsymbol{\omega}')\cosh r+\boldsymbol{c}(\boldsymbol{\omega}')^{\dagger}\sinh r\Big\}\ ,\end{aligned}\tag{B.34a}$$

$$\partial_t\boldsymbol{c}(\boldsymbol{\omega}') = -i\omega'\boldsymbol{c}(\boldsymbol{\omega}')-i\sqrt{\frac{\kappa}{2\pi}}\Big(\boldsymbol{\alpha}(\boldsymbol{t})\cosh r+\boldsymbol{\alpha}(\boldsymbol{t})^{\dagger}\sinh r\Big)\ ,\tag{B.34b}$$

$$\partial_t\mathbf{b}(\boldsymbol{t}) = -i\delta_q\mathbf{b}(\boldsymbol{t})-\frac{\varepsilon_{\mathrm{d},q}}{2}e^{-i\delta_{\mathrm{d},q}t}-i\sqrt{\frac{\gamma_1}{2\pi}}\int_{-\infty}^{\infty}\mathrm{d}\omega'\boldsymbol{d}(\boldsymbol{\omega}')\ ,\tag{B.34c}$$

$$\partial_t\boldsymbol{d}(\boldsymbol{\omega}') = -i\omega'\boldsymbol{d}(\boldsymbol{\omega}')-i\sqrt{\frac{\gamma_1}{2\pi}}\mathbf{b}(\boldsymbol{t})\ ,\tag{B.34d}$$

where the explicit time-dependence of the operators $\boldsymbol{c}(\boldsymbol{\omega})(\boldsymbol{t})$ and $\boldsymbol{d}(\boldsymbol{\omega})(\boldsymbol{t})$ has been omitted. Next we integrate Eqs. B.34band B.34d from a past reference time t_0 until the experiment time t, and define the input field operators:

$$\mathbf{a}_{\textbf{in}}(\boldsymbol{t}) = \frac{-i}{\sqrt{2\pi}}\int_{-\infty}^{\infty}\mathrm{d}\omega'\boldsymbol{c}(\boldsymbol{\omega}')(\boldsymbol{t_0})e^{-i\omega'(t-t_0)}\tag{B.35a}$$

$$\mathbf{b}_{\textbf{in}}(\boldsymbol{t}) = \frac{-i}{\sqrt{2\pi}}\int_{-\infty}^{\infty}\mathrm{d}\omega'\boldsymbol{d}(\boldsymbol{\omega}')(\boldsymbol{t_0})e^{-i\omega'(t-t_0)}\tag{B.35b}$$

so that Eqs. B.34aand B.34c can be rewritten as[3]:

$$
\begin{aligned}
\partial_t \boldsymbol{\alpha}(\boldsymbol{t}) =& - i\Omega_a[r]\boldsymbol{\alpha}(\boldsymbol{t}) - i\frac{\varepsilon_{\mathrm{d,a}}\cosh r}{2}e^{-i\delta_{\mathrm{d,a}}t} - i\frac{\varepsilon_{\mathrm{d,a}}\sinh r}{2}e^{i\delta_{\mathrm{d,a}}t} \\
&- \frac{\kappa}{2}\boldsymbol{\alpha}(\boldsymbol{t}) + \sqrt{\kappa}\left(\boldsymbol{a}_{\mathbf{in}}(\boldsymbol{t})\cosh r - \boldsymbol{a}_{\mathbf{in}}(\boldsymbol{t})^\dagger \sinh r\right) \qquad \text{(B.37a)} \\
\partial_t \mathbf{b}(\boldsymbol{t}) =& - i\delta_q \mathbf{b}(\boldsymbol{t}) - \frac{\varepsilon_{\mathrm{d},q}}{2}e^{-i\delta_{\mathrm{d},q}t} - \frac{\gamma_1}{2}\mathbf{b}(\boldsymbol{t}) + \sqrt{\gamma_1}\mathbf{b}_{\mathbf{in}}(\boldsymbol{t}) \qquad \text{(B.37b)}
\end{aligned}
$$

These are the quantum Langevin equations (QLE) for the BO and transmon modes, where the input fields amount to noisy contributions with zero mean. They obey the commutation relations: $\left[\mathbf{a}_{\mathbf{in}}(\boldsymbol{t}), \mathbf{a}_{\mathbf{in}}(\boldsymbol{t'})^\dagger\right] = \boldsymbol{\delta}(\boldsymbol{t}-\boldsymbol{t'})$, $\left[\mathbf{a}_{\mathbf{in}}(\boldsymbol{t}), \mathbf{a}_{\mathbf{in}}(\boldsymbol{t'})\right] = 0$ (same for $\mathbf{b}_{\mathbf{in}}(\boldsymbol{t})$). The temperature of the oscillator environment is defined through the thermal occupancy $\bar{n}_{\mathrm{th}}$ such that:

$$
\begin{aligned}
\langle \boldsymbol{a}_{\mathbf{in}}(\boldsymbol{t})^\dagger \boldsymbol{a}_{\mathbf{in}}(\boldsymbol{t'})\rangle &= \bar{n}_{\mathrm{th}}\boldsymbol{\delta}(\boldsymbol{t}-\boldsymbol{t'}) \ , \qquad \text{(B.38a)} \\
\langle \boldsymbol{a}_{\mathbf{in}}(\boldsymbol{t})\boldsymbol{a}_{\mathbf{in}}(\boldsymbol{t'})^\dagger\rangle &= \left(1+\bar{n}_{\mathrm{th}}\right)\boldsymbol{\delta}(\boldsymbol{t}-\boldsymbol{t'}) \ , \qquad \text{(B.38b)}
\end{aligned}
$$

and similarly for the transmon. Interestingly the drive on the resonator could have been omitted in the Hamiltonian, and included directly at the level of the QLE by replacing $\mathbf{a}_{\mathbf{in}}(\boldsymbol{t})$ by $\mathbf{a}_{\mathbf{in}}(\boldsymbol{t}) - i(\varepsilon_{\mathrm{d,a}}/2\sqrt{\kappa})e^{-i\delta_{\mathrm{d,a}}t}$ (similarly for the transmon). Indeed, a drive propagating through the feedline is nothing but a displacement of the bath field by a classical amplitude.

In addition, Eqs. B.34b and B.34d could have also been integrated from a future time t_1 until the experiment time t, defining the output filed operators:

$$
\begin{aligned}
\mathbf{a}_{\mathbf{out}}(\boldsymbol{t}) &= \frac{i}{\sqrt{2\pi}}\int_{-\infty}^{\infty} \mathrm{d}\omega' \boldsymbol{c}(\boldsymbol{\omega'})(\boldsymbol{t_1})e^{-i\omega'(t-t_1)} \ , \qquad \text{(B.39a)} \\
\mathbf{b}_{\mathbf{out}}(\boldsymbol{t}) &= \frac{i}{\sqrt{2\pi}}\int_{-\infty}^{\infty} \mathrm{d}\omega' \boldsymbol{d}(\boldsymbol{\omega'})(\boldsymbol{t_1})e^{-i\omega'(t-t_1)} \ . \qquad \text{(B.39b)}
\end{aligned}
$$

---

[3] Specifically, integration of Eq. B.34d from a past reference time t_0 yields:

$$
\boldsymbol{d}(\boldsymbol{\omega'})(\boldsymbol{t}) = \boldsymbol{d}(\boldsymbol{\omega'})(\boldsymbol{t_0})e^{-i\omega'(t-t_0)} - i\sqrt{\frac{\gamma_1}{2\pi}}\int_{t_0}^{t} \mathrm{d}\tau \mathbf{b}(\boldsymbol{\tau})e^{-i\omega'(t-\tau)} \ , \qquad \text{(B.36)}
$$

So that the last term of Eq. B.34c reads:

$$
-i\sqrt{\frac{\gamma_1}{2\pi}}\int_{-\infty}^{\infty} \mathrm{d}\omega' \boldsymbol{d}(\boldsymbol{\omega'}) = \sqrt{\gamma_1}\mathbf{b}_{\mathbf{in}}(\boldsymbol{t}) - \gamma_1\int_{t_0}^{t} \mathrm{d}\tau \mathbf{b}(\boldsymbol{\tau})\delta(t-\tau) \ ,
$$

where we exchanged time and frequency integrals, and used the identity A.2. Finally, the dirac distribution splits on the border of the integral: $\int_{t_0}^{t} \mathrm{d}\tau \mathbf{b}(\boldsymbol{\tau})\delta(t-\tau) = \mathbf{b}(\boldsymbol{t})/2$ so that one recovers Eq. B.37b. A similar line of reasoning holds for the $\boldsymbol{\alpha}$ mode.

The output fields follow similar properties as the input fields. Finally they satisfy the closure relations[4]:

$$\mathbf{a}_{\mathbf{out}}(\boldsymbol{t}) + \mathbf{a}_{\mathbf{in}}(\boldsymbol{t}) = \sqrt{\kappa}\big(\boldsymbol{\alpha}(\boldsymbol{t})\cosh r + \boldsymbol{\alpha}(\boldsymbol{t})^\dagger \sinh r\big) \ , \tag{B.41a}$$

$$\mathbf{b}_{\mathbf{out}}(\boldsymbol{t}) + \mathbf{b}_{\mathbf{in}}(\boldsymbol{t}) = \sqrt{\gamma_1}\mathbf{b}(\boldsymbol{t}) \ . \tag{B.41b}$$

Together, the QLE B.37a and the input-output relation B.41a fully capture the dynamics of the squeezed photons in contact with their environment. It is here described in terms of the incoming and outcoming fields of the bare mode **a**, which correspond to the physical port used to drive and read-out the BO.

---

[4] Integrating Eq. B.34d from a future reference time t_1 yields:

$$\boldsymbol{d}(\boldsymbol{\omega}')(\boldsymbol{t}) = \boldsymbol{d}(\boldsymbol{\omega}')(\boldsymbol{t_1})e^{-i\omega'(t-t_1)} + i\sqrt{\frac{\gamma_1}{2\pi}}\int_t^{t_1} \mathrm{d}\tau \mathbf{b}(\boldsymbol{\tau})e^{-i\omega'(t-\tau)} \ , \tag{B.40}$$

Further integrating the previous equation, and Eq. B.36 over all frequencies yields:

$$\int_{-\infty}^{\infty} \mathrm{d}\omega' \boldsymbol{d}(\boldsymbol{\omega}')(\boldsymbol{t}) = i\sqrt{2\pi}\mathbf{b}_{\mathbf{in}}(\boldsymbol{t}) - i\sqrt{\frac{\pi\gamma_1}{2}}\mathbf{b}(\boldsymbol{t}) \ ,$$

$$\int_{-\infty}^{\infty} \mathrm{d}\omega' \boldsymbol{d}(\boldsymbol{\omega}')(\boldsymbol{t}) = -i\sqrt{2\pi}\mathbf{b}_{\mathbf{out}}(\boldsymbol{t}) + i\sqrt{\frac{\pi\gamma_1}{2}}\mathbf{b}(\boldsymbol{t}) \ ,$$

where we used again the splitting of the dirac distribution. From the last two equations we deduce the input-output relation for mode **b**, and we can proceed similarly for mode $\boldsymbol{\alpha}$.

BIBLIOGRAPHY

Aquino, Nava, José Alberto, de Sousa, and Rogério (2023). "Model for 1/f Flux noise in Superconducting Aluminum Devices: Impact of External Magnetic Fields". In: (cit. on p. 97).

Aspelmeyer, Markus, Tobias J. Kippenberg, and Florian Marquardt (Dec. 2014). "Cavity optomechanics". In: *Rev. Mod. Phys.* 86 (4), pp. 1391–1452 (cit. on p. 3).

Ball, Philip (2021). "First quantum computer to pack 100 qubits enters crowded race". In: *Nature* 599, p. 542 (cit. on p. 92).

Basdevant, Jean-Louis and Jean Dalibard (2002). *Quantum Mechanics*. Springer (cit. on p. 3).

Bernat, T. P., N. B. Alexander, and J. L. Kaae (2007). "Thermal and electrical conductivities of electroplated gold". In: *Fusion Science and Technology* 51.4, pp. 782–785 (cit. on p. 101).

Bertet, P., I. Chiorescu, G. Burkard, K. Semba, C. J. P. M. Harmans, D. P. DiVincenzo, and J. E. Mooij (Dec. 2005). "Dephasing of a Superconducting Qubit Induced by Photon Noise". In: *Phys. Rev. Lett.* 95 (25), p. 257002 (cit. on pp. 73, 85).

Besedin, Ilya and Alexey P. Menushenkov (2018). "Quality factor of a transmission line coupled coplanar waveguide resonator". In: *EPJ Quantum Technology* 5.1, p. 2 (cit. on p. 39).

Bienfait, A., P. Campagne-Ibarcq, A. H. Kiilerich, X. Zhou, S. Probst, J. J. Pla, T. Schenkel, D. Vion, D. Esteve, J. J.L. Morton, K. Moelmer, and P. Bertet (2017). "Magnetic resonance with squeezed microwaves". In: *Phys. Rev. X* 7 (4), pp. 1–11 (cit. on pp. 52, 122).

Bienfait, A., J. J. Pla, Y. Kubo, X. Zhou, M. Stern, C. C. Lo, C. D. Weis, T. Schenkel, D. Vion, D. Esteve, J. J. L. Morton, and P. Bertet (Feb. 2016). "Controlling spin relaxation with a cavity". In: *Nature* 531.7592, pp. 74–77 (cit. on p. 102).

Bishop, Lev S., J. M. Chow, Jens Koch, A. A. Houck, M. H. Devoret, E. Thuneberg, S. M. Girvin, and R. J. Schoelkopf (2009). "Nonlinear response of the vacuum Rabi resonance". In: *Nat. Phys.* 5.2, pp. 105–109 (cit. on p. 52).

Blais, Alexandre, Arne L. Grimsmo, S. M. Girvin, and Andreas Wallraff (May 2021). "Circuit quantum electrodynamics". In: *Rev. Mod. Phys.* 93 (2), p. 025005 (cit. on pp. 3, 5, 11, 55, 66, 69–71, 136).

Blais, Alexandre, Ren Shou Huang, Andreas Wallraff, S. M. Girvin, and R. J. Schoelkopf (2004). "Cavity quantum electrodynamics for superconducting electrical circuits: An architecture for quantum computation". In: *Phys. Rev. A* 69 (6), pp. 1–14 (cit. on pp. 6, 7, 12, 71).

Boissonneault, Maxime, J. M. Gambetta, and Alexandre Blais (June 2008). "Nonlinear dispersive regime of cavity QED: The dressed dephasing model". In: *Phys. Rev. A* 77 (6), p. 060305 (cit. on p. 69).

— (Jan. 2009). "Dispersive regime of circuit QED: Photon-dependent qubit dephasing and relaxation rates". In: *Phys. Rev. A* 79 (1), p. 013819 (cit. on pp. 66, 69).

Bonsen, Tobias, Patrick Harvey-Collard, Maximilian Russ, Jurgen Dijkema, Amir Sammak, Giordano Scappucci, and Lieven M. K. Vandersypen (2022). *Probing the Jaynes-Cummings ladder with spin circuit quantum electrodynamics*. eprint: `arXiv:2203.05668` (cit. on p. 52).

Bothner, D., M. Knufinke, H. Hattermann, R. Wölbing, B. Ferdinand, P. Weiss, S. Bernon, J. Fortágh, D. Koelle, and R. Kleiner (2013). "Inductively coupled superconducting half wavelength resonators as persistent current traps for ultracold atoms". In: *New J. Phys* 15, p. 093024 (cit. on p. 39).

Boutin, Samuel, David M. Toyli, Aditya V. Venkatramani, Andrew W. Eddins, Irfan Siddiqi, and Alexandre Blais (2017). "Effect of Higher-Order Nonlinearities on Amplification and Squeezing in Josephson Parametric Amplifiers". In: *Phys. Rev. Applied* 8 (5), pp. 1–22 (cit. on pp. 16, 36).

Boyd, Robert W. (2008). *Nonlinear Optics*. Academic Press (cit. on pp. 14, 15).

Braak, D. (Aug. 2011). "Integrability of the Rabi Model". In: *Phys. Rev. Lett.* 107 (10), p. 100401 (cit. on p. 66).

Braunstein, Samuel L. and Robert I. McLachlan (Feb. 1987). "Generalized squeezing". In: *Phys. Rev. A* 35 (4), pp. 1659–1667 (cit. on p. 16).

Bravyi, Sergey, David P. DiVincenzo, and Daniel Loss (2011). "Schrieffer-Wolff transformation for quantum many-body systems". In: *Annals of Physics* 326 (10), pp. 2793–2826 (cit. on p. 68).

Bruhat, L. E, T. Cubaynes, J. J. Viennot, M. C. Dartiailh, M. M. Desjardins, A. Cottet, and T. Kontos (Oct. 2018). "Circuit QED with a quantum-dot charge qubit dressed by Cooper pairs". In: *Phys. Rev. B* 98 (15), p. 155313 (cit. on p. 124).

Burd, S. C., R. Srinivas, H. M. Knaack, W. Ge, A. C. Wilson, D. J. Wineland, D. Leibfried, J. J. Bollinger, D. T. C. Allcock, and D. H. Slichter (2021). "Quantum amplification of boson-mediated interactions". In: *Nature Physics* 17.8, pp. 898–902 (cit. on pp. 10, 11, 121).

Carmichael, H. J., G. J. Milburn, and D. F. Walls (1984). "Squeezing in a detuned parametric amplifier". In: *Journal of Physics A: Mathematical and General* 17 (2), pp. 469–480 (cit. on pp. 9, 19, 41).

Carusotto, Iacopo, Andrew A. Houck, Alicia J. Kollár, Pedram Roushan, David I. Schuster, and Jonathan Simon (2020). "Photonic materials in circuit quantum electrodynamics". In: *Nature Physics* 16.3, pp. 268–279 (cit. on p. 4).

Castellanos-Beltran, M. A., K. D. Irwin, G. C. Hilton, L. R. Vale, and K. W. Lehnert (2008). "Amplification and squeezing of quantum noise with a tunable Josephson metamaterial". In: *Nature Physics* 4 (12), pp. 928–931 (cit. on p. 14).

Caves, Carlton M. (Apr. 1981). "Quantum-mechanical noise in an interferometer". In: *Phys. Rev. D* 23 (8), pp. 1693–1708 (cit. on p. 13).

Chang, C. W. Sandbo, Carlos Sabı´n, P. Forn-Dı´az, Fernando Quijandrı´a, A. M. Vadiraj, I. Nsanzineza, G. Johansson, and C. M. Wilson (Jan. 2020). "Observation of Three-Photon Spontaneous Parametric Down-Conversion in a Superconducting Parametric Cavity". In: *Phys. Rev. X* 10 (1), p. 011011 (cit. on p. 16).

Chen, Xi, Ze Wu, Min Jiang, Xin-You Lü, Xinhua Peng, and Jiangfeng Du (2021). "Experimental quantum simulation of superradiant phase transition beyond no-go theorem via antisqueezing". In: *Nature Communications* 12.1, p. 6281 (cit. on pp. 11, 121).

Clarke, John and Frank K. Wilhelm (2008). "Superconducting quantum bits". In: *Nature* 453.7198, pp. 1031–1042 (cit. on p. 119).

Clerk, A. A., K. W. Lehnert, P. Bertet, J. R. Petta, and Y. Nakamura (2020). "Hybrid quantum systems with circuit quantum electrodynamics". In: *Nature Physics* 16.3, pp. 257–267 (cit. on pp. 3–5).

Cohen-Tannoudji, Claude, Jacques Dupont-Roc, and Gilbert Grynberg (2001). *Processus d'interaction entre photons et atomes*. EDP Sciences - CNRS Éditions (cit. on p. 1).

Connolly, Thomas, Pavel D. Kurilovich, Spencer Diamond, Heekun Nho, Charlotte G. L. Bøttcher, Leonid I. Glazman, Valla Fatemi, and Michel H. Devoret (2023). *Coexistence of nonequilibrium density and equilibrium energy distribution of quasiparticles in a superconducting qubit*. arXiv: `2302.12330 [quant-ph]` (cit. on p. 97).

Contamin, Lauriane, T. Cubaynes, W. Legrand, M. Marganska, M. Villiers, M. M. Desjardins, M. C. Dartiailh, V. Vinel, Z. Leghtas, A. Thiaville, S. Rohart, A. Cottet, M. R. Delbecq, and T. Kontos (Feb. 2023). "Inhomogeneous magnetic fields interacting with spinful states in a double quantum dot: Evidence for a staggered spin-orbit interaction". In: *Phys. Rev. B* 107 (8), p. 085152 (cit. on p. 124).

Contamin, Lauriane, Lucas Jarjat, William Legrand, Audrey Cottet, Takis Kontos, and Matthieu R. Delbecq (2022). "Zero energy states clustering in an elemental nanowire coupled to a superconductor". In: *Nature Communications* 13.1, p. 6188 (cit. on p. 124).

Cottet, Audrey, Matthieu C. Dartiailh, Matthieu M. Desjardins, Tino Cubaynes, Lauriane C. Contamin, Matthieu Delbecq, Jérémie J. Viennot, Laure E. Bruhat, Benoit Douçot, and Takis Kontos (2017). "Cavity QED with hybrid nanocircuits: From atomic-like physics to condensed matter phenomena". In: *J. Phys.: Condens. Matter* 29 (43) (cit. on pp. 3, 56, 123).

Cottet, Audrey and Takis Kontos (Oct. 2010). "Spin Quantum Bit with Ferromagnetic Contacts for Circuit QED". In: *Phys. Rev. Lett.* 105 (16), p. 160502 (cit. on p. 124).

Cubaynes, T., L. C. Contamin, M. C. Dartiailh, M. M. Desjardins, A. Cottet, M. R. Delbecq, and T. Kontos (2023/04/03 2020). "Nanoassembly technique of carbon nanotubes for hybrid circuit-QED". In: *Applied Physics Letters* 117.11, p. 114001 (cit. on p. 124).

Danilin, Sergey, João Barbosa, Michael Farage, Zimo Zhao, Xiaobang Shang, Jonathan Burnett, Nick Ridler, Chong Li, and Martin Weides (2022). "Engineering the microwave to infrared noise photon flux for superconducting quantum systems". In: *EPJ Quantum Technology* 9 (1), pp. 1–22 (cit. on p. 96).

Dassonneville, R., R. Assouly, T. Peronnin, A.A. Clerk, A. Bienfait, and B. Huard (2021). "Dissipative Stabilization of Squeezing Beyond 3 dB in a Microwave Mode". In: *PRX Quantum* 2 (2), p. 1 (cit. on pp. 66, 121).

Delbecq, M. R., V. Schmitt, F. D. Parmentier, N. Roch, J. J. Viennot, G. Fève, B. Huard, C. Mora, A. Cottet, and T. Kontos (Dec. 2011). "Coupling a Quantum Dot, Fermionic Leads, and a Microwave Cavity on a Chip". In: *Phys. Rev. Lett.* 107 (25), p. 256804 (cit. on p. 124).

Desjardins, M. M., L. C. Contamin, M. R. Delbecq, M. C. Dartiailh, L. E. Bruhat, T. Cubaynes, J. J. Viennot, F. Mallet, S. Rohart, A. Thiaville, A. Cottet, and T. Kontos (2019). "Synthetic spin–orbit interaction for Majorana devices". In: *Nature Materials* 18.10, pp. 1060–1064 (cit. on p. 124).

Desjardins, M. M., J. J. Viennot, M. C. Dartiailh, L. E. Bruhat, M. R. Delbecq, M. Lee, M. -S. Choi, A. Cottet, and T. Kontos (2017). "Observation of the frozen charge of a Kondo resonance". In: *Nature* 545.7652, pp. 71–74 (cit. on p. 124).

Devoret and Martinis (2004). "Implementing Qubits with Superconducting Integrated Circuits". In: *Quantum Information Processing* 3.1, pp. 163–203 (cit. on p. 34).

Devoret and Schoelkopf (2013). "Superconducting Circuits for Quantum Information: An Outlook". In: *Science* 339.March, pp. 1169–1175 (cit. on p. 92).

Eddins, A., J. M. Kreikebaum, D. M. Toyli, E. M. Levenson-Falk, A. Dove, W. P. Livingston, B. A. Levitan, L. C. G. Govia, A. A. Clerk, and I. Siddiqi (Jan. 2019). "High-Efficiency Measurement of an Artificial Atom Embedded in a Parametric Amplifier". In: *Phys. Rev. X* 9 (1), p. 011004 (cit. on pp. 19, 51, 76, 78, 80, 88, 119, 121).

Eddins, A., S. Schreppler, D. M. Toyli, L. S. Martin, S. Hacohen-Gourgy, L. C.G. Govia, H. Ribeiro, A. A. Clerk, and I. Siddiqi (2018). "Stroboscopic Qubit Measurement with Squeezed Illumination". In: *Phys. Rev. Lett.* 120, p. 40505 (cit. on p. 52).

Eichler, Christopher and Andreas Wallraff (2014). "Controlling the dynamic range of a Josephson parametric amplifier". In: *EPJ Quantum Technology* 1.1, p. 2 (cit. on p. 116).

Fink, J. M., M. Göppl, M. Baur, R. Bianchetti, P. J. Leek, A. Blais, and A. Wallraff (2008). "Climbing the Jaynes–Cummings ladder and observing its nonlinearity in a cavity QED system". In: *Nature* 454.7202, pp. 315–318 (cit. on p. 52).

Fink, J. M., L. Steffen, P. Studer, Lev S. Bishop, M. Baur, R. Bianchetti, D. Bozyigit, C. Lang, S. Filipp, P. J. Leek, and A. Wallraff (Oct. 2010). "Quantum-To-Classical Transition in Cavity Quantum Electrodynamics". In: *Phys. Rev. Lett.* 105 (16), p. 163601 (cit. on p. 52).

Frattini, N. E., V. V. Sivak, A. Lingenfelter, S. Shankar, and M. H. Devoret (Nov. 2018). "Optimizing the Nonlinearity and Dissipation of a SNAIL Parametric Amplifier for Dynamic Range". In: *Phys. Rev. Applied* 10 (5), p. 054020 (cit. on pp. 24, 37, 39, 116, 117).

Frattini, N. E., U. Vool, S. Shankar, A. Narla, K. M. Sliwa, and M. H. Devoret (2017). "3-wave mixing Josephson dipole element". In: *Appl. Phys. Lett.* 110.22, p. 222603 (cit. on pp. 15, 37, 39, 117).

Frisk Kockum, Anton, Adam Miranowicz, Simone De Liberato, Salvatore Savasta, and Franco Nori (2019). "Ultrastrong coupling between light and matter”. In: *Nature Reviews Physics* 1.1, pp. 19–40 (cit. on pp. 52, 121).

Gambetta, Jay, Alexandre Blais, M. Boissonneault, A. A. Houck, D. I. Schuster, and S. M. Girvin (Jan. 2008). “Quantum trajectory approach to circuit QED: Quantum jumps and the Zeno effect”. In: *Phys. Rev. A* 77 (1), p. 012112 (cit. on p. 121).

Gambetta, Jay, Alexandre Blais, D. I. Schuster, A. Wallraff, L. Frunzio, J. Majer, M. H. Devoret, S. M. Girvin, and R. J. Schoelkopf (2006). “Qubit-photon interactions in a cavity: Measurement-induced dephasing and number splitting”. In: *Phys. Rev. A* 74 (4), pp. 1–14 (cit. on pp. 71, 73).

Google Quantum AI (2023). “Suppressing quantum errors by scaling a surface code logical qubit”. In: *Nature* 614.7949, pp. 676–681 (cit. on p. 92).

Gottesman, Daniel, Alexei Kitaev, and John Preskill (June 2001). “Encoding a qubit in an oscillator”. In: *Phys. Rev. A* 64 (1), p. 012310 (cit. on p. 16).

Grimm, A., N. E. Frattini, S. Puri, S. O. Mundhada, S. Touzard, M. Mirrahimi, S. M. Girvin, S. Shankar, and M. H. Devoret (2020). “Stabilization and operation of a Kerr-cat qubit”. In: *Nature* 584.7820, pp. 205–209 (cit. on p. 37).

Gyenis, András, Agustin Di Paolo, Jens Koch, Alexandre Blais, Andrew A. Houck, and David I. Schuster (Sept. 2021). “Moving beyond the Transmon: Noise-Protected Superconducting Quantum Circuits”. In: *PRX Quantum* 2 (3), p. 030101 (cit. on p. 119).

Haroche, Serge and Jean-Michel Raimond (2006). *Exploring the Quantum: Atoms, Cavities, and Photons*. Oxford, England: Oxford University Press (cit. on pp. 1, 2).

Harvey-Collard, Patrick, Guoji Zheng, Jurgen Dijkema, Nodar Samkharadze, Amir Sammak, Giordano Scappucci, and Lieven M. K. Vandersypen (Sept. 2020). “On-Chip Microwave Filters for High-Impedance Resonators with Gate-Defined Quantum Dots”. In: *Phys. Rev. Appl.* 14 (3), p. 034025 (cit. on p. 8).

Herrmann, L. G., F. Portier, P. Roche, A. Levy Yeyati, T. Kontos, and C. Strunk (Jan. 2010). “Carbon Nanotubes as Cooper-Pair Beam Splitters”. In: *Phys. Rev. Lett.* 104 (2), p. 026801 (cit. on p. 124).

Hillmann, Timo, Fernando Quijandrı´a, Göran Johansson, Alessandro Ferraro, Simone Gasparinetti, and Giulia Ferrini (Oct. 2020). “Universal Gate Set for Continuous-Variable Quantum Computation with Microwave Circuits”. In: *Phys. Rev. Lett.* 125 (16), p. 160501 (cit. on p. 16).

Huang, Sihao, Benjamin Lienhard, Greg Calusine, Antti Vepsäläinen, Jochen Braumüller, David K. Kim, Alexander J. Melville, Bethany M. Niedzielski, Jonilyn L. Yoder, Bharath Kannan, Terry P. Orlando, Simon Gustavsson, and William D. Oliver (2021). "Microwave Package Design for Superconducting Quantum Processors". In: *PRX Quantum* 2.2, p. 020306. eprint: `2012.01438` (cit. on pp. 101, 106, 112).

Huebl, Hans, Christoph W. Zollitsch, Johannes Lotze, Fredrik Hocke, Moritz Greifenstein, Achim Marx, Rudolf Gross, and Sebastian T. B. Goennenwein (Sept. 2013). "High Cooperativity in Coupled Microwave Resonator Ferrimagnetic Insulator Hybrids". In: *Phys. Rev. Lett.* 111 (12), p. 127003 (cit. on p. 6).

İmamoğlu, A., D. D. Awschalom, G. Burkard, D. P. DiVincenzo, D. Loss, M. Sherwin, and A. Small (Nov. 1999). "Quantum Information Processing Using Quantum Dot Spins and Cavity QED". In: *Phys. Rev. Lett.* 83 (20), pp. 4204–4207 (cit. on p. 3).

Janvier, C., L. Tosi, L. Bretheau, Ç. Ö. Girit, M. Stern, P. Bertet, P. Joyez, D. Vion, D. Esteve, M. F. Goffman, H. Pothier, and C. Urbina (2023/02/09 2015). "Coherent manipulation of Andreev states in superconducting atomic contacts". In: *Science* 349.6253, pp. 1199–1202 (cit. on p. 6).

Jaynes, E.T. and F.W. Cummings (1963). "Comparison of Quantum and Semiclassical Radiation Theories with Application to the Beam Maser". In: *Proceedings of the IEEE*, pp. 89–109 (cit. on p. 50).

Johansson, J. R., P. D. Nation, and Franco Nori (2012). "QuTiP: An open-source Python framework for the dynamics of open quantum systems". In: *Computer Physics Communications* 183.8, pp. 1760–1772 (cit. on p. 62).

Kessler, E. M. (July 2012). "Generalized Schrieffer-Wolff formalism for dissipative systems". In: *Phys. Rev. A* 86 (1), p. 012126 (cit. on p. 77).

Kitzman, J. M., J. R. Lane, T. Stefanski, N. R. Beysengulov, D. Tan, K. W. Murch, and J. Pollanen (Jan. 2022). "Vantablack Shielding of Superconducting Qubit Systems". In: *Journal of Low Temperature Physics* 208.5-6, pp. 467–474 (cit. on p. 97).

Koch, Jens, Terri M. Yu, Jay Gambetta, A. A. Houck, D. I. Schuster, J. Majer, Alexandre Blais, M. H. Devoret, S. M. Girvin, and R. J. Schoelkopf (Oct. 2007). "Charge-insensitive qubit design derived from the Cooper pair box". In: *Phys. Rev. A* 76 (4), p. 042319 (cit. on pp. 54, 56, 70, 76, 97).

Krieger, Jonas (2015). *Design of a superconducting magnetic shield*. ETH Zurich (cit. on p. 97).

Krinner, Sebastian, Nathan Lacroix, Ants Remm, Agustin Di Paolo, Elie Genois, Catherine Leroux, Christoph Hellings, Stefania Lazar, Francois

Swiadek, Johannes Herrmann, Graham J. Norris, Christian Kraglund Andersen, Markus Müller, Alexandre Blais, Christopher Eichler, and Andreas Wallraff (2022). "Realizing repeated quantum error correction in a distance-three surface code". In: *Nature* 605.7911, pp. 669–674 (cit. on p. 92).

Kubo, Y., F. R. Ong, P. Bertet, D. Vion, V. Jacques, D. Zheng, A. Dréau, J.-F. Roch, A. Auffeves, F. Jelezko, J. Wrachtrup, M. F. Barthe, P. Bergonzo, and D. Esteve (Sept. 2010). "Strong Coupling of a Spin Ensemble to a Superconducting Resonator". In: *Phys. Rev. Lett.* 105 (14), p. 140502 (cit. on pp. 6, 7).

Kumar, P., S. Sendelbach, M. A. Beck, J. W. Freeland, Zhe Wang, Hui Wang, Clare C. Yu, R. Q. Wu, D. P. Pappas, and R. McDermott (2016). "Origin and Reduction of 1 /f Magnetic Flux Noise in Superconducting Devices". In: *Physical Review Applied* 6.4, pp. 1–5 (cit. on p. 97).

Lachance-Quirion, Dany, Yutaka Tabuchi, Arnaud Gloppe, Koji Usami, and Yasunobu Nakamura (2019). "Hybrid quantum systems based on magnonics". In: *Applied Physics Express* 12.7, p. 070101 (cit. on p. 3).

Landig, A. J., J. V. Koski, P. Scarlino, U. C. Mendes, A. Blais, C. Reichl, W. Wegscheider, A. Wallraff, K. Ensslin, and T. Ihn (2018). "Coherent spin–photon coupling using a resonant exchange qubit". In: *Nature* 560.7717, pp. 179–184 (cit. on pp. 6–8).

Lemonde, Marc-Antoine, Nicolas Didier, and Aashish A. Clerk (2016). "Enhanced nonlinear interactions in quantum optomechanics via mechanical amplification". In: *Nature Communications* 7.1, p. 11338 (cit. on pp. 11, 84).

Leroux, C., L. C. G. Govia, and A. A. Clerk (Mar. 2018). "Enhancing Cavity Quantum Electrodynamics via Antisqueezing: Synthetic Ultrastrong Coupling". In: *Phys. Rev. Lett.* 120 (9), p. 093602 (cit. on pp. 9, 11, 50–52, 63, 85, 119).

Lescanne, Raphaël, Marius Villiers, Théau Peronnin, Alain Sarlette, Matthieu Delbecq, Benjamin Huard, Takis Kontos, Mazyar Mirrahimi, and Zaki Leghtas (2020). "Exponential suppression of bit-flips in a qubit encoded in an oscillator". In: *Nature Physics* 16.5, pp. 509–513 (cit. on p. 116).

Lienhard, Benjamin, Jochen Braumuller, Wayne Woods, Danna Rosenberg, Greg Calusine, Steven Weber, Antti Vepsalainen, Kevin Obrien, Terry P. Orlando, Simon Gustavsson, and William D. Oliver (2019). "Microwave Packaging for Superconducting Qubits". In: *IEEE MTT-S International Microwave Symposium Digest* 2019-June, pp. 275–278. arXiv: `1906.05425` (cit. on p. 103).

LIGO (2013). "Enhanced sensitivity of the LIGO gravitational wave detector by using squeezed states of light". In: *Nature Photonics* 7.8, pp. 613–619 (cit. on p. 14).

Lü, Wen Ning, Xin Zhu, Fan Wu, Li-Tuo Shen, Zhen-Biao Yang, and Shi-Biao Zheng (Dec. 2022). "Critical quantum sensing based on the Jaynes-Cummings model with a squeezing drive". In: *Phys. Rev. A* 106 (6), p. 062616 (cit. on p. 121).

Lü, Ying Wu, J. R. Johansson, Hui Jing, Jing Zhang, and Franco Nori (Mar. 2015). "Squeezed Optomechanics with Phase-Matched Amplification and Dissipation". In: *Phys. Rev. Lett.* 114 (9), p. 093602 (cit. on pp. 11, 121).

Lupaşcu, A., S. Saito, T. Picot, P. C. de Groot, C. J. P. M. Harmans, and J. E. Mooij (2007). "Quantum non-demolition measurement of a superconducting two-level system". In: *Nature Physics* 3.2, pp. 119–123 (cit. on p. 119).

Macklin, C., K. O'Brien, D. Hover, M. E. Schwartz, V. Bolkhovsky, X. Zhang, W. D. Oliver, and I. Siddiqi (2023/04/05 2015). "A near–quantum-limited Josephson traveling-wave parametric amplifier". In: *Science* 350.6258, pp. 307–310 (cit. on p. 116).

Mallet, François, Florian R. Ong, Agustin Palacios-Laloy, François Nguyen, Patrice Bertet, Denis Vion, and Daniel Esteve (2009). "Single-shot qubit readout in circuit quantum electrodynamics". In: *Nature Physics* 5.11, pp. 791–795 (cit. on p. 119).

Malnou, M., D. A. Palken, B. M. Brubaker, Leila R. Vale, Gene C. Hilton, and K. W. Lehnert (May 2019). "Squeezed Vacuum Used to Accelerate the Search for a Weak Classical Signal". In: *Phys. Rev. X* 9 (2), p. 021023 (cit. on p. 14).

Marković, D., S. Jezouin, Q. Ficheux, S. Fedortchenko, S. Felicetti, T. Coudreau, P. Milman, Z. Leghtas, and B. Huard (July 2018). "Demonstration of an Effective Ultrastrong Coupling between Two Oscillators". In: *Phys. Rev. Lett.* 121 (4), p. 040505 (cit. on p. 121).

Mergenthaler, M., S. Paredes, P. Müller, C. Müller, S. Filipp, M. Sandberg, J. B. Hertzberg, V. P. Adiga, M. Brink, and A. Fuhrer (2021). "Ultrahigh vacuum packaging and surface cleaning for quantum devices". In: *Review of Scientific Instruments* 92.2. arXiv: `2010.12090` (cit. on p. 98).

Metelmann, A., O. Lanes, T-Z. Chien, A. McDonald, M. Hatridge, and A. A. Clerk (2022). *Quantum-limited amplification without instability*. eprint: `arXiv:2208.00024` (cit. on pp. 12, 29, 31, 49).

Mi, X., M. Benito, S. Putz, D. M. Zajac, J. M. Taylor, Guido Burkard, and J. R. Petta (2018). "A coherent spin–photon interface in silicon". In: *Nature* 555.7698, pp. 599–603 (cit. on pp. 6, 7).

Mi, X., J. V. Cady, D. M. Zajac, P. W. Deelman, and J. R. Petta (2023/03/27 2017). "Strong coupling of a single electron in silicon to a microwave photon". In: *Science* 355.6321, pp. 156–158 (cit. on p. 6).

Milburn, G. and D. F. Walls (1981). "Production of squeezed states in a degenerate parametric amplifier". In: *Optics Communications* 39 (6), pp. 401–404 (cit. on p. 9).

Minev, Zlatko K., Zaki Leghtas, Shantanu O. Mundhada, Lysander Christakis, Ioan M. Pop, and Michel H. Devoret (2021). "Energy-participation quantization of Josephson circuits". In: *npj Quantum Information* 7.1, p. 131 (cit. on p. 35).

Mirrahimi, Mazyar and Pierre Rouchon (2015). *Dynamics and Control of Open Quantum Systems* (cit. on pp. 41, 133, 134).

Molinari, Luca Guido (2017). "Notes on Wick's theorem in many-body theory". In: arXiv: `1710.09248 [math-ph]` (cit. on p. 73).

Murch, K. W., S. J. Weber, K. M. Beck, E. Ginossar, and I. Siddiqi (2013a). "Reduction of the radiative decay of atomic coherence in squeezed vacuum". In: *Nature* 499 (7456), pp. 62–65 (cit. on pp. 52, 122).

Murch, K. W., S. J. Weber, C. Macklin, and I. Siddiqi (2013b). "Observing single quantum trajectories of a superconducting quantum bit". In: *Nature* 502.7470, pp. 211–214 (cit. on pp. 14, 119).

Nakamura, Y., Yu. A. Pashkin, and J. S. Tsai (1999). "Coherent control of macroscopic quantum states in a single-Cooper-pair box". In: *Nature* 398.6730, pp. 786–788 (cit. on p. 54).

Nigg, Simon E., Hanhee Paik, Brian Vlastakis, Gerhard Kirchmair, S. Shankar, Luigi Frunzio, M. H. Devoret, R. J. Schoelkopf, and S. M. Girvin (June 2012). "Black-Box Superconducting Circuit Quantization". In: *Phys. Rev. Lett.* 108 (24), p. 240502 (cit. on p. 35).

O'Connell, A. D., M. Hofheinz, M. Ansmann, Radoslaw C. Bialczak, M. Lenander, Erik Lucero, M. Neeley, D. Sank, H. Wang, M. Weides, J. Wenner, John M. Martinis, and A. N. Cleland (2010). "Quantum ground state and single-phonon control of a mechanical resonator". In: *Nature* 464.7289, pp. 697–703 (cit. on p. 6).

Ong, F. R., M. Boissonneault, F. Mallet, A. C. Doherty, A. Blais, D. Vion, D. Esteve, and P. Bertet (Jan. 2013). "Quantum Heating of a Nonlinear Resonator Probed by a Superconducting Qubit". In: *Phys. Rev. Lett.* 110 (4), p. 047001 (cit. on pp. 66, 121).

Ong, F. R., M. Boissonneault, F. Mallet, A. Palacios-Laloy, A. Dewes, A. C. Doherty, A. Blais, P. Bertet, D. Vion, and D. Esteve (Apr. 2011). "Circuit QED with a Nonlinear Resonator: ac-Stark Shift and Dephasing". In: *Phys. Rev. Lett.* 106 (16), p. 167002 (cit. on p. 119).

Petersson, K. D., L. W. McFaul, M. D. Schroer, M. Jung, J. M. Taylor, A. A. Houck, and J. R. Petta (2012). "Circuit quantum electrodynamics with a spin qubit". In: *Nature* 490.7420, pp. 380–383 (cit. on p. 1).

Place, Alexander P. M., Lila V. H. Rodgers, Pranav Mundada, Basil M. Smitham, Mattias Fitzpatrick, Zhaoqi Leng, Anjali Premkumar, Jacob Bryon, Andrei Vrajitoarea, Sara Sussman, Guangming Cheng, Trisha Madhavan, Harshvardhan K. Babla, Xuan Hoang Le, Youqi Gang, Berthold Jäck, András Gyenis, Nan Yao, Robert J. Cava, Nathalie P. de Leon, and Andrew A. Houck (2021). "New material platform for superconducting transmon qubits with coherence times exceeding 0.3 milliseconds". In: *Nature Communications* 12.1, p. 1779 (cit. on p. 98).

Planat, Luca, Rémy Dassonneville, Javier Puertas Martínez, Farshad Foroughi, Olivier Buisson, Wiebke Hasch-Guichard, Cécile Naud, R Vijay, Kater Murch, and Nicolas Roch (2019). "Understanding the Saturation Power of Josephson Parametric Amplifiers Made from SQUID Arrays". In: *Phys. Rev. Applied* 11 (3), pp. 1–12 (cit. on pp. 24, 30, 36, 117).

Pozar, David M. (2011). *Microwave Engineering*. 4th. Wiley (cit. on pp. 5, 44, 93, 96, 100).

Qin, Wei, Adam Miranowicz, Peng-Bo Li, Xin-You Lü, J. Q. You, and Franco Nori (Mar. 2018). "Exponentially Enhanced Light-Matter Interaction, Cooperativities, and Steady-State Entanglement Using Parametric Amplification". In: *Phys. Rev. Lett.* 120 (9), p. 093601 (cit. on pp. 9, 11, 50–52, 85, 119).

Ranadive, Arpit, Martina Esposito, Luca Planat, Edgar Bonet, Cécile Naud, Olivier Buisson, Wiebke Guichard, and Nicolas Roch (2022). "Kerr reversal in Josephson meta-material and traveling wave parametric amplification". In: *Nature Communications* 13.1, p. 1737 (cit. on p. 37).

Ranjan, V., S. Probst, B. Albanese, T. Schenkel, D. Vion, D. Esteve, J. J. L. Morton, and P. Bertet (2023/02/09 2020). "Electron spin resonance spectroscopy with femtoliter detection volume". In: *Applied Physics Letters* 116.18, p. 184002 (cit. on pp. 7, 8).

Regal, C. A., J. D. Teufel, and K. W. Lehnert (2008). "Measuring nanomechanical motion with a microwave cavity interferometer". In: *Nature Physics* 4.7, pp. 555–560 (cit. on p. 3).

Rieger, D., S. Günzler, M. Spiecker, A. Nambisan, W. Wernsdorfer, and I. M. Pop (2022). *Fano Interference in Microwave Resonator Measurements* (cit. on p. 58).

Rigetti, Chad, Jay M. Gambetta, Stefano Poletto, B. L. T. Plourde, Jerry M. Chow, A. D. Córcoles, John A. Smolin, Seth T. Merkel, J. R. Rozen, George A. Keefe, Mary B. Rothwell, Mark B. Ketchen, and M. Steffen (Sept. 2012). "Superconducting qubit in a waveguide cavity with a coherence time approaching 0.1 ms". In: *Phys. Rev. B* 86 (10), p. 100506 (cit. on pp. 73, 85).

Rodrigues, I. C., D. Bothner, and G. A. Steele (2019). "Coupling microwave photons to a mechanical resonator using quantum interference". In: *Nature Communications* 10.1, p. 5359 (cit. on p. 7).

Samkharadze, N, G Zheng, N Kalhor, D Brousse, A Sammak, U C Mendes, A Blais, G Scappucci, and L M K Vandersypen (2018). "Strong spin-photon coupling in silicon". In: *Science* 359 (March), pp. 1123–1127 (cit. on pp. 6–8).

Scarlino, P., J. H. Ungerer, D. J. van Woerkom, M. Mancini, P. Stano, C. Müller, A. J. Landig, J. V. Koski, C. Reichl, W. Wegscheider, T. Ihn, K. Ensslin, and A. Wallraff (July 2022). "In situ Tuning of the Electric-Dipole Strength of a Double-Dot Charge Qubit: Charge-Noise Protection and Ultrastrong Coupling". In: *Phys. Rev. X* 12 (3), p. 031004 (cit. on p. 9).

Schuster, D. I., A. A. Houck, J. A. Schreier, A. Wallraff, J. M. Gambetta, A. Blais, L. Frunzio, J. Majer, B. Johnson, M. H. Devoret, S. M. Girvin, and R. J. Schoelkopf (Feb. 2007). "Resolving photon number states in a superconducting circuit". In: *Nature* 445 (7127), pp. 515–518 (cit. on p. 66).

Schuster, D. I., A. P. Sears, E. Ginossar, L. DiCarlo, L. Frunzio, J. J. L. Morton, H. Wu, G. A. D. Briggs, B. B. Buckley, D. D. Awschalom, and R. J. Schoelkopf (Sept. 2010). "High-Cooperativity Coupling of Electron-Spin Ensembles to Superconducting Cavities". In: *Phys. Rev. Lett.* 105 (14), p. 140501 (cit. on p. 6).

Schuster, D. I., A. Wallraff, A. Blais, L. Frunzio, R.-S. Huang, J. Majer, S. M. Girvin, and R. J. Schoelkopf (Mar. 2005). "ac Stark Shift and Dephasing of a Superconducting Qubit Strongly Coupled to a Cavity Field". In: *Phys. Rev. Lett.* 94 (12), p. 123602 (cit. on p. 74).

Serniak, K., S. Diamond, M. Hays, V. Fatemi, S. Shankar, L. Frunzio, R.J. Schoelkopf, and M.H. Devoret (July 2019). "Direct Dispersive Monitoring of Charge Parity in Offset-Charge-Sensitive Transmons". In: *Phys. Rev. Appl.* 12 (1), p. 014052 (cit. on p. 96).

Shani, Inbar, Emanuele G. Dalla Torre, and Michael Stern (Feb. 2022). "Coherence properties of a spin in a squeezed resonator". In: *Phys. Rev. A* 105 (2), p. 022617 (cit. on pp. 12, 52, 77, 85).

Shen, Li-Tuo, Chun-Qi Tang, Zhicheng Shi, Huaizhi Wu, Zhen-Biao Yang, and Shi-Biao Zheng (Aug. 2022). "Squeezed-light-induced quantum phase transition in the Jaynes-Cummings model". In: *Phys. Rev. A* 106 (2), p. 023705 (cit. on pp. 11, 121).

Siddiqi, I., R. Vijay, M. Metcalfe, E. Boaknin, L. Frunzio, R. J. Schoelkopf, and M. H. Devoret (Feb. 2006). "Dispersive measurements of superconducting qubit coherence with a fast latching readout". In: *Phys. Rev. B* 73 (5), p. 054510 (cit. on p. 119).

Sivak, V.V., N.E. Frattini, V.R. Joshi, A. Lingenfelter, S. Shankar, and M.H. Devoret (May 2019). "Kerr-Free Three-Wave Mixing in Superconducting Quantum Circuits". In: *Phys. Rev. Applied* 11 (5), p. 054060 (cit. on pp. 37, 116).

Slusher, R. E., L. W. Hollberg, B. Yurke, J. C. Mertz, and J. F. Valley (Nov. 1985). "Observation of Squeezed States Generated by Four-Wave Mixing in an Optical Cavity". In: *Phys. Rev. Lett.* 55 (22), pp. 2409–2412 (cit. on p. 13).

Souquet, J-R., M. J. Woolley, J. Gabelli, P. Simon, and A. A. Clerk (2014). "Photon-assisted tunnelling with nonclassical light". In: *Nature Communications* 5.1, p. 5562 (cit. on p. 123).

Steck, Daniel A. (2007). *Quantum and Atom Optics* (cit. on pp. 24, 63, 129).

Stockklauser, A., P. Scarlino, J. V. Koski, S. Gasparinetti, C. K. Andersen, C. Reichl, W. Wegscheider, T. Ihn, K. Ensslin, and A. Wallraff (2017). "Strong coupling cavity QED with gate-defined double quantum dots enabled by a high impedance resonator". In: *Phys. Rev. X* 7 (1), pp. 1–5 (cit. on pp. 6, 8).

Swartz, E. T. and R. O. Pohl (July 1989). "Thermal boundary resistance". In: *Rev. Mod. Phys.* 61 (3), pp. 605–668 (cit. on p. 99).

Teufel, J. D., Dale Li, M. S. Allman, K. Cicak, A. J. Sirois, J. D. Whittaker, and R. W. Simmonds (2011). "Circuit cavity electromechanics in the strong-coupling regime". In: *Nature* 471.7337, pp. 204–208 (cit. on pp. 6, 7).

Tinkham, Michael (1996). *Introduction to Superconductivity: Second Edition*. Dover (cit. on p. 36).

Viennot, J. J., M.C. Dartiailh, A. Cottet, and T. Kontos (2015). "Coherent coupling of a single spin to microwave cavity photons". In: *Science* 349 (6246), pp. 408–411 (cit. on pp. 7, 124).

Viennot, J. J., X. Ma, and K. W. Lehnert (Oct. 2018). "Phonon-Number-Sensitive Electromechanics". In: *Phys. Rev. Lett.* 121 (18), p. 183601 (cit. on pp. 3, 66).

Villiers, M., W. C. Smith, A. Petrescu, A. Borgognoni, M. Delbecq, A. Sarlette, M. Mirrahimi, P. Campagne-Ibarcq, T. Kontos, and Z. Leghtas (2023). "Dynamically enhancing qubit-photon interactions with anti-squeezing". In: arXiv: `2212.04991 [quant-ph]` (cit. on pp. 12, 41).

Vine, Wyatt, Mykhailo Savytskyi, Arjen Vaartjes, Anders Kringhøj, Daniel Parker, James Slack-Smith, Thomas Schenkel, Klaus Mølmer, Jeffrey C. McCallum, Brett C. Johnson, Andrea Morello, and Jarryd J. Pla (Apr. 2023). "In situ amplification of spin echoes within a kinetic inductance parametric amplifier". In: *Science Advances* 9.10, p. 1593 (cit. on pp. 121, 123).

Visser, P. J. De, J. J.A. Baselmans, P. Diener, S. J.C. Yates, A. Endo, and T. M. Klapwijk (2011). "Number fluctuations of sparse quasiparticles in a superconductor". In: *Physical Review Letters* 106 (16), pp. 1–4 (cit. on p. 96).

Vool, Uri and Michel Devoret (2023/02/09 2017). "Introduction to quantum electromagnetic circuits". In: *International Journal of Circuit Theory and Applications* 45.7, pp. 897–934 (cit. on p. 4).

Wallraff, A., D. I. Schuster, A. Blais, L. Frunzio, R. - S. Huang, J. Majer, S. Kumar, S. M. Girvin, and R. J. Schoelkopf (2004). "Strong coupling of a single photon to a superconducting qubit using circuit quantum electrodynamics". In: *Nature* 431.7005, pp. 162–167 (cit. on pp. 6, 52).

Walls, D. F. (1983). "Squeezed states of light". In: *Nature* 306.5939, pp. 141–146 (cit. on pp. 9, 13, 15).

Walls and Milburn (2008). *Quantum Optics*. Springer (cit. on p. 16).

Wang, C., Y. Y. Gao, I. M. Pop, U. Vool, C. Axline, T. Brecht, R. W. Heeres, L. Frunzio, M. H. Devoret, G. Catelani, L. I. Glazman, and R. J. Schoelkopf (2014). "Measurement and control of quasiparticle dynamics in a superconducting qubit". In: *Nature Communications* 5 (1), pp. 1–7 (cit. on p. 96).

Wellstood, Frederick C., Cristian Urbina, and John Clarke (1987). "Low-frequency noise in dc superconducting quantum interference devices below 1 K". In: *Applied Physics Letters* 50 (12), pp. 772–774 (cit. on p. 97).

Wilen, C. D., S. Abdullah, N. A. Kurinsky, C. Stanford, L. Cardani, G. D'Imperio, C. Tomei, L. Faoro, L. B. Ioffe, C. H. Liu, A. Opremcak, B. G. Christensen, J. L. DuBois, and R. McDermott (2021). "Correlated charge noise and relaxation errors in superconducting qubits". In: *Nature* 594.7863, pp. 369–373 (cit. on p. 96).

Woods, W., G. Calusine, A. Melville, A. Sevi, E. Golden, D.K. Kim, D. Rosenberg, J.L. Yoder, and W.D. Oliver (July 2019). "Determining Interface Dielectric Losses in Superconducting Coplanar-Waveguide Resonators". In: *Phys. Rev. Appl.* 12 (1), p. 014012 (cit. on pp. 97, 98).

Wu, Ling-An, H. J. Kimble, J. L. Hall, and Huifa Wu (Nov. 1986). "Generation of Squeezed States by Parametric Down Conversion". In: *Phys. Rev. Lett.* 57 (20), pp. 2520–2523 (cit. on pp. 13, 15).

Xiang, Ze-Liang, Sahel Ashhab, J. Q. You, and Franco Nori (Apr. 2013). "Hybrid quantum circuits: Superconducting circuits interacting with other quantum systems". In: *Rev. Mod. Phys.* 85 (2), pp. 623–653 (cit. on pp. 4, 5).

Xie, Ji-kun, Sheng-li Ma, Ya-long Ren, Xin-ke Li, and Fu-li Li (Jan. 2020). "Dissipative generation of steady-state squeezing of superconducting resonators via parametric driving". In: *Phys. Rev. A* 101 (1), p. 012348 (cit. on p. 121).

Yan, Fei, Simon Gustavsson, Archana Kamal, Jeffrey Birenbaum, Adam P Sears, David Hover, Ted J. Gudmundsen, Danna Rosenberg, Gabriel Samach, S. Weber, Jonilyn L. Yoder, Terry P. Orlando, John Clarke, Andrew J. Kerman, and William D. Oliver (2016). "The flux qubit revisited to enhance coherence and reproducibility". In: *Nature Communications* 7.1, p. 12964 (cit. on p. 97).

Yurke, B., L. R. Corruccini, P. G. Kaminsky, L. W. Rupp, A. D. Smith, A. H. Silver, R. W. Simon, and E. A. Whittaker (Mar. 1989). "Observation of parametric amplification and deamplification in a Josephson parametric amplifier". In: *Phys. Rev. A* 39 (5), pp. 2519–2533 (cit. on p. 13).

Zeytinoğlu, Sina, Ataç İmamoğlu, and Sebastian Huber (June 2017). "Engineering Matter Interactions Using Squeezed Vacuum". In: *Phys. Rev. X* 7 (2), p. 021041 (cit. on p. 10).

Zhong, Changchun, Mingrui Xu, Aashish Clerk, Hong X. Tang, and Liang Jiang (Oct. 2022). "Quantum transduction is enhanced by single mode squeezing operators". In: *Phys. Rev. Research* 4 (4), p. L042013 (cit. on pp. 10, 121).

Zhu, C. J., L. L. Ping, Y. P. Yang, and G. S. Agarwal (Feb. 2020). "Squeezed Light Induced Symmetry Breaking Superradiant Phase Transition". In: *Phys. Rev. Lett.* 124 (7), p. 073602 (cit. on pp. 11, 121).

Pierre Soulages (Rodez, 1919 - Nîmes, 2022)
Peinture, 324 x 362 cm (Polyptyque J), 1987
Huile sur toile, 324 x 362 cm
Musée cantonal des Beaux-Arts de Lausanne. Don de Pierre Soulages en hommage à Olivier Pauli, 2017
Inv. 1999-06

Dynamically Enhancing Qubit-Photon Interactions with Anti-Squeezing

Marius Villiers
Quantic team

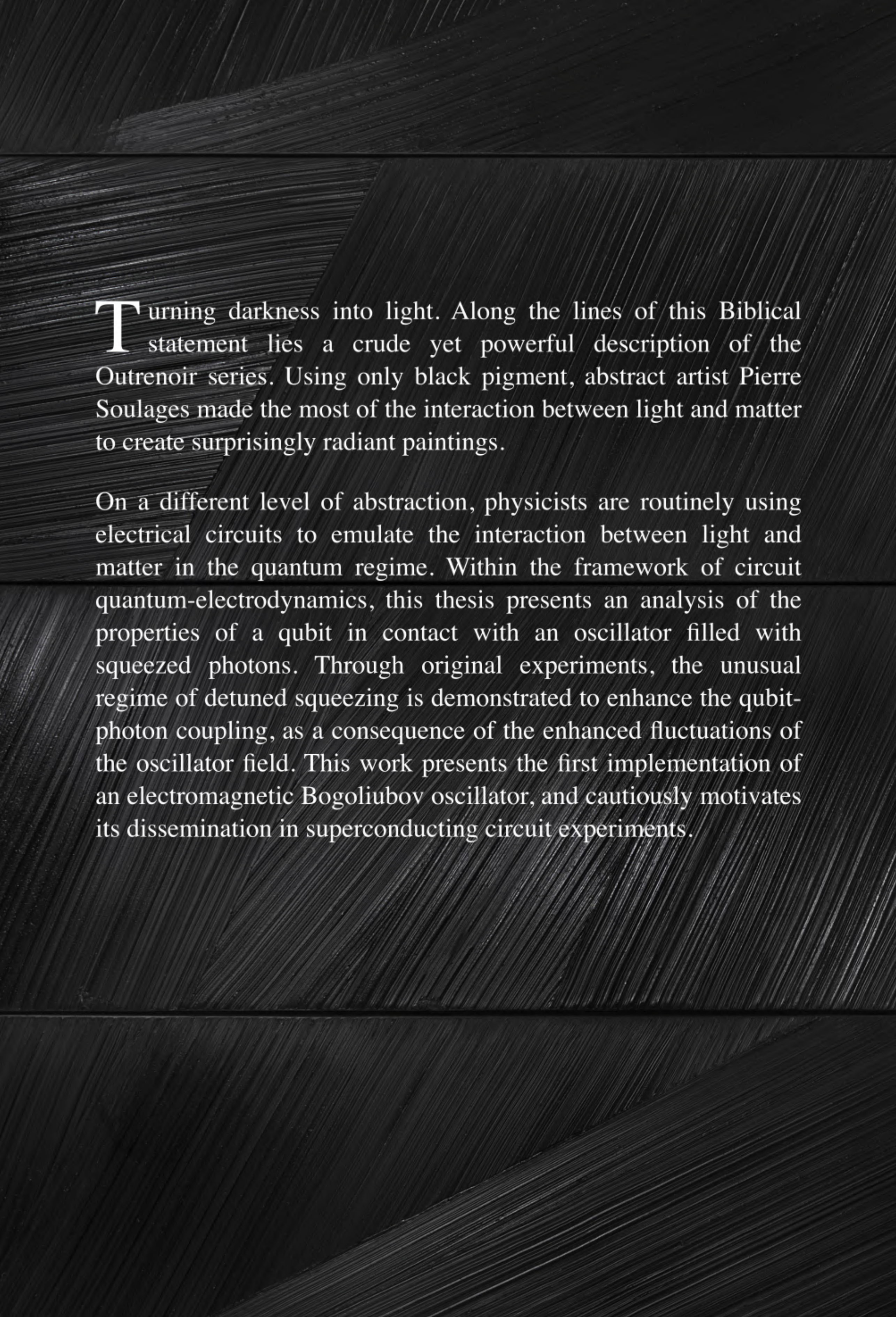

Turning darkness into light. Along the lines of this Biblical statement lies a crude yet powerful description of the Outrenoir series. Using only black pigment, abstract artist Pierre Soulages made the most of the interaction between light and matter to create surprisingly radiant paintings.

On a different level of abstraction, physicists are routinely using electrical circuits to emulate the interaction between light and matter in the quantum regime. Within the framework of circuit quantum-electrodynamics, this thesis presents an analysis of the properties of a qubit in contact with an oscillator filled with squeezed photons. Through original experiments, the unusual regime of detuned squeezing is demonstrated to enhance the qubit-photon coupling, as a consequence of the enhanced fluctuations of the oscillator field. This work presents the first implementation of an electromagnetic Bogoliubov oscillator, and cautiously motivates its dissemination in superconducting circuit experiments.